



**Politecnico
di Torino**

ScuDo
Scuola di Dottorato ~ Doctoral School
WHAT YOU ARE, TAKES YOU FAR

Doctoral Dissertation
Doctoral Program in Mechanical Engineering (36th Cycle)

**A combined analytical, numerical and experimental
technique for investigating stress-singularity effects
on Very High Cycle Fatigue of adhesive joints**

Davide Pederbelli

Supervisors

Prof. Luca Goglio, Supervisor

Prof. Davide Salvatore Paolino, Co-Supervisor

Doctoral Examination Committee:

Prof. Filippo Berto, *Referee*, Università La Sapienza, Italy

Dr. Ausonio Tuissi, *Referee*, CNR - ICMATE, Italy

Prof. Andrea Bernasconi, Politecnico di Milano, Italy

Prof. Massimo Rossetto, Politecnico di Torino, Italy

Prof. Andrea Tridello, Politecnico di Torino, Italy

Politecnico di Torino
June 2024

Declaration

I hereby declare that the contents and organisation of this dissertation constitute my own original work and does not compromise in any way the rights of third parties, including those relating to the security of personal data. The writing of the following manuscript was performed without the use of AI programs.

The work presented in this manuscript is based on the following papers published on international journals:

- D. Pederbelli, A. Tridello, D. S. Paolino, L. Goglio, Effects of singular and non-singular stress fields on very high cycle fatigue life of adhesive joints, *Fatigue & Fracture of Engineering Materials & Structures*, 2023, 47 (1), 124 – 139, <https://doi.org/10.1111/ffe.14171>
- D. Pederbelli, L. Goglio, D. S. Paolino, M. Rossetto, A. Tridello, Effect of loading frequency on the fatigue response of adhesive joints up to the VHCF regime, *Applied Sciences*, 2023, 13 (23), 12967, <https://doi.org/10.3390/app132312967>

The PhD defence is presented in complete fulfilment of the Doctorate School (ScuDo) requirements of Politecnico di Torino for obtaining the Doctoral title.

.....

Davide Pederbelli

Turin, 20th June 2024

Abstract

Modern engineered structures are currently developed with advanced materials for improving mechanical performances or to better meet the design requirements. For example, the capability to withstand multiple combinations of design loads or the in-service solicitations in a broad frequency spectrum. To do so, lightweight design approaches combining the simultaneous adoption of different materials are typically followed. In this regard, an efficient method for coupling different mechanical components is performed by using adhesive joints. These materials have the capability to save mass, connect different shapes and ensure a smoother stress distribution compared to conventional joining methods (e.g., welding, riveting, ...).

An issue that often arises in designing adhesively bonded joints regards the presence of stress-singularities. These originate at the material interface as a consequence of discontinuities in the boundary conditions. Singular stress fields represent a concern during the design of mechanical connections as they could trigger cracks within the joint. Under severe loads plasticity can compensate the singularity effects, nevertheless under low-amplitude loads this feature could weaken the joint integrity, reducing its service life and thus generating failures. Appropriate design plans should therefore be implemented to produce more reliable apparatus.

Moreover, structural design and analysis approaches assume mechanical properties in numerical codes as frequency, or load, independent for simplicity of calculation or due to the lack of experimental data. Such approach could lead to under/overestimate the structural responses, implying overdesign or failures in static, dynamic, thermal, or cyclic loading conditions.

The work proposed in this manuscript investigates both the effects of singular and non-singular stress fields on the Very High Cycle Fatigue (VHCF) performance of adhesively bonded butt-joints (aluminium 7075 T6 - SikaPower®-1277 Epoxy resin) and loading-frequency effects under conventional excitations (i.e., 5, 25, 50 Hz) and the ultrasonic ones (i.e., 20 kHz) adopted in VHCF. To do so, analytical, numerical and experimental methods have been adopted. Analytical models were used for both design the VHCF specimen and for achieve a stress singularity-free joint. Numerical techniques of Global-Local Finite Elements type studied the stress distributions in detail. Finally, fatigue experiments in both HCF and VHCF extracted S–N outcomes ad probability assessments were performed by using ad-hoc developed statistical models.

The suitability of the overall approach is numerically confirmed and a substantial increase of the joint life is experimentally observed if the singularity is removed. Nonetheless, a non-singular configuration leads to higher scatter data compared to the original specimen configuration.

Fatigue tests assessing the loading-frequency effects have shown an important impact of this phenomenon for the investigated adhesive. Indeed, test data present a clear separation, in the range of order of magnitudes of cycles, between low and high frequencies. The interpolation of fatigue strengths at $N=2 \cdot 10^6$ suggests a precise trend and such information is exploitable to extract values out of the experimental range. The experimental variability is present but has a minor impact on data.

Contents

<i>List of Figures</i>	1
<i>List of Tables</i>	4
1 <i>Introduction</i>	6
2 <i>Theoretical background</i>	14
2.1 <i>Adhesive joints</i>	14
2.1.1 <i>Main aspects of this technology</i>	14
2.1.2 <i>Fundamental models to assess the joint stress distribution.</i>	28
2.2 <i>Very High Cycle Fatigue</i>	47
2.2.1 <i>State of the Art for adhesive joints.</i>	49
2.2.2 <i>Testing machines</i>	52
2.3 <i>Statistical methods for S-N curves</i>	57
2.3.1 <i>Elements of Probability</i>	57
2.3.2 <i>A statistical fatigue model</i>	60
2.4 <i>Stress singularity</i>	67
2.4.1 <i>Bogy mathematical framework</i>	81
2.4.2 <i>Removal of the stress-singularity</i>	96
2.5 <i>Strategies to reduce the numerical model size</i>	98
2.5.1 <i>Sub-Modelling</i>	99
2.6 <i>1D Axial vibrations</i>	106
3 <i>A combined analytical, numerical and experimental technique for investigating stress-singularity effects on VHCF of adhesive joints</i>	109
3.1 <i>Preparatory activities: mechanical tests of the bulk adhesive and aluminium specimens</i>	109
3.2 <i>VHCF specimen design and analysis</i>	114

3.3	<i>Removal of the stress-singularity and model analysis</i>	122
3.4	<i>Development of Global-Local FE models: approaches and results</i>	131
3.5	<i>The joint manufacturing</i>	147
3.6	<i>Preliminary static tests</i>	150
3.7	<i>VHCF tests</i>	151
3.8	<i>Assessing loading-frequency behaviours</i>	160
4	<i>Conclusions</i>	167
	<i>Bibliography</i>	171

List of Figures

<i>Figure 1: Possible welding issues.</i>	17
<i>Figure 2: Example of failure mode for a composite plate with a fastener connection. Original from [48].</i>	18
<i>Figure 3: Examples of hybrid joints.</i>	20
<i>Figure 4: Configurations of adhesive joints. Original from [68].</i>	26
<i>Figure 5: Main failure modes of adhesive joints: (a) cohesive failure, (b) adhesive failure, (c) substrate failure.</i>	27
<i>Figure 6: Single-lap joint under traction loads. Original from [73]</i>	29
<i>Figure 7: Single-lap joint model under Volkersen analysis. Original from [73]</i>	30
<i>Figure 8: Elastic and plastic distribution within the bond line. Original from [72].</i>	33
<i>Figure 9: Elemental diagram of the adherend-adhesive sandwich. Original from [92].</i>	35
<i>Figure 10: Some joint configurations. Original from [92]</i>	36
<i>Figure 11: Example of tubular joint. Original from [77]</i>	38
<i>Figure 12: Infinitesimal element of a tubular joint. Original from [77]</i>	39
<i>Figure 13: Explored bonded structures. Original from [103].</i>	42
<i>Figure 14: Physical and numerical interpretation of CZM.</i>	45
<i>Figure 15: Mixed-mode CZM. Original from [129]</i>	46
<i>Figure 16: Zero-thickness CZM elements.</i>	46
<i>Figure 17: The fish-eye morphology in VHCF failures of metallic materials. Original from [136]</i>	49
<i>Figure 18: Specimen with defects: (a) internal, (b) external, (c) internal and external. Original from [21]</i>	50
<i>Figure 19: Fracture surfaces for (a) original specimen and with (b) internal, (c) external, (d) internal and external defects. Original from [21].</i>	51
<i>Figure 20: Time investment for performing VHCF test up to 10^7 (grey) and 10^8 (green). Original from [19].</i>	52
<i>Figure 21: Schematic description of UFTM.</i>	54
<i>Figure 22: UFTM developed at Politecnico di Torino</i>	56
<i>Figure 23: Example of a Duplex S - N curve.</i>	60

Figure 24: Example of a corner between different material interfaces where a singular stress profile can be foreseen	68
Figure 25: Modelling a singular corner with enriched, transition and standard Finite Elements	81
Figure 26: Bonded wedges under normal and shear loading. Original from [178].	82
Figure 27: Parallelograms of physically relevant material combination. Origin from [178].	85
Figure 28: Roots for single material wedges. Original from [178]	87
Figure 29: Real solutions for $D(a, b, \alpha, \beta; p) = 0$. Equal wedge case. Original form [178].	90
Figure 30: Complex solutions for $D(a, b, \alpha, \beta; p) = 0$. Equal wedge case. Original form [178].	91
Figure 31: Solutions for $D(a, b, \alpha, \beta; p) = 0$. Composite Half Plane. Original form [178]	93
Figure 32: Solutions for $D(a, b, \alpha, \beta; p) = 0$. Composite Full Plane. Original form [178]	95
Figure 33: Global-local models of a structure [207]	100
Figure 34: Terminology and main steps of the global-local methodology [207]	102
Figure 35: Scheme for global-local procedure [207]	103
Figure 36: Schematic representation of the zooming technique [15]	104
Figure 37: Schematic representation of different hierarchical mathematical models. Original from [15]	105
Figure 38: Vibrations of 1D structures [210].	107
Figure 39: Shape of the aluminium specimen ($A=70\text{mm}$, $B=55\text{mm}$, $C=20\text{mm}$, $G=50\text{mm}$, $L=200$, $R=15\text{mm}$, $T=5\text{mm}$, $W=12.5\text{mm}$).	110
Figure 40: Shape of the bulk adhesive specimen ($=4\text{mm}$, $=12.5$, $=50\text{mm}$, $=20$, $=12\text{mm}$, 75mm (75), $=8\text{mm}$, $=12.5$, $=2$)	110
Figure 41: Produced adhesive specimens.	111
Figure 42: Tensile testing phase.	112
Figure 43: Stress-strain curves of the bulk adhesive.	113
Figure 44: The work-flow to achieve a VHCF specimen. Original from [215]	114
Figure 45: Axisymmetric horn configuration.	115
Figure 46: Simulated testing condition with properly applied displacements	117
Figure 47: Current longitudinal stress distribution for the $18\ \mu\text{m}$ displacement case	118
Figure 48: Singular VHCF adhesive joint.	118
Figure 49: Longitudinal stress distribution for the selected level of external displacements. Original from [215]	119
Figure 50: VHCF adhesive joint modal shapes.	122
Figure 51: Design maps defining the presence/absence of the stress-singularity. Original from [216]	125
Figure 52: Angular evolution of the Bogy determinant, Plane strain solutions.	126
Figure 53: Angular evolution of the Bogy determinant, Plane stress solutions.	127
Figure 54: Bogy determinant for each explored adhesive angle, Plane strain conditions.	128
Figure 55: Bogy determinant for each explored adhesive angle, Plane stress conditions.	128
Figure 56: Singularity-free VHCF specimen, FE description. Original from [215]	129

Figure 57: Trends of extracted elastic natural frequencies. _____	130
Figure 58: Sub-model for the singular specimen. Original from [215] _____	132
Figure 59: Sub-model for the non-singular specimen. Original from [215] _____	133
Figure 60: Longitudinal displacements, left interface. _____	134
Figure 61: Longitudinal displacements, right interface. _____	134
Figure 62: Longitudinal deformations, left interface. _____	135
Figure 63: Longitudinal stress, left interface. _____	136
Figure 64: Longitudinal deformations, right interface. _____	136
Figure 65: Longitudinal stress, right interface. _____	137
Figure 66: Longitudinal stress distribution, singular model. Original from [215] _____	138
Figure 67: Longitudinal stress distribution, non-singular model. Original from [215] _____	139
Figure 68: SIF investigations, left interface. _____	141
Figure 69: SIF investigations, right interface. _____	141
Figure 70: Directions for stress recovery. Original from [215] _____	143
Figure 71: Longitudinal stress on the T-direction. Original from [215] _____	144
Figure 72: Longitudinal stress on the R-direction. Original from [215] _____	145
Figure 73: Transversal stress on the R-direction. _____	146
Figure 74: Shear stress on the R-direction. _____	146
Figure 75: Set of singular specimens. _____	148
Figure 76: Set of non-singular specimens. _____	148
Figure 77: Manufacturing and joining process: (a) application of the adhesive in a liquid phase; (b) alignment of the joint _____	149
Figure 78: Singular and non-singular load-displacement curves. _____	150
Figure 79: Singular (a) and non-singular (b) setups during VHCF tests. Original from [215] _____	152
Figure 80: S-N raw data after failures or run-out. Original from [215] _____	153
Figure 81: Fracture surfaces of non-singular specimens. _____	156
Figure 82: Fracture surfaces of singular specimens. _____	157
Figure 83: P-S-N curves for singular and non-singular cohesive failures. Original from [215] _____	158
Figure 84: Longitudinal stress map resulting from a quasi-static loading condition. Original from [216] _____	161
Figure 85: Recovered stress for the static and dynamic case. Original from [216] _____	162
Figure 86: Boundary conditions derived from the testing configuration. _____	163
Figure 87: Loading-frequency S-N raw data after failures or run-out. _____	164
Figure 88: P-S-N curves at P=50% assessing loading-frequency effects between VHCF and conventional fatigue tests. Original from [216] _____	165
Figure 89: Strength distribution for 10%, 50%, 90% probability levels at $N=2 \cdot 10^6$ cycles. Original from [216] _____	166

List of Tables

<i>Table 1: Williams results from [161]</i>	70
<i>Table 2: Mathematical features for Fixed-Free and Free-Free configurations</i>	108
<i>Table 3: Material properties extracted by tensile test or referenced by literature</i>	113
<i>Table 4: Extracted natural frequencies.</i>	116
<i>Table 5: Local geometrical conditions that avoid the stress-singularity.</i>	124
<i>Table 6: SIF and singularity exponent investigations</i>	142
<i>Table 7: Standard deviation form processed data with ML and optimization.</i>	165

1 Introduction

Engineering practice makes extensive use of advanced materials for creating cutting-edge and market-competitive products in many technological sectors. Indeed, due to several factors like more stringent pollution regulations, mission profile constraints and the general interest for improving the product performances, nowadays mechanical components are specifically thought and developed to be light weight with distinctive requirements of strength, toughness, fatigue and dynamic performances. This means that a technological transition, from using classical configurations and materials in favour of innovative ones, is taking place. For example, when convenient and possible from a manufacturability perspective, metal components are replaced with ad-hoc designed carbon-fibre parts whereas connection elements, such as mechanical joints, are designed accordingly [1].

In a complex mechanical system, whatever the specific domain and application of interest, mechanical joints accomplish the specific purpose of connecting structural members for transmitting forces and moments from a member to another and their proper working conditions during the whole mission lifespan is one of the major concern for designers, analysts and test specialists. In practice, joints are considered as the “weakest ring” in the system chain and their failure could produce catastrophic collapses in the absence of specific redundancies properly accounted for fail-safe or safe life approaches.

Among the several types of joints, structural adhesives represent an interesting alternative to conventional connection techniques [2], even though each type of joint presents specific advantages and disadvantages. For example, if compared

with welding or riveting, adhesives do not alter the mechanical or the thermal properties of the substrate material. Moreover, they do not introduce macroscopic stress concentrations introduced by a clamped threaded element or by permanent residual stresses [3]. The use of adhesive as a joining substance allows reducing the overall mass budget by removing the presence of additional elements (e.g., rivets, nuts,...) as well as permits a permanent connection between substrate of different materials (e.g., metal-composite, composite-ceramic, etc,...). Furthermore, complex shapes (e.g., curved, not straight or not flat) can be easily joined by adhesive as it is liquid in the initial state.

There are many engineering field that exploit the interesting features of adhesive such as in the aerospace for improving the connection performances between parts of different materials [4] or as innovative method for capturing space debris for future space missions [5]. In this regard, many configurations can be distinguished as the so-called single or double-lap joint, stepped joint, butt-joint or tubular joint, just to mention a few among all the possible shapes. Using a configuration instead of another one requires the adoption of suitable mathematical models, analytical or numerical. These should be capable of correctly capturing the behaviours of interest in order to have a clear picture of the current internal stresses, comparing them with allowable material properties, extracting the failure reservoir according to a failure theory and then assessing the margin of safety.

As mentioned before, each joint configuration requires a specifically developed mathematical model and the interest in such research activities are still progressing since the early 50's [6]. Most of them can describe the overall structural behaviours with a reasonable level of accuracy as [7–9]. Nevertheless, localized features, such as stress singularities, are often not predictable from both analytical and numerical schemes [10]. In general, a stress singularity is a point region in a component where the stress magnitude is infinite and the main reasons that trigger such features are ascribable to material and geometrical facts. Indeed, in an adhesive joint stress singularities arise due to the material discontinuities introduced by the adhesive layer itself, between two or more material substrates, under specific and localized angular conditions. From the mathematical perspective, modelling a stress singularity requires the adoption of specific techniques and calculation schemes as [11,12]. Analytical models accounting for it

are typically solved by using eigenproblems in which the problem unknown is the so-called singularity exponent. Numerical schemes based on Finite Elements implement singularity-based nodal formulations, capable of capturing both the stress trends far from the singular region and those very close to it [13].

With specific emphasis on numerical aspects for studying the stress singularity, a major issue regards the size of the Finite Elements model. Indeed, for capturing the singularity, progressive mesh refinements are needed, even up to an approximate element size of 10^{-5} mm [14], which means that the model could be described by hundred thousand elements. Model sizes like this can significantly slow down the analysis procedure or even prohibit the analysis phase. To overcome this issue, specific Finite Element procedures as the so-called Global-Local (or Submodelling) schemes permit to increase the detail of investigation while keeping the model size manageable from conventional personal computer or work stations [15].

The study of stress singularity with analytical, numerical and experimental methods is of particular importance for predicting the joint failure. Indeed, adhesive joints can be subjected to three main classes of failure modes, namely the cohesive (i.e., the inter-adhesive), the adhesive (i.e., the disconnection from the substrate) and the substrate failure. In the everyday practice, adhesive joints are designed to withstand the acting loads with a margin, but, if the failure cannot be avoided, this has to be of cohesive type. In fact, a cohesive failure is associated with the capability of sustaining the highest loads whereas the adhesive with the lowest one. In this regard, stress singularities make prone the joint to fail under an adhesive mode as this feature is localized at the adhesive-substrate interface thus reducing the joint performances. For that reason, the problem of stress singularity is experiencing innovative analysis techniques aiming at improving the mechanical design. Indeed, if in the past, the analysis of the stress singularity just wanted to understand the severity of the singularity under prescribed geometrical and mechanical conditions, recent approaches intend to figure out the conditions that prevent the emerging of singularity under load events [16,17]. Approaches like this allow to increase the capability of sustaining loads in a more effective and efficient manner as well as the joint endurance under fatigue actions.

With respect to fatigue, the conventionally explored range is up to $10^6 - 10^7$ cycles, namely the High Cycle Fatigue (HCF) range, and components that express run-out data within this interval are typically thought as endowed of an infinite fatigue life. Up to this interval, material characterizations are typically performed with hydraulic machines as this equipment can easily sustain related testing times. However, more advanced engineering products are requested to work even further than 10^7 cycles under stress magnitudes below the conventional fatigue limit. These conditions are associated with the so-called Very High Cycle Fatigue (VHCF, $N > 10^7$) range [18]. In the VHCF, experimental campaigns cannot equip themselves with conventional machines, like in the HCF, since testing just one sample could take about one year (e.g., if $N = 10^9$). For that reason, Ultrasonic Fatigue Testing Machines (UFTM) that work at 20 kHz are adopted to speed up the testing time [19].

If for metal structures the cornerstone capable of describing the mechanical behaviour in VHCF is pretty clear, in the case of adhesive joints similar conclusions are still progressing [20,21]. As a general observation, the VHCF of metal expresses a different failure mode, namely from an external-initiating to an internal-initiating crack nucleation (e.g., from a defect, inclusion or a void), which is associated to particular geometrical patterns describing the failure surfaces. In the case of adhesive, even though some VHCF experiments have been performed, their amount is still not enough for extracting phenomenological laws and final conclusions. In general, the existence of possible failure modes when passing from HCF to VHCF in the $S - N$ diagram requires the adoption of specific methods for describing experimental fatigue curves. For that purpose, advanced statistical models capable of taking into account both specimen failures and run-out have been developed and applied [22].

Another critical point for materials and components in general pertains the existence of strain-rate and loading-frequency effects during the in-service operations as a result of fluctuating loads with different frequencies or speeds of application [23]. Such effects are complex and potentially harmful for the safe working conditions. Indeed, loading-frequency effects affect both the nominal fatigue life and the mechanical strengths [24]. In fact, under such occurrences, mechanical features tend to diminish as the frequency of application increases. This could lead to anticipated failures or unexpected dynamic responses. Loading-

frequency and strain-rate behaviours are complex to be properly captured and anticipated. For example, due to the lack of experimental findings, or due to a simplistic modelling approach, analysts and designers in charge of the project tend to assume that load and frequency are independent material properties. This assumption is not a-priori wrong but should be assessed case-by-case. A schematization like this could be valid for metallic structures but too restrictive in the case of high-performance structures that are produced with engineered materials.

The work presented in this thesis provides analytical, numerical and experimental investigations on the fatigue performances of adhesive joints. More specifically, adhesively bonded joint combining metal substrates with an epoxy resin (aluminium 7075 T6 – SikaPower® 1277) are studied under VHCF loads properly applied with UFTM apparatus. Two main classes of joints are of special interest, namely singular and non-singular, and experiments aim at understanding and quantifying the consequences of both the presence and the absence of the stress singularity on fatigue endurance. Statistical aspects of this occurrence are studied accordingly. To accomplish this purpose, analytical relationships for designing the specimen and for removing the stress singularity are applied. Numerical schemes, which belong to the class of Global-Local Finite Element procedure, precisely extract the stress distribution near the critical region of material interface under test loads. Once accomplished this first research step, the specimen in the best experimental conditions (i.e., the non-singular specimen) undergoes to low-frequency fatigue test in order to characterize and extract structural behaviours as a consequence of loading-frequency effects.

The work is organized into three main chapters. Chapter 2 offers a literature and conceptual survey of theoretical aspects and methods that will be further exploited for the applied research. Precisely, Section 2.1 offers a description of the adhesive technology from historical developments, applicative perspectives and comparison with respect to classical joining procedures. Moreover, the fundamental and the most widely known mathematical models (i.e., analytical and numerical) assessing the stress distribution within the joint will be presented and reviewed in detail. Section 2.2 focuses on VHCF aspects. Specific features arising in this innovative fatigue regime, the mechanical testing techniques that are necessary to explore it, as well as the state of the art for adhesively bonded joint

will be illustrated. Discussing fatigue aspects, Section 2.3 outlines statistical aspects when dealing with S – N curve. Thus, a generalized statistical fatigue model capable of taking into account data from both failed specimens and run-out will be presented and illustrated. Section 2.4 discusses the presence of stress singularities in mechanical components, the mathematical models developed to account for it, with special emphasis on the Bogy mathematical framework, then the numerical strategy for removing such features from any physical specimen. Section 2.5 provides details regarding Finite Element techniques for both reducing the numerical model size and for increasing the detail of the investigation without blowing up the model size. Then, in Section 2.6 a quick revision of the mathematical equation of 1D vibrating structure is covered. Indeed, such model will drive the design of the VHCF specimen.

Chapter 3 addresses the applied research. In this part, the analytical, the numerical and the experimental methods, previously introduced, will be applied for investigating the mechanical performances of the selected adhesively bonded butt-joints under alternated tension – compression loads. Precisely, in the VHCF range, the consequences of the presence and the absence of the stress singularity on the joint life will be the point of interest. Once understood such behaviours, the specimen in the best mechanical condition (i.e., without stress singularity) will undergo conventional low-frequency fatigue tests for assessing and quantifying the loading-frequency effects.

Section 3.1 describes the preliminary activities that were performed for characterizing the bulk materials according to existing standards. Section 3.2 accounts for the VHCF specimen design. In this context, analytical and numerical procedures will be adopted for extracting the nominal (i.e., singular) test item to be tested. In Section 3.3 the previously developed singular specimen is properly modified according to the geometrical information that were extracted from the Bogy inverse mathematical framework. Section 3.4 investigates the current stress distribution under applied loads with properly developed Global–local FE models. These analyses aim at confirming the goodness of the analytical approach and the magnitude of the stress levels sustained by the adhesive layer. Section 3.5 provides details in the merit of the technological and the manufacturing procedures for producing the specimens to test. Section 3.6 exposes the experimental outcomes of static tests that were performed for assessing the

similarities in terms of static responses between singular and non-singular components. Section 3.7 focuses on ultrasonic VHCF testing and related experimental outcomes in terms of probability – stress – number of cycle (P – S – N) curves between singular and non-singular specimens and fracture surfaces. Then, Section 3.8 addresses the further experimental campaign on loading-frequency behaviours, conducted through a conventional Instron® hydraulic testing machine, thus comparing such results to those from VHCF.

Finally, Chapter 3 specifically collects and summarizes the main findings of the research work.

2 Theoretical background

2.1 Adhesive joints

2.1.1 Main aspects of this technology

The adhesion technology has a long story over centuries. A full and comprehensive definition of the term “adhesion” is not straightforward and the commonly accepted one was proposed by Wu [25]: “*Adhesion refers to the state in which two dissimilar bodies are held together by intimate interfacial contact such that mechanical force or work can be transferred across the interface. The interfacial forces holding the two phases together may arise from van der Waals forces, chemical bonding, or electrostatic attraction. Mechanical strength of the system is determined not only by the interfacial forces, but also by the mechanical properties of the interfacial zone and the two bulk phases.*” In this context, adhesives are one of the most exploited possibilities to accomplish the purposes of the adhesion. Adhesives are materials that can guarantee a permanent joining between two similar or dissimilar substrates. The spreading of adhesives on both sides of substrates creates bonds that, after the curing process, establish the mechanical continuity of a single body thus transmitting and distributing stresses between members.

One of the earliest discovery of adhesive bonding applications dates back to the Middle Pleistocene era ($\approx 200\,000$ years ago) for joining stones with a birch-bark-tar adhesive [26], namely a plant-based substance. Throughout the human history, both Neanderthal and middle-age populations used and implemented different types of materials such as gums, plant resins and bitumen, for the purpose of joining parts to make tools, or to improve waterproofing and sealing performances of materials [27]. Evidence of applications was also found from ancient Egyptians

for manufacturing papyrus as well as from ancient Greek and ancient Romans for the construction of Colosseum and Pantheon [28]. Moreover, according to the Greek myth of Dedalus and Icarus, a wax joining material was employed in the production of feathers wings to escape from the Minotaur labyrinth. Other unconventional uses of adhesive mechanisms have been also recognized in nature among animal and vegetable species as material for elaborating traps [29].

Even though the first constituents of adhesives were totally composed by nature-based material due to the available substances, the greatest technological advancement in this domain is ascribable from about 1900s. From that moment, the development and the application of the first engineered materials was pushed forward. Currently, adhesives are composed by polymeric chains (e.g., in the form of epoxy, polyurethane or acrylic forms). Adhesives typologies can be classified in two main categories namely structural and non-structural. The class of structural adhesives aims at connecting materials which can be subjected to severe stress states. This class should provide specific mechanical performances in terms of strength and stiffness as well as durability and aging capabilities. Non-structural adhesive, by contrast, are also named as holding adhesives as they are not required to carry intense loads. Typically, packaging and pressure-sensitive tapes belong to this class.

Nowadays, adhesives of the structural class find widespread applications in many technological fields due to their capabilities of joining both equal and different materials (e.g., metals-to-metals, metals-to-composites, ceramics-to-composites,...) without introducing damages to the substrate materials like in the case of conventional joining methods. Moreover, adhesives can offer a permanent connection while expressing almost smooth stress profiles along the bonding line. This aspect is of prominent importance as the key function of an adhesive connection is to transfer load thus creating a load path between the substrates even in the case of curved or not-smooth surfaces that could be not easily jointed. Above all, the aeronautic and aerospace make extensive use of adhesively bonded technologies particularly for mass saving purposes or for increasing the reliability of the connection. Indeed, adhesive are currently adopted for connecting both primary and secondary structures of airplanes [30], launch vehicle and rockets [31] and for repairing purposes [32]. Other non-conventional applications in this field regard the use of adhesive for capturing and removing space debris [5]. The

adoption of adhesives is not restricted to the aerospace field and it is undoubtedly widely applied in the automotive industry in the form of a single or a multi-material constituent [33], for repairing purposes [34] and for reducing the system mass thus achieving reduced consumptions. Other remarkable applications that are worth mentioning are in the field of marine for bonding parts of vessels [35] and medical implementations [36]

In the following, the main aspect of the adhesive joint technology compared with respect to classic joining methods, advantages and disadvantages of this technology, typical configurations and failure modes, will be presented and reviewed.

- Conventional joining methods Vs adhesive joints

Engineering products make extensive use of connection techniques for joining simple or complex shapes as well as similar and dissimilar materials to establish the mechanical continuity for creating a load path, toughening specific zones of a component or for repairs purposes. Currently, there are many possibilities for connecting materials such as welding or fastening but all of them have several drawbacks for which the use of adhesive technologies is considered an excellent candidate for a possible replacement. The choice of which joining technique should be used depends on several factor such as reliability and accessibility levels, mechanical performance to be achieved, environmental conditions and, last but not least, developing and production costs.

Whatever the specific methodology (e.g.,TiG, MIG,...), welding structures offer a permanent connection among components. However, this methodology directly implies the alteration of the basic material thus provoking mechanical and thermal distortions. Performances of structures exploiting such joining technique are particularly sensitive in the area of the welded toe, which is the weakest ring of the whole connection as depicted in Figure 1. Welding defects like incomplete penetration, material excess and the presence of impurities in the welding toe [37] as well as residual stresses after the joining process [38] and the quality and the shape [39,40] of the welding toe, are the main root causes of failures. Especially, the presence of such defects affects fatigue life performances [41] and crack growth mechanisms [42]. Moreover, not all the materials can be welded together but they have to respect physical and chemical requirements.

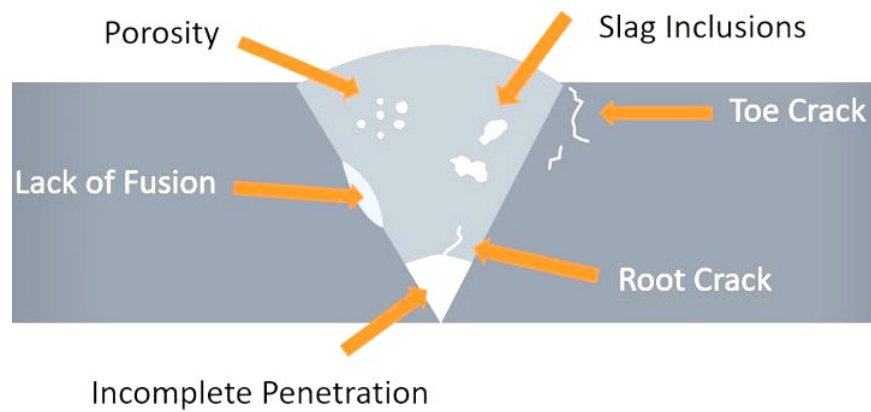


Figure 1: Possible welding issues.

When welding is not applicable or a specific disassembly requirement is present in the design of a component, fastening techniques such as bolted, riveted, screwed or threaded connections, can accomplish the joining purposes by linking structures through spot elements. Even though fastening has less influence in terms of thermal distortion than welding, this approach is anyhow critical for both the substrates and the spot element from the mechanical point of view. In fact, the substrates drilling and machining are typically required for the placement of the connection elements whereas the fastener is exposed to mixed loading conditions [43] induced by the mechanical assembly. In this latter circumstance, the use of such technique should be carefully assessed due to the possible loss of contact, especially under dynamic [44] or cyclic loads [45], or due to fatigue conditions [46]. Besides, critical aspects in using fastening connections are evident for non-metallic structures like fibre-based composite materials. Such materials are massively exposed to fail under condition like pull-out, bearing, shear out, tear out and cleavage, as reported in Figure 2, in addition to delamination, fibre breakage and matrix damage which are caused by the creation of the access hole and the clamping force [47]. Furthermore, different shapes and footprints, at fixed fastening element typology, can significantly reduce the load-bearing capability under tension conditions [48].

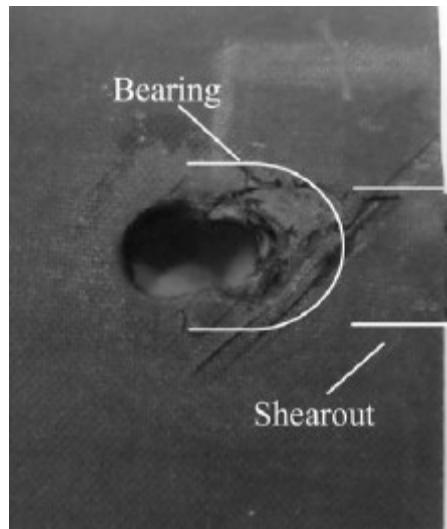


Figure 2: Example of failure mode for a composite plate with a fastener connection. Original from [48].

In this context, adhesive joints have many peculiarities that allow to overcome the majority of problems related to the aforementioned connections. In general, the joint design and the adhesive selection should be compatible to the current loading conditions of a specific application. Typically, adhesive joints are designed to avoid, or at least minimize, peeling and cleavage stresses and stress concentration as these last are the main driver of component failures due to the through the thickness strength is usually lower than the in plane one [3].

The specific physical and chemical nature of adhesive is also suitable for joining different materials such as metal-composite, metal-ceramic, composite-wood or plastics both in thick or thin configurations. Adhesives are particularly suitable for lightweight applications as the mass contribution provided by such materials is exceptionally low in terms of stiffness and strength-to mass characteristics. Once the joining process is completed, the stress distribution within the bonding area is much more regular and, in the case of a properly addressed design, usually free of stress concentrations compared to those achieved when applying fasteners or welding procedures. If some adhesive surplus is squeezed out from the bonding region this can be simply removed by adopting mechanical tools without corrupting the substrates. The proper application of adhesives, typically, just requires the adherend pre-treatments for increasing the surface roughness and this action present low criticalities with low levels of damages. If curved and smooth geometrical shapes are to be achieved, adhesives can accomplish this task easily as their initial state can adapt to several

configurations compared to applying fasteners which predominantly require flat surfaces. Similarly, the versatility of such material can be exploited for sealing or isolating joints of mechanical parts from highly degrading environments that can corrupt the structural integrity of the mechanical joint itself. Adhesives are also suitable as dissipative media for impacts or vibrations due to interesting performances of energetic absorption [49].

However, also adhesive bonding methods present some disadvantages and drawbacks. One of the main criticalities is attributed to the placement of the bonding material between the substrates. Indeed, the surface preparation should be carefully approached with mechanical tools and chemical substances to guarantee a uniform adhesion. Often, this procedure may introduce uncertainties in terms of bonding quality such as introduced defects or air bubbles, remaining particles and not properly connected regions, especially in the case of a manual preparation. Besides, reaching a uniform adhesion requires the permanent application of pressures over a certain timeframe through weights of mechanical fixtures. This aspect thus introduces the right selection or design of such devices that must ensure the correct application of pressure without leakage. Once the joint is accomplished, the bonded joint denies visual inspection possibilities to evaluate the level of readiness and reliability of the connection. Moreover, the mechanical performance of adhesively bonded joints is sensitive to the current environmental conditions (i.e., humidity and temperature) that are present during the joining process. In fact, performing the curing sequence with calm air at room temperature leads to mechanical characteristics that can be quite different if the same process is conducted in the oven with stages of warming up. Furthermore, the exposure of adhesive joints to the wrong chemical solvents (e.g., for cleaning purposes) can completely destroy the connection, as the solvent basically promote the degradation of the joint by erosive mechanisms.

The knowledge of the aforementioned pros and cons led, in the last few years, the arising of new trends in design and manufacturing mechanical joints. The emerging tendency refers to the coupling of adhesives with classical techniques (e.g., adhesive and welding, adhesive and bolts,...). Such joint types are depicted in Figure 3 and are usually called “hybrid joints”. Essentially, the purpose is to include the specific advantages of each joining technique within a synergic design

in order to increase the whole joint performances thus minimizing both stress distribution and possibility of failures [50].

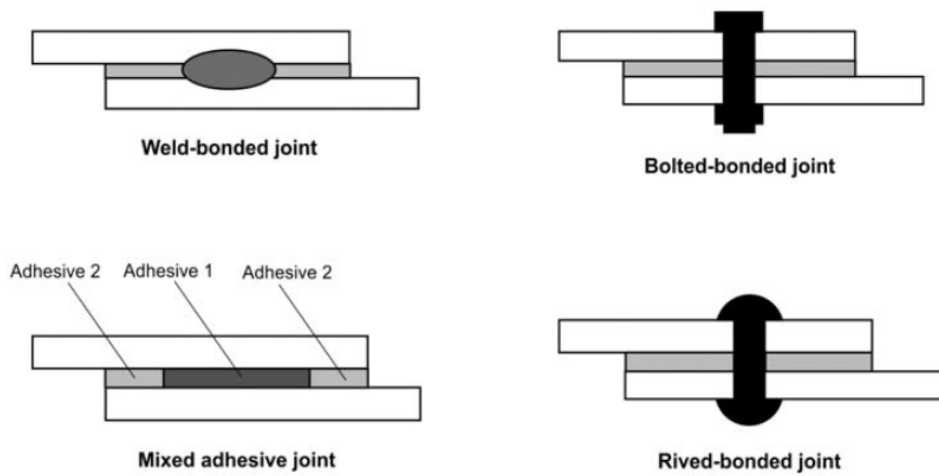


Figure 3: Examples of hybrid joints.

- Effect of environmental conditions on mechanical performances

The analysis of environmental conditions addresses the problem of understanding and quantifying how loads of mechanical, thermal, hygroscopic nature affect the structural responses of joints at fixed or variable geometrical conditions. Investigating the environmental effects is of particular importance as adhesive joints should demonstrate a load bearing capacity even at extreme conditions or under variable circumstances. This kind of investigation has a relevant experimental background and ad-hoc tests are typically performed to extract parameters of specific behaviours such as stress – number of cycles curves in the case of fatigue characterizations, coefficients of thermal expansion or conductivities in the case of thermal stresses, etc... . Performing such tests is thus fundamental for establishing phenomenological laws based on experimental observations, for extracting mechanical parameters and for correlating, validating or even updating numerical models. Moreover, investigating environmental effects can help in overcoming possible scepticism and unknowns if joints have to demonstrate specific capabilities under aggressive environments. In fact, lack of knowledge could lead the lack of confidence and ability in preserving the structural integrity of the whole mechanical system.

One of the earliest investigations on fatigue failures of bonded joints was performed by Gilmore and Shaw [51] who experimentally demonstrated the

importance and the level of sensitivity to environmental effects in the case of CFRP-epoxy adhesive components, under several combinations of temperature and humidity. It was observed a tendency to cohesively fail when hot and humid conditions were present, whereas the substrate rupture as the thermal conditions approached the ambient ones. The root cause of such phenomenon was attributed to the increased stiffness of the adhesive as the temperature decreased.

Zhang *et al.* [52] experimentally examined the consequences of temperature and humidity on pultruded GFRP adhesively-bonded double-lap joints at constant magnitude fatigue loading. Overall, it was observed a severe reduction in the fatigue life when components were exposed to such conditions. Particularly, humidity had the main consequence. It was responsible of shifting the failure mode from adhesive to interfacial (i.e., weakening mechanism at fibre/matrix bond) whereas the increase of temperature mainly produced stiffness degradation.

Fatigue and static failures of CFRPs-steel bonded unions were investigated by Borrie *et al.* [53] under mixed marine (i.e., saline at 0.5% of NaCl) and temperature conditions. In general, it was observed a global reduction of 10-15% of strength performances and the longer the exposure the higher the degradation of the joint. Fatigue performance has exhibited premature failures due to the degradation of the epoxy matrix.

Better views of failure mechanisms, failure modes and the transition between static and fatigue loads were investigated by Castro Sousa *et al.* [54] under temperature and humidity conditions with coupled experimental and numerical methods. As already highlighted by previous studies, these conditions reduce the mechanical performance of joints and, in the case of explored environments, fatigue performances were degraded up to the times of the nominal possibility of the virgin materials. Moreover, the exposure to thermal and hygroscopic fields imposed a failure mode change from purely cohesive to mixed adhesive-cohesive. This particular aspect was explained numerically due to the presence of newly created stress concentrations during the cyclic loads.

The effects of dynamic environments have been assessed by several studies and, especially, by concentrating on different aspects of this matter such as vibration loading and strain-rate (e.g., impacts or loading frequency) effects on mechanical responses as well as the coupling of dynamic with thermal fields.

Pang *et al.* [55] and Reis *et al.* [56] concentrated on fatigue performances under vibration and variable frequency loads through numerical and experimental methods. In Pang *et al.* [55] the main outcome consisted in the definition of a damage factor to be introduced into the numerical model to account for the material degradation during vibration loads whereas Reis *et al.* [56] experimentally observed that, in the case of epoxy adhesives, there is a variable dependency of the loading frequency when coupons are tested in shear. Indeed, experimental data show marginal variations when load magnitudes are high while greater scatters are foreseen in the case of loads of low amplitude.

Strain-rate dependence and impact behaviours were successfully reviewed by Machado *et al.* [57] who provided a comprehensive overview on how adhesive and adhesive joints behave under loads of such nature. The author gave a clear picture regarding the typical challenges in terms of testing and modelling aspects when dealing with such loads. In general, the problem is particularly complex and demanding as material can show both degradation and enhancement on mechanical properties (e.g., the increase of shear and tensile strength as the strain-rate increases whereas the fracture energy is prone to suffer degradation mechanisms with material embrittlement). The complexity of this matter was explored by Taniguci *et al.* [58] in the case of CFRP laminates under high strain-rates and it was found that mechanical properties in the longitudinal direction were almost independent to strain-rate effects compared to those in transverse direction.

Goglio *et al.* [23] and Goda and Sawa [59] explored the performances of epoxy bi-component adhesives under high strain-rates. Both studies demonstrated that testing bulk material under tension-compression loading conditions produced increasing levels of strength due to the increasing application of loading-rates.

Fracture problems under high rates of mode I testing (i.e., peeling) were investigated by Blackman *et al.* [60] for a tough adhesive undergoing high strain rate. Material testing revealed a reduction of about 40% of fracture energy (i.e.,) compared to the static value of the virgin material. Moreover, the increase of applied strain rate also had consequences of testing methods. Precisely, under slow testing processes (i.e., quasi-static) both the DCB and the TDCB produced similar experimental results whereas, in the case of faster conditions, TDCB

induced quicker and less controllable cracks compared to the DCB coupons. The knowledge of this last aspect is undoubtedly fundamental for extracting reliable material parameters during characterization activities.

Similar experiments were conducted by Sun *et al.* [61] in the view of mode II (i.e., shear sliding) for calibrating numerical models. For such fracture mode, ENF tests revealed a moderate sensitivity to strain-rate effect up to loading speeds in the range of 1000 mm/s. For that reason, the developed numerical model was able to approximate the test data with no specific efforts.

Gupta *et al.* [62] investigated the influence of strain-rate on the toughening mechanism of Tin-glass/epoxy components and related failure modes. Essentially, the experimental study confirmed the trend such that mechanical performances proportionally increase with the strain-rate whereas failure modes suffered of important variations as the strain-rate increases. Precisely, in the case of Tin-glass/epoxy coupons, strain-rate of low amplitude trigger mixed cohesive and adhesive failure while increasing the testing speed the failure becomes predominantly adhesive.

An analogous investigation was conducted by Wang *et al.* [24] for assessing both mechanical properties and failure behaviour of single-lap adhesive CFRP and aluminium joints. As before, this study provided a further confirmation that increasing the applied rate of strain had an equivalent effect of strengthening and stiffening the coupon. Based on the current explored material configuration, failure modes were not massively affected by the increasing of strain loads and these were mainly of cohesive type within the adhesive and fiber-tear failure within the substrates. However, the increase of loading rates produced variations in the area proportion associated to failure modes namely the widest cohesively failed area was ascribable to quasi-static testing circumstances.

The combined effect of both strain-rate and thermal and strain-rate and hygrothermal environments has been object of several studies for understanding the coupled phenomenon and thus quantifying the variation of mechanical responses.

Banea *et al.* [63] discovered that the thermal effect has a major impact on mechanical features of a one-component epoxy adhesive compared to strain-rate effects. Precisely, both the tensile strength and the Young's Modulus showed a

decreasing trend in the explored high thermal range (i.e., 25-150 °C) while performing tensile tests at different speeds (i.e., 0.1, 1, 10 mm/min).

Coupled behaviours at low temperatures (i.e., -40, -20 °C) were investigated by Jia *et al.* [64,65] for both a polymer-based and a epoxy-based adhesive. In the case of a polyurethane adhesive [64], the simple superposition of both thermal and mechanical effects for extracting the final response was not possible. Indeed, at fixed temperature, the adhesive demonstrated a strong dependence on the strain-rate level and vice-versa and this means that the behaviour was fully coupled. Mechanical performance for the explored material, in terms of Young's Modulus and strengths, showed almost comparable behaviour at fixed thermal conditions whilst increasing magnitudes while reducing the temperature. The epoxy case study [65] was tested under similar thermal and mechanical conditions as before. Experimental results demonstrated a significant increment in strength at both room and low temperature. However, at low temperature, high strain-rates induced stiffness degradations whereas strain to failures presented complex trends due to possible localized temperature increase.

Strain rate dependence at both low and high temperatures (i.e., -20, 80 °C) were studied by Viana *et al.* [66] by comparing responses under quasi-static and impact testing methods for a crash resistant epoxy adhesive. In general, experimental results demonstrated the adhesive capability of absorbing higher loads for impact compared to those in quasi-static. Precisely, at room and low temperature impact failure were observed in the substrates whereas in quasi-static within the adhesive layer. At high temperatures it was observed that the amount of absorbed energy was higher for impacts rather than quasi-static. For the latter condition the energy trend presented a decreasing variation whereas for impact was for foreseen.

Coupled strain-rate and hygroscopic mechanisms were investigated by Zhang *et al.* [67], on top of others, with the special purpose of understanding the evolution of strengths and fracture modes of a crash-toughened epoxy adhesive. The explored configurations revealed that the most significant consequence was ascribable to the hygrothermal exposure rather than strain-rate effects. However, such environment mostly affected the failure loads, whereas insignificant changes

in the joint stiffness, failure modes (i.e., mixed interfacial) and fracture surfaces between the virgin specimen (i.e., not exposed) and the exposed one.

- Typical configuration adopted in the mechanical design

Complex mechanical platforms are typically composed by many types of systems, sub-systems and parts all of them produced with different materials and connected among their selves through specific elements. For studying analytically, numerically or experimentally the mechanical behaviour of a really implemented connection, is common practice to reproduce its mechanical and geometrical configuration through ad-hoc designed specimens when isolated from surrounding structural details. In the case of adhesives, this concept originates some geometrical configurations such as Single-Lap Joint (SLJ), Double-Lap Joint (DLJ), Scarf, Butt Joint (BJ) and many others as reported in Figure 3Figure 4. All of them are possible alternatives in the mechanical design and development of a joint but the final decision mainly relies on trade-off and evaluation activities that also consider pre-application (e.g., cost, design and production methods,...), application (i.e., cure factors) and post-application (e.g., loading and environmental constraints) factors as well as the specific features of the loading conditions such as intensity, direction and time-dependence nature [68].


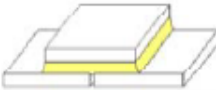






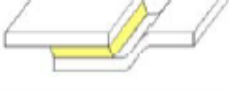
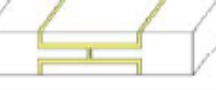

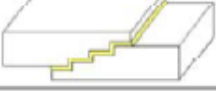

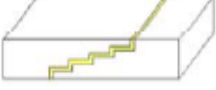
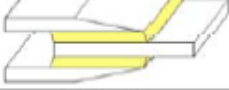




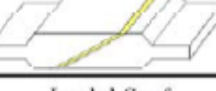


	JOINT TYPE	COMMENTS	JOINT TYPE	COMMENTS	
Single Lap Joints	Simple 	Simplest bonded joint, but suffers from offset load path with associated stress concentration and peel.	Strapped Joints	Single 	Similar principle to single lap joint. Bending and peel experienced due to stiffness mismatch and central discontinuity in adherends.
	Taper or Bevelled (external scarf) 	Tapers reduce stress concentration.		Double 	Similar principle to double lap joint. Reduces bending and peel seen with single strap. Central discontinuity in adherends.
	Radiused 	Radii reduce stress concentration.		Bevelled 	Bevels reduce stress concentration.
	Double Step 	Minimises joint weight but lowers joint strength due to discontinuity in laminate.		Radiused 	Radii reduce stress concentration.
	Rebated or Joggle 	Alignment of adherends to avoid offset load path, but 'kink' may compromise strength.		Recessed Double 	Discontinuity between strap and adherends, plus central discontinuity between adherends. Thinning of adherends to accept recessed straps reduces strength.
	Stepped 	Discontinuity in laminate (see Double Step).		Stepped Lap	Simple 
Double Lap Joints	Simple 	Eliminates majority of bending and peel stresses found with single simple overlap.	Recessed 		As above, but recessing creates smooth external surface.
	Bevelled 	Bevels reduce stress concentration.	Single Taper (ideal scarf) 		Increased bond area. Avoids discontinuities in stepped lap geometry.
	Radiused 	Radii reduce stress concentration.	Double Taper 	Increased bond area compared to single taper.	
Bonded Doublers	Single Sided 	Provides localised thickening and stiffening. Similar transfer in bond to simple single lap.	Scarf	Increased Thickness Scarf 	Increased bond area. Thicker adherends in bond area increase strength of joint zone.
	Double Sided 	Provides localised thickening and stiffening. Similar transfer in bond to simple double lap.		Landed Scarf 	Increased bond area, but discontinuity at lands.

Figure 4: Configurations of adhesive joints. Original from [68].

- Failure modes in bonded joints

As described above, bonded joints aim at connecting parts for transferring loads from a member to another one. If the joint is wrongly designed or the in-service actions exceed the design loads, over stresses or severe stress concentrations could originate within both the adhesive layer or the substrates, thus leading to the joint collapse. In this framework, there are essentially 3 main failure modes namely cohesive failure, adhesive failure and the substrate failure, as depicted in Figure 5.

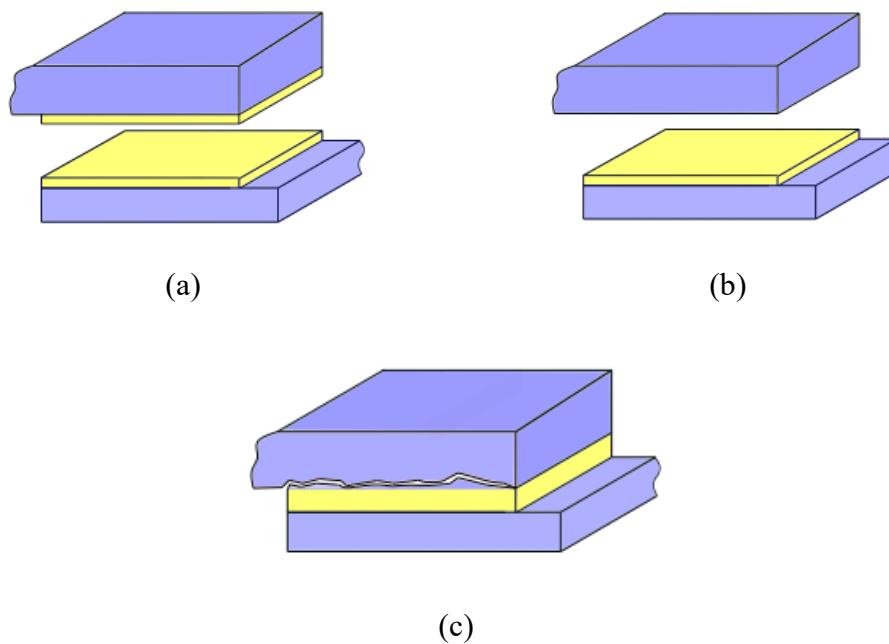


Figure 5: Main failure modes of adhesive joints: (a) cohesive failure, (b) adhesive failure, (c) substrate failure.

The cohesive failures originate and progress within the adhesive layer only. Once the damage occurred till the final failure, the clear presence of the adhesive is observable on both substrates. Such failure could be triggered by shear, peeling and cleavage loads, or their combination. Clearly, design of adhesive joints is oriented to prevent any kind of failure during the product life however, if the failure is impossible to prevent, this should be of the cohesive type. Cohesive failure is, substantially, index of having produced a good joint as the purposes of the adhesion between the adhesive and the substrates is accomplished.

The adhesive failure, also called debonding or interface failure, totally originates between the adhesive and the substrate thus making visible the

substrate interface areas. The main causes of such failure mode are attributed to wrong manufacturing, and contamination during the joint preparation.

The substrate failure, as suggested by the nomenclature, uniquely involves the substrates and can happen everywhere in it. Basically, this failure is a symptom of a wrong selection, or design, of substrate materials compared to the expected load levels. The substrate failure mainly affects substrates made by composite materials that alternate layers of fibres to layers of matrix. Due to the higher complexity of the adopted materials [69] for triggering the substrate failure, such mode is typically divided based on the typology of the substrate failure as i) tensile fibre fracture, ii) compressive fibre fracture (i.e., fibre kinking), iii) tensile matrix failure, iv) compressive matrix failure and v) shear matrix failure.

2.1.2 Fundamental models to assess the joint stress distribution.

Stress and strength predictions are a fundamental part in the design process of adhesive joints. The knowledge of acting loads, their magnitude and distribution within the adhesive layer as well as the comparison to allowable strength values constitutes the central part in joints analysis. To do so, different mathematical models, close-form solutions, numerical frameworks and analysis techniques have been developed to reach this goal. In particular, the interest in adopting and developing analytical schemes is still present as they can predict the structural behaviours with a reasonable accuracy and this feature is suitable for a fast implementation in the view of a quick design answer. This is testified by the wide number of contributions that are currently present in the technical literature for the different joint configurations (e.g., single-lap, double-lap, tubular,...). However, even though all of them play an important role in the knowledge advancement, just a few are significant building blocks and steps forward in this discipline.

There are some important aspects in discussing, presenting and, then, using a physical-mathematical model: *i*) every model is developed for a specific purpose, *ii*) all the models are wrong but some of the are more useful than others [70] and *iii*) the applicability of a model also depends from external aspects. Even though these concepts could appear as philosophical statements they have some practical consequences, very often forgotten from engineers. Firstly, a model that is developed under certain conditions and assumptions could fit to analyse the

variation of a generic quantity X along the Y direction but, perhaps, the vice-versa (i.e., the variation of Y along X) is not permitted. Secondly, the fact that all the models are intrinsically wrong relies on the impossibility of predicting behaviours in a deterministic sense. However, under certain conditions, hypotheses or levels of observation, statistical phenomena can be sufficiently captured by deterministic models (e.g., particles motion in fluids) and non-linear behaviours can be restricted and approximated by linear equations. Finally, the proficient use of a mathematical model also depends on the level of awareness of the end user, the amount of details and information that are of interest and, last but not least, the available amount of resources for the model implementation. A priori, there is not a totally good or a totally bad model but a suitable or a not suitable model for a specific purpose.

The aim of this paragraph is to illustrate the fundamental models that have been developed for stress and strength analysis of adhesively bonded joints in terms of both closed-form solutions and numerical frameworks. The main features, advantages and disadvantages, strengths and weaknesses will be pointed out. Much part of models review is inspired by the works of Carpenter [71], daSilva *et al.* [72,73], Ramalho *et al.* [74], Tserpes *et al.* [75], Rodríguez *et al.* [76], Dragoni and Goglio [77], He [78], Ramalho [79] who provided extensive unified descriptions of such mathematical schemes as well as the original papers developed by researchers.

The most simplistic approach to analyse a bonded joint assumes purely rigid adherend capable of transferring the external loads to the bonded area. In the case of a single-lap joint under traction loads as depicted in Figure 6, the adhesive is subjected to a purely constant shear. This condition is easily described by dividing the external load with the bonding area as reported in Eq. (2.1.1)

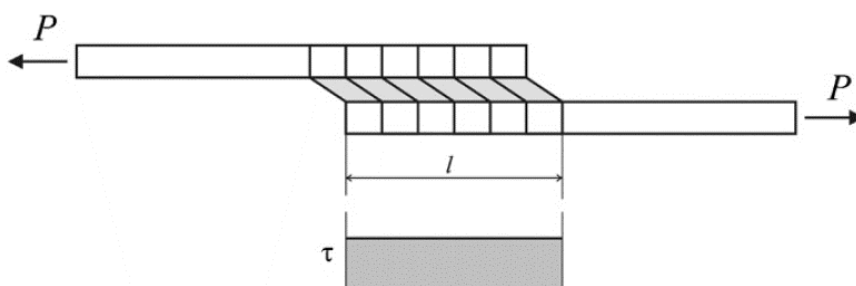


Figure 6: Single-lap joint under traction loads. Original from [73]

$$\tau = \frac{P}{bl} \quad \text{Eq. (2.1.1)}$$

Where P is the acting loads, b the bonding width and l the bonding length.

Is it clear that this model is the crudest as it neglects many features that are present in the reality (e.g., peeling and transversal stresses) as well as it does not consider the free-edge effect. However, this model allows a fast evaluation of the principal stress contribution.

Volkersen [6] introduced the so-called differential shear by removing the previous hypothesis of rigid adherend thus introducing the flexibility of such members, as reported in Figure 7. In such a way, the shear variation in the adhesive thickness is permitted along the loading coordinate whereas the adherend can deform only in tension.

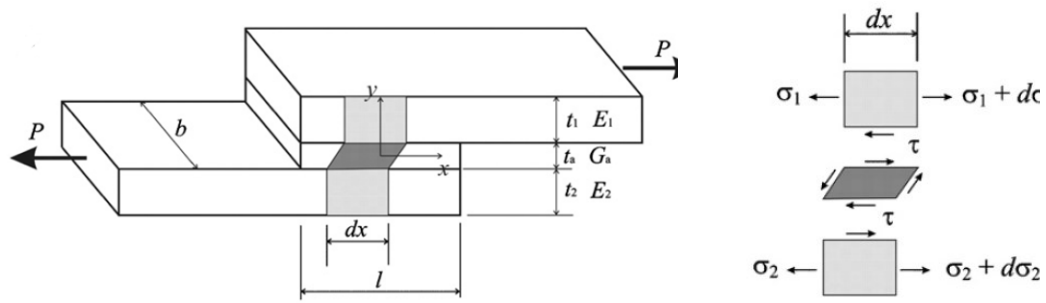


Figure 7: Single-lap joint model under Volkersen analysis. Original from [73]

Mathematically, Volkersen found that the shear distribution was dependent by hyperbolic functions as reported in Eq. (2.1.2)

$$\tau = \frac{P}{bl} \frac{w \cosh(wX)}{2 \sinh\left(\frac{w}{2}\right)} + \left(\frac{\psi - 1}{\psi + 1}\right) \frac{w \sinh(wX)}{2 \cosh\left(\frac{w}{2}\right)} \quad \text{Eq. (2.1.2)}$$

where $w = (1 + \psi)\phi$, $\psi = t_t/t_b$, $\phi = G_a l^2 / E t_t t_a$, $X = x/l$, $-1/2 \leq X \leq 1/2$ and P is the applied load, b and l are the bonding width and length respectively, G_a is the adhesive shear modulus, E the adherend elasticity modulus, t_t the upper adherend thickness, t_b the lower adherend thickness and t_a the adhesive thickness. Even if such model is slightly more advanced, the effects introduced by a not aligned load path is missing. This misalignment produces coupled bending moments and transverse forces at the joint ends when traction

loads are applied. As a result, the joint is prone to rotate thus introducing coupled shear and peeling actions within the adhesive layer. For that purpose, Goland and Reissner [7] quantified both the influence of bending moments and transverse loads by two factors namely the bending moment factor (k_{GR}) and the transverse force factor (k_{GR}'), reported in Eq. (2.1.3)

$$k_{GR} = \frac{\cosh(u_2 c)}{\cosh(u_2 c) + 2\sqrt{2} \sinh(u_2 c)} \quad \text{Eq. (2.1.3)}$$

$$k_{GR}' = \frac{k_{GR} c}{t} \sqrt{3(1 - \nu^2) \frac{\tilde{P}}{tE}}$$

where

$$u_2 = \sqrt{\frac{3(1 - \nu^2)}{2} \frac{1}{t} \sqrt{\frac{\tilde{P}}{tE}}} \quad \text{Eq. (2.1.4)}$$

and c is half of the bonding length, t is the adherend thickness, E the elasticity modulus of the adherends, ν is the Poisson's ratio and \tilde{P} is the traction load per unit width. These parameters were extremely useful for understanding the amount of bending and transversal force introduced by the misalignments and, in the case of small k and k' values, such contribution could be reasonably omitted or treated as parasite effects. The definition of these factors facilitated the extraction of peeling and shear stresses as reported in Eq. (2.1.5) and Eq. (2.1.6) respectively

$$\sigma = \frac{1}{\Delta} \frac{\tilde{P} t}{c^2} \left[\left(R_2 \lambda^2 \frac{k_{GR}}{2} + \lambda k_{GR}' \cosh(\lambda) \cos(\lambda) \right) \cosh\left(\frac{\lambda x}{c}\right) \cos\left(\frac{\lambda x}{c}\right) \right. \\ \left. + \left(R_1 \lambda^2 \frac{k_{GR}}{2} + \lambda k_{GR}' \sinh(\lambda) \sin(\lambda) \right) \sinh\left(\frac{\lambda x}{c}\right) \sin\left(\frac{\lambda x}{c}\right) \right] \quad \text{Eq. (2.1.5)}$$

where $\lambda = \gamma \frac{c}{t}$, $\gamma^4 = 6 \frac{E_a}{E} \frac{t}{t_a}$ and $R_1 = \cosh(\lambda) \sin(\lambda) + \sinh(\lambda) \cos(\lambda)$, $R_2 = \sinh(\lambda) \cos(\lambda) - \cosh(\lambda) \sin(\lambda)$, $\Delta = 1/2 (\sinh(2\lambda) + \sin(2\lambda))$.

$$\tau = -\frac{1}{8} \frac{\tilde{P}}{c} \left[\frac{\beta c}{t} (1 + 3k_{GR}) \frac{\cosh\left(\left(\frac{\beta c}{t}\right)\left(\frac{x}{c}\right)\right)}{\sinh\left(\frac{\beta c}{t}\right)} + 3(1 - k_{GR}) \right] \quad \text{Eq. (2.1.6)}$$

where $\beta = 8 \frac{G_a t}{E t_a}$. Finally, the calculation of edge moments and transverse force was performed according to Eq. (2.1.7) and Eq. (2.1.8) respectively.

$$M = \frac{\tilde{P}t}{2} k_{GR} \quad \text{Eq. (2.1.7)}$$

$$V = \frac{\tilde{P}t}{c} k_{GR}' \quad \text{Eq. (2.1.8)}$$

The most evident limitation in the Goland and Reissner model regards the absence of any adhesive-related parameter in the calculation of k_{GR} , k_{GR}' factors as well as the applicability to equal adherends only. Moreover, such model works well in the case of short overlap and loads of small magnitude.

Attempts in improving such model that are worth mentioning are the works of Allman [80], Renton and Vinson [81,82], Wu *et al.* [83], Tsai *et al.* [84], Ojalvo and Eidinoff [85], Oplinger [86], and, more recently, Zhao *et al.* [87] and Jiang *et al.* [88] who basically removed the equal material hypothesis on the adherends and tried to include the presence of the adhesive layer within their models starting from the Goland and Reissner scheme.

Hart-Smith concentrated on both single-lap [89] and double-lap [8] joints for both improving the Goland and Reissner model and for exploring elastic-plastic behaviours. Firstly, Hart-Smith realized that the bending moment factor presented in Eq. (2.1.3) was too conservative, thus, a more precise definition for calculating the maximum acting stress was

$$k_{HS} = \frac{1}{1 + \zeta c + \frac{\zeta^2 c^2}{6}} \quad \text{Eq. (2.1.9)}$$

where $\zeta^2 = \tilde{P}/D$. Eq. (2.1.10) leads to the alternative bending moment definition

$$M = \tilde{P} \left(\frac{t + t_a}{2} \right) k_{HS} \quad \text{Eq. (2.1.10)}$$

which includes the adhesive thickness contribution. Secondly, Hart-Smith provided calculation models for the shear and the peel stress distributions in the

case of balanced adherends. In such case, under pure linear elastic behaviours, the shear component was modelled as

$$\tau = A_1 \cosh(2\lambda'x) + C_1 \quad \text{Eq. (2.1.11)}$$

where $\lambda' = \sqrt{\left[\frac{1+3(1-\nu^2)}{4}\right] \frac{2G_a}{t_a E t}}$, $A_1 = \frac{G_a}{t_a E t} \left[\tilde{P} + \frac{6(1-\nu^2)M}{t} \right] \frac{1}{2\lambda' \sinh(2\lambda'c)}$ and $C_1 = \frac{1}{2c} \left[\tilde{P} - \frac{A_1}{\lambda'} \sinh(2\lambda'c) \right]$. Whereas the peel contribution was modelled as

$$\sigma = A_2 \cosh(\chi x) \cos(\chi x) + B_2 \sinh(\chi x) \sin(\chi x) \quad \text{Eq. (2.1.12)}$$

$$\text{and } \chi^4 = E_a / 2Dt_a, A_2 = -\frac{E_a M [\sin(\chi c) - \cos(\chi c)]}{t_a D \chi^2 e^{\chi c}}, A_2 = -\frac{E_a M [\sin(\chi c) + \cos(\chi c)]}{t_a D \chi^2 e^{\chi c}}.$$

Moreover, the joints shear stress response was also explored under perfectly elastic-plastic behaviours with a bi-linear trend while the peel stress was kept in a purely linear elastic condition. In Figure 8, the adopted elastic and plastic regions within the bondline are depicted as well as the adopted shear stress-deformation relationship.

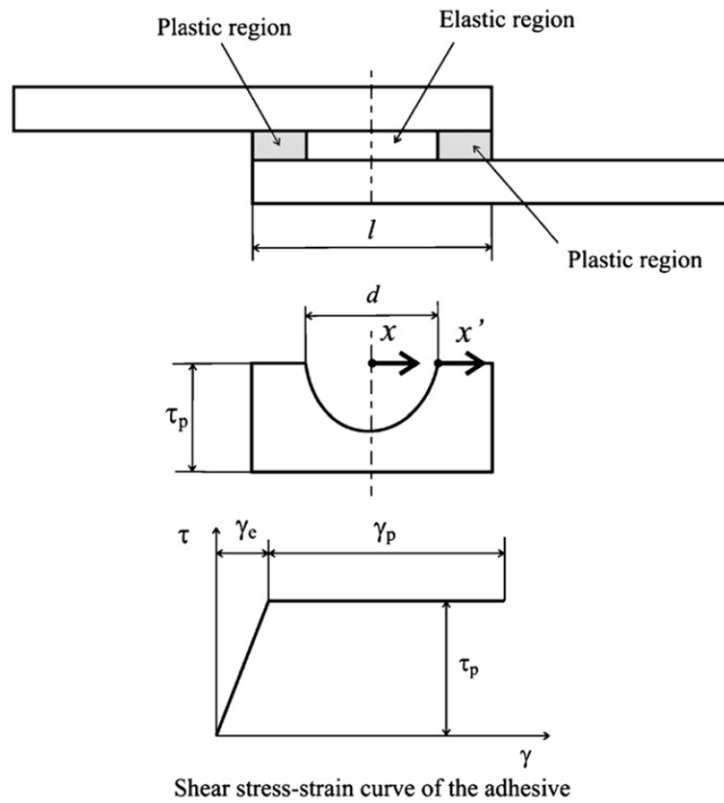


Figure 8: Elastic and plastic distribution within the bond line. Original from [72].

The problem of Hart-Smith was addressed to find both the shear stress, Eq. (2.1.13a), and the shear deformation Eq. (2.1.13b), iteratively.

$$\tau = A \cosh(2\lambda' x) + \tau_p(1 - K) \quad \text{Eq. (2.1.13a)}$$

$$\gamma = \gamma_e \{1 + 2K[(\lambda' x')^2 + \lambda' x' \tanh(\lambda' d)]\} \quad \text{Eq. (2.1.13b)}$$

where τ_p is the plastic adhesive shear value, γ_e is the linear part of the shear deformation and A a constant which depends on τ_p . Precisely, the iterative scheme aimed to search the value of K and d by exploiting some auxiliary equations, until K reaches a convergent value.

Additional works that are worth mentioning are Delale *et al.* [9] who introduced a non-linear material model of the adhesive while considering its thickness neglectable for stress post-processing purposes. Adherends were assumed as an elastic continuum with anisotropic properties and the material non-linearity was managed starting from a non-linear energy function. Tong [90] expanded the works of Hart-Smith by considering arbitrary non-linearities embedded within the stress-strain equations. The adopted solution scheme was based on integrated functions in the case of balanced adherends. Such approach achieved formulas for characterizing failures in pure shear, peeling and mixed modes. Luo and Tong [91] expanded the analysis by developing a rather complex fully-coupled non-linear equations in the form of closed form solutions. To reach the goal, their model was based on both large deflections of adherend as well as peel and shear strains. Such model demonstrated useful to enrich the edge moment factor definition, reported in Eq. (2.1.14), and it was compared with non-linear Finite Elements and theoretical results proving extremely satisfactory outcomes for a wide range of material and geometrical parameters.

$$k_{LT} = \frac{1 - \delta_f}{1 + \beta_k c \coth(\beta_k l) + \delta_m} \quad \text{Eq. (2.1.14)}$$

where $\beta_k = \sqrt{F/D_1}$, δ_f and δ_m are parameters depending to mechanical and geometrical properties and to the applied load magnitude.

Bigwood and Crocombe [92] recognized the valuable contribution of the original Goland and Reissner approach, as well as the Goland and Reissner – based schemes, for producing design relationships going beyond the simple single

lap joint configuration. Bigwood and Crocombe modelled the adhesive-adherend union as a sandwich structure where external shear, bending and traction loads act at the edge of the of overlap whereas adhesive peeling and shear stresses works in the adhesive mid-thickness, as illustrated in Figure 9.

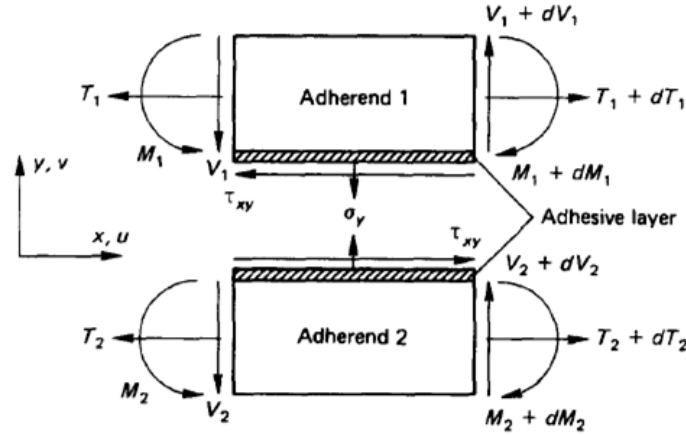


Figure 9: Elemental diagram of the adherend-adhesive sandwich. Original from [92].

Such idealization, properly managed in the view of equilibrium equations, was exploited for extracting both the shear stress and peeling stress differential model as reported in Eq. (2.1.15a) and Eq. (2.1.15b)

$$\frac{d^3 \tau_{xy}}{dx^3} - K_1 \frac{d\tau_{xy}}{dx} = -K_2 \sigma_y \quad \text{Eq. (2.1.15a)}$$

$$\frac{d^4 \sigma_y}{dx^4} + K_3 \sigma_y = K_4 \frac{d\tau_{xy}}{dx} \quad \text{Eq. (2.1.15b)}$$

where $K_1 = \frac{4G_a}{t} \left(\frac{1-\mu_1^2}{E_1 h_1} + \frac{1-\mu_2^2}{E_2 h_2} \right)$, $K_2 = \frac{6G_a}{t} \left(\frac{1-\mu_1^2}{E_1 h_1} - \frac{1-\mu_2^2}{E_2 h_2} \right)$, $K_3 = \frac{E_a}{t} \left(\frac{1}{D_1} + \frac{1}{D_2} \right)$, $K_4 = \frac{E_a}{2t} \left(\frac{h}{D_1} - \frac{h}{D_2} \right)$, D_i and μ_i are the flexural stiffness of the adherend and the Poisson's ratio respectively. It can be easily observed that Eq. (2.1.15a,b) are coupled among their selves through the K_2, K_4 factors. Further manipulations involving additional derivations were required to decouple Eq. (2.1.15a,b) leading to seventh and six order differential equations as reported in Eq. (2.1.16a) and Eq. (2.1.16b)

$$\frac{d^7 \tau_{xy}}{dx^7} - K_1 \frac{d^5 \tau_{xy}}{dx^5} - K_3 \frac{d^3 \tau_{xy}}{dx^3} - K_5 \frac{d\tau_{xy}}{dx} = 0 \quad \text{Eq. (2.2.16a)}$$

$$\frac{d^6 \sigma_y}{dx^6} - K_1 \frac{d^4 \sigma_y}{dx^4} + K_3 \frac{d^2 \sigma_y}{dx^2} - K_5 \sigma_y = 0 \quad \text{Eq. (2.2.16b)}$$

where $K_5 = (K_1 K_3 - K_2 K_4)$.

Solving Eq. (2.1.16a,b) required the identification of proper solutions, reported in Eq. (2.1.17a,b)

$$\begin{aligned} \tau_{xy} = & C_1 \cosh(m_1 x) \\ & + C_2 \sinh(m_1 x) + C_3 \cosh(n_1 x) \cosh(n_2 x) \\ & + C_4 \cosh(n_1 x) \sin(n_2 x) \\ & + C_5 \sinh(n_1 x) \cos(n_2 x) \\ & + C_6 \sinh(n_1 x) \sin(n_2 x) + C_7 \end{aligned} \quad \text{Eq. (2.2.17a)}$$

$$\begin{aligned} \sigma_y = & D_1 \cosh(m_1 x) \\ & + D_2 \sinh(m_1 x) + D_3 \cosh(n_1 x) \cos(n_2 x) \\ & + C_4 \cosh(n_1 x) \sin(n_2 x) \\ & + C_5 \sinh(n_1 x) \cos(n_2 x) + C_6 \sinh(n_1 x) \sin(n_2 x) \end{aligned} \quad \text{Eq. (2.2.17b)}$$

where m_{1-2} and n_{1-2} are root functions and C_{1-7} , D_{1-6} depends on the applied boundary conditions at the edge of the overlap, as depicted in Figure 10. Clearly, the edge boundary conditions are sensitive to the external loads set that are not reported in the picture to avoid a lack of generality.

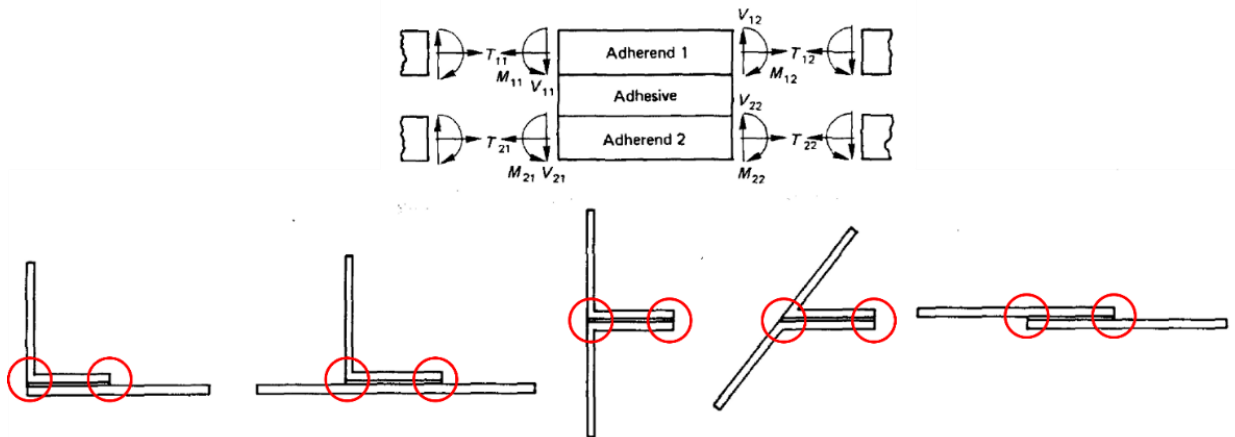


Figure 10: Some joint configurations. Original from [92]

The main advantage of such model relies in the capability of expanding the analysis configurations which is particularly useful in the view of a preliminary numerical verification. Moreover, such scheme considers the possibility of different adherend parameters when deriving the coupled shear and peeling stress equations.

Goglio and Rossetto [93] adapted the Bigwood and Crocombe model for producing a closed-form scheme of a double-lap configuration. To do so, the specific symmetrical features of such geometry under traction loads were essential to approach the problem. The object of the analysis was addressed to a comparative study among closed-form solutions that were available in the literature for the same problem. Mathematically, Goglio and Rossetto adopted Eq. (2.1.17a) for their analysis whereas the peel stress was recovered in a post-processing phase. It is important to remark that the analysis was defined in the mid-thickness to overcome singularity-related problems which implies to do not satisfy the traction-free condition. In such a way, the C_{1-7} constants definition followed the same process as in [92] while adding a further equation for defining the remaining unknown namely the bending moment. Assuming Finite Elements results as a reference, they found that the developed analytical model was able to reproduce both the trend and the magnitude of numerical outcome whereas past analytical formulations were acceptable only in the case of a very flexible adhesive compared to the adhesive properties.

The mathematical models recalled above, mostly approached the problem directly, namely deriving the stress differential equations, finding a generalized solution and thus imposing some boundary conditions for a specific geometry and load cases. However, other logics were developed without invalidating the classical formulations. For example, Luo and Tong [94] applied linear and high order displacement theories to better approximate the stress distributions within the adhesive thickness. Especially, in the case of thick adhesive, using high order schemes were found much more adequate than simple linear approximations. In fact more realistic stress patterns were extracted and verified by Finite Element tools. Radice and Winson [95] produced a robust, but quite complex to derive, analytical model based on a-priori assumed Airy stress function as in Eq. (2.1.18)

$$\phi = A_0(x) + zA_1(x) + \sum_{n=2}^{\infty} z^n A_n(x) \quad \text{Eq. (2.1.18)}$$

where the functions $A_0(x), A_1(x), A_n(x)$ does not present a specific formulation in principle. However, for the effectiveness of the model, $A_0(x), A_1(x), A_n(x)$ functions cannot randomly select but have to show suitable features that satisfy the edge boundary condition in advance. In such a way, in the view of a generalized model, the scheme was able to deduce both the displacement and the stress distributions. Sawa *et al.* [96] adapted the 2D elasticity with bi-harmonic Airy stress functions for studying similar problems. The effects of Young moduli ratio, thickness ratio and lengths ratio of the adherend as well as the adhesive-to-adherend thickness ratio were investigated in the view of the interface stress distribution. Of particular importance, Sawa offered an interesting overlook about the presence of the stress-singularity at the material interface as the analysis of this feature was normally omitted by classical models. For a single-lap configuration, the evolution of the stress-singularity was found particularly sensitive to the explored joint parameters. Precisely, the worst-case scenario was foreseen in the case of thin adherends with small Young's modulus. Moreover, the intensity of the singularity was found inversely proportional to the adhesive-to-adherend thickness ratio (i.e., the lower the ratio the greater the intensity).

Another class of geometries that captured attention from technical literature is tubular joints, whose configuration is reported in Figure 11.

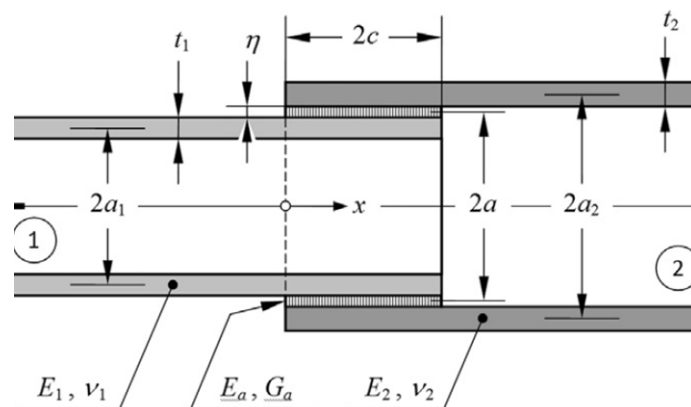


Figure 11: Example of tubular joint. Original from [77]

Even though these joints find widespread applications in mechanical products, the research is less expanded compared to single and double-lap configurations. Nonetheless, models such as Lubkin and Reissner [97], Shi and Cheng [98], Nayeb-Hashemi [99], Pungo and Carpintieri [100], Nemes *et al.* [101] and Nemes and Lachaud [102] can be clearly identified as milestones in tubular joints advancement, thus representing the baseline in the mechanical design of such components. Lubkin and Reissner [97] approached the problem firstly through the analysis of the infinitesimal structural element depicted in Figure 12. Basically, Lubkin and Reissner provided a re-interpretation of the work of Goland and Reissner [7], which was initially developed for a flat junction, by adopting the following assumptions: *i*) tubular adherends are schematized as thin shells capable of sustaining axial, shear and bending actions whereas the axial stress can vary over the thickness; *ii*) the adhesive is modelled as an elastic spring bed capable of transmitting both shear and peel stresses which are constant over the adhesive thickness and depend only to the axial coordinate; *iii*) shear circumferential stress is omitted in the analysis as the system is supposed to be not able to support torsional loads; *iv*) the presence of the moment factor is disregarded due to the specific geometrical feature.

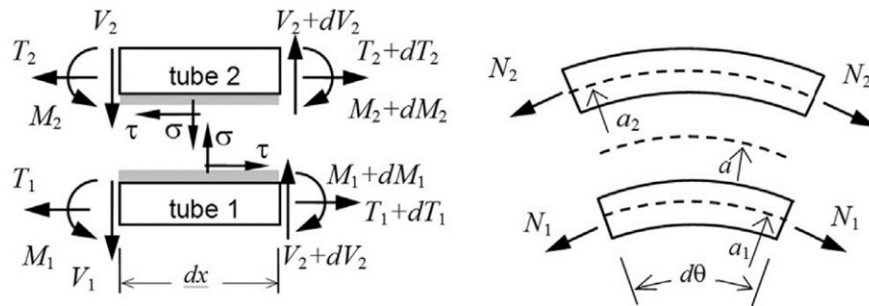


Figure 12: Infinitesimal element of a tubular joint. Original from [77]

Starting from the Goland and Reissner heritage, the hypotheses *i*)-*iv*) lead to a fully coupled systems of differential equations where two involve fourth-order derivatives and one second-order derivative. Classically, such system is written in terms of non-dimensional functions as reported in the following:

$$\left\{ \begin{array}{l} g_1^{IV} + (K_1^4 + \gamma_{11}^4)g_1 - \gamma_{12}^4 g_2 - \frac{3a}{a_1} g_3^{II} - \frac{3\Lambda_1 a}{a_1} g_3 = -\frac{3\Lambda_1 a}{a_1} \\ g_2^{IV} + (K_2^4 + \gamma_{22}^4)g_2 - \gamma_{12}^4 g_1 - \frac{3a}{a_2} g_3^{II} - \frac{3\Lambda_2 a}{a_2} g_3 = -\frac{3\Lambda_2 a}{a_2} \\ g_3^{II} + \left(\frac{B_2^2}{a_2} + \frac{B_1^2}{a_1}\right) a g_3 - (B_2^2 g_2^{II} + B_1^2 g_1^{II}) + \Lambda_2 B_2 g_2 - \Lambda_1 B_1 g_1 = \frac{B_2^2 a}{a_2} - \frac{B_1^2 a}{a_1} \end{array} \right. \quad \text{Eq. (2.1.19)}$$

where the coefficients $B_i^2 = (1 - \nu_i^2) \left(\frac{2c}{t_i}\right)^2 \frac{t_i G_a}{\eta E_i}$, $K_i = 12(1 - \nu_i^2) \left(\frac{2c}{t_i}\right)^2 \left(\frac{t_i}{a_i}\right)^2$,
 $\Lambda_i = 2\nu_i \left(\frac{2c}{t_i}\right)^2 \frac{t_i}{a_i}$, $\gamma_{ij}^4 = 12(1 - \nu_i^2) \left(\frac{2c}{t_i}\right)^3 \frac{2c a E_a t_j}{t_i a_i E_j \eta}$.

The system represented by Eq. (2.1.19) must be associated to boundary conditions, based on the external loads at the overlap ends, to find the adequate problem solution. It is clearly visible that the research of a closed-form solution appears much more complex compared to flat joints, even though authors in the original paper stated that "...solution is possible by standard methods" as the model is linear. Such difficulty relies on the impossibility of separating the stress behaviours in the mathematical treatment of tubular joints thus prohibiting the decoupling of differential equations.

Shi and Cheng [98] described the stress distribution by adopting a cylindrical reference system as opposite of Lubkin and Reissner [97]. Essentially, the mathematical model assumed the presence of σ_r (i.e., radial), σ_θ (i.e., hoop), τ_{rz} (i.e., radial-axial) and σ_z (i.e., normal) stress components in the adherends, whereas σ_z in the adhesive was negligible. Within the tubes, the normal stress was described as a linear combination of unknown functions of the direction. That approach led to a set of differential equation that were solved in terms of an eigenvalue-eigenvector problem.

Nayeb-Hashemi [99] found a solution for tension and torsion problems. The working hypotheses assumed the adherends capable of absorbing only axial tension while the adhesive was subjected to a radial-dependent shear stress. In the case of purely axial loads, such adhesive shear stress was schematized as

$$\tau_a = \frac{G_a}{\ln R_3 - \ln R_2} \frac{u_2 - u_1}{r} \quad \text{Eq. (2.1.20)}$$

Where R_2, R_3 are the tube radii in contact with the adhesive and the axial displacements in the respective tubes, whose explicit formulation reported in Eq. (2.1.21), was solution of axial differential equations.

$$\begin{aligned} u_1(\zeta) &= \frac{1}{E_1(R_2^2 - R_1^2)} [C_1\zeta + C_2 - E_2(R_4^2 - R_3^2)u_2] \\ u_2(\zeta) &= C_3e^{\theta_a\zeta} + C_4e^{-\theta_a\zeta} - \frac{1}{\theta_a^2} B(C_1\zeta + C_2) \end{aligned} \quad \text{Eq. (2.1.21)}$$

Where $\zeta = x/L$ is the normalized coordinate, C_{1-4} are constants deduced from the adopted loading conditions at the tube ends, B is a constant function of mechanical and geometrical parameters and θ_a the solution of the associated eigenproblem.

The works of Nemes et al. [101] and Nemes and Lachaud [102] approached the stress problem by assuming less straightforward distributions, within both the adhesive and adherend, as a function of the adherend-derivative. Precisely,

$$\begin{aligned} \tau_{rz}^{(1)} &= \frac{r_i^2 - r^2}{2r} \frac{d\sigma_{zz}^{(1)}}{dz} \\ \sigma_{\theta\theta}^{(1)} &= \frac{r_i^2 - r^2}{2} \frac{d^2\sigma_{zz}^{(1)}}{dz^2} \end{aligned} \quad \text{Eq. (2.1.22)}$$

$$\begin{aligned} \tau_{rz}^{(c)} &= \frac{r_i^2 - r_{ic}^2}{2r} \frac{d\sigma_{zz}^{(1)}}{dz} \\ \sigma_{\theta\theta}^{(c)} &= \frac{r_i^2 - r_{ic}^2}{2} \frac{d^2\sigma_{zz}^{(1)}}{dz^2} \end{aligned} \quad \text{Eq. (2.1.23)}$$

$$\begin{aligned} \tau_{rz}^{(2)} &= \frac{(r_e^2 - r^2)(r_{ic}^2 - r_i^2)}{2r(r_{ec}^2 - r_e^2)} \frac{d\sigma_{zz}^{(1)}}{dz} \\ \sigma_{\theta\theta}^{(2)} &= \frac{(r_e^2 - r^2)(r_{ic}^2 - r_i^2)}{2(r_{ec}^2 - r_e^2)} \frac{d^2\sigma_{zz}^{(1)}}{dz^2} \end{aligned} \quad \text{Eq. (2.1.24)}$$

where the superscripts (1), (c), (2) are associated to the inner tube, the adhesive and the second tube respectively whereas are the internal and the external radii of the tubular component and are the internal and the external radii of the adhesive

layer. The closing equation is the one modelling the behaviour, reported in Eq. (2.1.25)

$$E \frac{d^4 \sigma_{zz}^{(1)}}{dz^4} + (B + C) \frac{d^2 \sigma_{zz}^{(1)}}{dz^2} + A \sigma_{zz}^{(1)} + \frac{D}{2} = 0 \quad \text{Eq. (2.1.25)}$$

Where $A - E$ are constants.

Even though not explicitly directed to the analysis of stress states, it is worth mentioning the work of Saito and Tani [103] who analytically explored the fundamental aspects of free-vibration of bonded joints, as depicted in Figure 13, for a viscoelastic-based adhesive. This approach relies on the Euler-Bernoulli beam theory and it was sufficiently effective in predicting the evolution of natural frequencies as the bonded overlap changes and results gave non-linear trends.

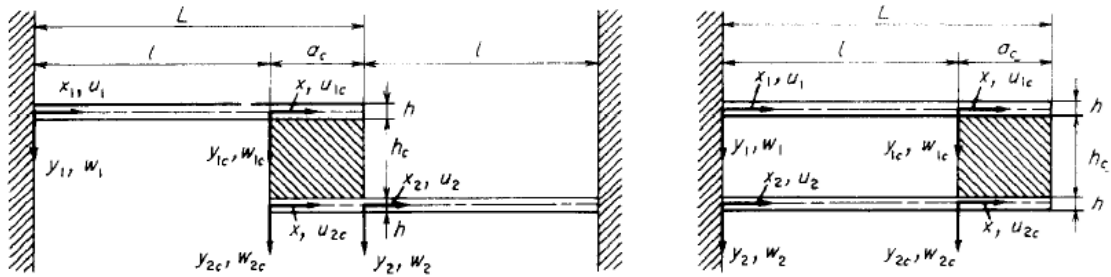


Figure 13: Explored bonded structures. Original from [103].

He and Rao [104] and Rao and He [105] analytically and numerically investigated the coupled transverse and longitudinal vibrations of bonded-lap joints. From the analytical perspective, the Hamilton's principle was followed for deriving the governing equations considering properly applied boundary conditions which led to a complex matrix system. The system solution was derived numerically due to the presence of both complex matrix values and non-linear contribution of a non-linear material model. It was found that the shear modulus produces a non-linear increase of the mechanical system whereas the increase of the adhesive thickness resulted in an increase of the loss factor.

It is evident the effort spent in describing and solving stress problems, by all the above-mentioned researchers, in a pure analytical manner. However, the introduction of numerical techniques, such as the Finite Element Method, completely revolutionised the analysis panorama for research and design

purposes. Indeed, it is a matter of fact that numerical techniques allowed the investigation of a wider set of both specimen configurations, no more restricted to the simplest geometries, and problem parameters in a easier fashion. For the specific case study of adhesively bonded joints, numerical techniques have been extensively adopted for studying multiple different problems and loading conditions. One of the earliest contribution was the work of Pirvics [106]. He investigated the bi-dimensional stress distribution of a purely homogeneous linear elastic bonded joint using the finite difference minimization of the internal energy. The work of Adams *et al.* [107–113] between the '70 and '80 can be considered as real milestones for a numerical interpretation and investigation of the structural behaviours of such joints. The interest was especially addressed to the analysis of spew fillet, its contribution in mitigating the stress concentration at the joint ends via linear and non-linear modelling techniques, as well as the stress distribution in tubular and cylindrical joint configurations. Several assessments on the influence of mechanical and geometrical parameters to the stress distribution were also performed by You *et al.* [114,115] who studied the impact of both the height and the angle of a chamfer close to the adhesive ends by elastic-plastic methods or Kumar and Pandey's [116] who developed bi- and tri-dimensional non-linear models of bonded joints. 3D assessment was particularly helpful as they revealed the presence of not intuitive strain and stress distributions that were not visible with a simple 2D analyses. Classical Finite Element demonstrated advanced capabilities in assessing the environmental effects on the structural response of bonded connections. For example, Crocombe *et al.* [117] investigated the consequences of the ageing. To do so, a Finite Element model was properly calibrated based on properly defined experimental parameters. Mubashar *et al.* [118] found that, for studying the cyclic moisture concentrations with ad-hoc Finite Elements, a model which neglects the time-dependent features produces not realistic results. In da Silva and Adams [119–121] Finite element models were adopted for investigating the state of the adhesive stress in temperature-dependent problems, once the experimental adhesive parameters were extracted by means of specific tests.

Numerical sensitivity analyses, based on geometrical parameters such as bonding length, bonding thickness and spew fillet, were performed by Grant *et al.* [122]. Finite Element models were produced, for predicting and simulating

bending and shear tests, for predicting failures numerically. In the case of a single-lap joint, the numerical study was effective in revealing an enhanced sensibility to the adhesive thickness. Moreover, it was also found that the joint becomes stronger when a specific geometrical spew fillet is applied at the joint ends.

The importance of dynamic performances of bonded connections were also studied by several remarkable studies. Kaya *et al.* [123] investigated the effect of the adhesive thickness, within a single-lap joint, on the natural frequency distribution and the sensibility of such geometry to the adopted damping through response analyses and 3D Finite Element models. The main outcome of this investigation was the precise evolution of natural frequencies, as the thickness increases. He [124] produced a numerical and experimental investigation on the modal and response properties of bonded beams. The Finite Element method was adopted for structural health monitoring purposes in the view of a reliable prediction for geometries with more complexities. Firstly, it was found that increasing the adhesive thickness produced a degradation of modal properties in terms of reduction of natural frequencies as the introduced mass contribution was higher than the stiffness contribution. Secondly, the Finite Element method was able to just capture the first few modes whereas those at higher values presented a numerical-experimental discrepancy of several hundreds of hertz. Torsional behaviours were explored by He [125] with a combined numerical and experimental approach. The numerical assessment explored the influence of both the elasticity modulus and the Poisson's ratio to the torsional frequencies. In general, both mechanical parameters play the role of enhancing the frequency content (i.e., higher values of material parameters push forward the natural frequency spectrum) but the major impact is attributed to the elasticity modulus. However, the impact of both parameters is not evident in terms of modal shapes which are essentially equal till 10 kHz.

One of the most recently adopted techniques to assess the structural behaviours of adhesive joints is the so-called Cohesive Zone Modelling (CZM). The CZM approach relies on the studies of Dugdale [126] and Barenblatt [127], who firstly postulated the idea of a cohesion and de-cohesion zone at the crack apex, and of Hillerborg *et al.* [128] who translated the theoretical studies in numerical models. Essentially, the CZM assumes the existence of a fracture process zone, which is schematized in Figure 14a, where the crack onset and progression originate. In

such zone cohesive forces oppose their contribution to the opening mechanism. Mathematically and numerically, this physical behaviour was translated into the concept of a cohesive surface of Figure 14b and then into cohesive elements which simulates the opening and closing mechanisms taking place during the loading cycles. The main assumption behind the CZM framework regards the adopted shapes of the cohesive forces, which are technically called traction-separation laws.

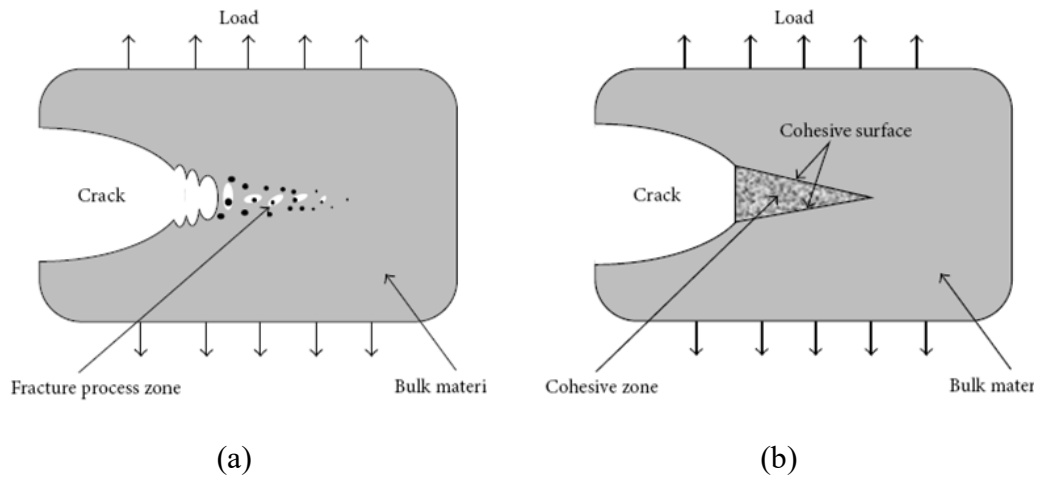


Figure 14: Physical and numerical interpretation of CZM.

Practically, such laws regulated the magnitude of the cohesive forces in opposition to the crack opening as a function of the level of separation during the generalized opening mechanisms, namely mode I, mode II and mode III, prescribed by the fracture mechanics theory. An example of mixed-mode behaviour is reported in Figure 15. Such trend is, essentially, the simultaneous combination of at least two modes contributing to the final mechanical response (e.g., modes I-II or I-III or II-III) and is valid for every element simulating the cohesive surface. The ascending part of the curves (i.e., hardening range) corresponds to a purely linear stress-displacement evolution till the first critical point (A) in which the damage onsets. The increase of the damage level is defined in the descending part of the curve (i.e., softening range) till the second critical point (B) which corresponds to the complete separation of the CZM elements.

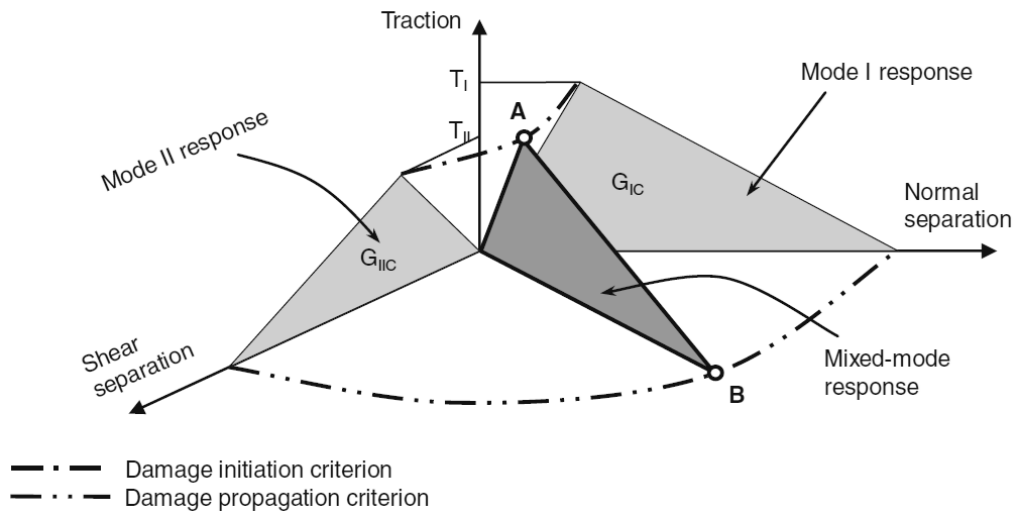


Figure 15: Mixed-mode CZM. Original from [129]

From a modelling perspective, there are two main classes of CZM elements namely zero-thickness elements and thickness representative [130]. The first type of elements, which are schematized in Figure 16, assumes the existence of a fictitious spring bed, with no mass contribution, between structural elements approximating both the adherends or the adhesive. On the contrary, the second type of CZM elements precisely approximate the shape, mass and inertia of a real layer between some media.

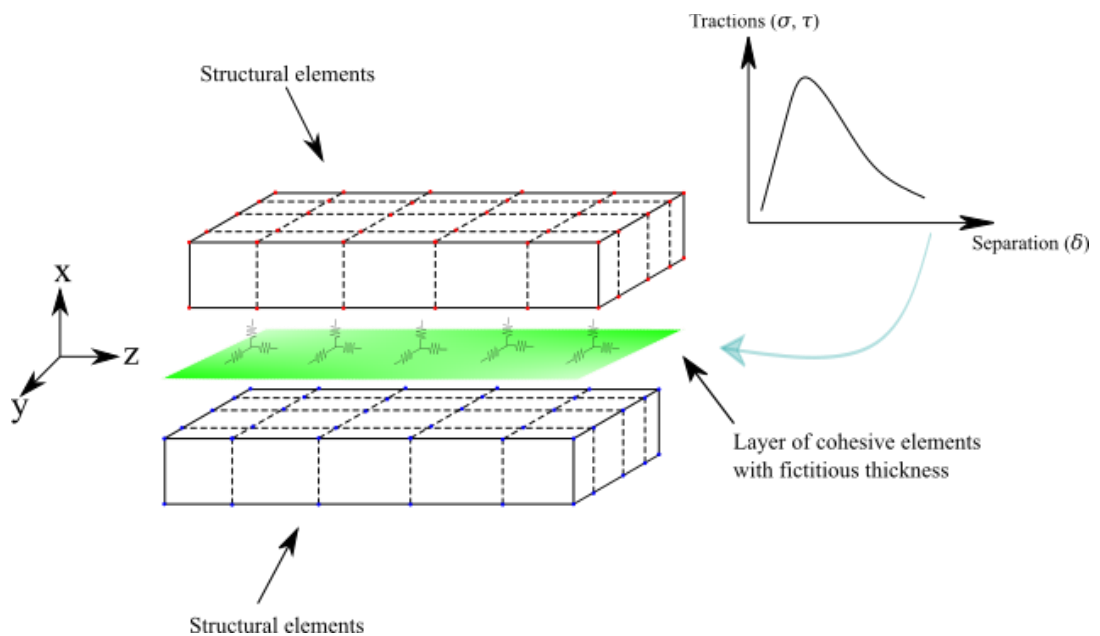


Figure 16: Zero-thickness CZM elements.

One of the most critical points in adopting the CZM approach regards the proper selection of the stress-displacement curve. Several laws exist in literature such as exponential, bi-linear, and trapezoidal and their influence on the

mechanical response has been assessed by several works, such as Alfano [131], who pointed out numerical problems for all the explored the stress-displacement shapes when the ratio of the interface toughness and the stiffness of the bulk material have comparable values, Campilho *et al.* [132] who found that the smaller bonding length the more influence of the CZM shape in terms of quality and precision of the numerical outcomes. Such influence is even more pronounced in the case of ductile materials rather than brittle ones. Gustafson and Waas [133] and Campilho *et al.* [134] performed sensitivity studies mostly oriented on the variation of mechanical and properties characterizing the CZM shape and it was found that the load bearing performances were affected by precise ratios of absorbable fracture energies, CZM strengths and bonding length as a geometrical parameter.

2.2 Very High Cycle Fatigue

Classical fatigue testing and material characterization typically rely on the hypothesis that, for many metallic materials, a horizontal fatigue limit in the S – N curve can exist (e.g., steel) or it can be assumed (e.g., aluminium) between 10^6 and 10^7 cycles namely up to the High Cycle Fatigue (HCF) regime. This means that if the applied load is lower than a specific stress threshold (i.e., $\sigma_A < \sigma^*$) the material specimen is supposed to be capable of sustain σ_A for an infinite number of cycles with no risks of failures or further degradations. Moreover, in the HCF range the component failure typically initiates from the external surface of the specimen and then progresses to the internal regions.

If the previous assumption could be considered valid in the past due to the less severe mechanical requirements in the systems design, less attention in anticipating possible catastrophic failures and a lower level of awareness in fatigue mechanisms beyond the boundary of 10^7 cycles, nowadays mechanical components are required to express enhanced fatigue characteristics in the range of the Very High Cycle Fatigue (VHCF, $N > 10^7$) keeping the reliability and safety requirements satisfied. Moreover, innovative testing machines such as Ultrasonic Fatigue Testing Machines can easily explore the VHCF range with no time issues compared to classical testing devices.

In the case of metals, Bathias [135] and Bathias *et al.* [136] provided an extensive material testing and characterization for demonstrating the absence of an infinite life in such materials through accelerated testing at 20 kHz up to $N = 10^9$. Apart recognizing that for the investigated materials such stress threshold does not exist, the failure was observed starting from the internal regions of the specimen and, more precisely, the initiation was triggered from internal inclusions and microstructural defects, as depicted in Figure 17, rather than plastic or slip band effects. In that case, the observed pattern was conventionally called as “fish-eye” morphology. Even though the fish-eye shape is the most popular and studied, other mechanisms as the sub-surface or surface initiation [137] can also exist and the difference between the two mechanisms basically depends on the material under investigation and the number of VHCF cycles. These experimental evidences highlighting the critical role of material internal features as root cause of failure initiation, pushed Murakami and Beretta [138] and Murakami and Endo [139] to establish a simple but effective criterion based on the size of the defect to assess its influence on the fatigue limit in terms of Stress Intensity Factor thus proposing this method as a basis for a reliable fatigue design.

The existence of multiple failure mechanisms between, for example, HCF and VHCF ranges (i.e., from external to internal initiation) makes much more complex the data analysis and the prediction of fatigue lives. Indeed, the classic single slope $S - N$ curve has been found no longer representative of test data and multiple slopes should be introduced to account for this [140]. Accordingly, the existence of such type of curve also implies the use of suitable probabilistic considerations for failures in the VHCF range going beyond the standardized approach based on Gaussian curves [18]. Several statistical models were developed and these are comprehensively reviewed in Tridello *et al.* [141].

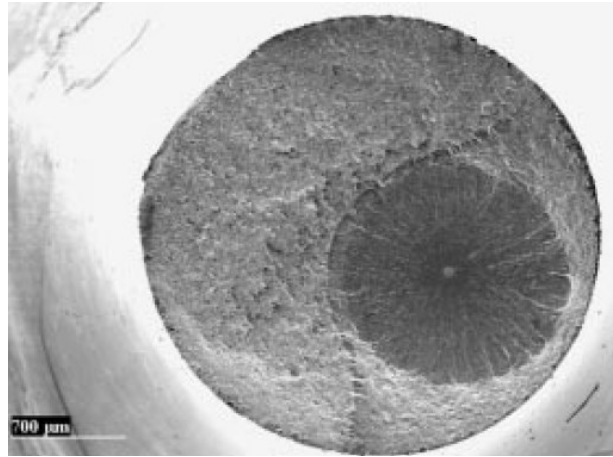


Figure 17: The fish-eye morphology in VHCF failures of metallic materials.
Original from [136]

2.2.1 State of the Art for adhesive joints.

Investigations that have been performed on VHCF responses of adhesives are quite limited as this topic is relatively new and not mature in the mechanical engineering sector. Hence, very few works are currently available in literature and, from the author's best knowledge, the works of Tridello *et al.* [20,21] represent the current state of the art in this field.

Tridello *et al.* [20] addressed the problem of establishing a design and verification methodology for butt-joints specimens and performed experiments on a cyanoacrylate adhesive as well. In particular, the developed design method is a three-step process. Firstly, through analytical calculations performed in the machine resonance conditions, the whole specimen length (i.e., an 1D bar structure) can be identified. Secondly, the use of a numerical frequency response analysis with prescribed displacement input loads permitted the investigation of the current state of stress on the bar structure. In this context, by assuming a negligible contribution provided by the adhesive layer on the axial bar stress distribution, the adhesive is placed along the bar axis at the fixed longitudinal stress of interest. In such a way, the bar specimen is thus divided in two components. Then, a final frequency response assesses the newly achieved configuration to verify the quality of the stress outcomes. The specimen design process was also corroborated with numerical mechanical and thermal-stress sensitivity analyses in order to investigate the effects of an imperfect adherend-

adhesive bonding, possible variations of material parameters (i.e., Elasticity modulus and loss factor) and the implications of coupled mechanical and thermal fields (i.e., conduction, free and forced convection) on the current stress distribution. For an unbonded area of 20%, the maximum stress increment was lower than 7.5% whereas the effects of the other quantities, in general, have marginal effects even lower than the incorrect bonding.

The full procedure described above was successfully applied for approaching the mechanical VHCF (up to) test of a cyanoacrylate adhesive. Testing coupons revealed interesting results and, to some extent, unexpected. First of all, it was observed a tendency to fail in both cohesive and mixed modes for adhesive with a higher scatter for cohesive ones. Then, the most interesting aspect regards the magnitude of the stress to trigger failures. Surprisingly, such values were very close to the current adhesive strength and the most probable explanation to account for these effects relies on strain-rate sensitivity of such type of adhesive.

Tridello et al. [21] exploited the findings presented before for investigating the VHCF performances of a structural epoxy(i.e., Betaforce 4600G) in case of artificially induced bonding defects, depicted in Figure 18, and no defects.

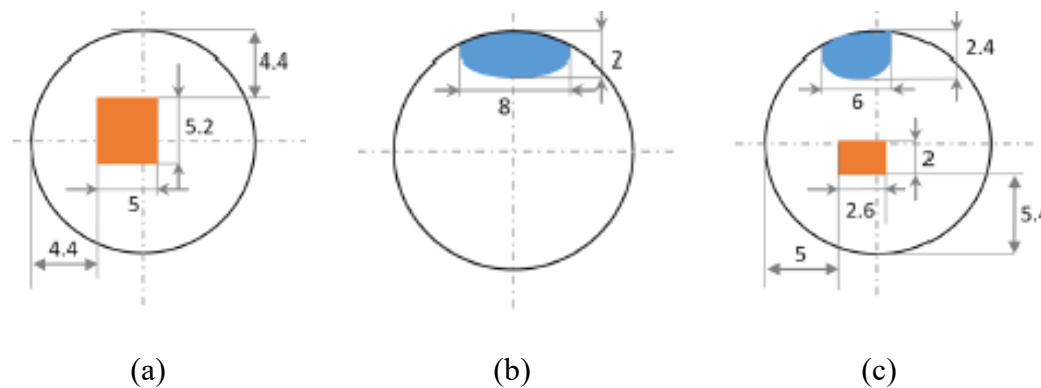


Figure 18: Specimen with defects: (a) internal, (b) external, (c) internal and external. Original from [21]

Experimental failures in VHCF showed that strength to failure levels were comparable to the tensile strength in the case of the free-of-defect specimens, as already observed in Tridello *et al.* [20], and this point reinforced the hypothesis of possible strain-rate effects. In the merit of specimen with defects, these last show

strength capabilities much lower than the free-of-defect coupon, as expected. Precisely, the strongest effect contributing to the decrease of fatigue performances was attributable to the internal damage, rather than the external one which just produced a light reduction. Moreover, the combined effect of internal-external defect was totally guided by the internal one.

An additional experimental finding concerns the shape and the distribution of fracture surfaces. These have been collected in Figure 19 for the whole specimen set. Essentially, the crack nucleation, the steady propagation and the final fracture areas were fully recognizable even though these last presented different features between the free-of-defect and the artificially damaged specimens.

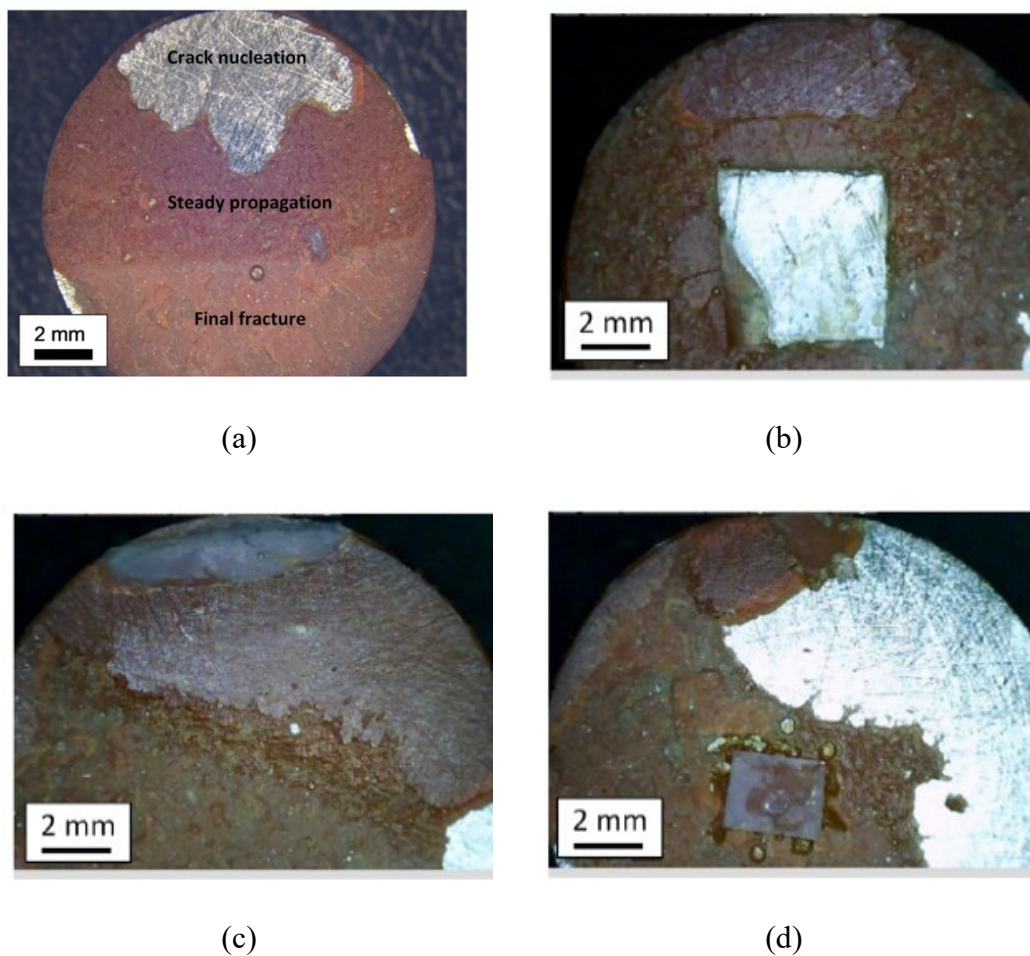


Figure 19: Fracture surfaces for (a) original specimen and with (b) internal, (c) external, (d) internal and external defects. Original from [21].

In the case of free-of-defect specimen, the crack nucleation region originated close to the free-edge and the main source was attributable to stress-singularity effects induced by the particular geometrical and material configuration. Indeed, this hypothesis was corroborated from the experimental evidence of an interfacial

(i.e., adhesive) failure as reported in Figure 19a. Both the steady propagation and the final fracture areas presented a cohesive nature. Such areas were distinguishable by different colours: the steady propagation zone was darker than the final fracture one and its size basically described the maximum area occupied by the fracture that guaranteed the 20 kHz resonance condition.

Very similar to the free-of-defect specimen case, the nucleation zone starts propagating from the external surface, in the case of internal large defect, and from the external defect in the case of the mixed configuration. This event confirmed the stress-singularity origin of failures for all the explored cases. Clearly, when referring to the stress-singularity this is just the idealization of an extremely high stress concentration at the material interface without the contribution of plastic mechanisms as the acting nominal loads are of low magnitude.

2.2.2 Testing machines

Performing tests in the VHCF range could be very time-consuming due to the large number of cycles for concluding the experiments. In Figure 20 the time requested for executing such tests is reported at varying of the applied testing frequency and it can clearly see that systems working at low frequencies can take even months for finishing the experiments. For that reason, different classes of testing systems that operate at different working frequencies were developed in order to boost the testing campaign [19].

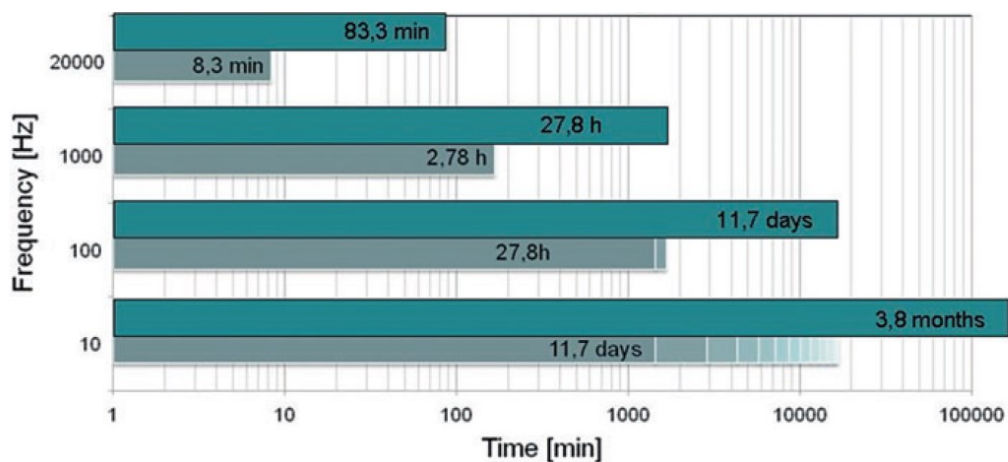


Figure 20: Time investment for performing VHCF test up to 10^7 (grey) and 10^8 (green). Original from [19].

Rotating bending machines are the earliest and, to some extent, the easiest way to perform VHCF tests. The available working range of such tools is below 200 Hz and this constitutes an important limitation for a fast and efficient material characterization. The working principle consists of the application of a bending load due to the rotational movement of an internal member. Initially, the specimen is subjected to a constant flexural load. Then, after the machine is actuated, the load varies the amplitude based on a sinusoidal motion. Apart from the relatively low frequency, one main drawback relies in the nature of the applied load. Basically, the bending load produces a variable stress distribution on the specimen cross-section which could invalidate the test outcomes.

The class of Servo-hydraulic test systems represents the most common tool that can be found in material testing departments. Its versatility in terms of loading condition, loading amplitudes and specimen shapes make it the right choice for multi-purpose material and metal testing. Typically, classic Servo-hydraulic machines can operate in the range of hundreds of Hz but, for testing in VHCF, advanced system were developed. These last can boost the test by adopting testing frequencies up to 1000 Hz. Such systems differ from classical Servo-hydraulic machines as they present reinforced members, shorter columns, a more powerful and stable control system and a reinforced base. such as random time-histories whereas, in the case of for VHCF testing equipment the main issue is related to the end of the test. In this test range, both the displacement and the strain are so limited and thus difficult to control with conventional measurement techniques.

Resonance Pulsation Test Systems are equipment that can accommodate an extended working frequency interval for VHCF testing, namely between 100 – 300 Hz. However, this test frequency cannot be selected freely as an independent parameter, but it is restricted by some technological constraints mainly determined by the specimen under test and this aspect is the main drawback in using such a technique. By contrast of testing frequencies, the range of applicable loads can vary consistently in the range of 5 kN to 1000 kN. Resonant machines allow testing in the lower VHCF range only (i.e., $\propto 10^7$) whereas only more advanced equipment working up to 1000 Hz are suitable to explore ranges up to 10^8 in a easier manner.

The need of extending the experimental range up to 10^9 , or even more, pushed forward the development of Ultrasonic Fatigue Testing Machines (UFTM). Historically, the interest in this type of testing systems started rising from 1950s from Mason [142], subsequently followed with the works of Willertz [143] and Rotem [144] and nowadays UFTM is the most adopted and suitable method for performing VHCF tests. The main feature that attracts the use of UFTM for VHCF experiments is the possibility of testing specimens with working frequencies in the range of 20 kHz, with both the specimen and the machine working in resonance conditions and this aspect considerably reduces the testing time (e.g., 14 hrs with 20 kHz for testing up to) compared to more classical equipment. The UFTM systems produce the cyclic loading through a set of different apparatuses assembled in series along the longitudinal axis. The main constituents are depicted in Figure 21 namely a piezoelectric transducer produced with piezoceramic materials, a booster and a horn which amplify and convey the excitation to the specimen and, of course, the specimen itself. An important aspect for designing the specimen under investigation regards the correct dimensions once the material is selected. In fact, for achieving the proper displacement and stress distribution along the longitudinal axis, the specimen has to respect a global size constraint which is expressed by Eq. (2.2.1) which is valid for a straight bar component

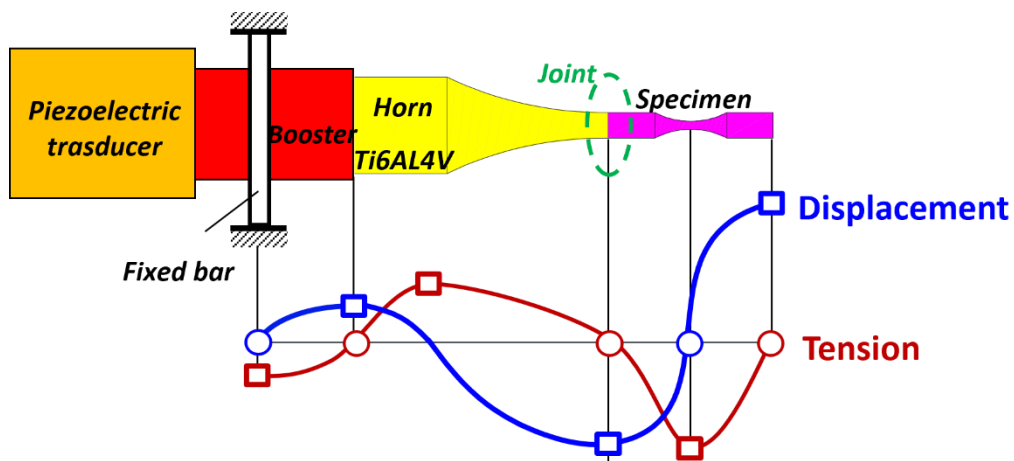


Figure 21: Schematic description of UFTM.

$$l = \frac{1}{2f} \sqrt{E/\rho} \quad \text{Eq. (2.2.1)}$$

where E/ρ is the elasticity modulus to density ratio and f is the frequency of the axial primary mode. Under such condition, the displacement presents a node in the middle of the specimen whereas stress nodes at the horn-specimen interface and at the end of the specimen too.

Among the whole system equipment, specific attention should be addressed to the horn design. Many geometrical alternatives are present in technical literature such as stepped, conical, exponential, catenoidal and Fourier [145] and all of them have precise shapes that were mathematically deduced. Investigations in this field are still active as demonstrated by the work of Rosca *et al.* [146] who designed and characterized an optimised axisymmetric ultrasonic horn which shape was extracted by employing optimization methods, elasticity laws, variational approaches and such configuration permitted a better nodal point positioning. Costa *et al.* [147] developed a horn structure capable of combining both tension and torsion for a bi-axial characterization during a single VHCF test. The followed approach for designing a bi-axial horn relies mainly on Finite Element Models and experimental methods. Results were satisfactory apart from specific and localized regions where predicted stress and displacement presented partial differences. Lin *et al.* [148] performed an analytical study for investigating the possibility of designing an innovative longitudinal step-type horn with tuneable and adjustable performance. To accomplish the research purposes, the authors focused on the effect of the electric impedance as well as the location of piezoelectric materials.

- Ultrasonic Fatigue Testing Machines developed at Politecnico di Torino

The research group “Mechanics of materials and joints” at Politecnico di Torino [149] developed its own UFTM for VHCF tests [150,151] which is depicted in Figure 22. The Politecnico di Torino UFTM is engineered to work with a central frequency at 20 kHz but, in to accommodate specimens of different materials, types and geometrical features, an extended frequency interval namely 20 ± 0.5 kHz was planned during the mechanical design. UFTM can perform tests under fully reversed tension-compression stress conditions ($R = -1$). It was originally designed for testing metallic specimens and subsequently adapted to characterize adhesive butt-joints. UFTM is constituted by the following apparatus:

(i) the ultrasonic generator (Branson DCX 4 kW, not visible in Figure 22), which provides a sinusoidal signal at 20 kHz; (ii) a piezoelectric transducer that converts the electrical signal in a mechanical vibration; (iii) two amplifying devices (i.e., a booster and a horn made of Ti-6Al-4V), designed to amplify and convey the magnitude of vibration to the tested specimen; (iv) the specimen under investigation; (v) a laser-displacement sensor providing the feedback signal for the control system and positioned at the specimen free end; (vi) cold air vortex tubes that keep the specimen temperature between [20 – 24] °C.

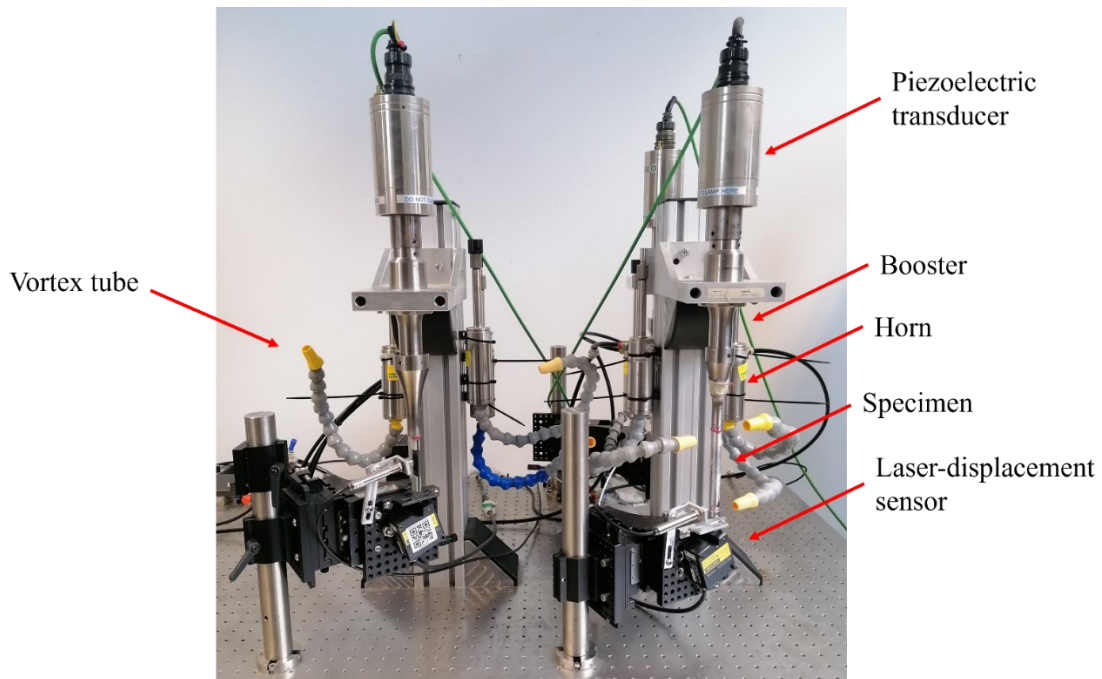


Figure 22: UFTM developed at Politecnico di Torino

During the VHCF test evolution, the adhesive layer is subjected to an alternated stress which is kept through a closed-loop control strategy and its working principle assumes that the displacement at the specimen free end is used as a feedback signal. A Proportional-Integrative-Derivative (PID) strategy defines the control system scheme. In essence, the displacement amplitude is the feedback control signal for the PID, where P is calculated as the difference between the test measured displacement amplitude and the displacement set point (i.e., a displacement value known from FEM analysis for the selected stress level), thus ensuring the required applied stress amplitude. The adopted input voltage to actuate the system is therefore modified and corrected by considering the output correction of the PID. However, it must be noted that due to the limited

temperature variation, the PID usually applies small corrections of the voltage to keep the stress amplitude constant.

A criterion based on the stiffness loss is adopted for finishing the VCHF test. In fact, apart from cases where the test ends following run-out (e.g., $N=10^9$), the test stops when the longitudinal frequency of the mechanical system falls below 19.5 kHz. Two cases can be observed: (i) the complete separation of the specimen under test or (ii) the specimen is still joined but the fracture surfaces were progressed enough to reduce the stiffness of the specimen without the complete separation. In the first circumstance no additional action should be performed whereas in the second circumstance an extra load (manual or automatic) should be applied to separate the members.

2.3 Statistical methods for S-N curves

The introduction of the VHCF testing technique, as an innovative method to extend the investigation range for materials and structures, revealed the presence of different failure mechanisms characterizing the collapse under alternating fatigue loadings [135]. In this context, if two distinct failure modes (e.g., internal-initiated and external-initiated failures) can exist, the conventional fatigue limit represented by a plateau in the S – N curve can be assumed as a transition region between these latter. Moreover, two failure mechanisms can also coexist as demonstrated by [135,152–154]. However, the conventional statistical approach to describe experimental data, as suggested by international standards such as ASTM E739-91 [155] or ISO 12107:2003 [156], consider such failure modes one at a time with a linear formulation for the mean fatigue life and a constant standard deviation. For that reason, when dealing with multiple failure mechanisms and failure sources, it is important to use a generalized data analysis framework capable to describe the S – N fatigue data distribution regardless the number of failure modes and causes.

2.3.1 Elements of Probability

Laws of probability arose in the XVII century for studying specific experimental findings that were not explicable with deterministic models but only with a level of confidence. Nowadays, the engineering practice extensively adopts

laws of probability to design structures, understand and describe experimental outcomes and for predicting potential responses of mechanical systems (e.g., random vibrations).

This Section has the purpose of briefly introducing some basic concepts of the theory of probability for better understanding the “language” adopted in Section 2.3.2 where these concepts are flow down into fatigue applications. A more complete and a wider discussion on similar topics is addressed in specific probability books like [157].

Three fundamental rules constitute the framework of the axiomatic probability theory, called Kolmogorov axioms. If Ω is a generic set and A an event sub-set, then $P[A]$ is a real number expressing the probability. In such a way, the main axiomatic rules are:

- The probability of A is a number between 0 – 1 (i.e., $0 \leq P[A] \leq 1$);
- A sure event has a probability of 1 (i.e., $P[\Omega \equiv A] = 1$);
- The joined probability of two events A, B is $P[A \cup B] = P[A] + P[B]$ if $P[A \cap B] = 0$

From those axioms, three theorems descend:

- Probability of mutually exclusive events (i.e., $P[\tilde{A}] = 1 - P[A]$);
- Total probability (i.e., $P[A \cup B] = P[A] + P[B] - P[A \cap B]$)
- Conditional probability (i.e., $P[A|B] = \frac{P[A \cap B]}{P[B]}, P[B] > 0$)

An event has a deterministic nature if all the measurements characterizing such event can be certainly predictable. A deterministic variable is the mathematical entity describing a deterministic event. If an event has the possibility of both happening or not happening under the same conditions, with no possibilities of knowing it certainly, this event is aleatory. An aleatory variable is the mathematical entity describing an aleatory event.

Aleatory variables can be continuous or discrete. For continuous variables, it can be defined $F_X(x)$ as the cumulative distribution function, the following expression

$$F_X(x) = P[X \leq x] \quad \text{Eq. (2.3.1)}$$

$F_X(x)$ express the probability that the aleatory variable X will have values lower than x and it can assume values between 0 – 1. In the case of continuous variables, can be expressed as follows

$$F_X(x) = \int_{-\infty}^x p_X(\rho) d\rho \quad \text{Eq. (2.3.2)}$$

where $p_X(x)$ is a fundamental relationship in the theory of probability, called probability density function.

The $p_X(x)$ function can be associated to different shapes (e.g., Poisson, geometric, χ -distribution, etc...) so with both discrete and continuous variables. Among these the most well-known and typically adopted model in engineering is the Gaussian (or Normal) distribution.

$$p_X(x) = \frac{1}{\sigma_X \sqrt{2\pi}} \exp \left[-\frac{1}{2} \left(\frac{x - \mu_X}{\sigma_X} \right)^2 \right] \quad \text{Eq. (2.3.3)}$$

where μ_X and σ_X are, respectively, the mean value and the standard deviation of X . Gaussian distribution is completely known from a probabilistic perspective by just knowing these values. Sometimes Eq. (2.3.3) is also written in terms of of the auxiliary variable $Z = \frac{X - \mu_X}{\sigma_X}$ as

$$p_X(x) = \frac{1}{\sqrt{2\pi}} e^{z^2/2} \quad \text{Eq. (2.3.4)}$$

Bernoulli distribution has a discrete nature and is particularly suitable for describing events like fatigue ruptures. In such case, $p_X(x)$ has the following definition

$$p_{X_k}(x) = \begin{cases} 1 - p & \text{for } x = 0 \\ p & \text{for } x = 1 \end{cases} \quad \text{Eq. (2.3.5)}$$

with mean value $\mu_{X_k} = p$ and variance $\sigma_{X_k}^2 = (1 - p)p$.

2.3.2 A statistical fatigue model

The case study for introducing a more precise statistical fatigue model is presented in the following for the so-called Duplex S – N curve, depicted in Figure 23. Such curve type is characterized by the two failure modes (i.e., surface nucleation and internal nucleation), a transition plateau stress between these last and a fatigue limit.

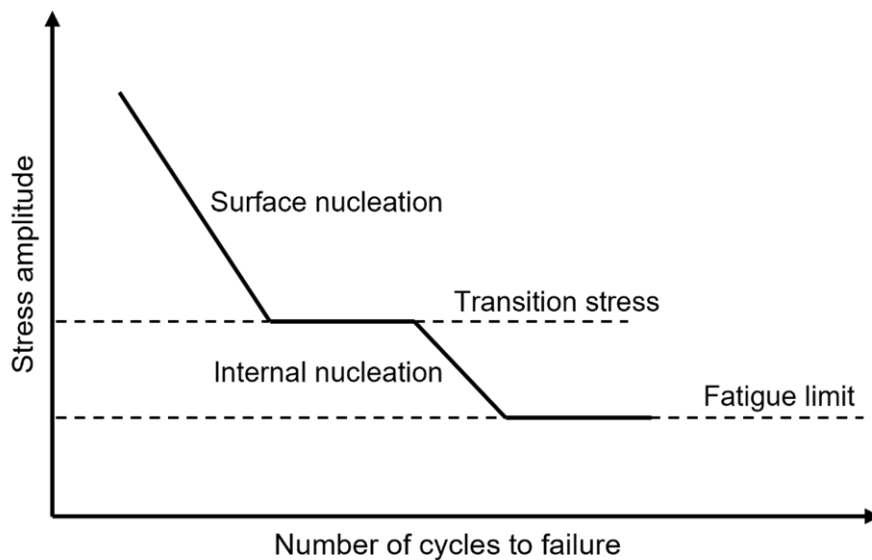


Figure 23: Example of a Duplex S - N curve.

In the case of a Duplex S – N curve, some working hypotheses are necessary for the proper model development, as stated by Paolino *et al.* [22]:

- Both the fatigue limit and the transition stress are random variable namely σ_{fl} and σ_{tr} and respectively. Both quantities are associated to a cumulative density function namely $F_{\sigma_{fl}}$ and $F_{\sigma_{tr}}$. Fatigue limit and transition stress can vary randomly from specimen to specimen;
- σ_{fl} and σ_{tr} are independent random variables;
- Each failure mode is a Bernoulli random variable;
- N_{int} and N_{surf} are the fatigue life associated to an internal failure mode ($M=int$). These are conditional random variables;
- N_{int} and N_{surf} are the fatigue life associated to a surficial failure mode ($M=surf$). These are conditional random variables;
- The event is sure (i.e., $P[X_t \leq X_t] = 1$)

From such hypotheses, some probabilistic equations can be directly derived. Eq. (2.3.6) express the probability of having a surface-initiated failure, whereas Eq. (2.3.7) regulates the probability of an internal-initiated failure.

$$P[M = surf] = F_{X_t} \quad \text{Eq. (2.3.6)}$$

$$P[M = int] = F_{X_l}(1 - F_{X_t}) \quad \text{Eq. (2.3.7)}$$

In terms of fatigue life, the probability level to have a surface-initiated failure of Y fatigue life smaller than a selected y value is dictated by Eq. (2.3.8) and similarly for the internal-initiated failure in Eq. (2.3.9)

$$\begin{aligned} P[Y \leq y, M = surf] &= P[Y \leq y | M = surf] \cdot P[M = surf] \\ &= F_{Y|surf} \cdot F_{X_t} \end{aligned} \quad \text{Eq. (2.3.8)}$$

$$\begin{aligned} P[Y \leq y, M = int] &= P[Y \leq y | M = int] \cdot P[M = int] \\ &= F_{Y|int} \cdot F_{X_l}(1 - F_{X_t}) \end{aligned} \quad \text{Eq. (2.3.9)}$$

The total probability is then achieved by using the Total Probability Theorem, as expressed in Eq. (2.3.10), which represents the statistical model S – N curves with two modes of failure

$$F_Y = F_{Y|surf}F_{X_t} + F_{Y|int}F_{X_l}(1 - F_{X_t}) \quad \text{Eq. (2.3.10)}$$

The cumulative distribution function, F_Y , in Eq. (2.3.10) has a direct relationship with the cumulative distribution functions of X_l , X_t , $Y|_{int}$ and $Y|_{surf}$. Regarding X_l , X_t , such random variables can be described by different probability models but a Gaussian type is preferred for the model development. Thus,

$$F_{X_l} = \Phi \left[\frac{x - \mu_{X_l}}{\sigma_{X_l}} \right] \quad \text{Eq. (2.3.11)}$$

$$F_{X_t} = \Phi \left[\frac{x - \mu_{X_t}}{\sigma_{X_t}} \right] \quad \text{Eq. (2.3.12)}$$

where $\Phi[\cdot]$ stands for the Gaussian cumulative distribution function. In a similar fashion, also the conditional probabilities for and can be considered under a normal distribution

$$F_{Y|surf} = \Phi \left[\frac{y - \mu_{Y|surf}}{\sigma_{Y|surf}} \right] \quad \text{Eq. (2.3.13)}$$

$$F_{Y|int} = \Phi \left[\frac{y - \mu_{Y|int}}{\sigma_{Y|int}} \right] \quad \text{Eq. (2.3.14)}$$

In Eq. (2.3.13) and Eq. (2.3.14) the model parameters $\mu_{Y|int}$ and $\sigma_{Y|int}$ depend on the applied stress magnitude. The simplest model that can be used for describing the trend of the mean value (i.e., $\mu_{Y|int}$, $\mu_{Y|surf}$, also known as location parameter) and of the standard deviation (i.e., $\sigma_{Y|int}$, $\sigma_{Y|surf}$, also known as scale parameter) considers a linear decreasing distribution of the location parameter [155,158] with an assumed constant value of the scale parameter as follows

$$\mu_{Y|int} = a_{Y|int} + x \cdot b_{Y|int} \quad \text{Eq. (2.3.15a)}$$

$$\mu_{Y|surf} = a_{Y|surf} + x \cdot b_{Y|surf} \quad \text{Eq. (2.3.15b)}$$

where $a_{Y|int}$, $b_{Y|int}$, $a_{Y|surf}$, $b_{Y|surf}$ are constant model parameters to be determined.

Finally, by introducing Eqs. (2.3.11) – (2.3.15) in Eq. (2.3.10), the final expression of F_Y is

$$F_Y = \Phi \left[\frac{y - (a_{Y|surf} + x \cdot b_{Y|surf})}{\sigma_{Y|surf}} \right] \Phi \left[\frac{x - \mu_{X_t}}{\sigma_{X_t}} \right] + \Phi \left[\frac{y - (a_{Y|int} + x \cdot b_{Y|int})}{\sigma_{Y|int}} \right] \Phi \left[\frac{x - \mu_{X_l}}{\sigma_{X_l}} \right] \left(1 - \Phi \left[\frac{x - \mu_{X_t}}{\sigma_{X_t}} \right] \right) \quad \text{Eq. (2.3.16)}$$

where the number of parameters of be determined is 10 (i.e, $a_{Y|surf}$, $b_{Y|surf}$, $\sigma_{Y|surf}$, $a_{Y|int}$, $b_{Y|int}$, $\sigma_{Y|int}$, μ_{X_t} , σ_{X_t} , μ_{X_l} , σ_{X_l}).

Eq. (2.3.16) is the fundamental model that accounts for Duplex S – N curves. Obviously, such model cannot cover and predict S – N with more than two failure modes (e.g., internal and external failures). However, other failure modes and sources can be foreseen during the in-service life of components and attributable to porosity, inclusions, voids, internal/external nucleation and scratches. To account for such modes, a generalization of Eq. (2.3.16) is necessary. For the sake

of brevity and without going into details, the model generalization basically extends the initial working hypothesis. Such generalization leads to an extended formulation of in Eq. (2.3.10) as follows

$$F_Y = \sum_{i=1}^m F_{X_{t_{i-1}}} (1 - F_{X_{t_i}}) \cdot \sum_{j=1}^{c_i} F_{Y|(i,j)} p_{j|i} \quad \text{Eq. (2.3.17)}$$

where m is the number of failure modes, c_i is number of failure causes generating the i^{th} failure mode, $F_{X_{t_i}}$ is the cumulative probability function associated with the i^{th} transition stress, $F_{Y|(i,j)}$ is the cumulative probability function for the fatigue lives of the i^{th} failure mode due to the j^{th} failure source and $p_{j|i}$ the probability of having the j^{th} failure cause within the i^{th} failure mode..

By assuming the existence of m transition stresses and Normal distributions for the random variables, $F_{X_{t_{i-1}}}$ and $F_{Y|(i,j)}$ assume the form

$$F_{X_{t_{i-1}}} = \Phi \left[\frac{x - \mu_{X_{t_{i-1}}}}{\sigma_{X_{t_{i-1}}}} \right] \quad \text{Eq. (2.3.18)}$$

$$F_{Y|(i,j)} = \Phi \left[\frac{y - (a_{Y|(i,j)} + b_{Y|(i,j)} \cdot x)}{\sigma_{Y|(i,j)}} \right] \quad \text{Eq. (2.3.19)}$$

where in Eq. (2.3.18) $\mu_{X_{t_0}} = \mu_{X_{t_i}}$ and $\sigma_{X_{t_0}} = \sigma_{X_{t_i}}$ whereas Eq. (2.3.19) is directly written in terms of the linear approximation.

Thus, the generalized statistical fatigue model valid for any possible failure source and modes is presented in the following

$$F_Y = \sum_{i=1}^m \Phi \left[\frac{x - \mu_{X_{t_{i-1}}}}{\sigma_{X_{t_{i-1}}}} \right] \left(1 - \Phi \left[\frac{x - \mu_{X_{t_i}}}{\sigma_{X_{t_i}}} \right] \right) \cdot \sum_{j=1}^{c_i} \Phi \left[\frac{y - (a_{Y|(i,j)} + x \cdot b_{Y|(i,j)})}{\sigma_{Y|(i,j)}} \right] p_{j|i} \quad \text{Eq. (2.3.20)}$$

For a model like this, the numbers of the involved parameters are dictated by

$$n_{par} = 2m + 3 \sum_{i=1}^m c_i + \sum_{i=1}^m (c_i - 1) \quad \text{Eq. (2.3.21)}$$

For example, in the case of 2 failure modes ($m = 2$) and just one failure cause for each of them ($c_1 = c_2 = 1$), which represents the case study of Duplex S – N curves, $n_{par} = 10$.

Some applications of the developed generalized framework are presented for clarification purposes, as addressed in the original paper of Paolino *et al.* [22]:

1. One failure mode due to one cause without fatigue limit ($m = 1, c_1 = 1, F_{X_{t_0}} = F_{X_1} = 1$)

$$F_Y = F_{Y|(1,1)} \quad \text{Eq. (2.3.22a)}$$

$$F_Y = \Phi \left[\frac{y - (a_{Y|(1,1)} + x \cdot b_{Y|(1,1)})}{\sigma_{Y|(1,1)}} \right] \quad \text{Eq. (2.3.22b)}$$

2. One failure mode due to one cause with fatigue limit ($m = 1, c_1 = 1, F_{X_{t_0}} = 1, F_{X_1} < 1$).

$$F_Y = F_{X_1} F_{Y|(1,1)} \quad \text{Eq. (2.3.23a)}$$

$$F_Y = \Phi \left[\frac{x - \mu_{X_1}}{\sigma_{X_1}} \right] \Phi \left[\frac{y - (a_{Y|(1,1)} + x \cdot b_{Y|(1,1)})}{\sigma_{Y|(1,1)}} \right] \quad \text{Eq. (2.3.23b)}$$

3. Two failure modes due to one cause without plateau and fatigue limit ($m = 2, c_1 = c_2 = 1, F_{X_{t_0}} = F_{X_1} = 1, F_{X_{t_2}} = 0$).

$$F_Y = (1 - F_{X_{t_1}}) F_{Y|(1,1)} + F_{X_{t_1}} F_{Y|(2,1)} \quad \text{Eq. (2.3.24a)}$$

$$F_Y = \left(1 - \Phi \left[\frac{x - \mu_{X_{t_1}}}{\sigma_{X_{t_1}}} \right] \right) \Phi \left[\frac{y - (a_{Y|(1,1)} + x \cdot b_{Y|(1,1)})}{\sigma_{Y|(1,1)}} \right] + \Phi \left[\frac{x - \mu_{X_{t_1}}}{\sigma_{X_{t_1}}} \right] \Phi \left[\frac{y - (a_{Y|(2,1)} + x \cdot b_{Y|(2,1)})}{\sigma_{Y|(2,1)}} \right] \quad \text{Eq. (2.3.24b)}$$

4. Two failure modes due to one cause without plateau and with fatigue limit ($m = 2, c_1 = c_2 = 1, F_{X_1} < 1$).

$$F_Y = F_{X_1} (1 - F_{X_{t_1}}) F_{Y|(1,1)} + F_{X_{t_1}} F_{Y|(2,1)} \quad \text{Eq. (2.3.25a)}$$

$$F_Y = \Phi \left[\frac{x - \mu_{X_l}}{\sigma_{X_l}} \right] \left(1 - \Phi \left[\frac{x - \mu_{X_{t_1}}}{\sigma_{X_{t_1}}} \right] \right) \Phi \left[\frac{y - (a_{Y|(1,1)} + x \cdot b_{Y|(1,1)})}{\sigma_{Y|(1,1)}} \right] \\ + \Phi \left[\frac{x - \mu_{X_{t_1}}}{\sigma_{X_{t_1}}} \right] \Phi \left[\frac{y - (a_{Y|(2,1)} + x \cdot b_{Y|(2,1)})}{\sigma_{Y|(2,1)}} \right] \quad \text{Eq. (2.3.25b)}$$

5. Two failure modes due to one cause with plateau and without fatigue limit ($m = 2, c_1 = c_2 = 1, F_{X_{t_0}} = F_{X_1} = 1, F_{X_{t_2}} = 0$). Such model has the same formulation of Eq. (2.3.23).
6. Two failure modes due to one cause with plateau and with fatigue limit ($m = 2, c_1 = c_2 = 1, F_{X_1} < 1$). Such model has the same formulation of Eq. (2.3.24).
7. One failure mode due to two causes without fatigue limit ($m = 1, c_1 = 2, F_{X_1} = 1, F_{X_{t_1}} = 0, p_{2|1} = 1 - p_{1|1}$).

$$F_Y = p_{1|1} F_{Y|(1,1)} + (1 - p_{1|1}) F_{Y|(1,2)} \quad \text{Eq. (2.3.26a)}$$

$$F_Y = p_{1|1} \Phi \left[\frac{y - (a_{Y|(1,1)} + x \cdot b_{Y|(1,1)})}{\sigma_{Y|(1,1)}} \right] \\ + p_{2|1} \Phi \left[\frac{y - (a_{Y|(1,2)} + x \cdot b_{Y|(1,2)})}{\sigma_{Y|(1,2)}} \right] \quad \text{Eq. (2.3.26b)}$$

8. One failure mode due to two causes with fatigue limit ($m = 1, c_1 = 2, F_{X_1} = 1, F_{X_{t_1}} = 0, p_{2|1} = 1 - p_{1|1}$).

$$F_Y = F_{X_l} (p_{1|1} F_{Y|(1,1)} + (1 - p_{1|1}) F_{Y|(1,2)}) \quad \text{Eq. (2.3.27a)}$$

$$F_Y = \Phi \left[\frac{x - \mu_{X_l}}{\sigma_{X_l}} \right] \left(p_{1|1} \Phi \left[\frac{y - (a_{Y|(1,1)} + x \cdot b_{Y|(1,1)})}{\sigma_{Y|(1,1)}} \right] \\ + p_{2|1} \Phi \left[\frac{y - (a_{Y|(1,2)} + x \cdot b_{Y|(1,2)})}{\sigma_{Y|(1,2)}} \right] \right) \quad \text{Eq. (2.3.27b)}$$

In Eq. (2.3.16), in the case of Duplex S – N curves, and in Eq. (2.3.20), in the case of a generalized statistical fatigue model, parameters were introduced as

quantities to be determined. In the following, the procedure for their extraction will be addressed. Without losing generality, the parameters extraction is addressed for the case of Duplex S – N curves as described in Paolino *et al.* [159,160].

The extraction of the model parameters is typically performed starting from the derivative of the cumulative probability function in Eq. (2.3.28) of failed specimens

$$f_Y = \frac{dF_Y}{dy} = \frac{\varphi \left[\frac{y - (a_{Y|surf} + x \cdot b_{Y|surf})}{\sigma_{Y|surf}} \right]}{\sigma_{Y|surf}} \Phi \left[\frac{x - \mu_{X_t}}{\sigma_{X_t}} \right] + \frac{\varphi \left[\frac{y - (a_{Y|int} + x \cdot b_{Y|int})}{\sigma_{Y|int}} \right]}{\sigma_{Y|int}} \Phi \left[\frac{x - \mu_{X_l}}{\sigma_{X_l}} \right] \left(1 - \Phi \left[\frac{x - \mu_{X_t}}{\sigma_{X_t}} \right] \right) \quad \text{Eq. (2.3.28)}$$

Where φ denotes the Gaussian probability density function.

The key aspect of the extraction procedure lies on the application of the Maximum Likelihood (ML) Principle. So, assuming the existence of (x_i, y_i) with $i = 1, \dots, n_f$ a set of failed specimens and (x_i, y_i^*) with $i = 1, \dots, n_r$ a set of run-out specimens in the experimental data set, the Likelihood function has the form

$$L[\boldsymbol{\theta}] = \prod_{i=1}^{n_f} f_Y[y_i; x_i, \boldsymbol{\theta}] \cdot \prod_{j=1}^{n_r} (1 - F_Y[y_j^*; x_j, \boldsymbol{\theta}]) \quad \text{Eq. (2.3.29)}$$

In Eq. (2.3.29), $\boldsymbol{\theta}$ represents the set of parameters to be determined (i.e., for Duplex S – N curves in number of 10: $a_{Y|surf}$, $b_{Y|surf}$, $\sigma_{Y|surf}$, $a_{Y|int}$, $b_{Y|int}$, $\sigma_{Y|int}$, μ_{X_t} , σ_{X_t} , μ_{X_l} , σ_{X_l}). Using the ML the research is addressed to the $\tilde{\boldsymbol{\theta}}$ set which maximize Eq. (2.3.29). ML principle was chosen due to several reasons. First, ML as a statistical estimator has good asymptotic properties (i.e., Normality, unbiased, efficiency and consistency). Then, the application of ML allows take into account also run-out specimens for the S – N calculation and this is a particular advantage with respect to other methods based on, for example, the least square methods.

From a computational perspective, Eq. (2.3.29) requires the application of an optimization algorithm for finding parameters. To do so, the `fminsearch` MatLab® function based on the Nelder-Mead simplex algorithm was adopted.

The adoption of Eq. (2.3.29) allows model parameters extraction for any probability level of failure (i.e., the quantile).

2.4 Stress singularity

This section addresses the main aspects of stress singularities in terms of mathematical and physical features as well as the most relevant papers published in this field of research. An initial overview of the stress singularities and the fundamental results in their analysis is illustrated. Such overview is organized according to a global timeline (i.e., from the oldest to the newest paper) and as much as coherent with the discussed topic. Furthermore, with a specific focus, the Bogy mathematical model to investigate and predict singularities in any kind of bi-material joint configurations, is presented and discussed. Finally, the removal of the stress singularity based on the inverse Bogy model is introduced. Such specific separation was followed as the Bogy mathematical framework represents the theoretical backbone of the research topic of this manuscript which is discussed in Section 3

Detection and quantification of geometrical and mechanical features that could endanger the mechanical performance of a component have always been an important topic in structural engineering. In particular, the investigations regarding stress-singularities, their nature and their consequences for safe working conditions, received special attentions from the scientific community in terms of analytical studies, numerical modelling and experimental assessments.

From a physical perspective, stress-singularities are point-regions in a component (e.g., corners, notches, material interfaces, etc.), as schematically depicted in Figure 24, where stress magnitudes theoretically tend to infinite values. In the neighbour regions of a stress singularity, the stress profile can be modelled and described as suggested by the following equation,

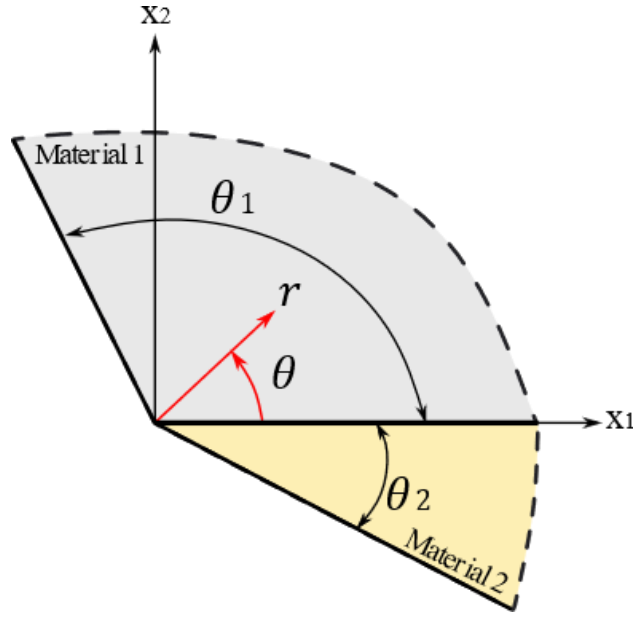


Figure 24: Example of a corner between different material interfaces where a singular stress profile can be foreseen

$$\sigma_{ij} = \sum_{k=1}^{\infty} K_k H_{ij}^k(\phi) \zeta^{-\lambda_k} + H.O.T \quad \text{Eq. (2.4.1)}$$

where σ_{ij} is the stress tensor, K is the generalized Stress Intensity Factor (gSIF), H radial functions depending on the local angle, ζ a non-dimensional coordinate which is function of the distance from the point of interest, λ_k is the k^{th} singularity exponent and is the smooth non-singular part of the stress. The use of gSIF is justified as the classical formulation of the SIF accounts for cracks. In the case of bonded unions, which is the main topic discussed in this manuscript, a stress singularity is also expected at the material interfaces, if local conditions are suitable to trigger this feature, or as a consequence of a free-edge effect. In particular, in the case of multi-material joints, stress singularities arise as a consequence of material discontinuity in presence of free-edge.

From Eq. (2.4.1) the mathematical condition that foresees the presence of a set of stress-singularities can be easily identified namely $0 < \lambda_k < 1 \forall k$ but nothing can be stated regarding the final “shape” of the stress profile (i.e., monotonic or oscillating).

Even though the concept of stress-singularity presents some contradictions with respect to the linear elasticity [161] as *i*) they violate the basic assumptions

of this subject and *ii*) locally the material should not respond as an elastic solid due to the exceedance of the elastic limit, the study of such characteristic still progresses from 1950.

One of the earliest contributions in this discipline was the one of Williams [162] who studied the problem of stress singularities resulting from different boundary conditions (i.e., free – free, clamped – clamped, clamped – free) in the case of homogeneous mono-material plates. According to Williams [162], the presence and the intensity of a singular feature could have been described by a set of eigenproblems in terms of harmonic functions, whose formulation strongly depends on the adopted boundary conditions (see Table 1). As normal practice in detecting singularities, the interest was addressed in finding one or more values of the singularity exponent (λ_k) such as $0 < \lambda_k < 1$. Analytically, Williams demonstrated that among the explored configurations, only the clamped – free plate may present the singular feature at the vertex for angles $\theta_1 + \theta_2 < 180^\circ$ whereas, between $180^\circ - 360^\circ$, all the configurations could exhibit the same property.

The before mentioned problem was also extended by Williams to cracks within an homogeneous mono-material component [163] as well as to crack in dissimilar media [164].

Similar conclusions were found by England [165] through eigenvalue-based analyses with much more mathematical efforts and complexity. Essentially, the Author remarked the strong dependence of the type of the stress singularity on the applied boundary conditions whereas the magnitude of the singularity was a direct consequence of the wedge angle. Dunn *et al.* [166] concentrated the efforts on singularities induced by notches. To do so, both analytical and numerical methods were employed and it was demonstrated that an increase of the notch angle produced increasing values in the singularity-dominated region but the strength of such singularity decreased.

Case	Applied BCs	Eigenfunction ($z = \lambda\alpha$)	Load condition	Constants
1	Free-Free	$\sin(z) = C_1 z$	Bending	$C_1 = \pm \frac{1-\nu}{3+\nu} \frac{\sin(\alpha)}{\alpha}$
			Extension	$C_1 = \pm \frac{\sin(\alpha)}{\alpha}$
2	Clamped-Clamped	$\sin(z) = C_2 z$	Bending	$C_1 = \pm \frac{\sin(\alpha)}{\alpha}$
			Extension	$C_1 = \pm \frac{1+\nu}{3-\nu} \frac{\sin(\alpha)}{\alpha}$
3	Clamped-Free	$\sin^2(z) = K_1^2 - K_2 z^2$	Bending	$K_1 = \pm \left[\frac{4}{(3+\nu)(1-\nu)} \right]^{\frac{1}{2}}$ $K_2 = \pm \left[\frac{1-\nu}{3+\nu} \right]^{\frac{1}{2}} \frac{\sin(\alpha)}{\alpha}$
			Extension	$K_1^2 = \pm \left[\frac{4}{(3-\nu)(1+\nu)} \right]^{\frac{1}{2}}$ $K_2 = \pm \left[\frac{1+\nu}{3-\nu} \right]^{\frac{1}{2}} \frac{\sin(\alpha)}{\alpha}$

Table 1: Williams results from [162]

Even though the problem of stress singularities in mono-material components is still valuable and an actual problem as demonstrated by the remarkable literature surveys of Sinclair [167,168] regarding mathematical, modelling and physical aspects of stress-singularities as well as the continuous research spent in this direction as Lazzarin *et al.* [169] in the case of V-shaped notches under mixed loading conditions, Ciavarella and Meneghetti [170] regarding the fatigue limit when notches are present, de Moiras [171] concerning the calculation of SIF through Finite Element Models and the force method, Berto *et al.* [172] in the

merit of out-of-plane singular stress fields for V-notches under in-plane shear load conditions, Zhu *et al.* [173] regarding mathematical and physical aspects of stress singularities at a crack tip, Shen *et al.* [174] for U-shapes and V-shaped notches with simplified methods and Radaj [175] who extensively reviewed the concepts of SIF in the case of 2D and 3D components as well as on notches, welded components etc..., modern structures are much more complex. Indeed, these latter are typically constituted by bi, tri or multi-material unions of different constituents such as composite, metals, ceramics, resins etc... thus, presenting the interaction between dissimilar properties (i.e., Modulus of Elasticity, Poisson's ratio, strain, strength) along a bondline.

Bogy [176] firstly approached the problem of bi-material connections under the assumption of classical, isotropic, homogeneous and electrostatic cylindrical bodies with orthogonal wedges. The Author manipulated the Airy stress function through the Mellin transform for passing from the physical plane to an auxiliary plane where the space of problem solutions was defined and accessible. Two parameters were employed to describe and approach the problem in the new domain namely (i.e., the Poisson's ratio) and (i.e., the Shear Modulus) in the framework of an eigenvalue analysis. Surprisingly, in the new domain, and where sufficient to investigate the configurations of interest and results clearly prescribed the type and the severity of the singular field. In particular, the most severe condition was found in the case of one theoretically rigid material (i.e., $\mu'/\mu'' = 0$) and the other constituent as elastic and incompressible (i.e., $\nu' = 1/2$).

Such description was furthermore refined and extended through the use of the so-called Dundurs parameters [177] that are reported in the following

$$\alpha = \frac{\bar{E}_1 - \bar{E}_2}{\bar{E}_1 + \bar{E}_2} \quad \text{Eq. (2.4.2a)}$$

$$\beta = \frac{\mu_1(1 - 2k_2) - \mu_2(1 - 2k_1)}{2[\mu_1(1 - k_2) + \mu_2(1 - k_1)]} \quad \text{Eq. (2.4.2b)}$$

where \bar{E}_j and k_j are respectively the Elasticity modulus and the kolosoff parameter in both plane stress and plane strain conditions as reported in the following

$$\bar{E}_j = \begin{cases} E_j & \text{in plane stress} \\ \frac{E_j}{1 - \nu_j} & \text{in plane strain} \end{cases} \quad \text{Eq. (2.4.3a)}$$

$$k_j = \begin{cases} \frac{3 - \nu_j}{1 + \nu_j} & \text{in plane stress} \\ 3 - 4\nu_j & \text{in plane strain} \end{cases} \quad \text{Eq. (2.4.3b)}$$

The availability of Dundurs parameters permitted to Bogy to reformulate its previous works. A more compact and effective formulation of his mathematical framework for investigating edge-singularity problems was postulated. Such framework is commonly known under the general term of ‘‘Bogy determinant’’ and its expression is reported in the following

$$D(a, b, \alpha, \beta, p) = A\beta^2 + 2B\alpha\beta + C\alpha^2 + 2D\beta + 2E\alpha + F \quad \text{Eq. (2.4.4)}$$

Where a, b are the local material angles, α, β the Dundurs parameters, p the complex variable and the $A - F$ functions that depend on the previous mathematical entities.

In particular, in [11] Bogy reformulated the problem of bonded edges in the case of $a + b = 360^\circ$ (i.e., a fully bonded body) whereas in [178] a further improvement removed the equality condition thus $a + b < 360^\circ$ (i.e., a non-completely bonded body). In both cases, Bogy described the singularity conditions in terms of intensity of the singularity exponent for several bi-material specimens.

Kelly *et al.* [12] proposed similar investigations like in Bogy [178] but they extended the observation to non-conventional configurations of scarf joints (i.e., $\theta + \phi = 180^\circ$, θ, ϕ are the local angle adopted in the paper) as well other possible geometries such as $\theta = 90^\circ$ and $0^\circ \leq \phi \leq 90^\circ$. The aim was oriented to the identification of possible non-singular geometries and the Authors were successful in term of design maps. However, such approach was limited in the sense that the results were extracted at fixed geometrical conditions aiming at understanding the mechanical properties of the joint constituents to be adopted to achieve a non-singular component. Even though the Authors achieved remarkable outcomes, the intrinsic limitation was attributed to the fact that there was not the possibility to understand the geometrical non-singularity conditions at fixed

material properties. Hein and Erdogan [179] also assessed the effect of material properties, in term of elastic ratio, to the singularity exponent but the main achievement was the development of a method for predicting both displacement and stress near the singularity of a bi-material wedge.

The remarkable works before mentioned were commonly based on 2D plane-stress and plane strain assumption as valid for describing a wide range of components and internal load conditions but almost nothing approached more complex physical situations. Such lack of knowledge was filled to some extent by the work of Liu *et al.* [180] who focused on stress-singularities around axisymmetric by-material interfaces like material inclusions. Their investigation was mainly analytically oriented and based on a Bogy-like approach with a considerable mathematical effort. The Authors found similar closed forms relationships in the path of the Bogy determinant with additional terms that characterize the axisymmetric nature of the problem under analysis. In addition, they also defined analytical relationships for capturing the stress distribution near the singularity apex that were compared with numerical outcomes. Numerical stress results were in satisfactory agreement with analytical extraction but presented some deviations.

The even more powerful capabilities of Finite Element Analysis tools made available even wider ranges of geometrical complexity, investigation capabilities going beyond linear elastic analysis as well as comparison with respect to analytical or experimental outcomes. In fact, Groth [181] exploited the capabilities of both Finite Element Methods and Bogy analytical relationships for investigating similar edge bonded problems. Especially, the Author concentrated on fully elastic single lap joints and his attention was focused on the research of multiple roots for the singularity exponent. Stress results in the neighbour regions of the singularity were well approximated by a two-term expansion in Eq. (2.4.1) and this evidence requested the necessity of establishing a fracture criterion for predicting the damage initiation (i.e., $K_y > K_{critic}$ of one or more gSIF). Indeed, it was understood that a sufficient characterization of a singular stress region, rather than a single point, could have been fully described in terms of the exponent and gSIF .

Quarter plane geometries were analysed by Reedy [182,183] under transverse tension, uniform temperature change and shear. In all the cases a singularity type in the form of Eq.(2.4.5) was found. Reedy provided some useful analytical expression of K in terms of the mechanical and geometrical properties of the specimen and acting loads. In particular, transverse tension case was described by Eq.(2.4.6) where E is the Elasticity modulus and ν is Poisson's ratio respectively, U^* is the applied displacement for the calculation and h is the specimen thickness, the thermal case by Eq.(2.4.7) where α is the thermal expansion coefficient and ΔT is the thermal variation, the shear case by Eq.(2.4.8) where G is the Shear modulus and U^* is the applied displacement for the calculation in this specific loading condition.

$$K = \sigma^* h^{1-\lambda} A(\nu) \quad \text{Eq. (2.4.5)}$$

$$\sigma^* = -\frac{\nu E}{(1+\nu)(1-2\nu)} \frac{U^*}{h} \quad \text{Eq. (2.4.6)}$$

$$\sigma^* = -\frac{E\alpha\Delta T}{(1-\nu)} \quad \text{Eq. (2.4.7)}$$

$$\sigma^* = -\frac{GU^*}{h} \quad \text{Eq. (2.4.8)}$$

In the general expression of K of Eq.(2.4.5), $A(\nu)$ is a dimensionless function that depends on the Poisson's ratio only. Such function was identified numerically by Reedy through curve fitting and discrete extraction methods.

The work of Wang and Rose [184] was a consistent step forward with respect to the works by Reedy. After emphasizing the importance of compact analytical solution to estimate K easily, the Authors illustrated more precise results and investigations in this direction. In particular the SIF could be described as a linear combination of peel and shear modes properly multiplied by a Poisson's dependent function as reported in Eq. (2.4.9)

$$K = [\sigma_{A,max} A(\nu) + \tau_{A,max} B(\nu)] h^\alpha \quad \text{Eq. (2.4.9)}$$

Where $\sigma_{A,max}$, $\tau_{A,max}$ are provided by bonded joint theories and $A(\nu)$, $B(\nu)$ the two dimensionless Poisson's functions. The trend of such functions was dictated by the joint configurations and their extraction was purely numerical with a curve-fitting approach. For example, for a squared edge

$$\begin{aligned} A(\nu) &= 0.836 - 2.23\nu + 6.29\nu^2 - 9.64\nu^3 \\ B(\nu) &= 3.12 - 15.8\nu + 40.1\nu^2 - 37.6\nu^3 \end{aligned} \quad \text{Eq. (2.4.10)}$$

and for a spew fillet

$$\begin{aligned} A_1(\nu) &= 0.226 + 0.284\nu - 3.48\nu^2 + 13.1\nu^3 - 16.9\nu^4 \\ B_1(\nu) &= -0.4 \\ A_2(\nu) &= 0.31 - 0.08\nu - 1.85\nu^2 + 20.8\nu^3 - 81.7\nu^4 + 91.3\nu^5 \\ B_2(\nu) &= 0.603 - 1.95\nu + 22.8\nu^2 + 81.3\nu^3 + 107\nu^4 \end{aligned} \quad \text{Eq. (2.4.11)}$$

The paramount importance of a more clear investigation and definition of the gSIF, K , was also recognized by Akisawa and Fleck [185]. To do so, the Authors studied the problem of bi-material unions with and without cracks via both analytical relationships and Finite Element Models. Precisely, Finite Element Models investigated the stress distribution around the singular point and analytical techniques based on contour integrals studied both region of dominance of the free-edge singularity and the intensity of K . Such region extended along a radial direction at $\theta \approx 45^\circ$ for about $0.1w$ (w the width of the specimen) whereas at the interface, $\theta \approx 0^\circ$, it extends for $0.03w$. Akisawa and Meng [186] refined the analyses published in [185] by considering the effects of plasticity with respect to the use of $K = K_c$ as a failure criterion for the crack onset. They found that such criterion is still valid under precise conditions such as $h > B \left(\frac{K_c}{\sigma_Y} \right)^{\frac{1}{1-\lambda}}$ where h is the thickness of the adhesive layer, B a non-dimensional parameter, σ_Y the uniaxial yield stress and λ the singularity exponent. The work of Lefebvre and Dillard [187] lies in the same path for investigating the gSIF as a failure initiation for fatigue application. Under the assumed geometrical specimens, the Authors found that a stress-singularity approach, for establishing a failure criterion, was accessible only if the singular zone was larger than the fracture process zone.

Goglio and Rossetto [10] exploited structural solutions (i.e., adherends schematized as beam-like or plate-like structures and adhesive like a spring bed) to develop an analytical framework, solved numerically with ad-hoc routines, in the path of [184] for extracting SIF, displacements and radial functions. Their proposed approach was thus compared with Finite Element Models over a wide set of geometrical parameters. Numerical extractions confirmed the results accuracy of their framework. However, the specific influence of the joint

geometry was systematically assessed by Goglio and Rossetto [14] in a complete numerical fashion Finite Element Models, for a single-lap joint configuration. They discovered that the edge angle is the parameter which plays the most important role to the stress exponent and stress field as well (i.e., the decrease of edge angle implies a steep decrease in for the stress exponent and stress field) whereas the edge shape contributes much less. The increase of the bond length produces a more uniform singular stress field whereas it is augmented in magnitude when the adhesive thickness increases. The Author also remarked the non-significance of comparing the SIFs when such parameters are attributed to different values.

Lazzarin *et al.* [188] spent efforts in pushing forward the analytical prediction capabilities of singular stress fields in bonded joints. Under the assumption of variable separable two-term stress expansion, the Authors developed a framework for predicting both the stress state and the angular functions taking into account the joint boundary conditions and the material properties only. Such framework was solved numerically with ad-hoc designed routines as the problem equations were of partial differential type. The Authors compared the analytical predictions with Finite Element results in the case of various geometries gaining confirmation of accuracy and robustness of their mathematical framework. A similar approach was followed by Quaresimin and Ricotta [189] for investigating the gSIF and the Strain Energy Release Rate (SERR) of joints. The Authors performed extensive numerical studies for predicting the gSIFs through linear analyses whereas the SERR was assessed completely in a non-linear fashion. Such studies were fundamental for establishing a life prediction method to be adopted.

The concept of the Intensity of Singular Stress Field (ISSF) [190] (i.e., ISSF: $K_{\sigma} = \lim_{r \rightarrow 0} \left[r^{1-\lambda} \cdot \sigma_{\theta}(r) \Big|_{\theta=\frac{\pi}{2}} \right]$) was exploited by Li *et al.* [191] for investigating better shear test conditions of lap joint configurations. Indeed, the research was addressed to minimize the contributions of bending to the ISSF when executing similar experiments. Minimum values of ISSF were found by increasing the substrate thickness and, in such case, strength predictions between single-lap and double-lap configurations were almost equal. ISSF was also exploited by Noda *et al.* [192] for investigating the change of such parameters over the bondline thickness of particular components such as plate butt joints and cylindrical butt

joints through mesh-independent strategies. In the case of plate butt joints, under the assumption of semi-infinite plate if $h/W < 0.01$ (h is the bondline thickness and W is the plate width), the normalized ISSF has uniform values. A similar constant tendency is foreseen in the case of cylindrical butt-joint if $h/D < 0.01$ (h is the bondline thickness and D is the joint diameter).

Even though the work of Lang and Mallick [193] was not explicitly developed in the field of stress singularity rather than stress concentration, they explored the effects of spew geometries placed in single lap joint at the edge interface. They found that the precise injection of an amount of extra adhesive was beneficial for some configurations in terms of stress distribution thus removing, of at least mitigating, the severity of a possible stress-singularity. However, to guarantee the achievement of higher stress performances, spews should have a precise geometry that could be difficult to manufacture.

The advancement in the research of even more performant adhesive joints lead to the development of mixed adhesive joints namely joints which adopt two, or more, bonding material along the bondline thickness for improving strength characteristics and stresses in sensible locations. In this context The singularity features in tri-material joints have been exploited by Breto *et al.* [194] for designing a tailored single-lap component which alleviates the singularity effects. The Authors proposed some material selection methodologies based on pure analytical approaches to accomplish such purpose. Similar configurations were also studied by Galvez *et al.* [195] for investigating the effects of the Young modulus on the ISSF. Numerical results showed that ISSF in the case of mixed adhesive joints is sensible to the mixed material selection. For instance, safety values of ISSF can be achieved if the central adhesive is much more rigid that the outer.

In the field of collapses induced by stress-singularities it is worth mentioning the work of Barroso *et al.* [196]. Under fully experimental conditions the Authors found that the presence of a stress singularity induces premature failures in components and such collapses prohibits proper strength characterizations. This issue was overcome by inserting some slight geometrical modifications at the material interfaces and tested specimens failed correctly thus presenting enhanced and more realistic load-bearing capabilities.

The last aspect in the field of stress-singularities that is worth mentioning pertains the specific use of numerical techniques such as Finite Element Methods for both modelling and identification purposes. Indeed, even though the above-mentioned closed form solutions and analytical relationships contained in handbooks, tables and manuals are extremely useful for a stress identification in a simple geometry, current engineering products are much more complex than simple coupons and suitable numerical tools could simplify, or make accessible, the analysis of complex shapes. To the purpose of stress singularity analysis, both classical and advanced Finite Element formulations have been used and developed. In this context, the term “classical” refers to the standard definition of the elemental displacement formulation [197], reported in Eq. (2.4.12), which is derived based on the Principle of Virtual Displacements

$$u = \sum_{i=1}^{Nn} N_i u_i \quad \text{Eq. (2.4.12)}$$

where N_i is the i^{th} element shape function, u_i the nodal displacement of the i^{th} node and Nn is the number of nodes within an element. Essentially, Eq. (2.4.12) states that every point within an element can be described as a linear combination of $N_i u_i$ over Nn . Standard formulation were adopted by Sinclair *et al.* [198,199] and Sinclair [200] to numerically estimate the singularity exponent through reliable criteria based on mesh progressive refinements in the view of protecting the structural integrity of components. Denoting m as the m^{th} mesh refinement stage, h_m the element size at the m^{th} refinement such as $h_m = h_{m-1}/SF$, where SF is a constant mesh scaling factor for $m \geq 2$, $\Delta\sigma_m = \sigma_m - \sigma_{m-1}$ the stress variation between recursive mesh refinements, after several mathematical arrangements the absolute-relative error can be defined as follows

$$\hat{\varepsilon} = \frac{|\Delta\sigma_m|}{|\sigma_m| \left(\frac{\Delta\sigma_{m-1}}{\Delta\sigma_m} - 1 \right)} \quad \text{Eq. (2.4.13)}$$

Conventionally, the stress outcome is thus classified according to three accuracy levels: *i*) satisfactory stress results; *ii*) good stress results; *iii*) excellent stress results. Values higher than 5% are automatically treated as unsatisfactory. Eq. (2.4.13) informs about the quality of mesh refined applied to the original set

of discretization for producing reliable stress results. However, nothing is stated regarding the “shape” of the stress-singularity. Numerically, as suggested by Sinclair *et al.* [199], the so-called power and logarithmic signature can be found by observing the evolution of stresses over the mesh refinements. Particularly, in the case of power singularities trends are ascribable to

$$\Delta\sigma_m \sim SF^\lambda \Delta\sigma_{m-1} \quad \text{Eq. (2.4.14)}$$

whereas, in the case of logarithmic singularities

$$\Delta\sigma_m \sim \Delta\sigma_{m-1} \quad \text{Eq. (2.4.15)}$$

as the m increases.

Eq. (2.4.14) and Eq. (2.4.15) are theoretical relationships even if numerically-based. Indeed, as example, λ is unknown at this stage and additional formulas are required for its research. In particular, for power singularities, the approximate value of λ (i.e., $\hat{\lambda}_m$ at the m^{th} refinement) is

$$\hat{\lambda}_m = \frac{\ln(\sigma_m/\sigma_{m-1})}{\ln(SF)} \quad \text{Eq. (2.4.16)}$$

and, accordingly, the percentage change of this quantity is

$$\delta\hat{\lambda}_m = \frac{|\hat{\lambda}_m - \hat{\lambda}_{m-1}|}{\bar{\lambda}_m} \cdot 100 \quad \text{Eq. (2.4.17)}$$

where $\bar{\lambda}_m = 1/2(\hat{\lambda}_m + \hat{\lambda}_{m-1})$. Numerically, the presence of a power singularity results in $\hat{\lambda}_m \sim \lambda$ and $\delta\hat{\lambda}_m \rightarrow 0$ as the m increases. Conventionally, a power singularity is observed in a model if $\delta\hat{\lambda}_m < 5\%$ and $\delta\hat{\lambda}_{m+1} < 5\%$.

A similar work logic is thus applied in the case of logarithmic singularities even though such stress shape is uniquely described in terms of stress variation only. In this case, the percentage change of this quantity is

$$\delta\Delta\sigma_m = \frac{|\Delta\sigma_m - \Delta\sigma_{m-1}|}{\Delta\sigma_m} \cdot 100 \quad \text{Eq. (2.4.18)}$$

Where $\overline{\Delta\sigma_m} = 1/2(\Delta\sigma_m + \Delta\sigma_{m-1})$. Logarithmic singularities in a model imply that $\delta\Delta\sigma_m \rightarrow 0$ as m increases. Thus, the criterion for a logarithmic singularity identification involves $\delta\Delta\sigma_m < 2\%$ and $\delta\Delta\sigma_{m+1} < 2\%$.

As demonstrated, Eqs. (2.4.13) - (2.4.18) are relatively simple and allow an easy detection and determination of both the mesh quality and the stress shape through spreadsheet for practical engineering applications.

Another class of Finite Element Methods belongs to the advanced formulations. Such formulations assume the presence of additional singular terms, within the definition of the elemental displacement, that enrich such field as illustrated in Eq. (2.4.19) [201].

$$u = \sum_{i=1}^{Nn} N_i u_i + \sum_j^{N_j} k_j \left(Q_j(r, \theta) - \sum_{i=1}^{Nn} N_i \bar{Q}_{ji}(r, \theta) \right) \quad \text{Eq. (2.4.19)}$$

where $N_i u_i$ is the standard part of Finite Element formulations, k_j is the generalized stress intensity factor due to an a-priori assumed displacement field $Q_j(r, \theta)$ (e.g., $Q_j(r, \theta) = r^\lambda f(\theta)$) and $\bar{Q}_{ji}(r, \theta)$ is the asymptotic displacement field at the i^{th} node.

Finite Elements crated based on Eq. (2.4.19) work adequately in a region where a stress-singularity exists, or is supposed to be present, but they could be not useful out of the critical region where standard formulations are good enough for representing the stress field. To connect both areas (i.e., the refined with enriched models and the one discretized with standard schemes) a transition region is thus required to guarantee the displacements compatibility as depicted in Figure 25. Such region is typically approached with elements presenting a so-called “zeroing” function $R(\zeta, \delta)$ [13] pre-multiplying the enriched part for the model as reported in equation Eq. (2.4.20).

$$u = \sum_{i=1}^{Nn} N_i u_i + R(\zeta, \delta) \sum_j^{N_j} k_j \left(Q_j(r, \theta) - \sum_{i=1}^{Nn} N_i \bar{Q}_{ji}(r, \theta) \right) \quad \text{Eq. (2.4.20)}$$

The shape of $R(\zeta, \delta)$ can present different form but, in general, $R(\zeta, \delta) = 0$ along boundaries with standard Finite Elements and $R(\zeta, \delta) = 1$ along those boundaries with enriched ones.

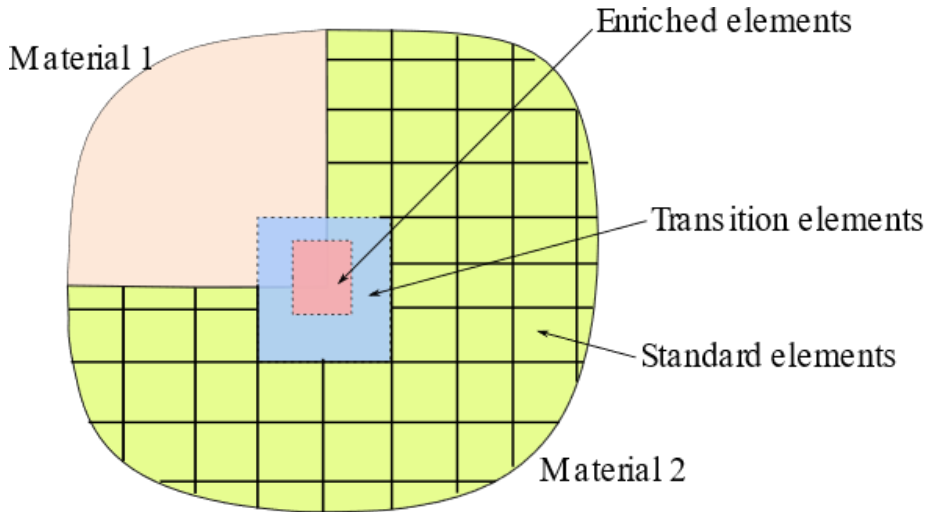


Figure 25: Modelling a singular corner with enriched, transition and standard Finite Elements

In this context, Pageau and Biggers [201] demonstrated that the size of the adopted enriched region strongly affects the convergence aspects of the stress intensity factor solution and a proper size is problem-dependent. In fact, the use of a too small refined zone make slowly converge the solution and, in some cases, it could produce a divergent outcome compared to an analytical result. Conversely, a wide enriched area can assure the convergency but requires longer calculation time.

2.4.1 Bogy mathematical framework

In this Section, the Bogy mathematical framework [178] for studying stress singularities between bi-material joints will be reviewed and explained in detail as well as the fundamental results associated with such model. The knowledge of such framework is fundamental to further approach the removal of stress singularities from a specimen as addressed in Section 2.4.2

Let us assume a 2D bi-material wedge as in Figure 26. Such structural detail is composed of two separated material regions (D', D'') of linear elastic, isotropic and homogenous properties namely the Shear modulus (μ', μ'') and Poisson's ratio (ν', ν'') and thus characterized by the two opening angles a, b ($a + b \leq 2\pi$). Let B the bonding line and B', B'' the bonding-free surfaces. Both a cylindrical coordinate system (r, θ) and a cartesian coordinate system (x_1, x_2) are located at

the material interface apex. The traction $(n'(r), n''(r))$ and the shear $(t'(r), t''(r))$ components compose the stress vector $(\boldsymbol{\tau})$ which, coupled with the displacement field (\mathbf{u}) , are the unknown of a boundary value problem.

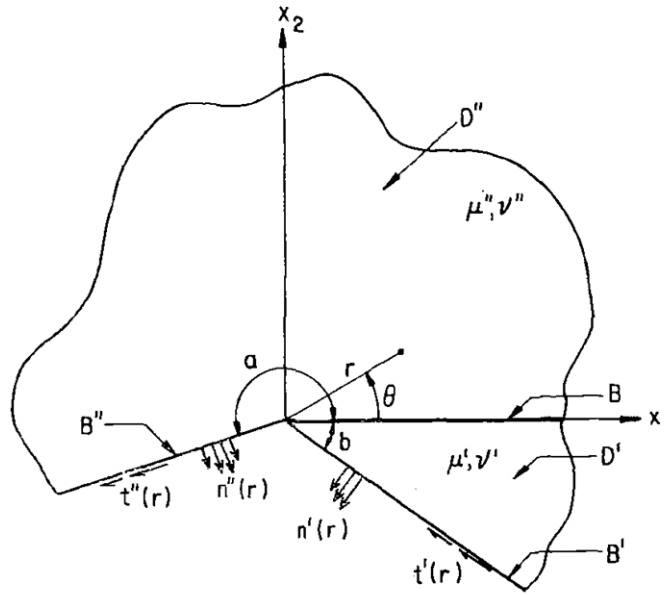


Figure 26: Bonded wedges under normal and shear loading. Original from [178].

By assuming the existence of the Airy stress function (ϕ) , Eq. (2.4.21) is valid on D', D''

$$\nabla^4 \phi = 0 \quad \text{Eq. (2.4.21)}$$

In polar coordinates can be defined the following set of equations

$$\begin{aligned} \tau_{rr} &= \frac{1}{r} \frac{\partial \phi}{\partial r} + \frac{1}{r^2} \frac{\partial^2 \phi}{\partial \theta^2} \\ \tau_{\theta\theta} &= \frac{\partial^2 \phi}{\partial r^2} \\ \tau_{r\theta} &= -\frac{1}{r} \frac{\partial^2 \phi}{\partial r \partial \theta} + \frac{1}{r^2} \frac{\partial \phi}{\partial \theta} \end{aligned} \quad \text{Eq. (2.4.22)}$$

$$\begin{aligned} \frac{\partial u_r}{\partial r} &= \frac{1}{2\mu} \left[\frac{1}{r} \frac{\partial \phi}{\partial r} + \frac{1}{r^2} \frac{\partial^2 \phi}{\partial \theta^2} - \left(1 - \frac{m}{4}\right) \nabla^2 \phi \right] \\ \frac{\partial u_\theta}{\partial r} - \frac{u_\theta}{r} + \frac{1}{r} \frac{\partial u_r}{\partial \theta} &= \frac{1}{\mu} \left(-\frac{1}{r} \frac{\partial^2 \phi}{\partial r \partial \theta} + \frac{1}{r^2} \frac{\partial \phi}{\partial \theta} \right) \end{aligned} \quad \text{Eq. (2.4.23)}$$

Where m is a coefficient such as

$$m = \begin{cases} 4(1 - \nu) & \text{in Plane strain} \\ \frac{4}{1 + \nu} & \text{in generalized Plane stress} \end{cases} \quad \text{Eq. (2.4.24)}$$

Eq. (2.4.22), (2.4.23) must satisfy the following boundary conditions

$$\begin{aligned} \tau'_{\theta\theta}(r, -b) = n'(r) & \quad \tau''_{\theta\theta}(r, a) = n''(r) \\ \tau'_{r\theta}(r, -b) = t'(r) & \quad \tau''_{r\theta}(r, a) = t''(r) \end{aligned} \quad \text{Eq. (2.4.25)}$$

$$\begin{aligned} \tau'_{\theta\theta}(r, 0) = \tau''_{\theta\theta}(r, 0) & \quad \tau'_{r\theta}(r, 0) = \tau''_{r\theta}(r, 0) \\ u'_r(r, 0) = u''_r(r, 0) & \quad u'_\theta(r, 0) = u''_\theta(r, 0) \end{aligned} \quad \text{Eq. (2.4.26)}$$

Particularly, Eq. (2.4.25) prescribes the magnitude of acting loads at the bonding-free surfaces whereas Eq. (2.4.26) imposes the continuity of stresses and displacements along the bonding line.

The adopted approach followed by Bogy relies on the application of the Mellin transform which formulation for a generic function $f(r)$ ($0 < r < \infty$) is represented by

$$F\{f; s\} = \int_0^\infty f(r)r^{s-1}dr \quad \text{Eq. (2.4.27)}$$

The application of Eq. (2.4.27) to Eqs. (2.4.21) - (2.4.26) leads to a mathematical system in the variables $a', b', c', d', a'', b'', c'', d''$ as reported in Eq. (2.4.28)

$$\begin{aligned} -\sin(bs)a' + \cos(bs)b' - \sin(bs + 2s)c' + \cos(bs + 2s)d' &= \frac{\hat{n}'(s)}{s}(s + 1) \\ s \cos(bs)a' + s \sin(bs)b' + (s + 2) \cos(bs + 2s)c' + (s + 2) \sin(bs + 2s)d' &= \frac{\hat{t}'(s)}{s} + 1 \\ \sin(as)a'' + \cos(as)b'' + \sin(as + 2s)c'' + \cos(as + 2s)d'' &= \frac{\hat{n}''(s)}{s}(s + 1) \\ s \cos(as)a'' - s \sin(as)b'' + (s + 2) \cos(as + 2s)c'' - (s + 2) \sin(as + 2s)d'' &= \frac{\hat{t}''(s)}{s} + 1 \\ b' + d' - b'' - d'' &= 0 \\ sa' + (s + 2)c' - sa'' - (s + 2)c'' &= 0 \\ \mu''sb' + \mu''(s + m')d' - \mu'sb'' - \mu'(s + m'')d'' &= 0 \\ \mu''sa' + \mu''(s + 2 - m')c' - \mu'sa'' - \mu'(s + 2 - m'')c'' &= 0 \end{aligned} \quad \text{Eq. (2.4.28)}$$

where $\hat{n}', \hat{n}'', \hat{t}', \hat{t}''$ are the traction and shear loads in the transformed domain.

In a more compact formulation, Eq. (2.4.28) can be rewritten as in the following

$$[\Delta]\{z\} = \{g\} \quad \text{Eq. (2.4.29)}$$

where

$$\Delta = \begin{bmatrix} -\sin(bs) & \cos(bs) & -\sin(bs+2s) & \cos(bs+2s) & 0 & 0 & 0 & 0 \\ s \cos(bs) & s \sin(bs) & (s+2) \cos(bs+2s) & (s+2) \sin(bs+2s) & 0 & 0 & 0 & 0 \\ \sin(as) & \cos(as) & \sin(as+2s) & \cos(as+2s) & 0 & 0 & 0 & 0 \\ s \cos(as) & -s \sin(as) & (s+2) \cos(bs+2s) & -(s+2) \sin(as+2s) & 0 & 0 & 0 & 0 \\ 0 & 1 & 0 & 1 & 0 & -1 & 0 & -1 \\ s & 0 & (s+2) & 0 & -s & 0 & -(s+2) & 0 \\ 0 & \mu''s & 0 & \mu''(s+m') & 0 & -\mu's & 0 & -\mu'(s+m'') \\ \mu''s & 0 & \mu''(s+2-m') & 0 & -\mu's & 0 & -\mu'(s+2-m'') & 0 \end{bmatrix}$$

Is the matrix of coefficients,

$$\{z\} = \{a' \quad b' \quad c' \quad d' \quad a'' \quad b'' \quad c'' \quad d''\}^t$$

the vector of unknowns and

$$\{g\} = \left\{ \frac{\hat{n}'(s)}{s}(s+1) \quad \frac{\hat{t}'(s)}{s} + 1 \quad \frac{\hat{n}''(s)}{s}(s+1) \quad \frac{\hat{t}''(s)}{s} + 1 \quad 0 \quad 0 \quad 0 \quad 0 \right\}^t$$

the loading vector.

Moreover, the introduction of Dundurs parameters expressed in Eq. (2.4.2) permitted to Bogy to further concisely express the determinant of Δ as

$$D(a, b, \alpha, \beta; p) = A\beta^2 + 2B\alpha\beta + C\alpha^2 + 2D\beta + 2E\alpha + F \quad \text{Eq. (2.4.30)}$$

where the functions depend on the p and s is the complex variable such as $s = p + i\omega$. In Eq. (2.4.31) the expression of functions is recalled.

$$\begin{aligned} A &= 4K(p, a)K(p, b) \\ B &= 2p^2 \sin^2(a)K(p, b) + 2p^2 \sin^2(b)K(p, a) \\ C &= 4p^2(p^2 - 1) \sin^2(a) \sin^2(b) + K[p, (a - b)] \\ D &= 2p^2[\sin^2(a) \sin^2(p, b) - \sin^2(b) \sin^2(p, a)] \\ E &= -D(a, b; p) + K(p, b) - K(p, a) \\ F &= K[p, (a + b)] \end{aligned} \quad \text{Eq. (2.4.31)}$$

and $K(p, x)$ an auxiliary function such as

$$K(p, x) = \sin^2(px) - p^2 \sin^2(x) \quad \text{Eq. (2.4.32)}$$

Bogy demonstrated that, based on the solution of Eq. (2.4.30), the stress field in both material regions could have been described as

$$\sigma = \begin{cases} O(r^{p-1}) & \text{if } p = p_R \\ O[r^{p_R-1} \cos(p_I \log r) \text{ or } r^{p_R-1} \sin(p_I \log r)] & \text{if } p = p_R + ip_I \\ O(\log r) & \text{if } D \neq 0 \text{ for } p_R \in]0 \div 1[, \frac{dD}{dp} = 0 \text{ at } p = 1 \\ O(1) & \text{if } D \neq 0 \text{ for } p_R \in]0 \div 1[, \frac{dD}{dp} \neq 0 \text{ at } p = 1 \end{cases} \quad \text{Eq. (2.4.33)}$$

In essence, the stress “shape” near a singular point was fully dependent on the topology of the mathematical solution found from Eq. (2.4.30) namely a power singularity, an oscillating singularity constituted by a real and a complex term, a logarithmic stress field or an almost constant distribution.

Some important features that are worth mentioning, in the view of singularity analysis, regarding the before mentioned Dundurs parameters, are graphically summarized in Figure 27. Let us define the 2D space where all the possible combinations in terms of Shear modulus and Poisson ratio could be identified respecting the formulation of Eq. (2.4.2a). In such open space, the introduction of some physical-based restrictions namely and further diminish the allowable space in the plane.

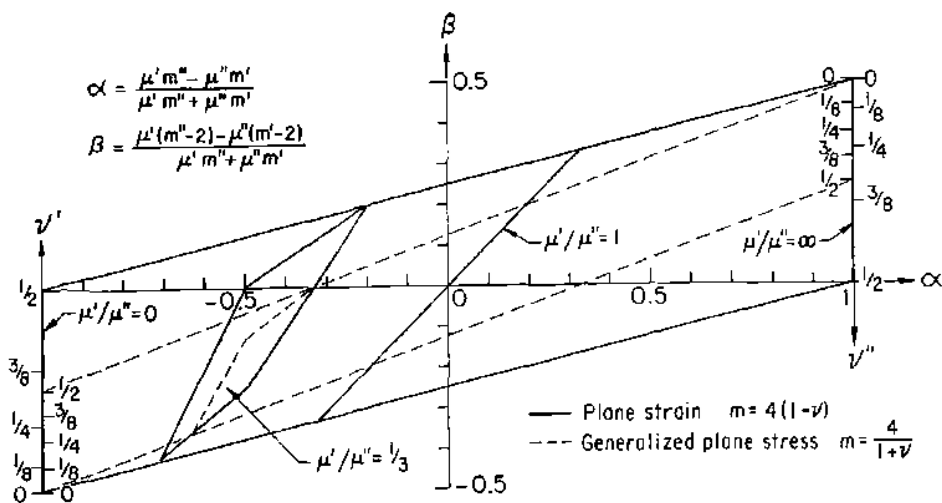


Figure 27: Parallelograms of physically relevant material combination. Origin from [178].

The introduction such of physical restrictions limits the allowable space to a particular parallelogram which is sensible to the adopted plane strain or generalized plane stress conditions as visible in Figure 27. Precisely, plane strain conditions occupy more allowable space and this means that the much more phenomena can be described within. Such plane strain parallelogram presents some lateral boundaries namely $\mu'/\mu'' = 0$ on the left side (i.e., $\alpha \rightarrow -1$), $\mu'/\mu'' = \infty$ on the right side (i.e., $\alpha \rightarrow +1$) whereas k -values from Eq. (2.4.3b) equal to $k_1 = 3, k_2 = 1$ in the upper diagonal edge and $k_1 = 2, k_2 = 3$. Moreover, assuming to work with finite and positive values of μ'/μ'' (i.e., $\alpha = \beta$), the allowable polygon is further reduced as demonstrated by the example in Figure 27 in the case of $\mu'/\mu'' = 1/3$. Furthermore, parallelograms collapse in a straight line for $\mu'/\mu'' = 1$ namely in the case of identical Shear moduli but, theoretically, different Poisson ratios. The case of identical materials arises when $\alpha = \beta = 0$ and thus the formulation of the Bogy determinant degenerates as

$$\mathbf{D}(a, b, 0, 0; p) = \sin^2[p(a + b)] - p^2 \sin^2(a + b) \quad \text{Eq. (2.4.34)}$$

that is the reformulation of the Williams [162] case for free-free conditions.

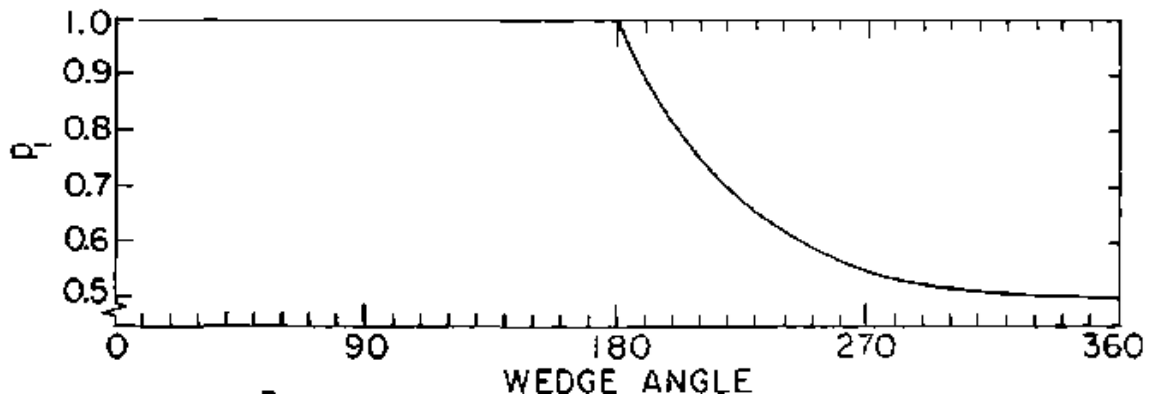
The characteristic of such diagram in Figure 27 allows the study of singularity explicitly and graphically as suggested by Dundurs [177]. Bogy implemented the insights of Dundurs for performing singularity evaluation based on $\mathbf{D}(a, b, \alpha, \beta; p) = 0$ in the framework of $\alpha - \beta$ plane.

Some useful results can be found by considering the limiting case $\mu'/\mu'' \rightarrow 0$ (i.e., $\mu' \rightarrow 0$ or $\mu'' \rightarrow \infty$) which leads to $\alpha \rightarrow -1$ and $\beta \rightarrow (2 - m')/m'$. In that circumstance the \mathbf{D} operator becomes factorable as reported

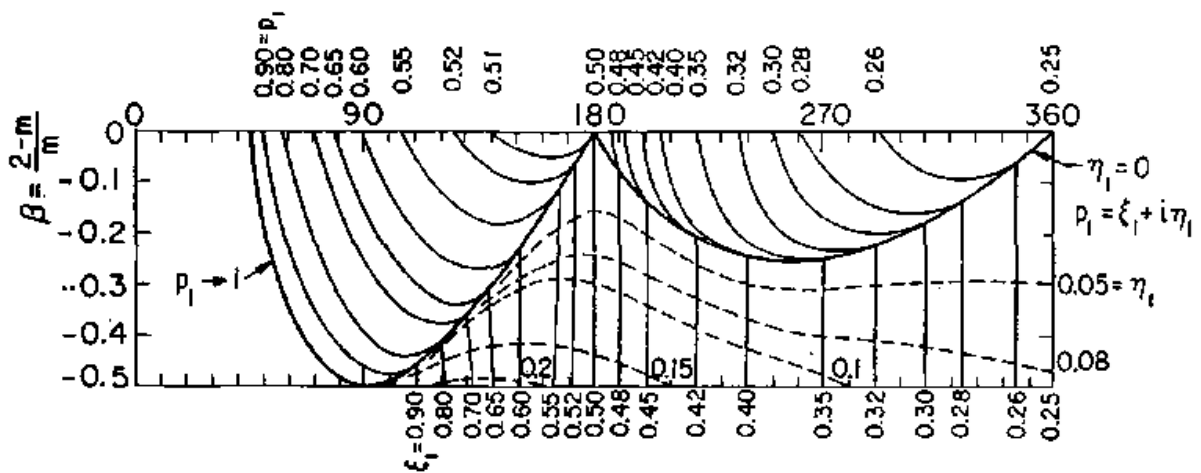
$$\begin{aligned} \mathbf{D}(a, b, -1, \beta; p) &= \\ &= 4[\sin^2(pa) - p^2 \sin^2(a)]\{[\sin^2(pb) - p^2 \sin^2(b)]\beta^2 \\ &\quad - 2p^2 \sin^2(b)\beta + \cos^2(pb) - p^2 \sin^2(b)\} \end{aligned} \quad \text{Eq. (2.4.35)}$$

The graphical outcome of Eq. (2.4.35) is represented in Figure 28. S Specifically, the trend of the first factor (i.e., $\sin^2(pa) - p^2 \sin^2(a)$) is reported in Figure 28(a) whereas the trend of the second factor (i.e., $\{[\sin^2(pb) - p^2 \sin^2(b)]\beta^2 - 2p^2 \sin^2(b)\beta + \cos^2(pb) - p^2 \sin^2(b)\}$) is depicted in Figure

28(b). In both cases, the wedge angle interval $0^\circ - 360^\circ$ is of interest. In particular, the study of the first factor is associated with the research of mathematical roots in the case of free-free configuration of an angle with opening a , whereas the second factor leads to the solution of a fixed-free single wedge angle of opening b . It is also interesting to observe that for a wedge angle of 360° $p_1=0.5$ which represents the case of a crack for linear elastic fracture mechanics.



(a) Traction on both faces



(b) One face fixed and tractions on the other

Figure 28: Roots for single material wedges. Original from [178]

The main outcome of Figure 28(a) pertains the existence of real solutions only for the first factor of $D(a, b, -1, \beta; p)$. such result could be particularly helpful for the analysis of $a + b$ wedge angle angles to determine curves passing through the $\alpha = \beta = 0$ point. From Figure 28(b), the solution curves are defined for the second factor of $D(a, b, -1, \beta; p)$ and these can assume both real of complex values depending on the mechanical and geometrical properties. In particular,

complex values are foreseen in the case of $-0.5 \leq \beta \leq 0$ for the $0^\circ - 360^\circ$ interval. In addition, Figure 28(b) suggests design-oriented solution, in terms of equation roots, as the b -value relies on different intervals. In particular, p -roots are not foreseen in the case of $b \leq \pi/4$; β -dependent real p -roots can exist in the range $\pi/4 \leq b \leq \pi/2$; β -dependent real or complex p -roots can exist in the range $\pi/2 \leq b \leq \pi$. In correspondance of $b = \pi$ the following equation summarizes the roots of the second factor of $\mathbf{D}(a, b, -1, \beta; p)$

$$\sin^2(p\pi)\beta^2 + \cos^2(p\pi) = 0 \quad \text{Eq. (2.4.36)}$$

whose solution is

$$p = \frac{1}{2} \pm \frac{i}{\pi} \tanh^{-1}(\beta) \quad \text{Eq. (2.4.37)}$$

The last b interval is $\pi < b < 2\pi$. In this case also the p -roots can be both real and complex based on the assumed β value.

The joined use of Figure 28(a) and Figure 28(b) is particularly helpful in the research of solutions for $\mathbf{D}(a, b, \alpha, \beta; p) = 0$ for any wedge and material combinations. In particular, Figure 28(a) applied to a wedge $a + b$ determines solutions passing through the point $\alpha = \beta = 0$, whereas, Figure 28(a) for a wedge of opening and Figure 28(b) for a wedge of opening are employed in the research of p -curves that intercept $\alpha = -1$.

One important problem remains: the transition from power singularities and logarithmic singularities. Such transition requires that no real roots exist in the range $]0, 1[$ and, mathematically, it is defined by the $\left. \frac{d\mathbf{D}}{dp} \right|_{p=1} = 0$. In general, such problem is complex and demanding. Anyhow, real to complex transitions should satisfy both the following conditions

$$\mathbf{D}(a, b, \alpha, \beta; p^*) = 0, \quad \left. \frac{d\mathbf{D}}{dp}(a, b, \alpha, \beta; p) \right|_{p=p^*} = 0 \quad \text{Eq. (2.4.38)}$$

In the following, the three cases explored in the Bogy original paper namely “Equal Angle wedges”, “Composite half plane”, and “Composite full planes” are presented.

1. Equal Angle wedges, $a = b$

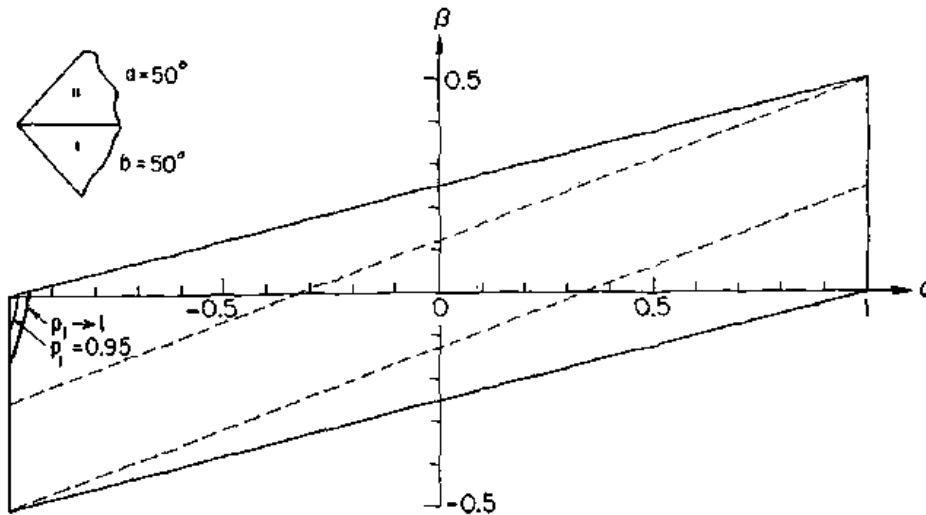
This case is the most straightforward and based on a one-parameter approach. Among all the possible combinations, particular examples are $a = b = \pi/2$ or $a = b = \pi$.

In the case of equal angles case $A - F$ functions of the Body determinant become $A = 4K^2(p, a)$, $B = 4p^2 \sin^2(a)K(p, a)$, $C = 4p^2(p^2 - 1) \sin^4(a)$, $D = E = 0$, $F = K(p, 2a)$ which simplify \mathbf{D} such as

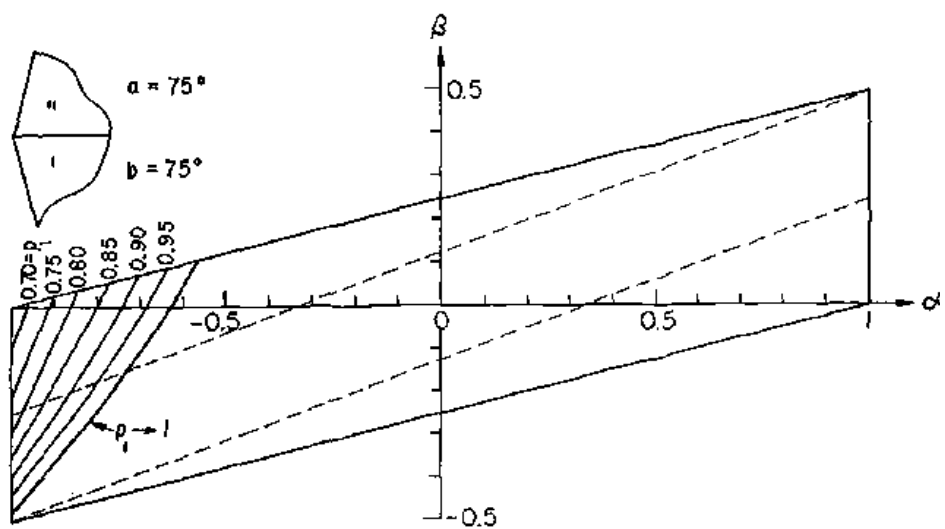
$$\mathbf{D}(a, b, \alpha, \beta; p) = A\beta^2 + 2B\alpha\beta + C\alpha^2 + F = 0 \quad \text{Eq. (2.4.39)}$$

Moreover, due to the special geometrical symmetry exhibited by this condition so that $\mathbf{D}(a, b, \alpha, \beta; p) = \mathbf{D}(a, a, -\alpha, -\beta; p)$, the solutions can be computed only in half of the parallelograms in the $\alpha - \beta$ plane.

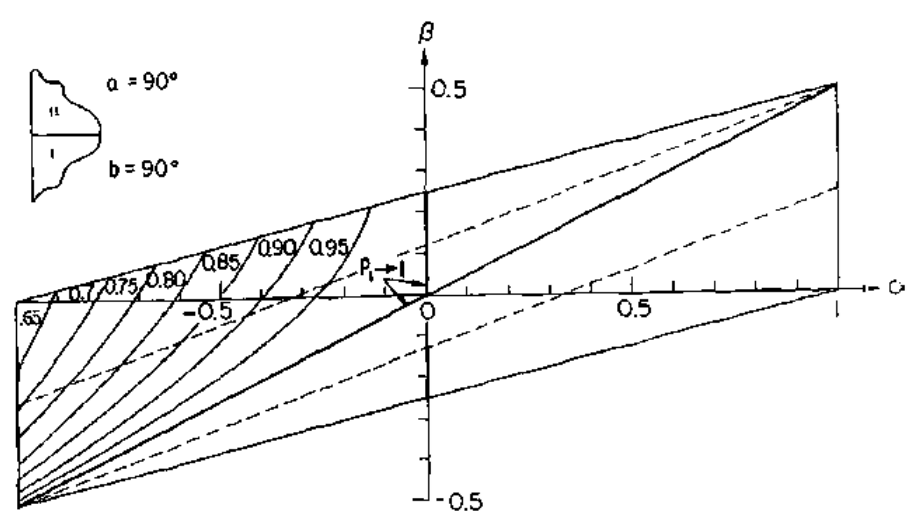
Classically, the analysis was conducted by observing that $B^2 - AC > 0$ thus Eq. (2.4.39) describes hyperbolic curves of solutions in the $\alpha - \beta$ plane. Such curves degenerate in a straight line passing through the origin when the F term disappears. In Figure 29 the p-hyperbola are depicted in the case of $2a < \pi$, which produces real eigenvalues only, whereas in Figure 30 the case $2a > \pi$ associated to complex eigenvalues.



(a)



(b)



(c)

Figure 29: Real solutions for $D(a, b, \alpha, \beta; p) = 0$. Equal wedge case. Original form [178].

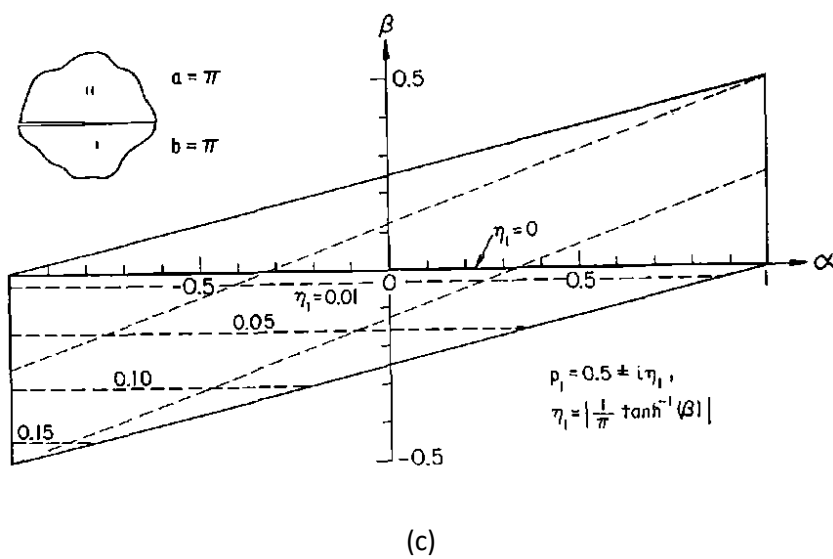
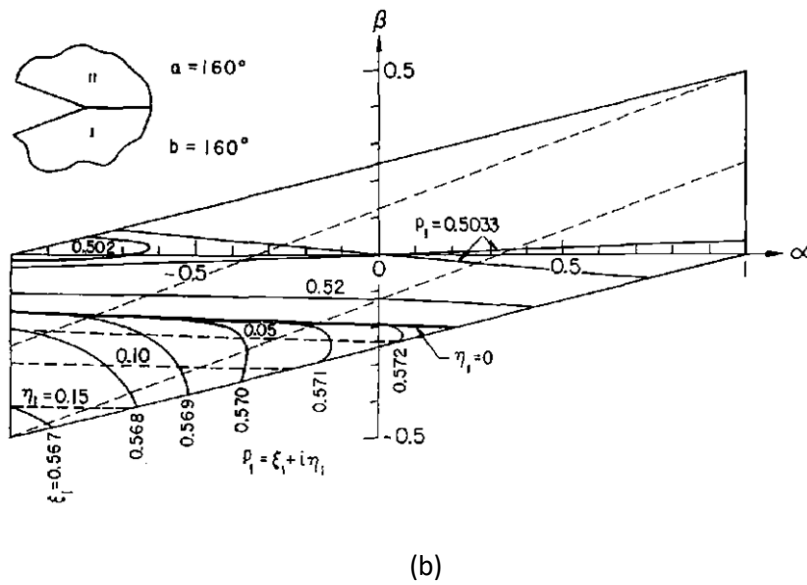
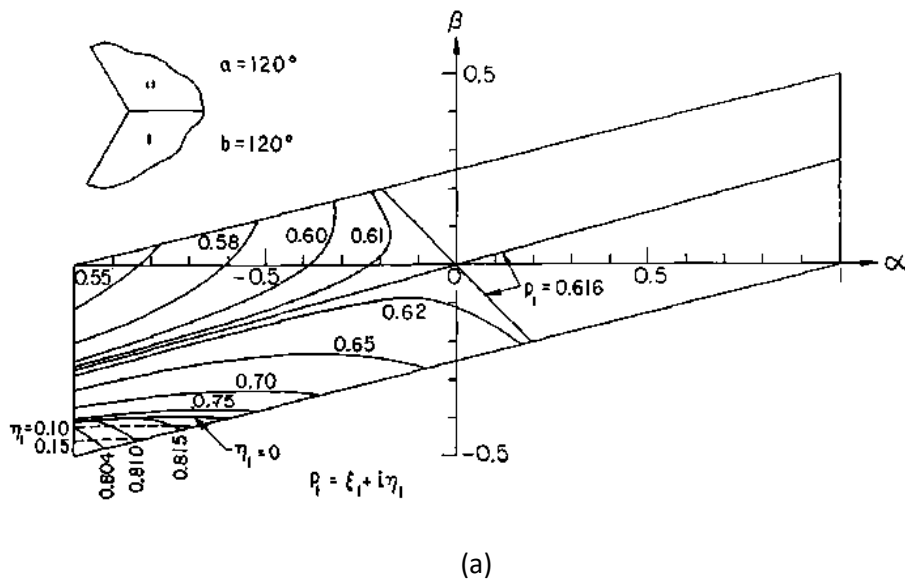


Figure 30: Complex solutions for $D(a, b, \alpha, \beta; p) = 0$. Equal wedge case. Original form [178].

In such cases, the limit condition of $p \rightarrow 1$ so that curves pass from the origin appears when $2a = \pi$, namely in the case of $F = 0$. Assuming a guess value of $p = p^*$ such as the F term disappear, the straight lines described by Eq. (2.4.34) can be described as

$$\beta = \frac{\sin^2(a)p^*}{p^{*2} \sin^2(a) - \sin^2(p^*a)} (p^* \pm 1)\alpha \quad \text{Eq. (2.4.40)}$$

In the case $2a \rightarrow \pi$, $p^* \rightarrow 1$ thus Eq. (2.4.36) defines the two lines at $\alpha = 0$ and $\beta = \alpha/2$. Moreover, if $2a \rightarrow 2\pi$, $p^* \rightarrow 0.5$ thus lines collapse into a unique line $\beta = 0$. The limit condition for $p \rightarrow 1$ establishes at $\left. \frac{dD}{dp} \right|_{p=1} = 0$ and explicitly

$$\alpha^2 - \frac{2 \sin^2(a) - a \sin(2a)}{\sin^2(a)} \alpha \beta = \frac{\sin^2(2a) - a \sin(4a)}{4 \sin^4(a)} \quad \text{Eq. (2.4.41)}$$

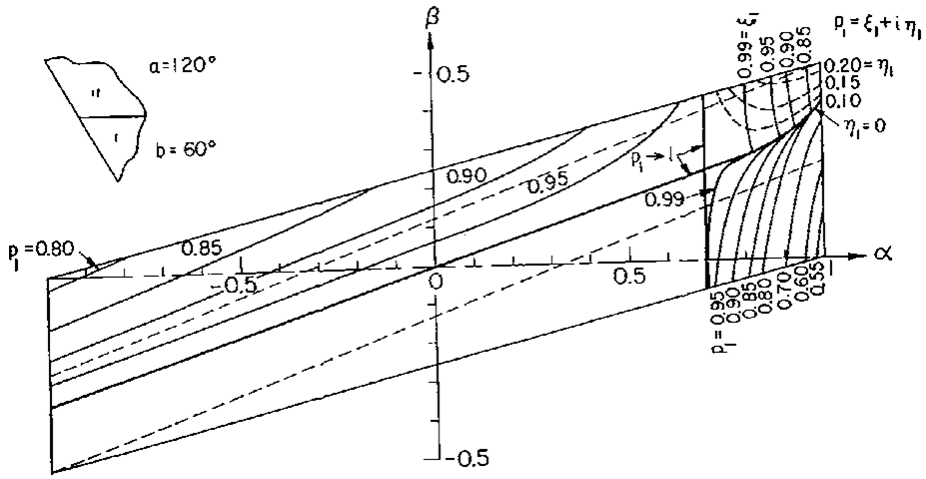
If $\alpha = -1$ Eq. (2.4.37) reduces to

$$\beta = \frac{\cos(2a)}{2 \sin^2(a)} \quad \text{Eq. (2.4.42)}$$

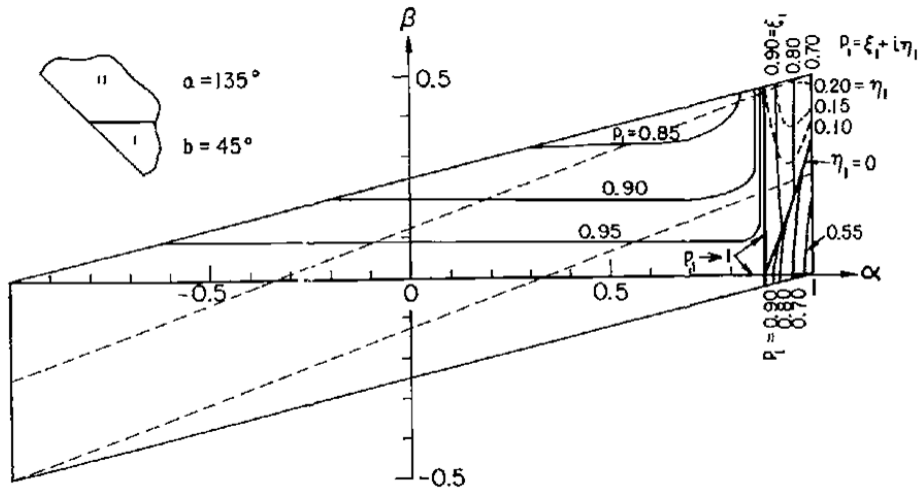
That corresponds to Eq. (2.4.36) for $p_1 \rightarrow 1$ when angles are defined between $\pi/4$ and $\pi/2$

2. Composite half plane, $a + b = \pi$

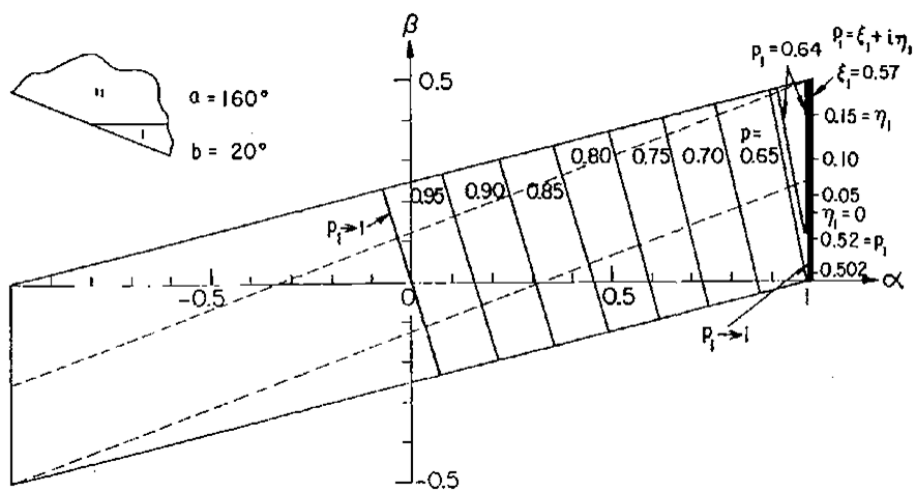
This class of wedges is expressed by the angular condition $\pi/2 \leq a \leq \pi$ and $b = \pi - a$ that satisfies $\pi/2 \geq b > 0$. The analysis of $a + b = \pi$ in the framework of Figure 28(a) suggests that solutions are of transition type (i.e., $p \rightarrow 1$) and these can lie on the $\alpha = \beta = 0$ point. From Figure 28(b), at varying of the value, different solutions could be foreseen as graphically illustrated in Figure 31. For example, if $\pi/4 < b \leq \pi/2$ as for Figure 31(a) only real roots can be extracted till an adequate β value trigger complex solutions.



(a)



(b)



(c)

Figure 31: Solutions for $D(a, b, \alpha, \beta; p) = 0$. Composite Half Plane. Original form [178]

In the case of $b = \pi - a$, the Bogy determinat in Eq. (2.4.30) provides the root-locus of limit $p \rightarrow 1$ as the two straight lines that intersect each other, namely

$$\alpha = \frac{\pi \sin(2a)}{(2a - \pi) \sin(2a) - 4 \sin^2(a)} \quad \text{Eq. (2.4.43)}$$

$$\beta = -\frac{\cos(2a)}{2 \sin^2(a)}$$

The line associated with the α term is vertical in the plane. It assumes values between 0 and 1 for $a = \pi/2$ and $a = \pi$. The line associated with the β term intercepts the origin with a slope between 1/2 and 0 at $\pi/2$ and $3\pi/4$, respectively. Such curves, in addition, represent the transition between real to complex eigenequations as demonstrated in the associated pictures in Figure 31.

3. Composite full planes, $a + b = 2\pi$

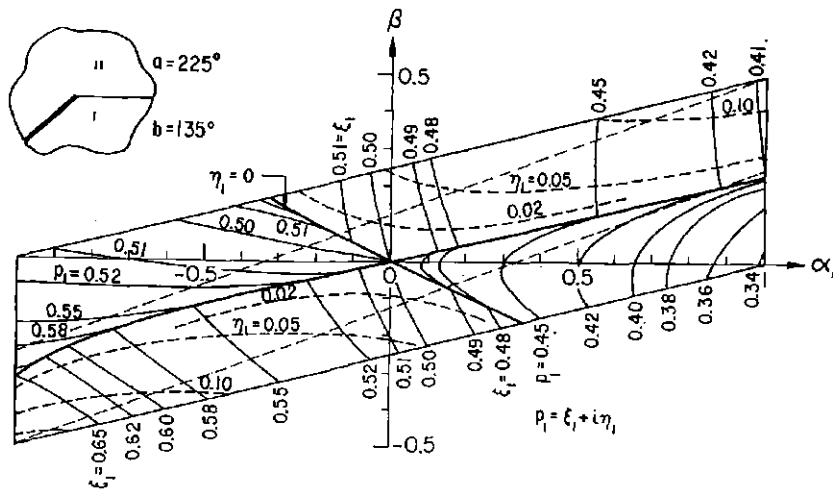
This case refers to a cracked bi-material configuration where the crack evolves along the material interface and root finding is much more complex than in the previous cases as illustrated in Figure 32. As executed for the before investigated configurations (i.e., Equal Angle wedges and Composite half plane) is worth to observe outcomes of Figure 28. In particular, Figure 28(a) highlights that the bi-material configuration $a + b = 2\pi$ can originate only $p = 0.5$ passing through the point $\alpha = \beta = 0$. In this circumstance the characteristic equation Eq. (2.4.30) becomes

$$\sin^4(a/2)[\sin^2(a/2)\beta + \cos^2(a/2)\alpha]^2 = 0 \quad \text{Eq. (2.4.44)}$$

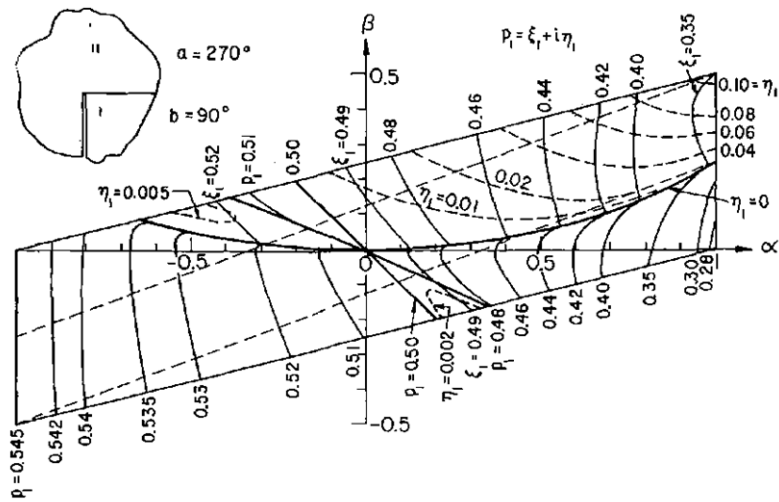
And thus

$$\beta = -\cot^2(a/2)\alpha \quad \text{Eq. (2.4.45)}$$

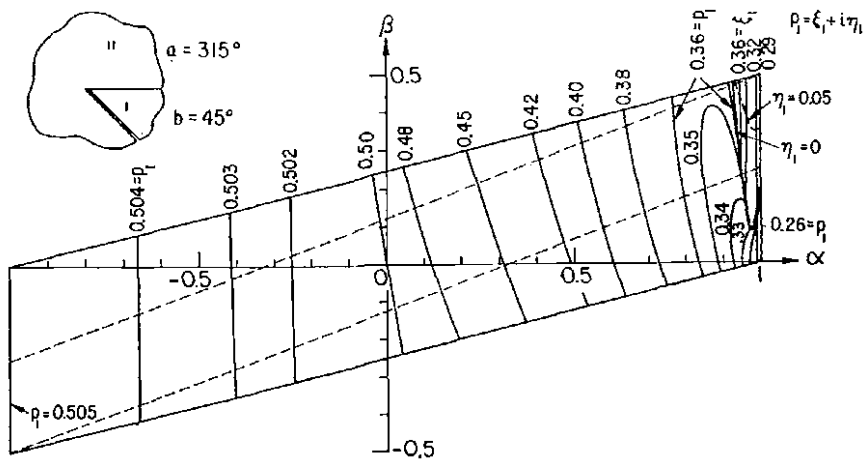
Particularly, the term $-\cot^2(a/2)$ is the curve slope and it varies based on the a value in input between 0, in correspondence of $a = \pi$, and $-\infty$ for $a = 2\pi$. Furthermore, along the strip defined by Eq. (2.4.45), $p = 0.5$ is a double root, the analysis of Eq. (2.4.38) suggests that on $p = 0.5$ the real-to-complex transition could occur.



(a)



(b)



(c)

Figure 32: Solutions for $D(a, b, \alpha, \beta; p) = 0$. Composite Full Plane. Original form [178]

2.4.2 Removal of the stress-singularity

Analyses performed to quantify the intensity of the singularity exponent are surely fundamental in the mechanical design of components. However, this procedure intrinsically assumes that such component is already available or cannot be further modified by manufacturing processes. In this framework, appears much more interesting to anticipate the possible geometrical and material configurations capable of excluding the presence of a singular feature, or at least of smoothing severe concentrations, thus originating a singularity-free component. Such modifications can be thought both as a-priori design change of the original component, by using suitable mathematical techniques for shaping the coupon, or a-posteriori mechanical workmanships that remove the stress-singularity with proper mechanical tools.

The relevant impact connected to the removal of such features for material testing purposes is testified by different works. For example, Xia *et al.* [202] adapted the standard geometry of an aluminium-Epoxy circular specimen to achieve results from tensile tests which were free of parasite edge effects introduced by the stress-singularity.

From a numerical interpretation, the works of Wu [16] for 2D and by Wu [17] for 3D linear elastic bi-material configurations, the removal of the singularity has a huge impact on the global stress distribution. Particularly, the stress trends resulted smoother along the material discontinuity.

Barroso *et al.* [203] produced and tested a composite-epoxy specimen with and without a suitable notch for removing the singularity. With such configurations it was demonstrated, both numerically and experimentally, that the removal of the singularity could lighten the edge load in correspondence of the material discontinuity. Indeed, the notched specimen could withstand more severe loads, up to two times higher than the nominal flat configuration.

Fedorov and Matveenko [204] performed an optimization study for removing the singularity from planar bi-material coupon. Their work was oriented in defining both geometric (i.e., local angles) and mechanical (i.e., material parameters) which avoid such features. Their approach essentially provided design maps for producing specimens based on the specific need of working at fixed geometrical or mechanical conditions.

From a mathematical perspective, removing the stress-singularity requires the manipulation of the Bogy framework (i.e., the Bogy determinant) reported in Eq. (2.4.30) where α, β are the dimensionless Dundurs parameters [177] in plane stress and plane strain conditions, as summarized in Eq. (2.4.46)

$$\alpha = \frac{\bar{E}_1 - \bar{E}_2}{\bar{E}_1 + \bar{E}_2}, \quad \beta = \frac{\mu_1(1 - 2k_2) - \mu_2(1 - 2k_1)}{2[\mu_1(1 - k_2) + \mu_2(1 - k_1)]} \quad \text{Eq. (2.4.46)}$$

with

$$\bar{E}_j = \begin{cases} E_j & \text{in plane stress} \\ \frac{E_j}{1 - \nu_j} & \text{in plane strain} \end{cases} \quad \text{Eq. (2.4.47a)}$$

$$k_j = \begin{cases} \frac{3 - \nu_j}{1 + \nu_j} & \text{in plane stress} \\ 3 - 4\nu_j & \text{in plane strain} \end{cases} \quad \text{Eq. (2.4.47b)}$$

Performing such investigations requires to impose an a-priori assumed positive value of the singularity exponent in its real part (i.e., $p_R \geq 1$) as well as the mechanical and the geometrical parameters. Essentially, the Dundurs parameters of the bi-material joint, one of the wedge angles and the value of α must be provided as input for the problem. Wu [16] illustrated that the solution should be found numerically, by employing iterative methods (e.g., Newton-Raphson), due to the presence of sinusoidal functions. A reasonably acceptable value for α to obtain a convergent solution is $1+10^{-4}$. Hence, the mathematical problem is solved in terms of the remaining angle θ . Different outcomes could exist in θ but the designer should consider the smallest one only. Assuming to work at fixed mechanical conditions, computing local condition preventing stress-singularities requires the use of a non-linear solver as the Bogy framework involves trigonometric functions in the equations. In such a way, the upper bound angular condition preventing the singularity is the outcome of the study. Clearly, one can extend such study by changing the initial angular condition provided as input in order to explore a wider configuration set thus deducing real design maps.

2.5 Strategies to reduce the numerical model size

Preparation of Finite Element Models (FEMs) assessing multi-physical problems (e.g., mechanical-thermal, fluid-structure interactions, etc...) is nowadays a fundamental part in design activities of industries and research groups. The possibilities made available from the use of FEM tools, since the early stages of their development [197,205,206], have permitted the detailed design of many engineering products such as space vehicles, rockets and satellites as well as lightweight components for the automotive industry or wind turbines for energy production. FEM tools such as NASTRAN® or ANSYS®, just to mention two among a plethora of software, implement many analyses technique, solution capabilities and routines for solving partial differential equations to find approximate solutions. Among the current capabilities of modern FEM software, it is worth mentioning strategies from the most classic static analysis to the advanced optimization techniques passing through the management of non-linearities (i.e., material, geometrical, contact) and dynamic behaviours (i.e., steady-state, transient, shocks, random, spectrum). However, the fundamental and the mandatory step within the analysis process of a component, a structure or a mechanical assembly, is the model preparation. Tasks such as geometrical cleaning (i.e., defeaturing) and simplifications are the preliminary part of the analysis process. The core phase consists of meshing the component, application of material properties and Boundary Conditions and setting up the analysis parameters. Indeed, at the end of this process, a FEM could be constituted by several hundred thousand, or even millions, of elements. In general, the size of a FEM depends on the specific purpose of the model, the field of application, the modelling skills of the analyst in charge of preparing the mathematical description and the available computer capabilities. Moreover, although the computer performances are even more advanced and normal personal computers can perform thousands of operations per second, it is unfeasible, and to some extends impossible, to require that a personal computer, or a cluster, can perform a complex analysis in a short time then save the outputs of a large FEM without paying the price in terms of computational cost (e.g., open the outcomes file, process outcomes for multi-step solutions, etc...). To by-pass this issue, specific mathematical and numerical techniques called *Component Mode Synthesis*

(CMS), *Super elements* or *Condensation*, *Sub-modelling* or *Global-Local* have been developed and implemented in commercial codes thus applied since the '70-'80s.

The idea behind all of these methodologies is to manage the model size by considering an alternative description that is representative of its physical characteristics without a lack of mathematical and mechanical properties. In the case of CMS, Super elements and Condensation this is usually accomplished by reducing the model size passing from tens of millions of elements to just a few thousand whereas, in the case of Sub-modelling, this concept permit to focus on a smaller part of the original FEM description where mesh refinements or hierarchical formulation can be applied to the localised detail. For the sake of completeness, CMS methods and Condensation techniques are usually grouped within the whole set of Global-Local methods. However, for the purposes of a clear and structured classification this overlap is here neglected.

In the following, only Sub-modelling method will be illustrated as it represents the adopted approach for the research activity. Thus, its main features, limitations and typical applications will be highlighted. In general, this chapter provides an overview regarding this technique instead of detailed and systematic literature review on this topic.

2.5.1 Sub-Modelling

The sub-modelling technique, also called Global-Local (GL) method, is a popular strategy in the area of computational mechanics aiming at increasing the level of detail in the analysis of components with complex geometric configurations, critical regions (e.g., holes, cutouts, fillets...) from that stress concentration could arise or that require a specific modelling strategy as their investigation is important for the proper accomplishment of a design. Although the even more enhanced capabilities of personal computers, this technique remains still valid as its potentialities and the smart features go beyond the brute-force of calculation of the new generation hardware. The term Global-Local could have different meanings within a design program and for the analysts in charge of performing the structural studies, as interestingly highlighted by Ransom and Knight [207]. By focusing, for example, on the half-wing of an aircraft, such component could be considered as a local element for the whole aircraft

configuration whereas the same part could be the global architecture where localized characteristics such as stringers, ribs, or stiffened panels are incorporated. The fundamental concept of this technique is clearly summarized by Reddy [208] “*The phrase global-local analysis is understood to be an analysis in which some parts of the domain or structure are identified, for reasons of accurate determination of stresses and displacements or for more refined analysis than in the remaining parts. The parts of refined analysis are termed local, and the remaining parts are called global. Typically, local regions are small in size compared to global regions, while the computational effort can be larger in local regions than in global regions*”.

In the following, the term *global model* will refer to the FEM of a structure or a component as depicted in Figure 33. Such description should present enough details to represent and capture the overall system behaviour. Conversely, the term *local model* will refer to the FEM of a specific structural detail which could be present, or not, within the global description.

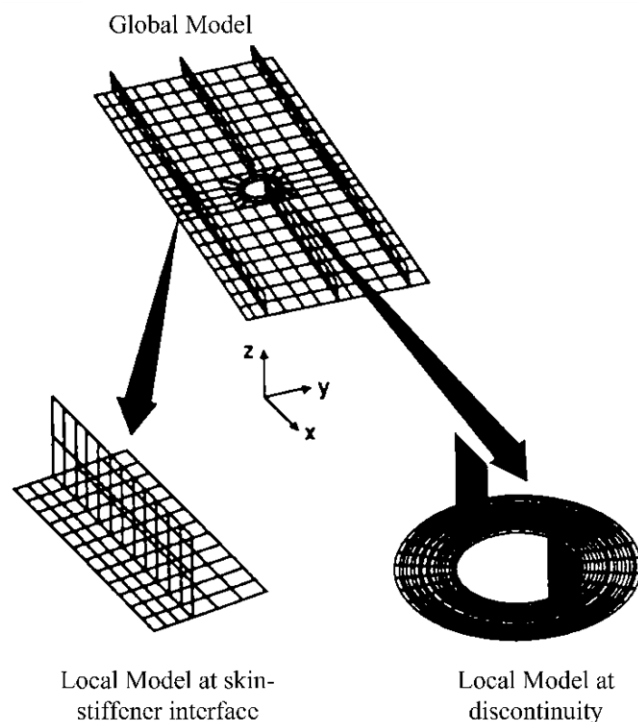


Figure 33: Global-local models of a structure [207]

An effective GL analysis requires four main ingredients, as depicted in Figure 34 for a surrogate of a half-wing structure:

1. An appropriate global analysis. This task is accomplished by the realization of a FEM capable of capturing the overall structural behaviour with a coarse discretization.
2. The capability to identify regions that require further investigations. The presence and the importance of a critical region, incorporated within the global model could be known a-priori or defined by iterative techniques.
3. A suitable strategy to select interpolation regions within the global model to define boundary conditions between global and local models.
4. An appropriate FEM local model for the accurate determination of the displacement, strain, stress or thermal fields. Such model is typically more, or much more, refined, compared to the global description.

The most challenging part in GL analyses belongs to point 3 of the previous list. Indeed, the proper definition of the boundary interface between both descriptions as well as the selected interpolation procedure for passing from global outcomes to local applied boundary conditions are the key step of this procedure.

Regarding the boundary interface definition, this step is problem dependent, in terms of geometry under analysis and magnitude of stress concentrations within the model. The commonly accepted criterion is based on the observation of the stress variation along a specific direction. A suitable boundary should be chosen where it has a very low influence so that the boundary should be far enough from the high stress gradients and stress concentrations. Other approaches are based on the use of the strain energy or the strain energy density as a method for selecting the right boundary.

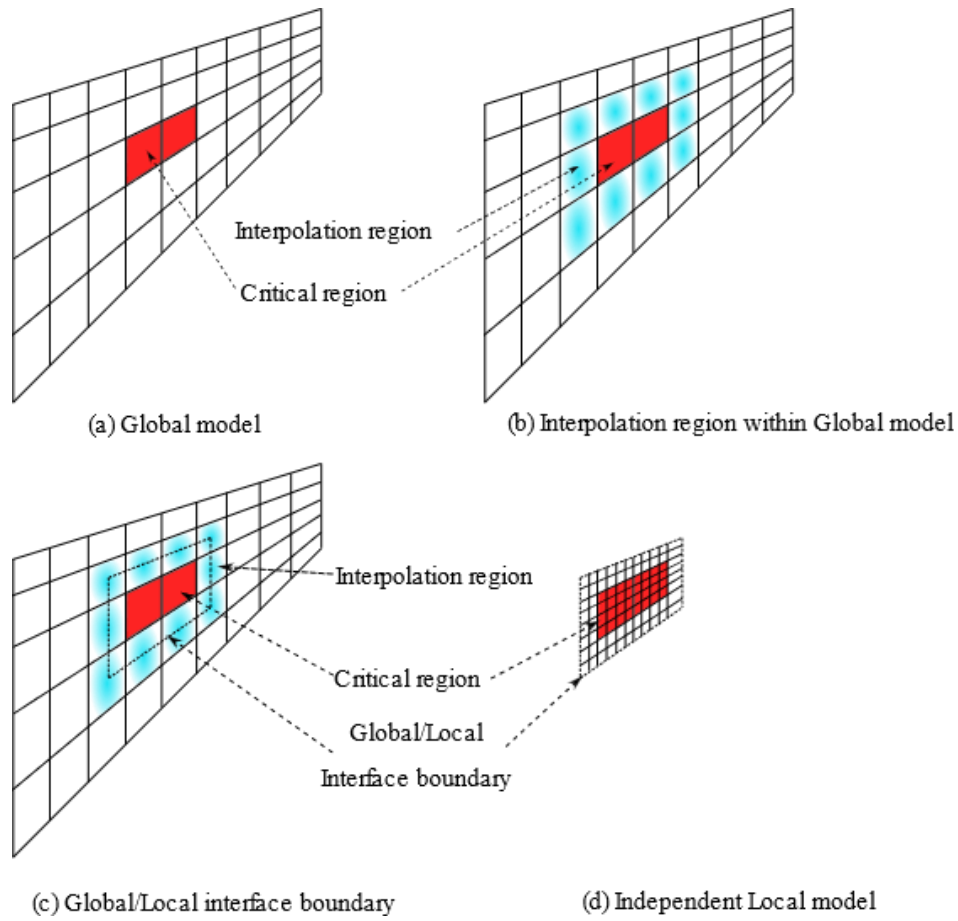


Figure 34: Terminology and main steps of the global-local methodology [207]

The interpolation procedure is the mathematical task that permits of passing the displacement information from a model to another. Assuming a one-way-coupling GL procedure (i.e., the displacements are just passed from the global model to the local one, and not vice-versa) there are many interpolation methods in literature [209] such as those based on polynomial function, least-square, Lagrangian methods, etc... . From a mathematical point of view, the problem is stated as reported in Eq. (2.5.1)

$$[\mathbf{S}(x_i, y_i)] \begin{Bmatrix} \mathbf{a}_1 \\ \mathbf{a}_2 \\ \vdots \\ \mathbf{a}_n \end{Bmatrix} = \begin{Bmatrix} \mathbf{f}_1 \\ \mathbf{f}_2 \\ \vdots \\ \mathbf{f}_n \end{Bmatrix} \quad \text{Eq. (2.5.1)}$$

where $\mathbf{S}(x_i, y_i)$ is the system matrix of interpolated function at (x_i, y_i) coordinates, the \mathbf{a} vector contains the system unknowns whereas the \mathbf{f} vector storages known field values (e.g., displacements). The definition of $\mathbf{S}(x_i, y_i)$ depends on the strategy adopted for the interpolation. Nevertheless, the best

choice to populate adopts the use of spline functions. Splines are polynomial relationships of m^{th} order, having $m - 1$ continuous derivatives, and are the most suitable local fit on a set of points.

In Figure 35 a possible scheme for GL analyses that implements the before mentioned steps is presented.

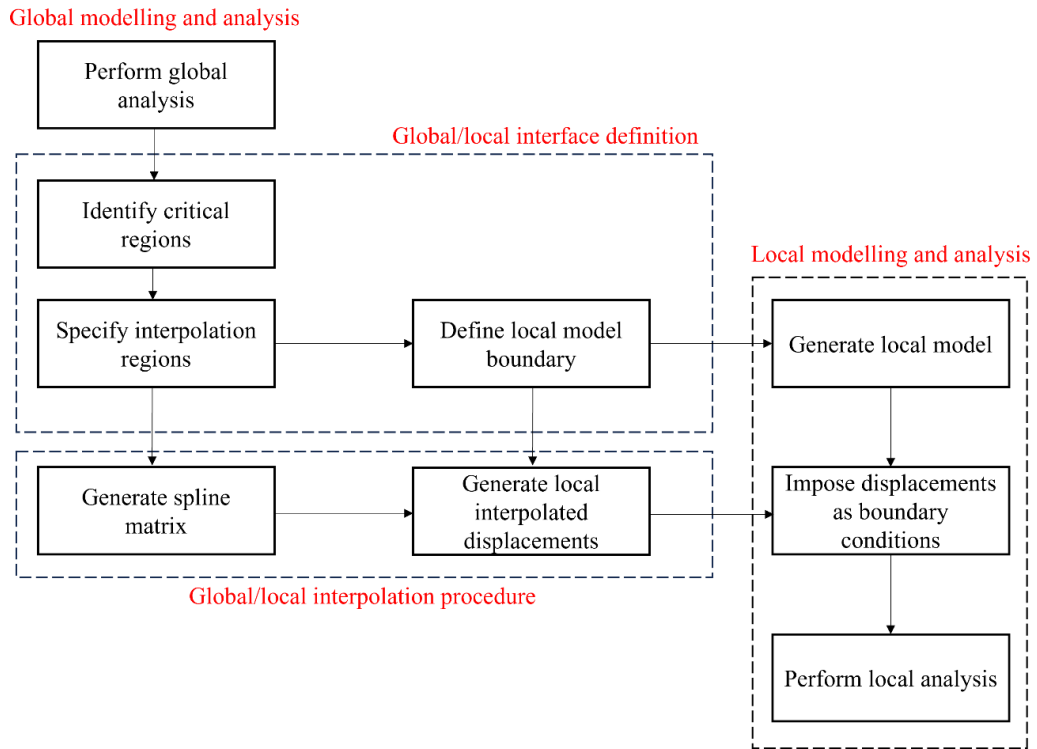


Figure 35: Scheme for global-local procedure [207]

As effectively revised by Noor [15] there are, essentially, four strategies ascribable to GL schemes namely *i*) the zooming technique, *ii*) the simultaneous application of two discretization methods, *iii*) the reduction methods, *iv*) the hierarchical mathematical models and/or numerical approximation techniques. Among these, attention will be given to the zooming technique and hierarchical mathematical models since they are the most adopted in practical applications.

Among the four possibilities before mentioned, the zooming technique and the use of hierarchical mathematical models and/or numerical approximation techniques are the most popular.

This zooming technique is the most intuitive. It allows the extraction of detailed structural outcomes by producing FE models by using an incremental

focus, as illustrated in Figure 36. Practically, after performing a suitable global investigation, the region of interest is extracted from such model, which is coarsely discretized, then, likewise an ocular zoom, this zone is refined with a higher number of elements or with higher order elements. There is not a restriction regarding the number of zooming levels to apply by this technique. Indeed, as depicted in Figure 36, between the original global model and the final local one, multiple stages of refinement could be exploited depending on the purpose of the analysis.

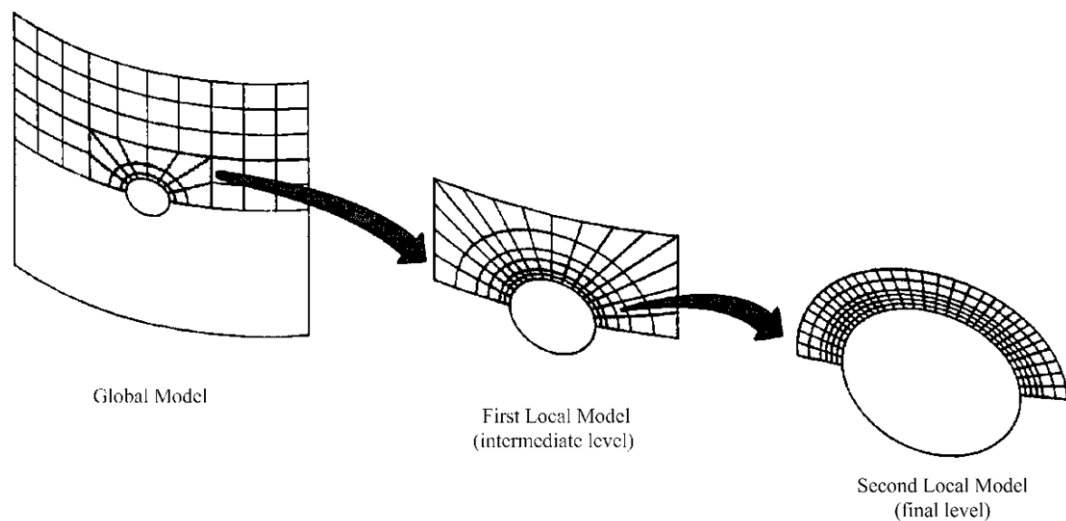


Figure 36: Schematic representation of the zooming technique [15]

In the application of this technique, prominent important is devoted to the treatment and management of the interfaces between models since this aspect affect the quality of the final outcomes. In principle, intuitive criteria and evaluations based on the engineering judgment were adopted to select the right boundary distance from the structural detail under investigation. More recently criteria based on strain energy function, strain energy density function, displacement and stress matching improved the decision-making process.

Conversely, the use of hierarchical models allows a differentiate modelling strategy of the whole structure. Indeed, the analyst can select the suitable mathematical model to apply to a specific part of a component based on available test data or structural modelling assumptions. For example, the stiffened panel with a circular hole depicted in Figure 37 shows different types of modelling of the structural element (i.e., panel or stiffener) under analysis with respect to the distance from the cut out. In particular, very far from the hole a classical beam and

panel theory is sufficient as higher accuracies are not mandatory and useful. The precision of the applied structural theory increases as the distance from the cut out reduces. In fact, a medium distance a higher deformable model is applied namely the thin-walled theory for the stiffener and the shear deformation theory for the panel. Finally, in the very proximity of the hole both the plate theory and the boundary layer theory are applied.

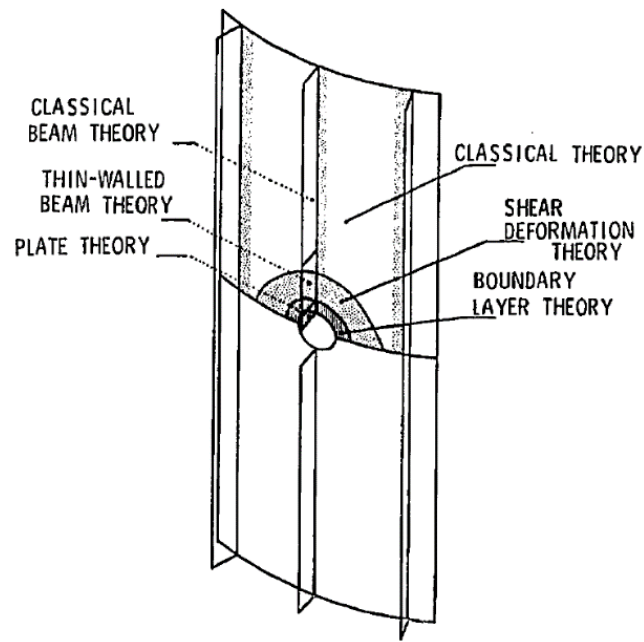


Figure 37: Schematic representation of different hierarchical mathematical models. Original from [15]

2.6 1D Axial vibrations

Performing numerical and experimental investigations on VHCF with UFTM requires the design of specimens working in resonance with the testing machine and, typically, the specimen under investigation is a bar-like structure (i.e., 1D coupon). For that reason, the main aspect of 1D vibrations will be reviewed in the following [210].

Vibration of 1D structures needs the introduction of some working assumptions for deducing the fundamental equations. Essentially:

1. After deformations, the cross-section is plane and perpendicular to the axis which remains straight
2. Material properties such as density and modulus of elasticity can vary with x but they are constant at a given cross-section
3. Material is linear elastic

These hypotheses allow extracting the strain-displacement equation and the constitutive equations. The specific nature of 1D vibrations gives the possibility of establishing such relationships in a easy manner as reported in Eq. (2.6.1)

$$\varepsilon(x, t) = \frac{\partial u(x, t)}{\partial x} \quad \text{Eq. (2.6.1a)}$$

$$\sigma = E\varepsilon \quad \text{Eq. (2.6.1b)}$$

The axial force acting on the cross area (A) can be simply calculated as in Eq. (2.6.2)

$$P(x, t) = \iint_A \sigma \, dA = A\sigma \quad \text{Eq. (2.6.2)}$$

Thus, the coupling of Eq Eq. (2.6.1) and Eq. Eq. (2.6.2) allow defining the direct relation between the strain and the applied load as

$$\frac{\partial u}{\partial x} = \frac{P}{AE} \quad \text{Eq. (2.6.3)}$$

The application of the 2nd Newton law allows deriving the axial equation of motion of the 1D configuration reported in Figure 38.

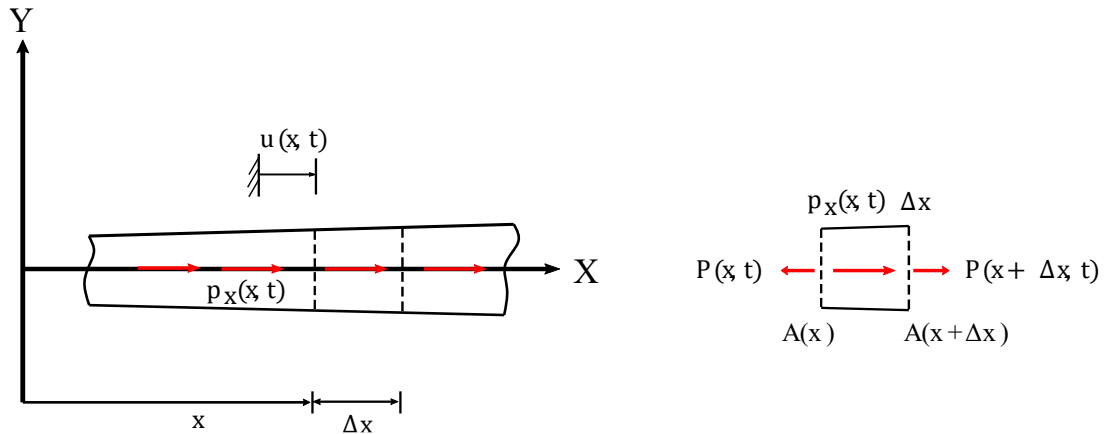


Figure 38: Vibrations of 1D structures [210].

Assuming the presence of an external load distribution , the equation of motion becomes

$$\frac{\partial P}{\partial x} + p_x = \rho A \Delta x \frac{\partial^2 u}{\partial t^2} \quad \text{Eq. (2.6.4)}$$

Then, substituting Eq. (2.6.3) in Eq. (2.6.4) leads to the differential equation of motion for 1D structures

$$\frac{\partial}{\partial x} \left(AE \frac{\partial u}{\partial x} \right) + p_x = \rho A \Delta x \frac{\partial^2 u}{\partial t^2} \quad 0 < x < L \quad \text{Eq. (2.6.5)}$$

The standard procedure for extracting the mode shapes and the natural frequencies of a vibrating bar described by Eq. (2.6.5) is the modal analysis. Performing such analysis requires the removal of removing the external load from the mathematical model then the introduction of a supposed harmonic motion for studying the modal properties of the system (i.e., natural frequencies and mode shapes). To further simplify the calculation, the geometrical and mechanical quantities are supposed as constant. In such a way the equation of motion can be written as

$$\frac{d^2 U}{dx^2} + \lambda^2 U = 0 \quad \text{Eq. (2.6.6)}$$

where

$$\lambda = \omega \sqrt{\frac{\rho}{E}} \quad \text{Eq. (2.6.7)}$$

Express the eigenvalue of the system.

Mathematically, solving Eq. (2.6.6) requires the use of a general solution in the form of

$$U(x) = A_1 \cos(\lambda x) + A_2 \sin(\lambda x) \quad \text{Eq. (2.6.8)}$$

where the A_1, A_2 coefficients are determined based on boundary conditions.

For the sake of brevity, in Table 2 are recalled the fundamental mathematical aspect when considering the Fixed-Free and Free-Free conditions for solving Eq. (2.6.8).

Boundary condition (Physical)	Fixed – Free conditions	Free – Free conditions
Applied Boundary Conditions (Mathematical)	$\begin{cases} U = 0 & x = 0 \\ \frac{dU}{dx} = 0 & x = L \end{cases}$	$\begin{cases} \frac{dU}{dx} = 0 & x = 0 \\ \frac{dU}{dx} = 0 & x = L \end{cases}$
A_1, A_2 determination	$\begin{cases} A_1 = 0 \\ A_2 \lambda \cos(\lambda L) = 0 \end{cases}$	$\begin{cases} A_2 = 0 \\ A_1 \lambda \sin(\lambda L) = 0 \end{cases}$
Set of solutions	$\lambda L = \frac{\pi}{2}, \frac{3\pi}{2}, \dots, \left(r - \frac{1}{2}\right) \pi$	$\lambda L = 0, \pi, 2\pi, \dots, k\pi$
Natural frequency distribution	$f_r = \frac{(2r - 1)}{4L} \left(\frac{E}{\rho}\right)^{1/2}$	$f_r = \frac{k}{2L} \left(\frac{E}{\rho}\right)^{1/2}$
Modal shape	$\phi_r(x) = \sin\left(\frac{2r - 1}{2} \frac{\pi x}{L}\right)$	$\phi_r(x) = \cos\left(\frac{k\pi x}{L}\right)$

Table 2: Mathematical features for Fixed-Free and Free-Free configurations

3 A combined analytical, numerical and experimental technique for investigating stress-singularity effects on VHCF of adhesive joints

This chapter illustrates in detail the analytical, numerical and experimental activities that were performed to investigate the adhesively bonded cylindrical butt-joint behaviours. Attention will be given to the steps performed to properly design, analyse and test butt-joints for capturing the most significant effects due to the presence/absence of the stress singularity and to the loading frequency.

A special attention is provided for designing the VHCF specimens, both singular and non-singular, by means of analytical and numerical techniques. Indeed, the numerical investigation and anticipation of mechanical responses of both specimens was performed with high precision and accuracy by using the Global-Local Finite Element Method. The knowledge of mechanical behaviours under the simulated working condition has permitted to further manufacture and test the coupons in the range of VHCF.

Quantifying the influence of the stress singularity to the joint life, through suitable probability-stress-number of cycles curves, gave space for investigating possible loading-frequency effects that occur when coupons in the best experimental conditions (i.e., without singularity) are loaded with different frequency excitations.

3.1 Preparatory activities: mechanical tests of the bulk adhesive and aluminium specimens

The bulk material parameters extraction is a fundamental step for the proper design and analysis of mechanical parts. In this context, the bulk materials of interest refer to the aluminium 7075 T6, which will be employed as substrate material of the joint, and the epoxy resin SikaPower® 1277, which will be employed as adhesive joining material. SikaPower® 1277 is a bi-component structural adhesive filled with glass spheres of 0.3 mm nominal diameter. It has enhanced features of mechanical toughness and impact strength. As declared by

the adhesive supplier, SikaPower® 1277 is particularly indicated for joining metallic, laminates and composite parts, especially for impact-sensitive applications. Possible fields of application can include the transportation and the general industrial engineering. SikaPower® 1277 is also suitable for the combined application with more classical joining procedures such as riveting and spot welding [211].

Testing of Aluminium and adhesive was performed in compliance with proper standards such as “ASTM E8/8M – 21, Standard Test Methods for Tension Testing of Metallic Material” [212] and BS EN ISO 527 – 2, Plastics - Determination of tensile properties [213]. On this basis, the two material specimens were designed with proper sizes and shapes as reported in Figure 39 and Figure 40.

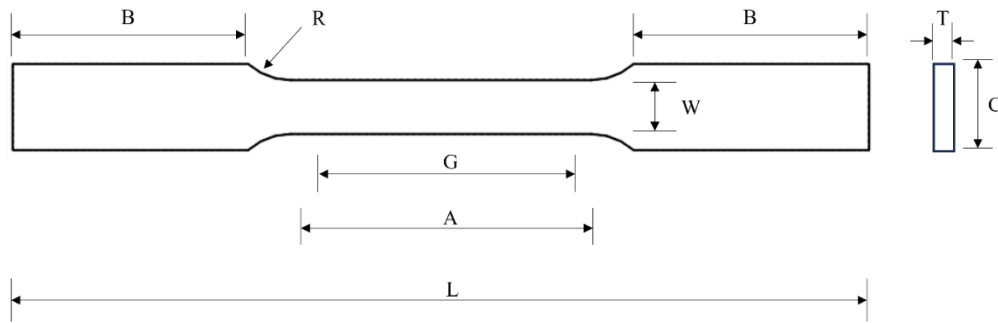


Figure 39: Shape of the aluminium specimen ($A=70\text{mm}$, $B=55\text{mm}$, $C=20\text{mm}$, $G=50\text{mm}$, $L=200$, $R=15\text{mm}$, $T=5\text{mm}$, $W=12.5\text{mm}$).

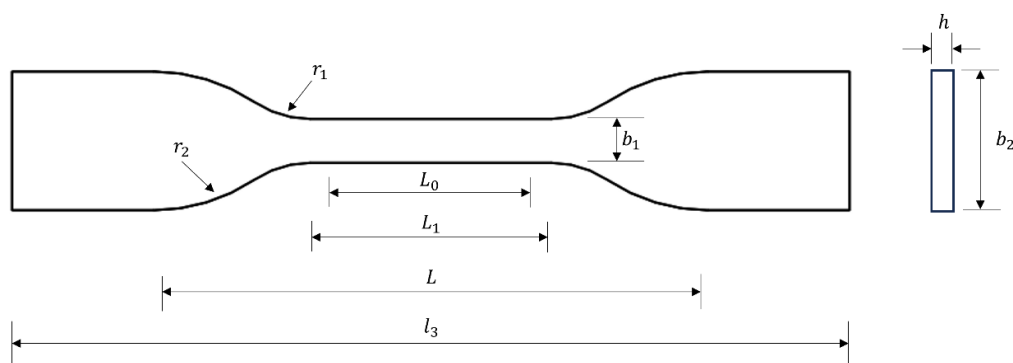


Figure 40: Shape of the bulk adhesive specimen ($h=4\text{mm}$, $b_1=12.5$, $L_0=50\text{mm}$, $b_2=20$, $L=12\text{mm}$, $L_1=75\text{mm}$ (75), $r_1=8\text{mm}$, $r_2=12.5$, $L_3=2$)

From a manufacturing perspective, the production of the aluminium specimen was executed by an external supplier through material plates. Conversely, the

SikaPower® 1277 specimen was performed in-house in the Politecnico di Torino laboratories. Since the original state of such material is liquid and highly viscid, an ad-hoc Teflon stamp was designed. Essentially, the liquid adhesive was squeezed into the stamp and then dried for 48 hr. The adhesive specimens achieved at the end of the process are illustrated in Figure 41.

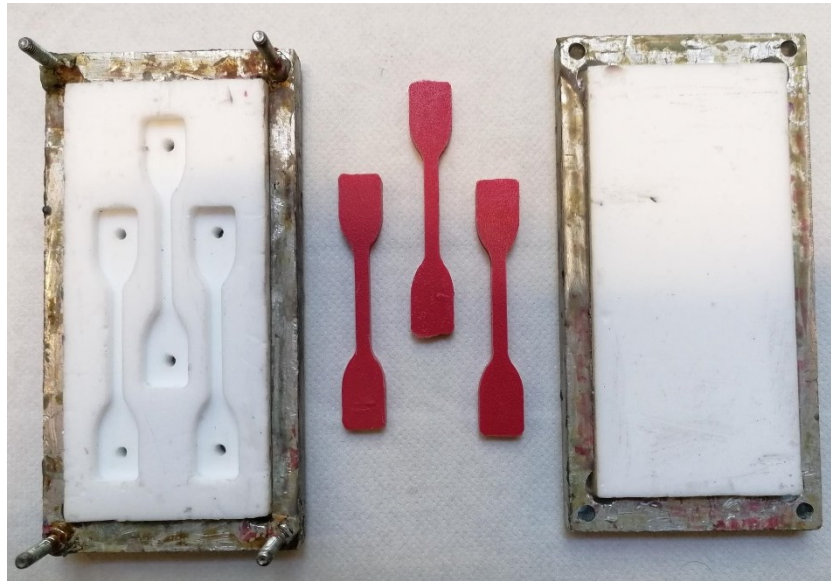


Figure 41: Produced adhesive specimens.

Five specimens for each material were adopted for the material characterization. This amount of specimens was chosen for, essentially, two reasons: *i*) aluminium 7075 T6 is a very well-known and popular material and testing such coupon was just performed as a “quality check” of the supplier goodness; *ii*) material properties of SikaPower® 1277 were already available from data sheet so testing such material was useful for confirmation purposes.

Tensile tests were performed by using an Instron® hydraulic testing machine at 5 mm/min for both materials, see Figure 42. An extensometer was installed on both specimens for the strain measurement. In order to avoid damage of this instrument, especially in the case of the adhesive, the data acquisition was stopped once the load dropped below the threshold of 98% of the recorded maximum load

value for each single specimen. Such decision was followed after a preliminary tensile test, without extensometer, which showed a sudden failure of the specimen. In Figure 43 the stress-strain curves of the bulk adhesive material are showed whereas in Table 3 the extracted material properties are summarised Here, properties of Ti-6Al-4V refer to those of the horn equipment for VHCF test that were already available from the work [20] whereas the loss factor of aluminium 7075 T6 was assumed as valid from the work of Mevada and Patel [214].



(a)



(b)

Figure 42: Tensile testing phase.

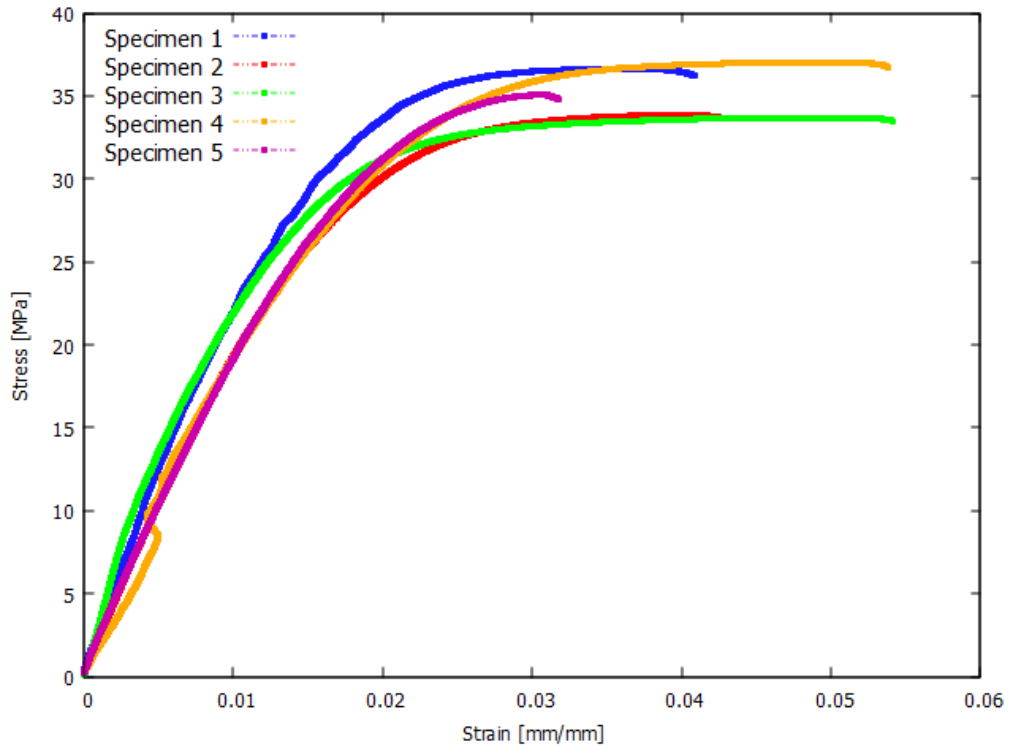


Figure 43: Stress-strain curves of the bulk adhesive.

Quantity	Symbol	Units	Materials		
			<i>Ti-6Al-4V</i>	<i>Al. 7075 T6</i>	<i>Sika Power® 1277</i>
Modulus of Elasticity	E	[MPa]	115000	71955 ± 224	2280 ± 533
Poisson's ratio	ν	[]	0.34	0.3	0.33
Max tensile stress	σ_{max}	[MPa]	950	610 ± 15	35.7 ± 1.4
Density	ρ	[g/cc]	4.39	2.80	1.1
Loss Factor	LF	[]	2.96·10 ⁻⁴	3.5·10 ⁻³	2·10 ⁻²

Table 3: Material properties extracted by tensile test or referenced by literature

3.2 VHCF specimen design and analysis

The system mechanical design has been performed with the purpose of creating a component capable of imposing a well-defined stress level, within the adhesive layer, in the UFTM resonance conditions. The geometry under investigation is part of the butt-joint class with a cylindrical configuration. Such geometry was selected for a few reasons: *i)* it fits well when coupled with the UFTM without creating interferences or joining issues and *ii)* there was a pre-existent technical heritage in dealing with cylindrical butt-joints [21].

To reach the goal of an effective design, the procedure proposed by Tridello *et al.* [20] has been followed and the key passages are summarized in Figure 44. As a general aspect, the whole design and verification process have been performed within the Ansys APDL simulation tool by adopting 4-node 2D axisymmetric elements. Choosing axisymmetric elements has permitted an easier model development, replacing a complex and demanding 3D analysis of a solid structure with just a 2D investigation. Thus, the exploitation of the joint characteristic has permitted to keep the total number of elements low.

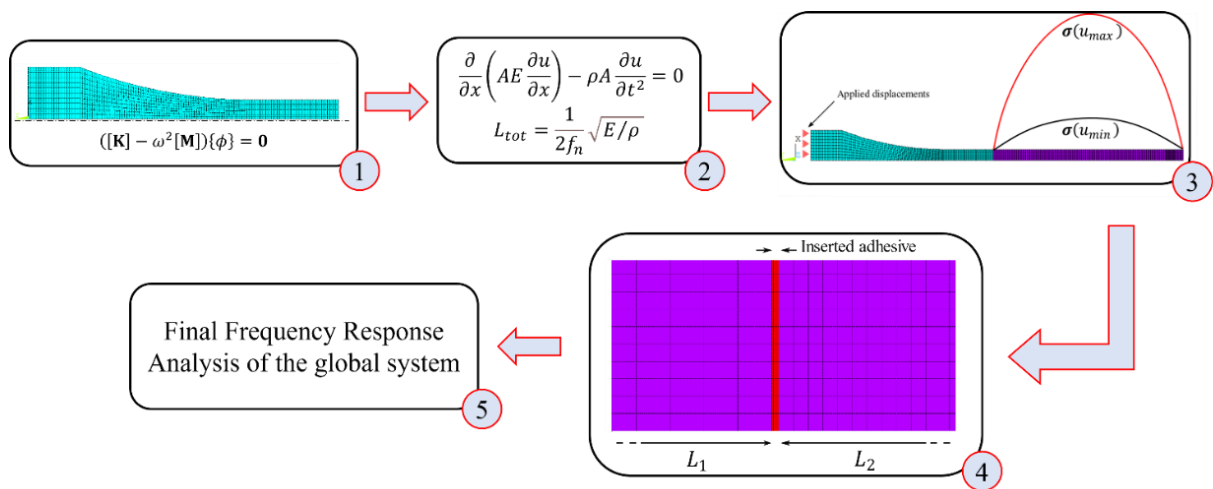


Figure 44: The work-flow to achieve a VHCF specimen. Original from [215]

In **Step 1** of Figure 44, the horn design was performed. This mechanical component has a great importance in testing specimens under VHCF as it conveys the excitation from the UFTM booster to the coupon. It must satisfy the 20 ± 0.5 kHz frequency requirement to work in the UFTM resonance conditions. To do so, a horn made of Ti-6Al-4V was designed and the final configuration is presented in

Figure 45. The correct size and dimensions were found by Tridello *et al.* [20] and here reported: $W_1 = 20$ mm, $W_2 = 7.3$ mm; $L_1 = 20$ mm, $L_2 = 67.52$ mm, $L_3 = 32.5$ mm, $R = 185.84$ mm.

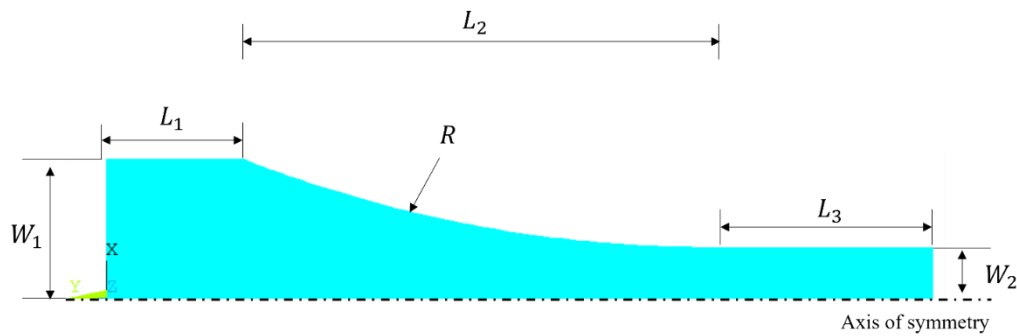


Figure 45: Axisymmetric horn configuration.

The goodness of the design was confirmed through an FE modal analysis in free-free boundary conditions (block Lanczos solver scheme). Such boundary conditions have been found as the closest approximation to the test reality. As a common practice in dealing with normal modes analysis of a component, it is useful to investigate a broader set of natural frequencies going beyond the specific interest of a frequency requirement. Indeed, in Table 4 (column two) the first 10 natural frequencies are reported.

Apart from the 1st fundamental mode that is a rigid body motion along the Y-coordinate, the 1st elastic mode has a frequency of 20195 Hz. This outcome guarantees that the design is compliant to the frequency requirement of 20 ± 0.5 kHz. Regarding the higher frequencies that characterize the horn behaviour, is interesting to observe that the difference between two successive frequencies (i.e., f_j and f_{j-1}) becomes even smaller as the fundamental mode number increases and this means an increase of the modal density. However, there is a very close similarity between the 5th and the 6th fundamental modes.

Fundamental
mode

System frequencies [Hz]

	Horn	Coupled system, no adhesive	Coupled system, with adhesive, 90°-90° interface	Coupled system, with adhesive, 43.5°-90° interface
1	0.000	0.000	0.000	0.0000
2	20195	8502.7	8506.8	8529.1
3	43050	20192	20165	20250
4	61538	31511	31337	31369
5	74955	42068	41813	41772
6	77645	51042	50307	50304
7	91941	61062	60310	60332
8	104330	69832	68319	68289
9	111430	75044	74993	74985
10	119280	78360	77237	77326

Table 4: Extracted natural frequencies.

In **Step 2**, the total length of the aluminium substrate is analytically calculated by exploiting the solution of the 1D equation of motion, in the case of free-free vibrations, that has been illustrated in Section 2.6. A simple arrangement of the natural frequency distribution presented in Table 2 permits to impose the system frequency and to calculate the bar length that satisfies the requirement

$$L_{tot} = \frac{k}{2f_n} \sqrt{E/\rho} \quad \text{Eq. (3.2.1)}$$

where, $k = 1$ to consider the 1st elastic mode, f_n is the horn 1st elastic mode and E, ρ the aluminium elasticity and density. Doing so, $L_{tot} = 125.5097 \text{ mm}$.

For an easier modelling, $L_{tot} = 125.5 \text{ mm}$ is the nominal length that has been considered.

The knowledge of the suitable bar length that has to be adopted for VHCF testing permitted the development of a specific FE model approximating the geometrical features of the whole assembly. The FE model has elements close to 2500 units. The numerical modal solution provided by the FE model is reported in Table 4 (column three) for the 10 fundamental modes. With respect to the frequency requirement, the natural frequency coincides perfectly and the deviation of 3 Hz is totally negligible. Moreover, it is interesting to observe that the coupling of the two components (i.e., the horn and the aluminium bar) produces a lower frequency in the range of 8.5 kHz that plays the role of the 1st elastic mode.

In *Step 3*, a Frequency Response Analysis (FRA) was performed aiming at simulating the test conditions thus observing the stress distribution along the bar axis. To do so, two levels of displacement namely 2.2 μm and 18 μm , that characterize the upper and the lower displacement limit values applicable by the UFTM machine, were applied at the horn base, as illustrated in Figure 46. In this case, the coupled system was excited in order to produce a response in resonance, so at 20192 Hz.

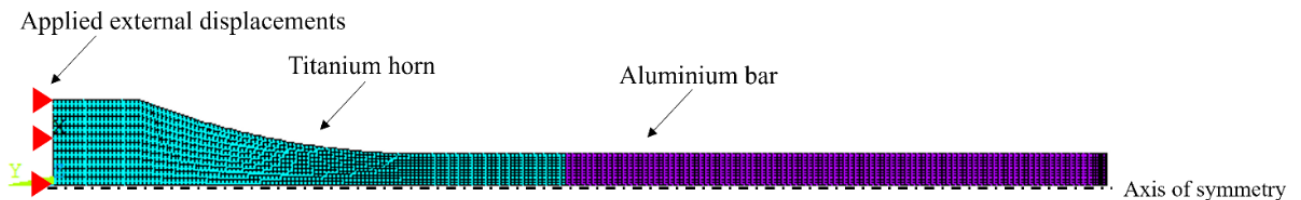


Figure 46: Simulated testing condition with properly applied displacements

The longitudinal stress (σ_Y) distribution for the highest displacement value (i.e., 18 μm) is reported in Figure 47. The interface line connecting the Titanium horn and the aluminium bar behaves as a stress node. Thus, there is a zero-stress value at the interface dividing the specimen in two well-separated stress regions: total compression on the horn and total tension on the bar, or vice-versa during the wave propagation.

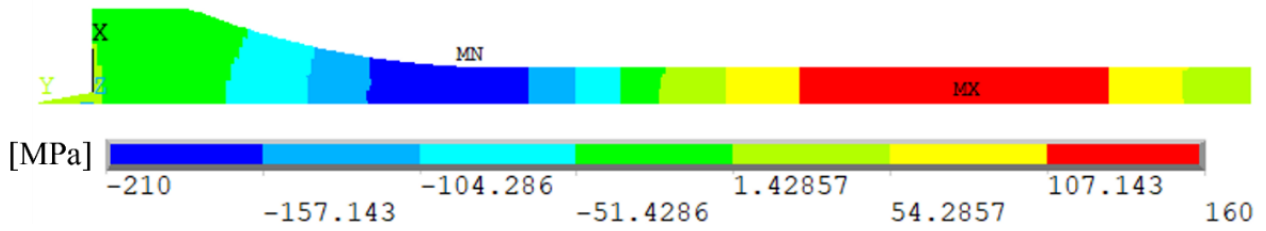


Figure 47: Current longitudinal stress distribution for the 18 μm displacement case

In *Step 4*, the thin adhesive layer of 0.3 mm was placed at a defined stress range, thus separating the aluminium substrate into two separated units as depicted in Figure 48.

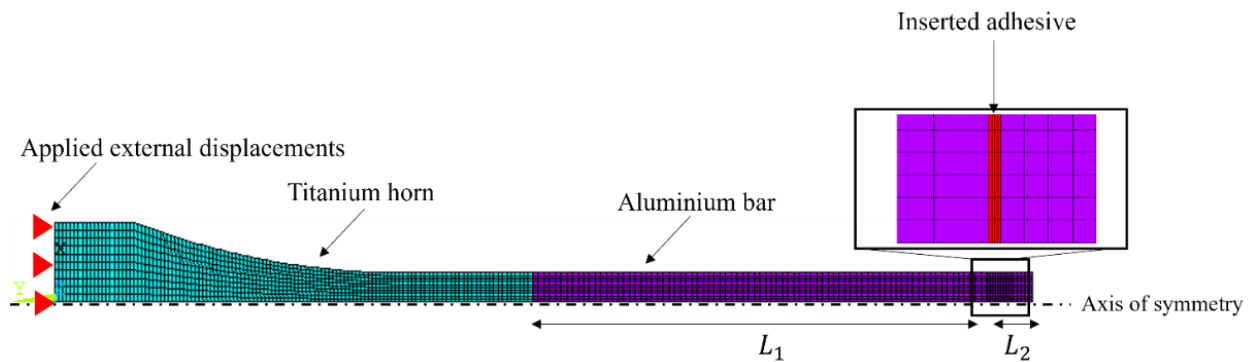


Figure 48: Singular VHCF adhesive joint.

Precisely, the proper definition of the adhesive positioning derives from the knowledge of the distribution with the FRA of *Step 3*, recovered along the axis, for both the applied displacement values as presented in Figure 49. Since the adhesive maximum stress is 35 MPa, the stress range is appropriate for investigating the VHCF response of the tested adhesive. Thus, the L_{tot} is divided in $L_{tot} = L_1 + L_2$ where $L_1 = 114.35 \text{ mm}$ and $L_2 = 11.15 \text{ mm}$ as presented in Figure 48.

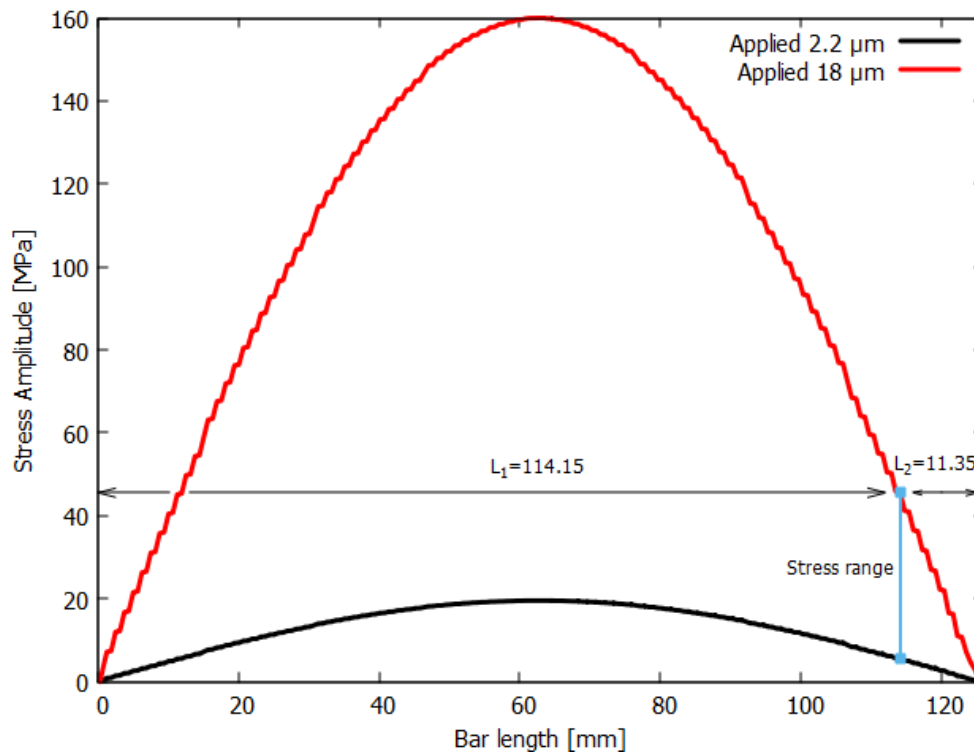


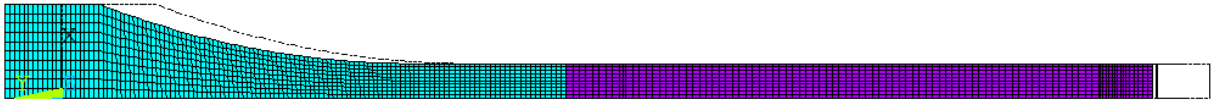
Figure 49: Longitudinal stress distribution for the selected level of external displacements. Original from [215]

In **Step 5**, the final step, a further modal analysis and an FRA were performed for verification purposes. The modal analysis, whose results are presented in Table 4 (column four), showed that the introduction of the adhesive layer between two substrates produces frequency variations in the frequency spectrum.

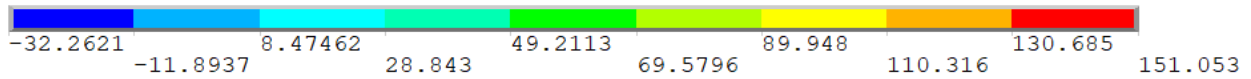
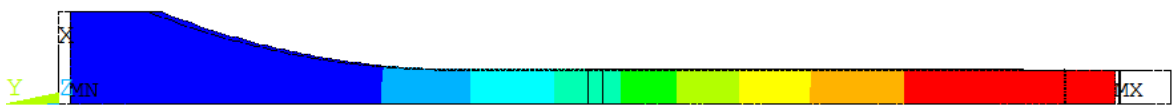
Especially, the 1st elastic mode dropped from 20192 Hz to 20165 Hz. Even if the resulting frequency still remains compliant with the frequency range exploitable from the UFTM, this observation has important design consequences that a designer should keep in mind when dealing with adhesive bonding. In fact, in spite of the approximately 30 Hz of reduction could be negligible compared to the reference of 20 kHz, FE analyses of large-scale structures tend to exclude from the model such thin layered contributions for different reasons, such as the purpose of the analysis, difficulties in modelling adhesive, etc... . However, it has been shown that the elasticity (and the mass) of a very thin layer could play an important role by changing and modifying the system mechanical response.

For the purpose of completeness, the 10 extracted modal shapes are reported in Figure 50. The coloured pattern refers to longitudinal displacements even if the

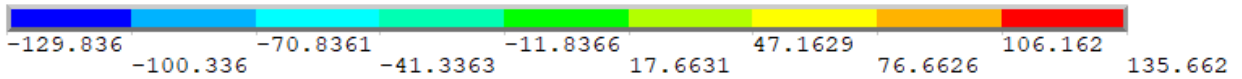
numerical scale is fictitious. The modal shape of interest is the 3rd (Figure 50 (c)) where the minimum and the maximum displacements are defined at the specimen stress node and at the specimen right end, respectively. Apart from the 1st mode which is a rigid body motion and the 9th mode which is prominently local, all the remaining modes are global modes (i.e., the specimen is globally in movement).



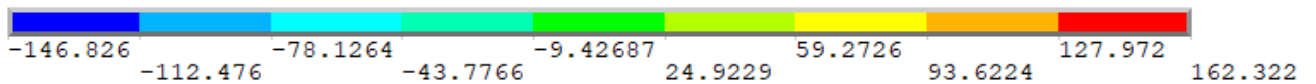
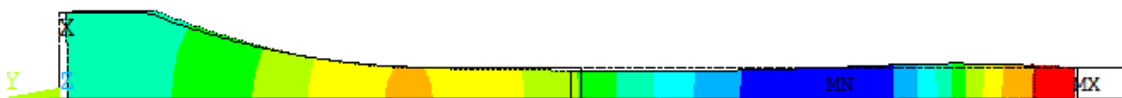
(a) Mode 1: Rigid body motion



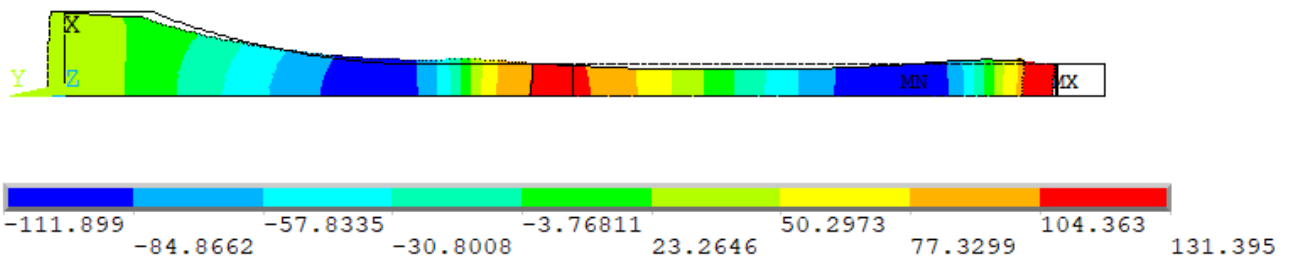
(b) Mode 2: 1st Elastic mode, Global mode



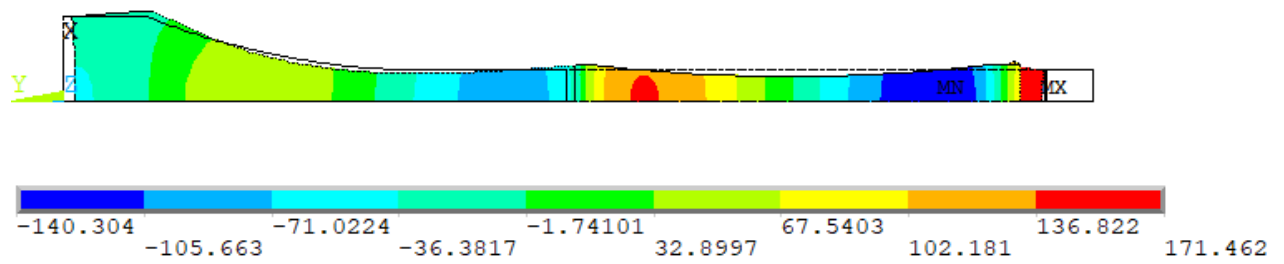
(c) Mode 3: 2nd Elastic mode, Global mode



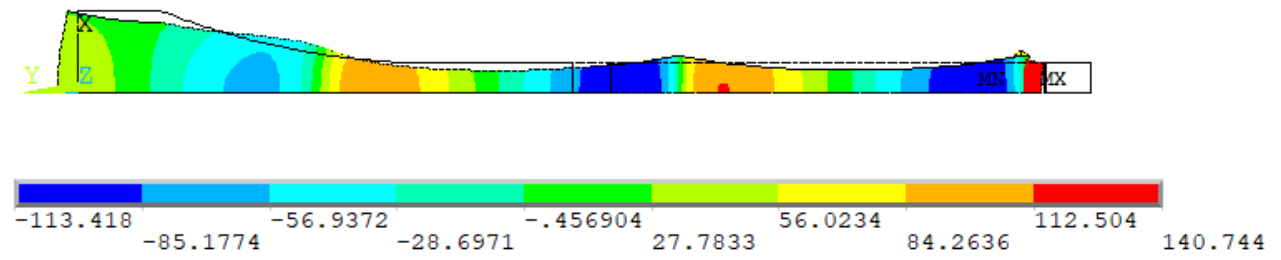
(d) Mode 4: 3rd Elastic mode, Global mode



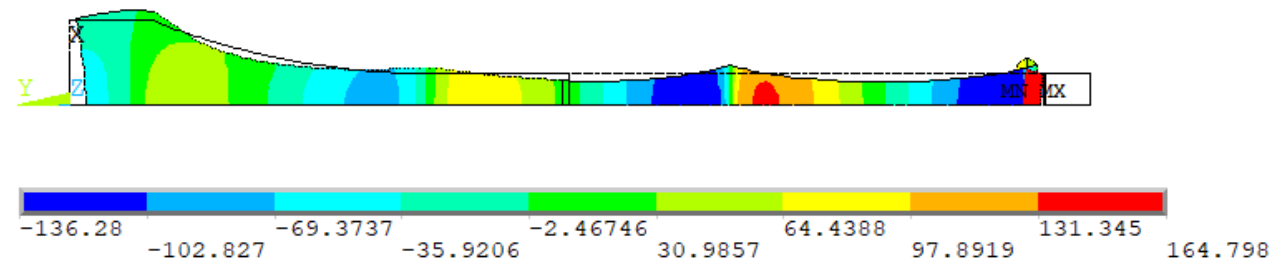
(e) Mode 5: 4th Elastic mode, Global mode



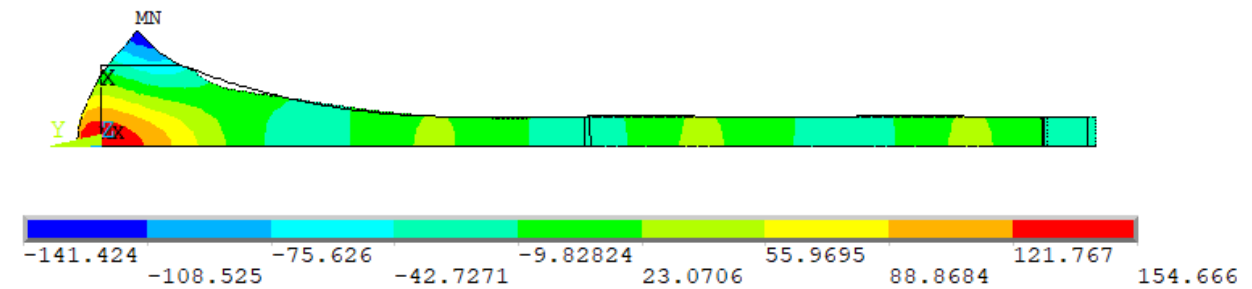
(f) Mode 6: 5th Elastic mode, Global mode



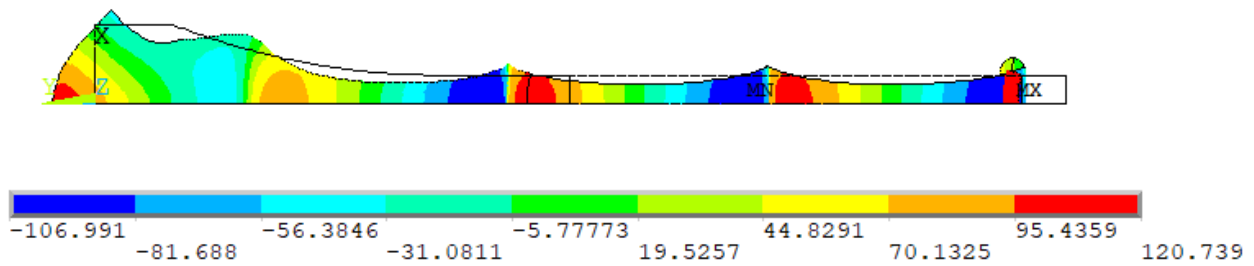
(g) Mode 7: 6th Elastic mode, Global mode



(h) Mode 8: 7th Elastic mode, Global mode



(i) Mode 9: 8th Elastic mode, Local mode



(j) Mode 10: 9th Elastic mode, Global mode

Figure 50: VHCf adhesive joint modal shapes.

The FRA was performed at the new fundamental frequency (i.e., 20165 Hz). In general, no relevant variations were appreciated and the stress results presented in Figure 49 as well as the stress interval [5.5 – 46] MPa remain confirmed.

3.3 Removal of the stress-singularity and model analysis

In the previous paragraph, a specimen capable of imposing a defined stress level that fits well with the testing machine was designed without any further requirements. That configuration presented a 90°- 90° interface, between the adhesive and the substrates, which originates a stress singularity. The aim is to design a specimen without the singular feature.

To reach this goal, an approach based on the Bogy determinant reformulation was followed. If, in principle, the Bogy determinant was used to study the order of the singularity (i.e., the λ exponent), at a defined plane stress or plane strain conditions, the inverse approach illustrated in Section 2.4.2 aims at determining the geometrical (local angles at fixed mechanical properties) or mechanical (at fixed geometrical terms) condition that remove the stress-singularity (i.e., $\lambda=0$). Geometrical conditions refer to the local wedge angles at the junction whereas mechanical conditions refer to the modulus of elasticity and, eventually, the Poisson ratio of one, or both, materials. In these terms, the mathematical problem is bi-dimensional at fixed mechanical conditions (θ_1 and θ_2 are the unknowns) or forth-dimensional at fixed geometrical conditions (E_1, μ_1, E_2, μ_2 are the unknowns).

The strategy that was followed in this work is based on the accurate knowledge of the adherend-adhesive mechanical properties. Indeed, these were known from

experimental tests, a datasheet reference or found in the literature. Then, working at fixed mechanical conditions.

Mathematically, the Bogy inverse problem was solved numerically by using the MATLAB tool. In this ambient, ad-hoc written non-linear routines, based on the Newton-Raphson scheme can find the correct solution. Precisely, a non-linear scheme was necessary due to the presence of sinusoidal and quadratic expressions. Moreover, to better approach the numerical implementation, a symbolic declaration of the $A - F$ terms of Eq. (2.4.22) presented was chosen. In details, the general complex root " p " was considered in its real part only, since $p_R \geq 1$ is the necessary mathematical condition to avoid the singularity. Wu [16] illustrated that the numerical problem admits a reasonably convergent solution if $p_R = 1 + 10^{-4}$.

The MATLAB codes consider the mechanical properties of the adopted materials, the plane stress/strain conditions and, more important, a defined adhesive angle at the edge as input data for the calculation. Thus, the bi-dimensional problem is restricted to a mono-dimensional one where the current unknown is the substrate angle that, coupled with the imposed adhesive angle, avoids the stress singularity.

From an operative point of view, the adhesive angles that were considered for the investigation are in the range , with a step angle of 10° , in order to study a broad range of possible configurations. The extracted solutions are collected in Table 5 and graphically represented in Figure 51.

Adhesive angle	Substrate angle	
	Plane stress	Plane strain
10	179.6	179.6
20	179.3	179.2
30	178.8	178.7
40	177.9	177.5
50	175.5	171.8
60	121.2	70.28
70	61.35	51.09
80	51.68	45.7
90	48.17	43.5
100	46.97	42.64
110	47.78	42.65
120	60.60	44.83

Table 5: Local geometrical conditions that avoid the stress-singularity.

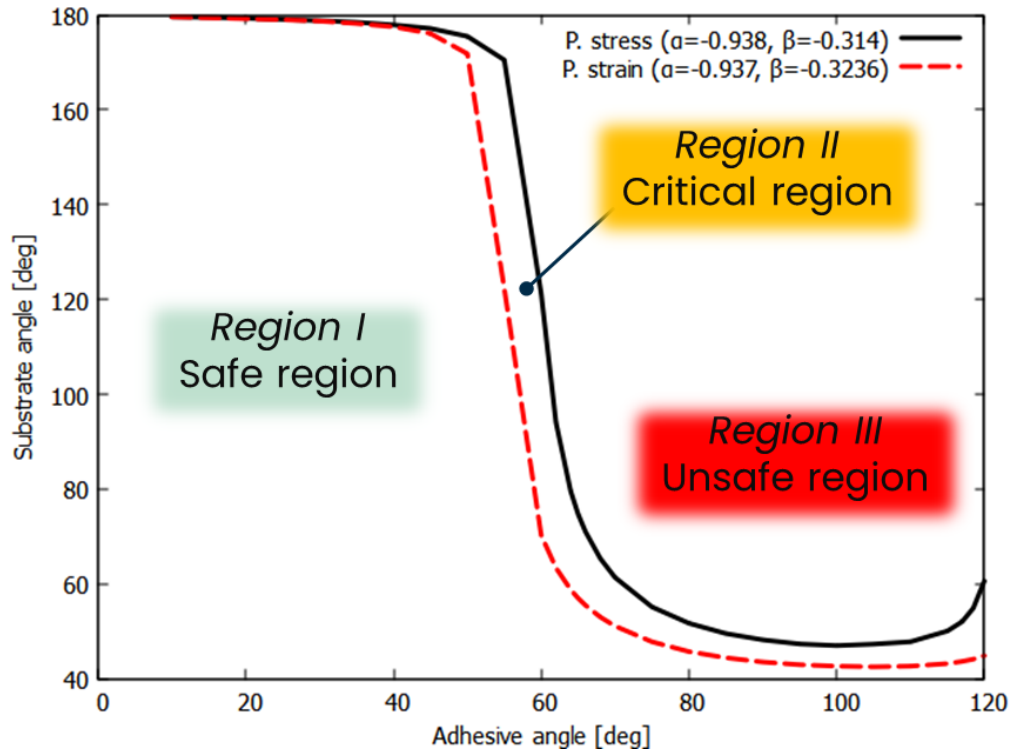


Figure 51: Design maps defining the presence/absence of the stress-singularity. Original from [216]

From a physical perspective, the red and the black curve in the map are the upper-bound conditions that ensure the absence of the singularity for the selected plane strain or plane stress conditions. Indeed, at fixed plane strain/stress condition and fixed adhesive angle, choosing a substrate angle below the critical angle reported in Table 5 assures the absence of stress singularity. Precisely, there are three well separated regions that can be highlighted. In Region I, all the adherend-adhesive angular combinations ensure the absence of the singularity regardless the mechanical plane strain/stress condition. In Region II, the area between the two curves is the most problematic. The designer should choose accurately the modelling strategy since the selection of plane strain or plane stress severely affects the final results. Conversely, in Region III all the angles exceed both limit conditions thus the presence of the singularity is certain.

For the purposes of completeness, in Figure 52 and Figure 53 the Bogy determinant curve in both plane strain and plane stress, respectively, are presented. The solution should be found in the range $[0 - 180]^\circ$ and, if multiple roots were present, the designer should consider the smaller only. In this particular case no multiple roots were observed. Is interesting to observe that, for both plane

strain/stress, when the explored adhesive angle is bounded between 10° and 50° ($10^\circ \leq \theta_1 \leq 50^\circ$) the Bogy determinant remains negative and intercepts a zero value in the range $[171.8 - 179.6]^\circ$, with a very small variation with respect to the variation of the adhesive angle. At $\theta_1 = 60^\circ$ there is a significant variation. Indeed, the substrate solution falls at $[171.8 - 179.6]^\circ$ for plane strain whereas the plane stress solution falls at $\theta_2 = 121.2^\circ$. Qualitatively, $\theta_1 = 60^\circ$ behaves like drift point characteristic for this type of joint. Beyond 70° ($\theta_1 \geq 70^\circ$) the solutions acquire their own values by assuming a curved pattern.

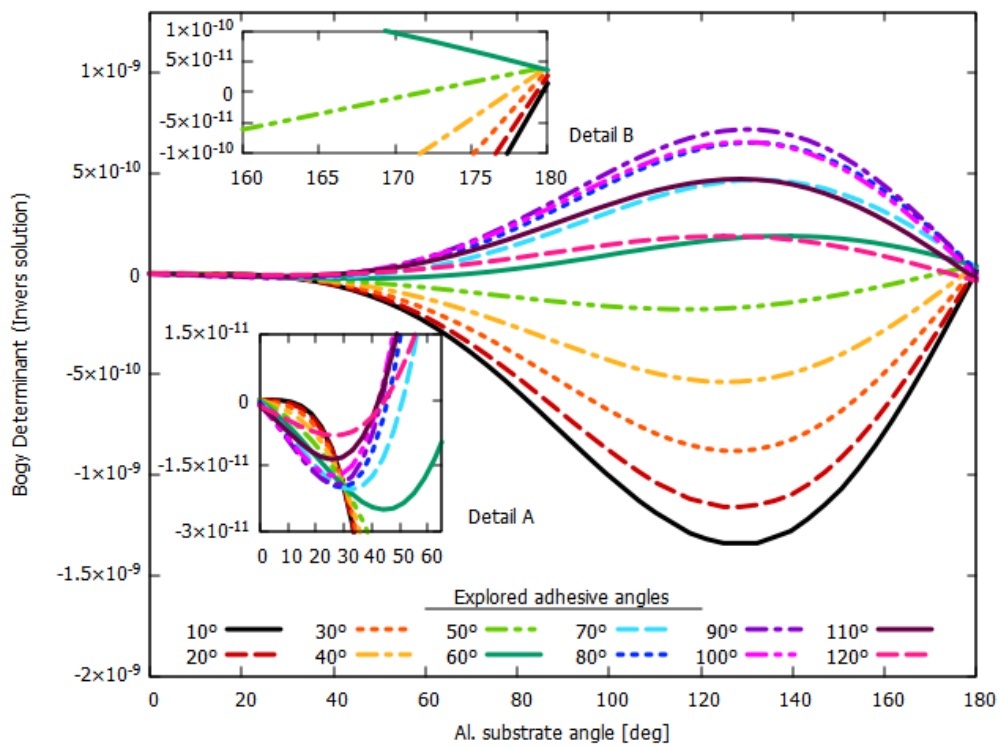


Figure 52: Angular evolution of the Bogy determinant, Plane strain solutions.

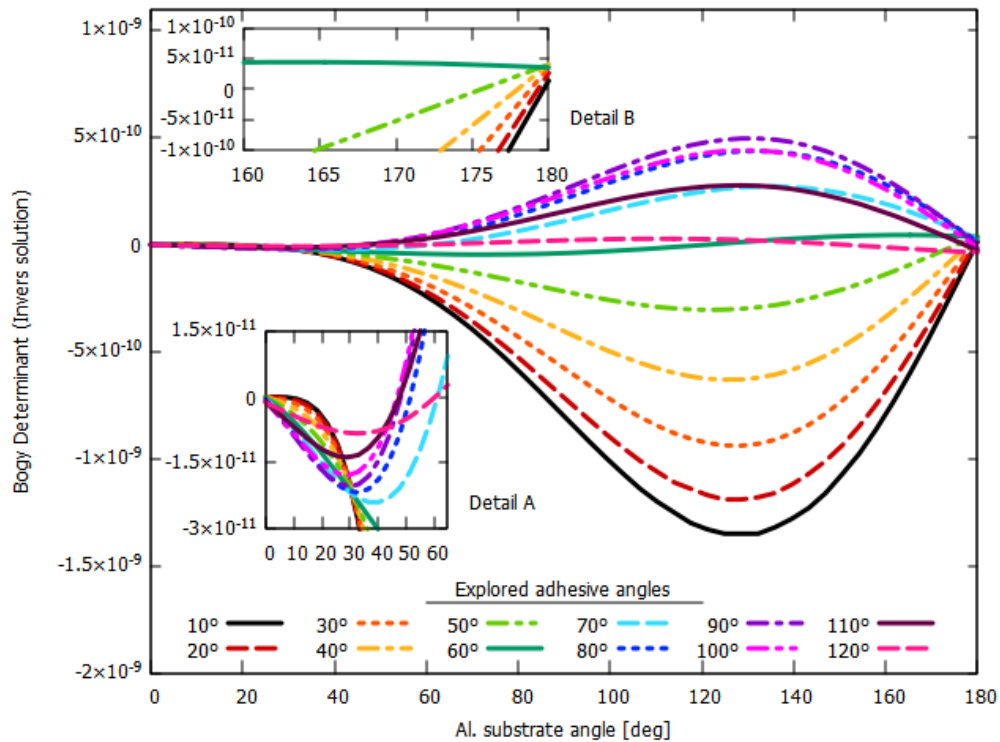


Figure 53: Angular evolution of the Bogy determinant, Plane stress solutions.

Once the angular solutions were known, a counter analysis was performed aiming at verifying that such numerical results were not a “lucky extraction” or affected by errors included in the MATLAB routines development. To do so, the original expression of the Bogy determinant (i.e., the direct solution) was considered. Essentially, the material properties, the substrate and the adhesive angles as well as the plane strain or stress condition were provided as input data. In this case, $p - root$, should not be contained in the $]0 - 1[$ interval.

In Figure 54 and Figure 55 the plane strain and plane stress Bogy trends are reported, respectively. The observations of these two plots and, especially, the close-up view near the 0 and 1 edges, ascertain the goodness of the approach that has been followed since no $p - root$ can be defined.

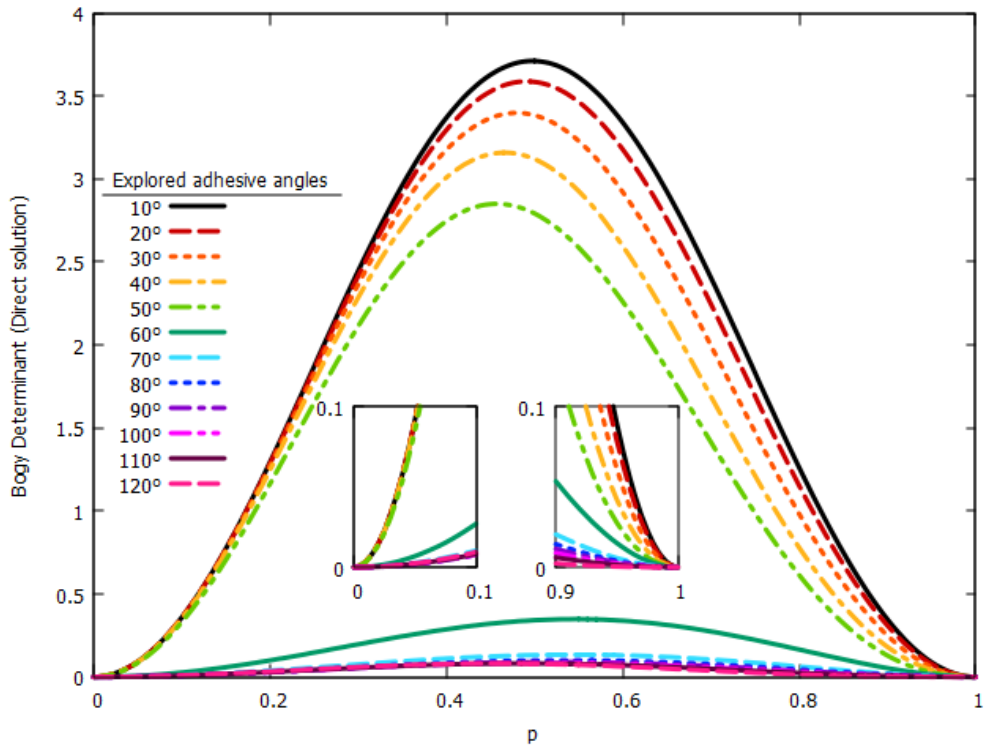


Figure 54: Bogy determinant for each explored adhesive angle, Plane strain conditions.

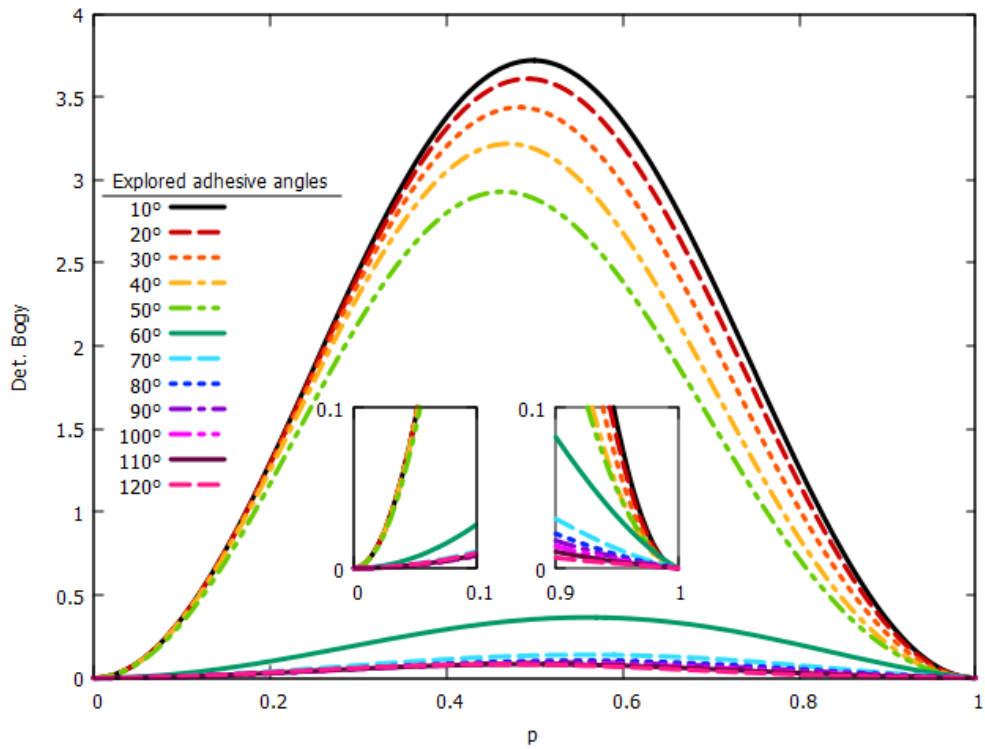


Figure 55: Bogy determinant for each explored adhesive angle, Plane stress conditions.

At this stage, from the broad set of non-singular solutions, just one configuration must be chosen for the FE modelling and, most important, for VHCF tests. The criterion that was adopted for selecting the most suitable configuration relies on the best similarity compared to the original singular specimen, described in the previous paragraph. Thus, the $\theta_1 = 90^\circ$ configuration on the adhesive side was selected. Such setup should present a straight external adhesive surface that can be physically obtained at the end of the manufacturing process. This hypothesis was considered valid and reasonable as, how will be clarified in the following, a dedicated manufacturing procedure was established to achieve this result. Regarding the substrate angle that satisfies the singularity absence, the one in plane strain condition was selected (i.e., $\theta_2 = 43.5^\circ$) in order to work in the safety conditions without the uncertainty introduced in Region II. In fact, the butt-joint under analysis is a middle-way between plane strain and plane stress conditions due to the axisymmetric configuration. Moreover, is usually preferred in FE analysis of joints to work in plane strain rather than in plane stress.

To sum-up the selected non-singular configuration consists of $\theta_1 = 90^\circ$, $\theta_2 = 43.5^\circ$ in plane strain conditions. This information was included within the FE model as presented in Figure 56. At the adhesive-adherend interface a suitable geometrical modification capable of guarantee the θ_2 substrate angle. Regarding the modelling aspects involved during such modification, a minimal mesh refinement was applied to the non-singular specimen in the region of interest to avoid the element corruption, element distortions or too high aspect ratio that could have been introduced by coarser meshes.

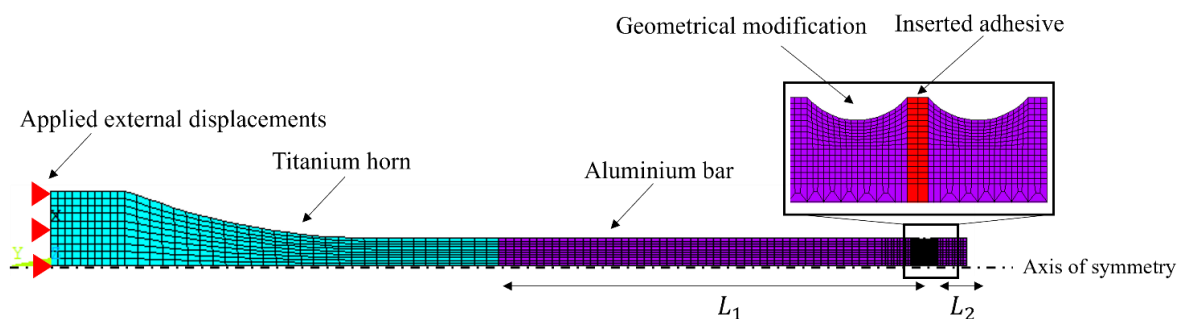


Figure 56: Singularity-free VHCF specimen, FE description. Original from [215]

A further FE modal analysis was performed aiming at verifying if the introduction of the geometrical modification still satisfies the frequency requirement of 20 ± 0.5 kHz. In Table 4 (last column) the numerical outcomes have been reported whereas in Figure 57 the frequency results for all the specimens analysed are graphically collected.

It is interesting to observe that the introduction of the geometrical modification pushes up the frequency related to the mode of interest (i.e., 3rd fundamental mode) of 85 Hz with respect to the 90° - 90° interface specimen and of 58 Hz with respect to the specimen without adhesive whilst it behaves like a sort of “attenuation device” for the remaining frequencies. In fact, for such frequencies, the specimen without adhesive presents the highest frequency values (apart for the horn) whereas, macroscopically, the introduction of both the adhesive and the geometrical modification does not produce sensible variations.

The knowledge of the actual working frequency for the specimen with adhesive and 90° - 43.5° interface is essential to confirm the design since the frequency requirement 20 ± 0.5 kHz is still satisfied. Then, the total specimen length (L_{tot}), found for the singular specimen, was maintained as valid.

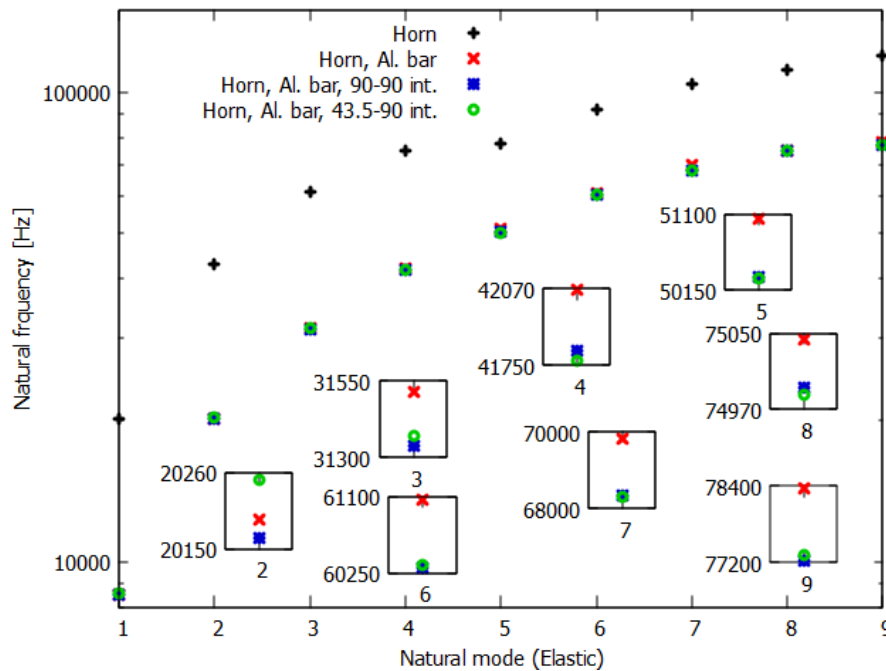


Figure 57: Trends of extracted elastic natural frequencies.

3.4 Development of Global-Local FE models: approaches and results

FE models of singular and non-singular coupons have a number of elements in the range of 5000 units that, for the current computer capability, represent an easily manageable size from the calculation time and analysis robustness point of view. Such models were built with the unique purpose of investigating the general structural behaviour thus verifying the overall design. To do so, a Global model philosophy was followed. Indeed, as an example, the stress recovery was performed along the bar axis without investigating a local detail or, more important, the adhesive was meshed with just two elements in the thickness direction, which is considerably not enough to simulate sufficiently its stress performances.

To overcome this issue, a Global-Local strategy was followed to better investigate the coupon and the stress details. Indeed, as described in Section 2.5, a Global-Local approach is a suitable technique to investigate structural details (e.g., fillet, edges, etc...).

To accomplish a reliable and effective Global-Local model, the modelling strategy consists of the identification of the right interface between the Global and the Local models, the identification of an interpolation region and the verification between Global and Local FE outcomes to evaluate the quality of the Local model.

The Ansys APDL Submodelling features were exploited to just identify the model boundaries where the region of interpolation was restricted to the line of interface between the two FE descriptions. A manual iterative procedure aiming at identifying the correct Local FE size, was performed. Indeed, a multi-purpose, or generalized size, is not available and the model boundary distances depend on both the physical phenomenon under analysis and the structural characteristics of the component.

The Local model boundary condition originates from the Global model displacements resulting from the FRA at 2.2 μm and 18 μm in the specimen resonance condition. Since the singular and the non-singular specimens present different natural frequencies, the analysis frequency should be considered

accordingly. The loading frequency is 20165 Hz in the case of a singular specimen and 20250 Hz for the non-singular coupon. The use of this frequency is legitimate not only because these are the specimen frequencies that satisfy the UFTM frequency requirement, but also because the testing machine is able to tune its loading frequency in order to keep the specimen resonance.

Structured meshes characterized the singular specimens as its geometry is predominantly straight whereas the non-singular model was approached with free-meshes in the curve region in order to better capture the geometrical peculiarities. The minimum element size for both models is proportional to 10^{-5} mm whilst the number of elements is in the range of 350 000.

The iterative process ended with the identification of the Local models, as presented in Figure 58 and Figure 59 for singular and non-singular geometries respectively, whose longitudinal dimensions are 11.35 mm from the adhesive midline on the left and on the right.

From the modelling point of view, the applied local boundary conditions arise from spline interpolation of global displacements along the model boundaries.

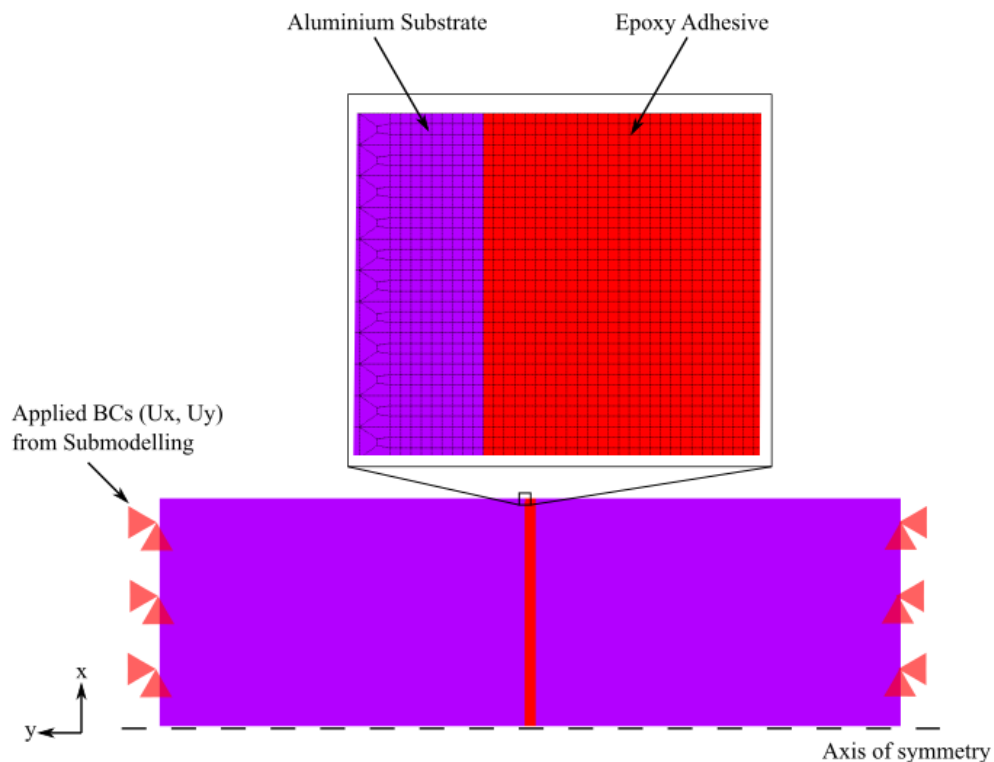


Figure 58: Sub-model for the singular specimen. Original from [215]

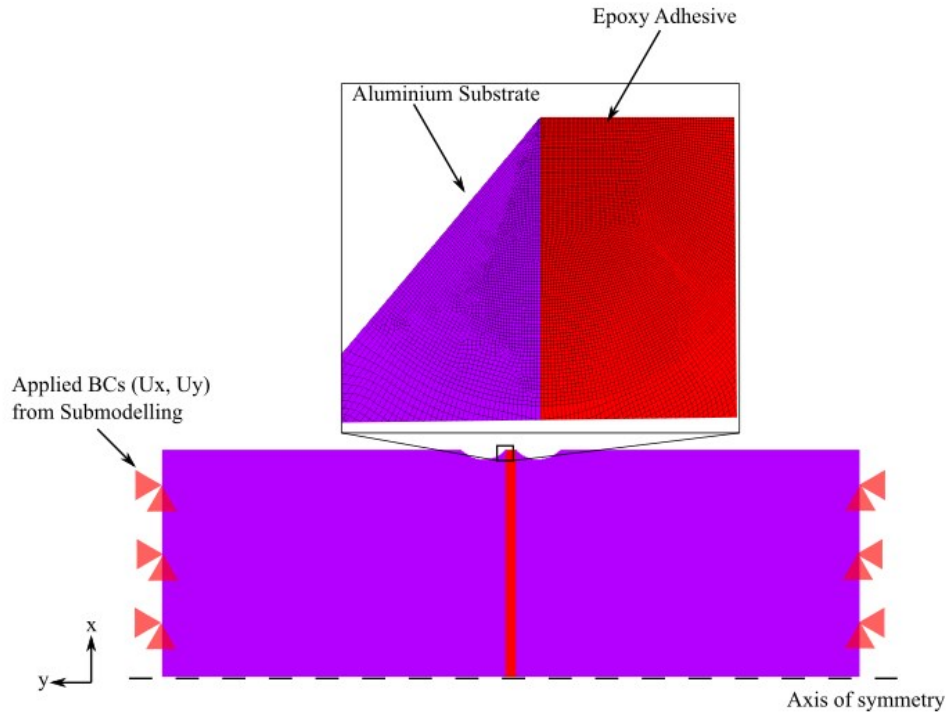


Figure 59: Sub-model for the non-singular specimen. Original from [215]

An important step during the model size research pertains to the displacement, deformations and stresses verification at the edges. Spline interpolation, even though it is a robust method, remains an approximation. Then, is a good practice in dealing with Global-Local techniques their check and the quantification of discrepancies between Global and Local quantities in order to be aware of possible modelling errors and further FE improvements.

In the following pictures related to the Global-Local approach, numerical results are presented for the 18 μm loading case, without losing generality and, most important for the selected final Local configuration.

In Figure 60 and Figure 61 the longitudinal (u_y) displacements recovered at the left interface are presented as this direction is the most important for the problem under analysis. In general, is clearly visible that the interpolation procedure correctly reproduces the global displacements at the local interface for both model edges. Regarding the displacement magnitude, it was expected that transversal behaviours were much lower than longitudinal ones as the relevant part of the structural excitation lies along the axis.

This observation was just a preliminary, but important, information: the correct displacement interpolation is the necessary condition to approach the research of the model interface in the correct way.

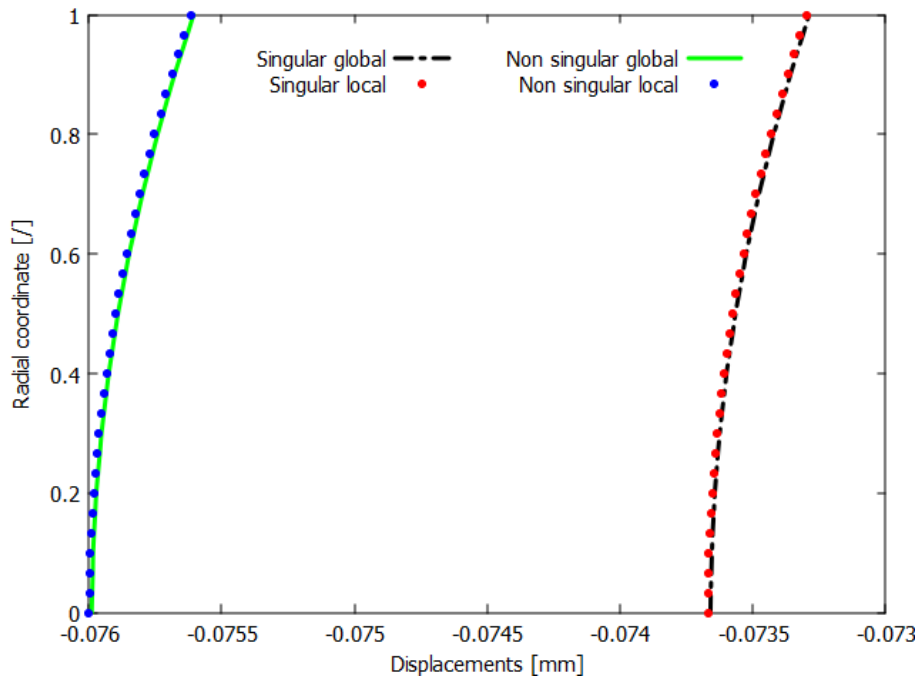


Figure 60: Longitudinal displacements, left interface.

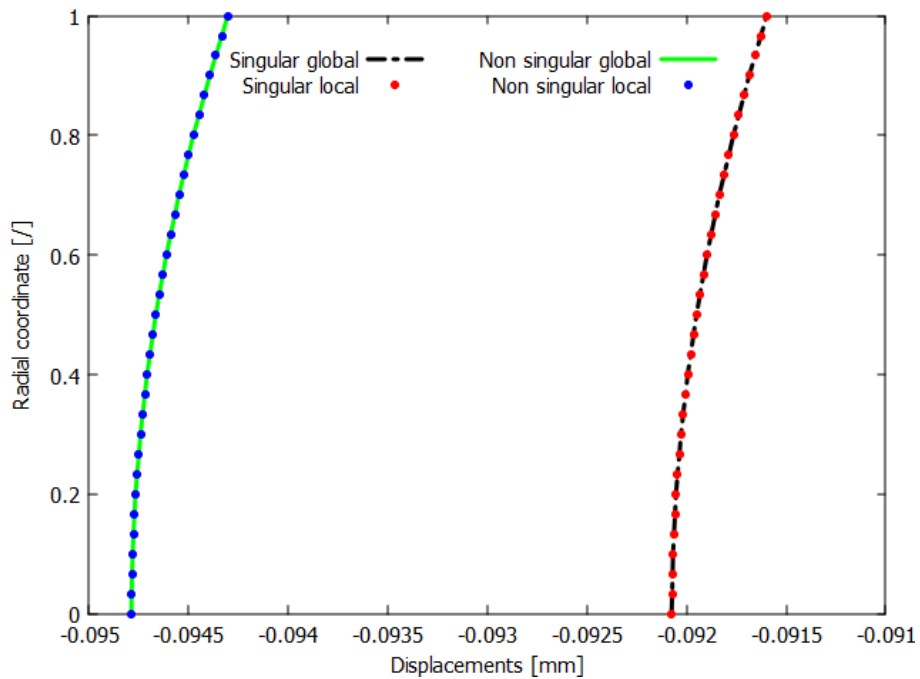


Figure 61: Longitudinal displacements, right interface.

After confirming the correctness of the interpolation, the real verification of Local models, in terms of size and boundaries, is based on the strain and stress

observation. In general, to the author's best knowledge, there is not a univocal criterion to accept or reject a specific strain and stress distribution that characterizes a Local model. Essentially, the Local strain and stress distribution, recovered at the Local model interface, should coincide (or to be reasonably close enough) with respect to the Global quantities defined in the same location. From a pragmatic perspective, the decision if these trends coincide or these are reasonably close enough, depends on the structural analysts, their experience, their feeling with the problem under analysis and, most importantly, the required level of accuracy. In any case, a price should be paid: an easy-to-reach Local model could present strain/stress distribution not very in line compared with the Global quantities but, on the contrary, the best closeness achievable among trends could imply an hard-to-obtain model. This remark emphasizes that, also in the case of Submodelling techniques that were developed for the specific purpose of refining investigations of local structural details, a balance between the model complexity and the result accuracy should be still maintained.

As similarly extracted for displacements, Figure 62 and Figure 63 illustrate the longitudinal deformations (ϵ_y) and the longitudinal stress (σ_y) for the left interface. Similar quantities are showed in Figure 64 and Figure 65 for the right interface.

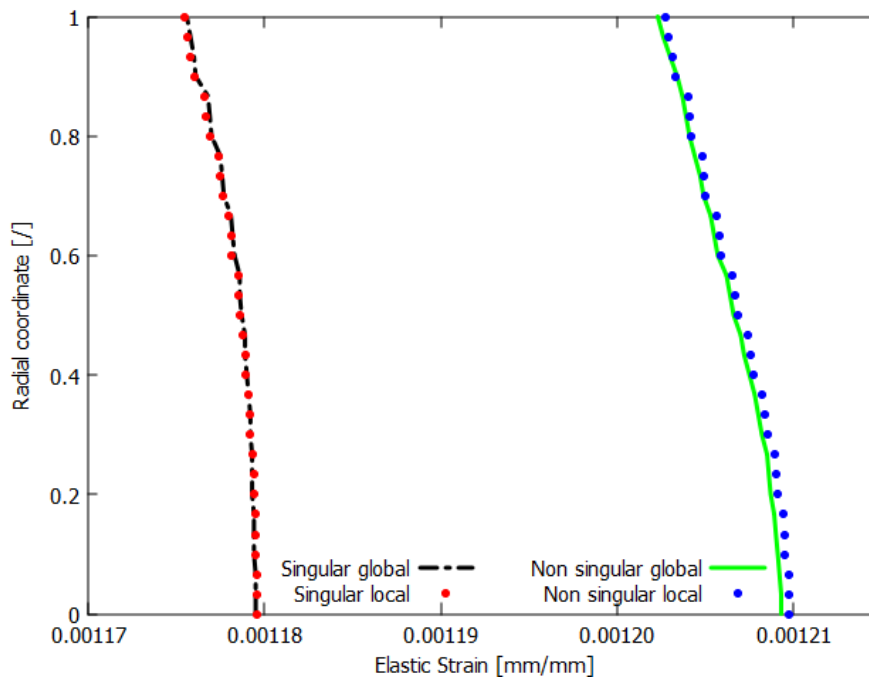


Figure 62: Longitudinal deformations, left interface.

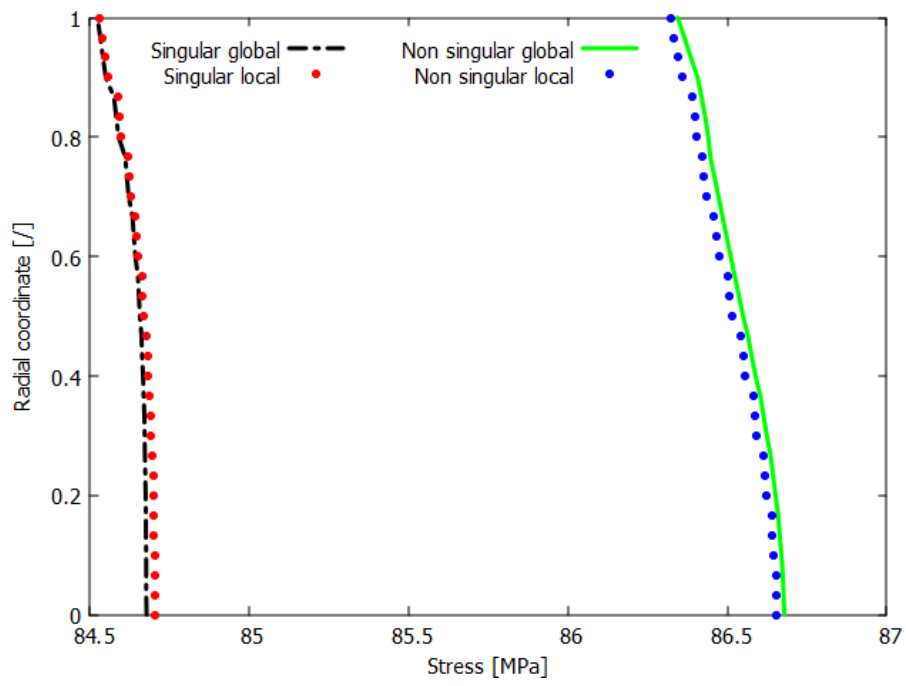


Figure 63: Longitudinal stress, left interface.

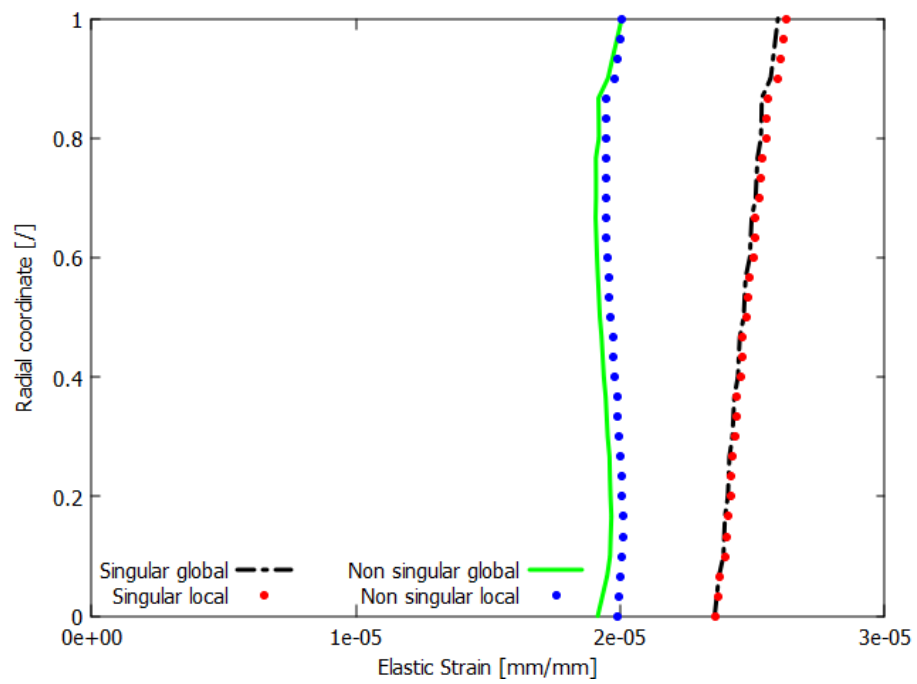


Figure 64: Longitudinal deformations, right interface.

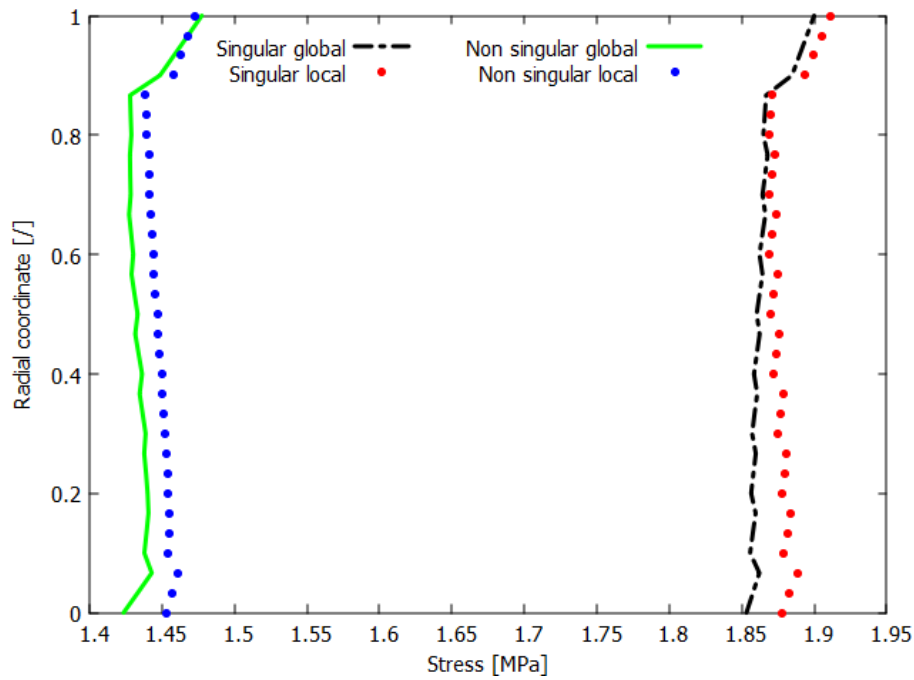


Figure 65: Longitudinal stress, right interface.

Strains are very well captured and reproduced by Local models and the number of discrepancies is negligible. On the contrary, even if discrepancies are present, the axial stress distribution shows an amount of difference between Global-and Local trend in the order 1% along the axis that is anyhow considerably low. Recovered stress, especially, present trend discrepancies that are mostly attributable to the fact that, at the edges, Local models showed a small difference in terms of mesh size compared to the Global descriptions. Such difference, combined to the stress recovery at the Gauss points with a copy procedure for passing to nodal values, is the main source responsible for stress deviations. It is also important to remember that, dealing with classical FEM implementation, the displacement is the master field thus strain and stress are derived quantities (strains are extracted by the derivation of the Lagrange polynomial whereas stress are extracted by multiplication for the material matrix). This procedure can accumulate, small, numerical errors that affect the final results.

However, the Global and Local trends are very similar and this means that the local model is adequate to study localized features.

Once the proper model boundaries for interpolating the global displacement distribution into a local description are identified, a refined FEA assessed the precise stress distribution near the critical model regions.

In Figure 66 and Figure 67, the σ_y distribution is presented for both singular and non-singular adherends-adhesive assembly, respectively. Both descriptions present a stress distribution that correctly decreases, in agreement to Figure 49, leading to a $\sigma_y = 0$ in correspondence of the right edge.

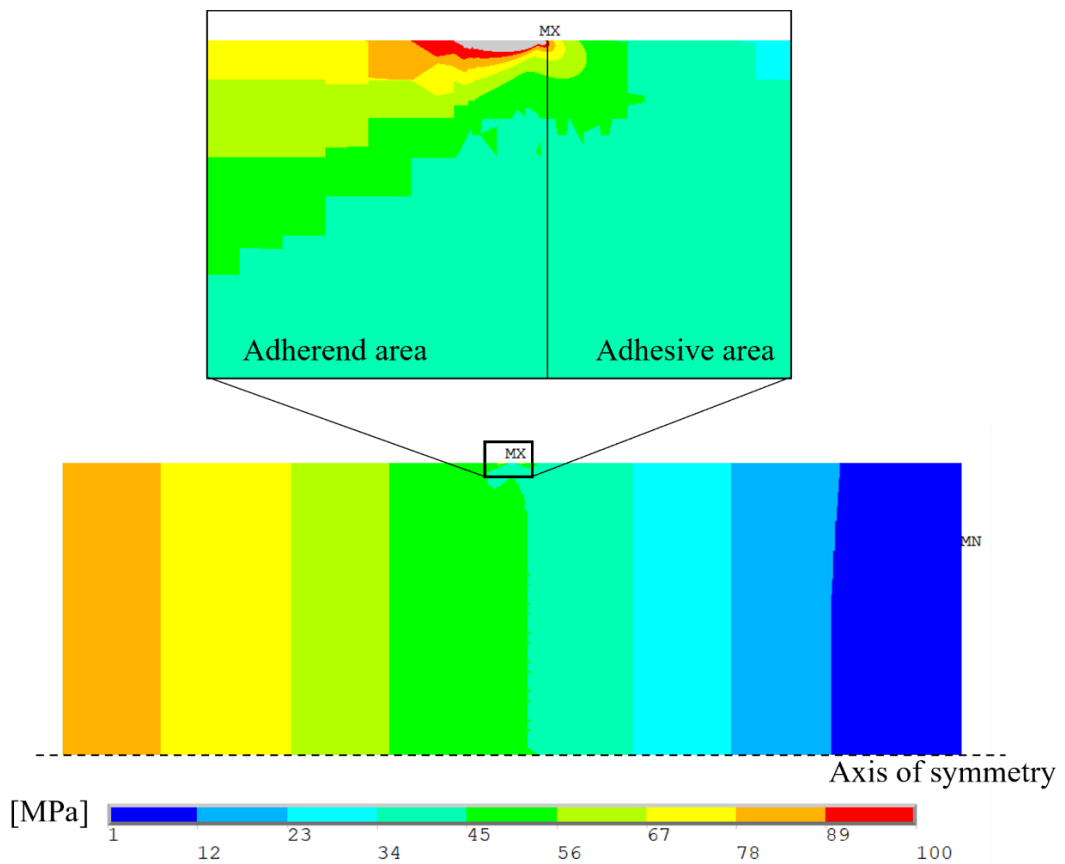


Figure 66: Longitudinal stress distribution, singular model. Original from [215]

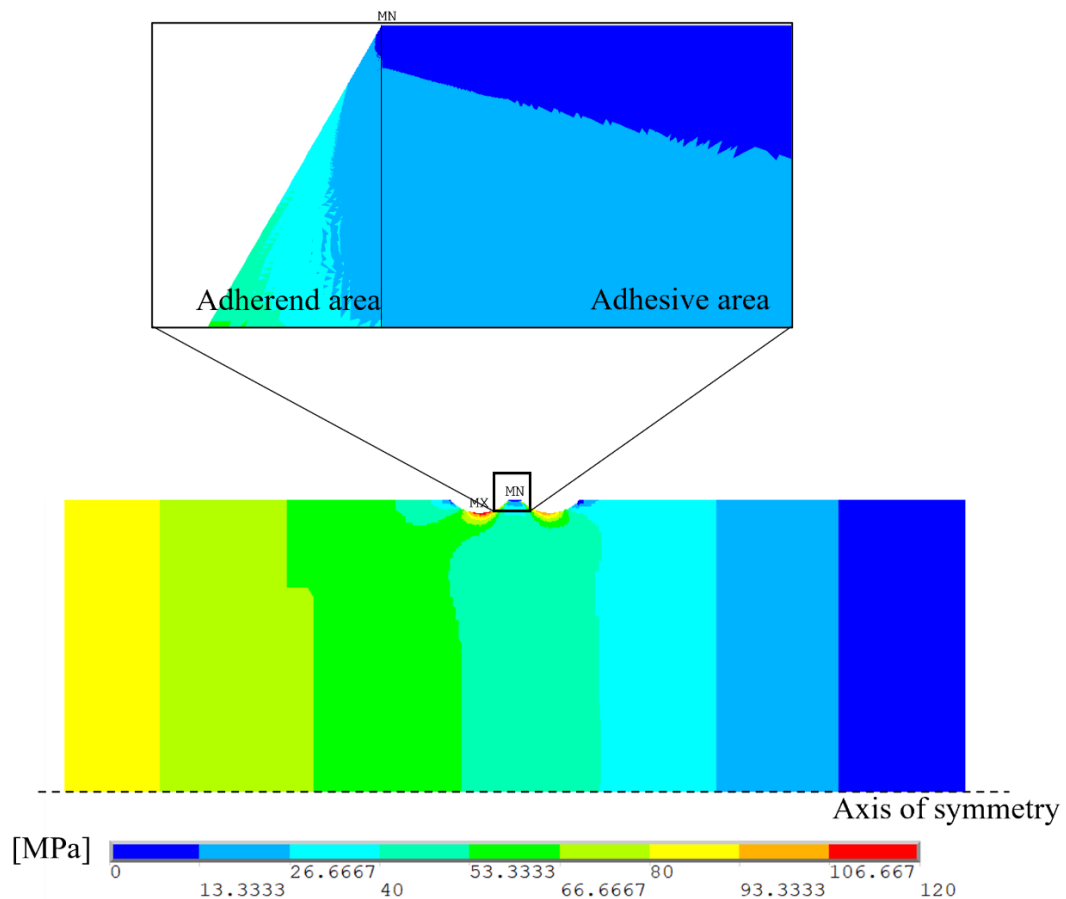


Figure 67: Longitudinal stress distribution, non-singular model. Original from [215]

In Figure 66 (close-up view) the stress field in correspondence to the singular region is presented by using a fictitious threshold of 100 MPa to highlight the structural region where the stress is supposed to grow without control. Furthermore, the grey region indicates that stress results go beyond the 100 MPa threshold. Even if such stress distribution could be unrealistic in the singular region, especially in the adhesive areas where the predicted stress exceeds the maximum stress (i.e., 35 MPa) and plasticity should compensate singularity effects, it can be observed that the local maximum stress should arise at the surficial adhesive-adherend interface, as expected.

In the merit of the non-singular specimen in Figure 67 such geometry presents the maximum stress value in the circular throat region whereas, at the material interface, the unbounded stress distribution was correctly avoided and removed.

An additional numerical assessment, focused on the verification of the singularity exponent, was performed as a side aspect of the main assessment.

Precisely, at fixed geometrical and mechanical conditions, the direct Bogy analysis can study the magnitude of the singularity with closed-form mathematical relations. In this context, the aim is to numerically verify the theoretical value along the material interface.

To do so, the FE stress results were extracted along a path of mm from the singular point. In order to perform such exponent extraction, as suggested by Goglio and Rossetto [14] for this type of investigation, a cylindrical coordinate reference system was preferred and centred on the nodal external interface.

The numerical stress values σ_R (radial stress), σ_θ (peeling or cleavage stress) and $\sigma_{R\theta}$ (shear stress) were analysed and post processed with an ad-hoc written MATLAB code that implements the numerical regression through the curve fitting toolbox and, especially by exploiting the `power1` function. Such function adopts the mathematical model

$$y = Ax^b \quad \text{Eq. (3.4.1)}$$

where y is the stress component of interest ($\sigma_R, \sigma_\theta, \sigma_{R\theta}$), A the stress intensity factor (H) for the i^{th} stress component, x the distance from the singular point and b the singularity exponent (λ). The numerical algorithm operates a calculation in order to find the H and λ values that best fit the numerical data.

Extracted FE stress outcomes were not totally used: as suggested by Goglio and Rossetto [14], the outcomes of the first two, or three, elements should be disregarded from the mathematical regression. Indeed, in the singular region and on these first elements nearby, the FE tool tries to find a convergent solution to an un-convergent problem. The knowledge of this issues required the exclusion of the first four data for all the stress components.

In Figure 68 and Figure 69 the stress components (coloured points representative of FEM outcomes) and the associated mathematical regression (coloured lines) are illustrated in bi-logarithm plots for the left and the right adhesive-adherend interface.

Mathematically, the regression algorithm was able to interpolate the radial and the peeling stress components as $R^2 \geq 0.999$ in both directions whereas a lower precision was achievable for the shear stress the presented an $R^2 = 0.95$. Indeed,

as visible in both plots, such shear component presents unexpected oscillation with respect to the σ_R and σ_θ . Such distribution was weird since the mesh was structured, regular with an aspect ratio ≈ 1 .

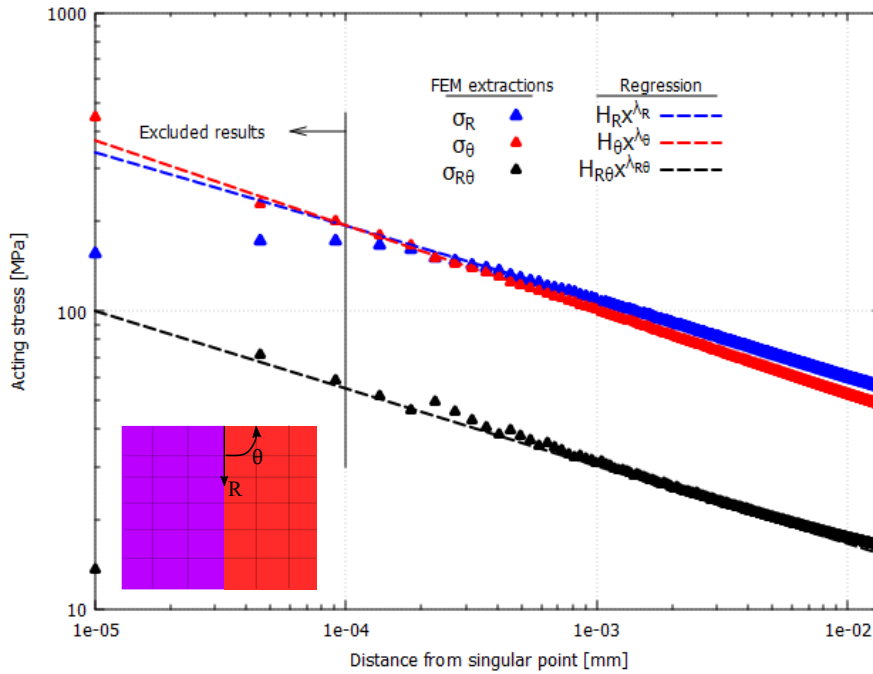


Figure 68: SIF investigations, left interface.

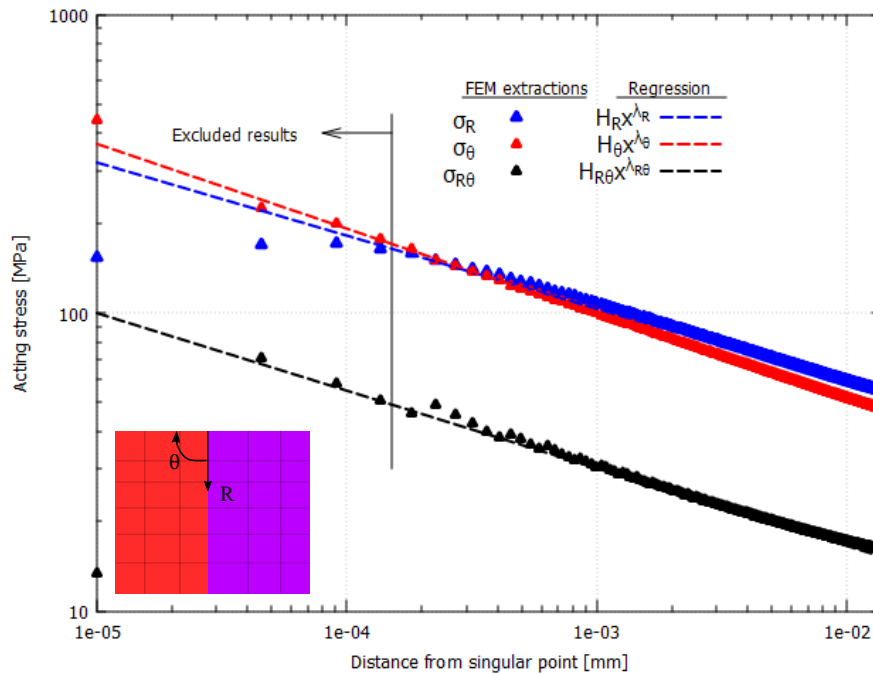


Figure 69: SIF investigations, right interface.

Regarding the research of SIF and λ , in Table 6 the numerical values are reported for all the stress components along both material interfaces ($\theta = 0^\circ$). If λ_B is the Bogy analytical value, the closest approximation is achieved by the peeling component only. Such assessment has shown the good accuracy in predicting the singularity exponent by numerical evaluations and, most important, the number of discrepancies introduced by these last.

	Stress component	λ ($\lambda_B = -0.275$)	H $MPa \cdot mm^\lambda$
Left Interface	σ_R	$\lambda_R = -0.246$	20
	σ_θ	$\lambda_\theta = -0.285$	14
	$\sigma_{R\theta}$	$\lambda_{R\theta} = -0.260$	5
Right interface	σ_θ	$\lambda_R = -0.245$	19
	$\sigma_{R\theta}$	$\lambda_\theta = -0.284$	14
	σ_R	$\lambda_{R\theta} = -0.260$	5

Table 6: SIF and singularity exponent investigations

FE outcomes reported in Figure 66 and Figure 67 provide the entire stress map for the Local specimens under the external acting loads. If, in the case of the singular specimen, the numerical model coincides with the specimen under test, for the non-singular specimen the working assumption of considering just one possible configuration among all the possibilities summarized in Table 5 was followed. The selected 43.5° - 90° configuration represents the upper-bound bi-material configuration to remove the singularity and, essentially, such geometry could be problematic for testing coupons since manufacturing inaccuracies could introduce uncontrollable deviation between the mathematical model and the physical coupon. So, a sensitivity analysis based on the manual reduction of the substrate angle, was performed. Two main aspects were considered while executing this study: *i*) a suitable bi-material configuration to be adopted during

testing and *ii*) the current workshop technological capabilities. Thus, the nominal 43.5° - 90° configuration was progressively modified within the FE tool on the aluminium substrate side. Doing so, a wider range of bi-material interfaces was arbitrarily considered and numerically explored: $[43.5, 40, 35, 30, 25]^\circ$ - 90° .

At this stage, five possible configurations are theoretically available as the range of solution was extended. The final decision on the adopted testing configuration will be based on the *i*) and *ii*) before-mentioned hypothesis through FE analyses. Essentially, in addition to the 43.5° - 90° FE model, other four mathematical descriptions (i.e., $[40, 35, 30, 25]^\circ$ - 90°) were produced by introducing a local geometrical modification at the bi-material interface. Clearly, the geometrical reduction of the substrate angle would have produced a modification of the fundamental frequency, but this aspect was neglected since this aspect was considered a second-order effect.

To better visualize the localized stress trends, is useful to collect stress data along the two directions, reported in Figure 70 (for the non-singular case, as an example), namely “T” (i.e., the external part of the thickness) and “R” (i.e., the adhesive midline) from the specimen axis to the external surface. Along these two directions the acting stresses have been extracted in a 2D cartesian reference system (X, Y). In the following plots, the numerical solutions are associated to the $18\ \mu\text{m}$ condition whereas these are depicted with a non-dimensional scale.

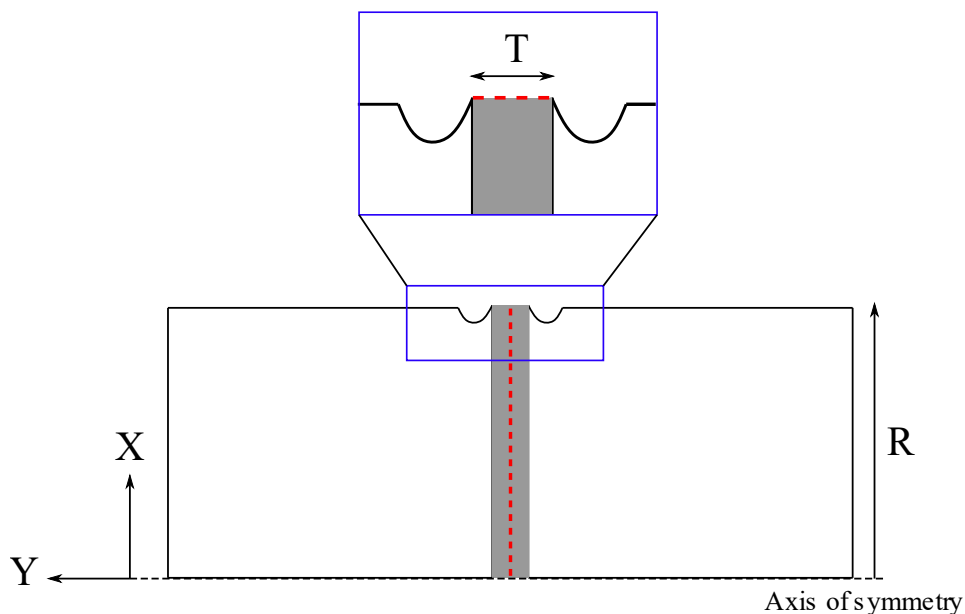


Figure 70: Directions for stress recovery. Original from [215]

In Figure 71 the longitudinal (σ_y) stress recovered on the “T” direction are reported for both singular and non-singular mathematical models.

A first important aspect pertains the substantial difference between the through the thickness singular (black dots in 43.5°- 90°) and non-singular (coloured lines for [40, 35, 30, 25]° - 90°) stress fields. Indeed, even though the singularity is a theoretical point where the stress is infinite as correctly reproduced by the numerical distribution, its effects affect the stress results in the whole adhesive extension. In fact, singular stress results are the highest along the whole adhesive extension. By contrast, the removal of the stress singularity globally mitigates the intensity of the mechanical stresses on the specimen surface. Moreover, localized stress concentrations progressively extinguished by reducing the substrate angle and a more uniform stress distribution is expected in the adhesive central regions.

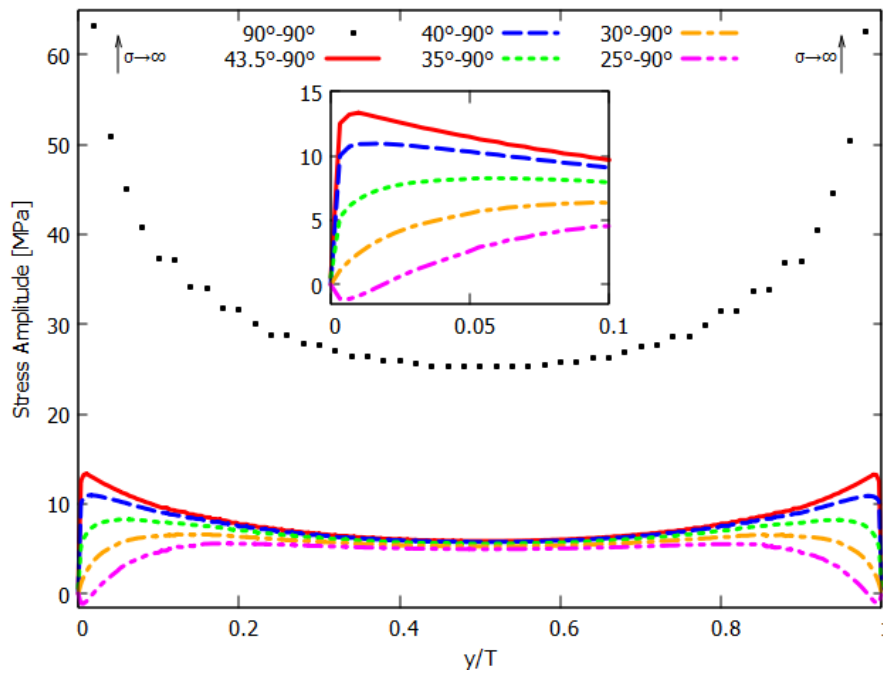


Figure 71: Longitudinal stress on the T-direction. Original from [215]

Figure 72, Figure 73 and Figure 74 illustrate the longitudinal, the transversal and the shear stresses that were recovered on the “R” direction as presented in Figure 70. There are, essentially, some important observations that can be deduced from these three stress components. From Figure 72 and Figure 73 can be easily quantified the stress increase on the specimen axis that results from the introduction of the geometrical modification. Indeed, by focusing on the

prominent stress component at the specimen axis, from nearly $\sigma_y = 46$ MPa resulting from the design of the singular specimen, all the non-singular configurations stand at $\sigma_y = 48$ MPa. Even if the difference is not excessive, the detailed knowledge of such “stress jump” is fundamental for the correct test setup. Furthermore, the removal of the stress singularity significantly modifies the stress trend along the radius. If in the case of the singular specimen there is a substantial constant σ_x, σ_y distribution up to 85% and 95% respectively, a non-singular edge produces a stress increment that makes more sensible the upper part of the joint. However, even present, such stress increment is limited and smaller than 9% for σ_y that is the most important component. Finally, regarding the shear stress, there are not severe consequences for this component. The stress profile, even if slightly modified, from a macroscopic point of view, remains controlled in magnitude and not critical.

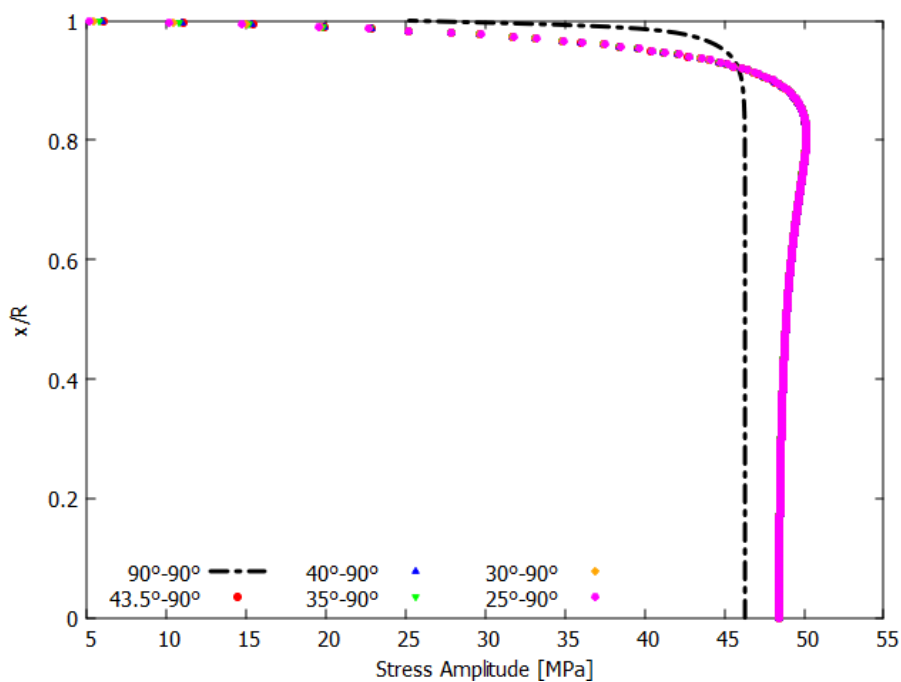


Figure 72: Longitudinal stress on the R-direction. Original from [215]

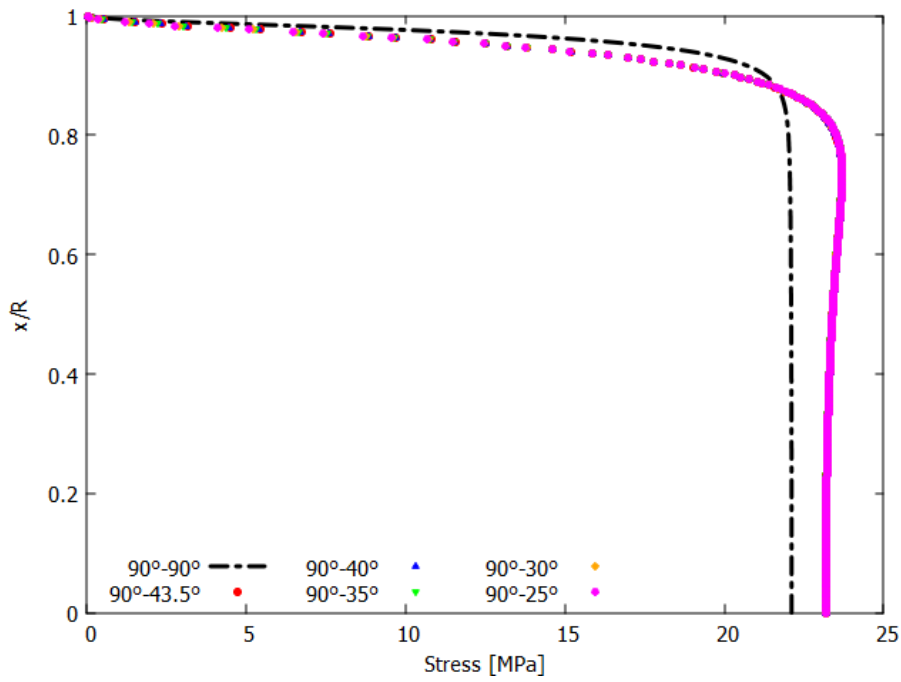


Figure 73: Transversal stress on the R-direction.

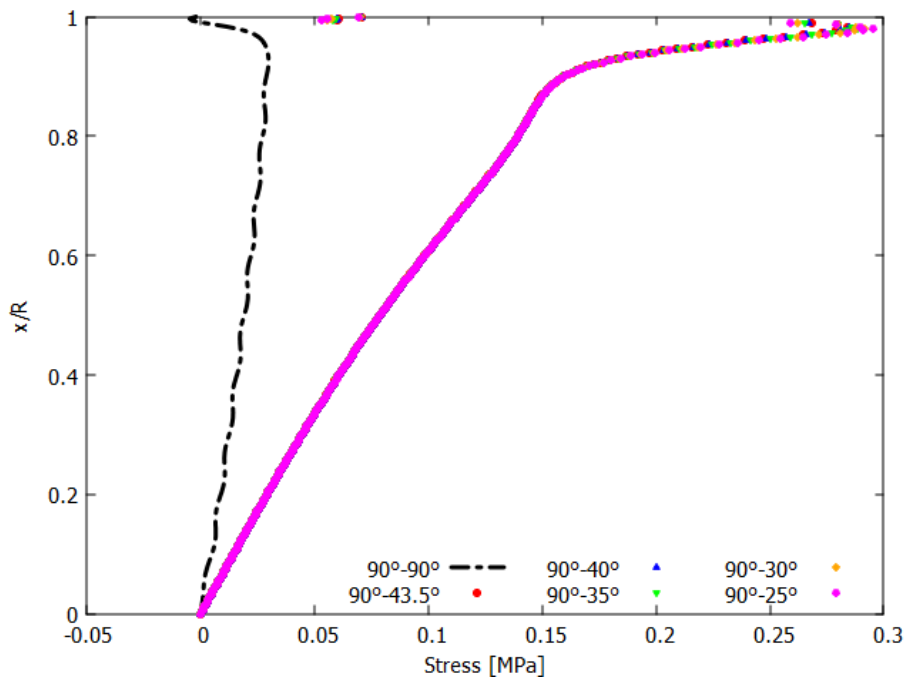


Figure 74: Shear stress on the R-direction.

The analysed profiles, with a special interest in the behaviour among non-singular coupons, were particularly helpful for selecting the most suitable specimen to use during the test phase. All the explored configurations are, potentially, good candidates since there are not spurious stress effects introduced by the further geometrical modification to reach the $[40, 35, 30, 25]^\circ - 90^\circ$

alternatives. Such observation satisfies the necessary condition of producing a suitable stress pattern.

The other important aspect relies on the manufacturability of the joint. As previously mentioned, the 43.5°- 90° could be problematic due to possible uncontrollable manufacturing issues that are always present. Similarly, it is not obvious that a mechanical workshop could produce any kind of joint. The best compromise was identified in the 35°- 90° configuration that, simultaneously, assures the fulfilment of the test objective and a reasonable manufacturing challenge for a mechanical workshop.

3.5 The joint manufacturing

The analyses performed in the previous paragraph have assisted the right choice, the mechanical design and the stress verification of singular and non-singular coupons. During manufacturing, many elements could jeopardize the final results implying differences between the mathematical models and the physical specimens such as the specimen misalignment, a different adhesive thickness, a not straight adhesive surface that characterizes the 35°- 90° configuration, etc... . To approach in the best way possible the manufacturing, a specific procedure has been implemented for the specific case of cylindrical butt-joints. In general, the joint realization was assisted by the 3D CAD tool SOLIDWORKS® where the specimen shapes were visualized and designed. In Figure 75 and Figure 76 the produced singular and non-singular adherends, respectively.

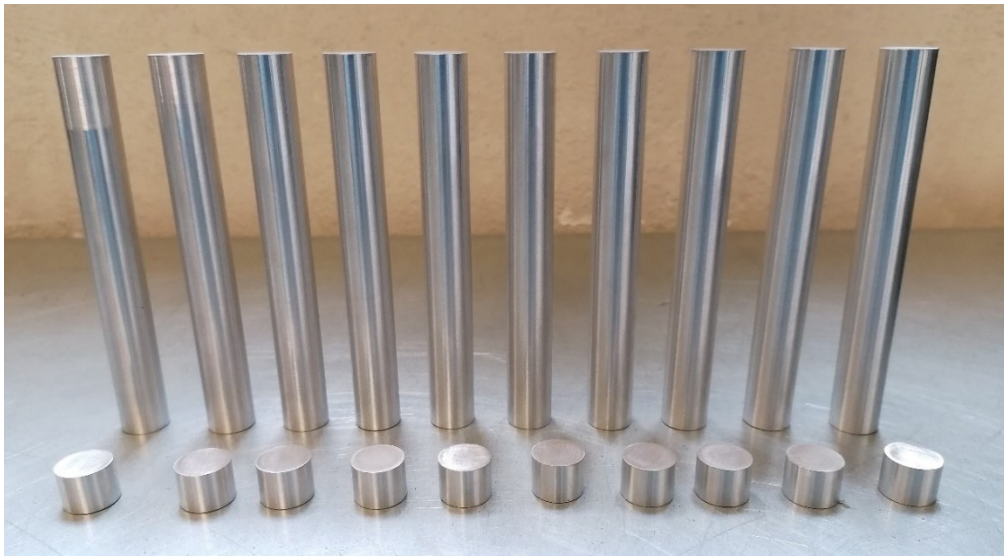


Figure 75: Set of singular specimens.



Figure 76: Set of non-singular specimens.

The joint manufacturing was performed by implementing the following steps :

1. Application of abrasive paper (class P800, 22.8 ± 1.5) on both free areas of the aluminium substrates to increase the surface roughness and thus the adhesion properties;
2. Cleaning the surfaces with acetone to remove impurities and aluminium powder residual;
3. Application of the adhesive on both sides of the joints, Figure 77(a);
4. Joint alignment through specific devices that were designed for this purpose (red blocks in Figure 77(b));

5. Application of a weight on top of the joint to maintain a permanent load during the curing time of 1 day at room temperature , as suggested by the adhesive supplier;
6. Removal of the surplus material out of the joint with a cutter, without compromise the edge integrity.

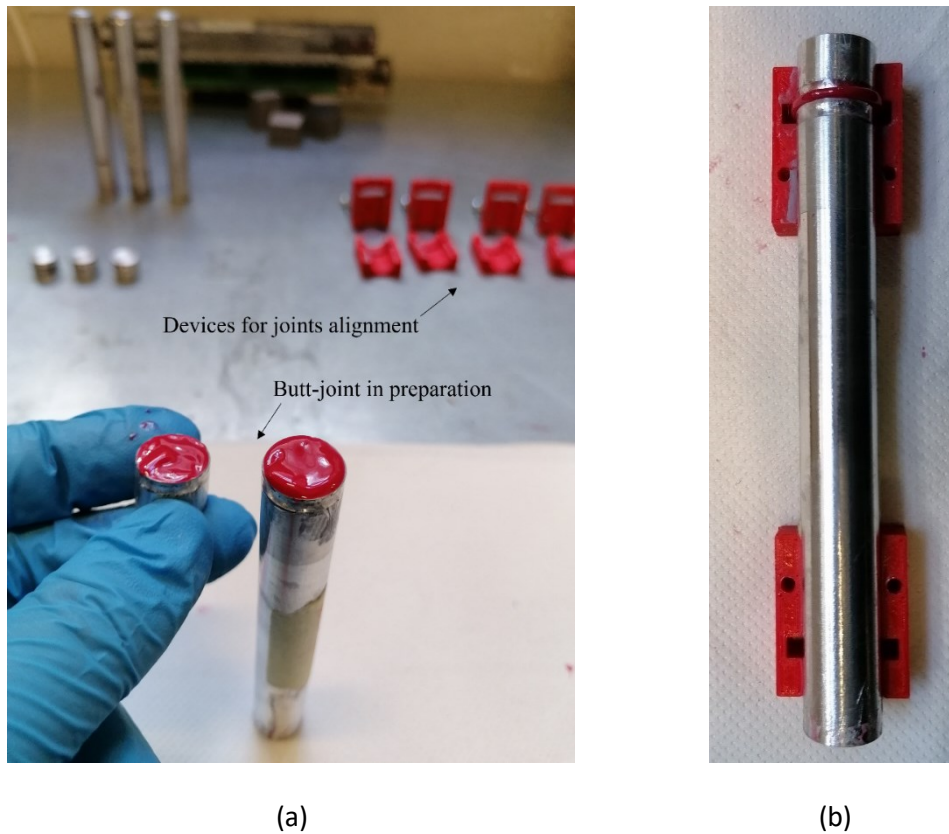


Figure 77: Manufacturing and joining process: (a) application of the adhesive in a liquid phase; (b) alignment of the joint

The illustrated procedure has a general validity. In fact, for VHCF tests (Section 3.7) the joined elements were the long and the small bars (Figure 77) as required by the design procedure to obtain an effective specimen working in resonance conditions, whereas, in the case of static tests (Section 3.6) and classic fatigue tests (Section 3.8), the elements involved were the two long bars only. In these last cases, the use of the longer members can avoid stress interferences produced by the grip mechanisms to the adhesive layer.

3.6 Preliminary static tests

Before performing VHCF experiments, preliminary static tests have been carried out aiming at comparing and verifying the mechanical performance between singular and non-singular joints. To do so, 12 specimens (6 singulars and 6 non-singular) were tested on an Instron® hydraulic testing machine at 2.5 mm/min of the crosshead speed. In Figure 78 the experimental load-displacement curves are reported. There is a substantial good agreement in the whole range of response. This is especially valid where the joint behaviour is linear (\approx max. 4000 N). After such load level, responses start differing among their selves but the resulting scatter is acceptable since it is in line with the pure mechanical behaviour of the bulk adhesive only. From a macroscopic perspective, the important aspect relies on the traceability of the curves slopes and the well captured maximum load.

The comparable behaviour, under purely static loads, for such different joints, is attributed to the presence of plasticity. Essentially, this effect produces a stress redistribution thus compensating the singularity effects at the edges.

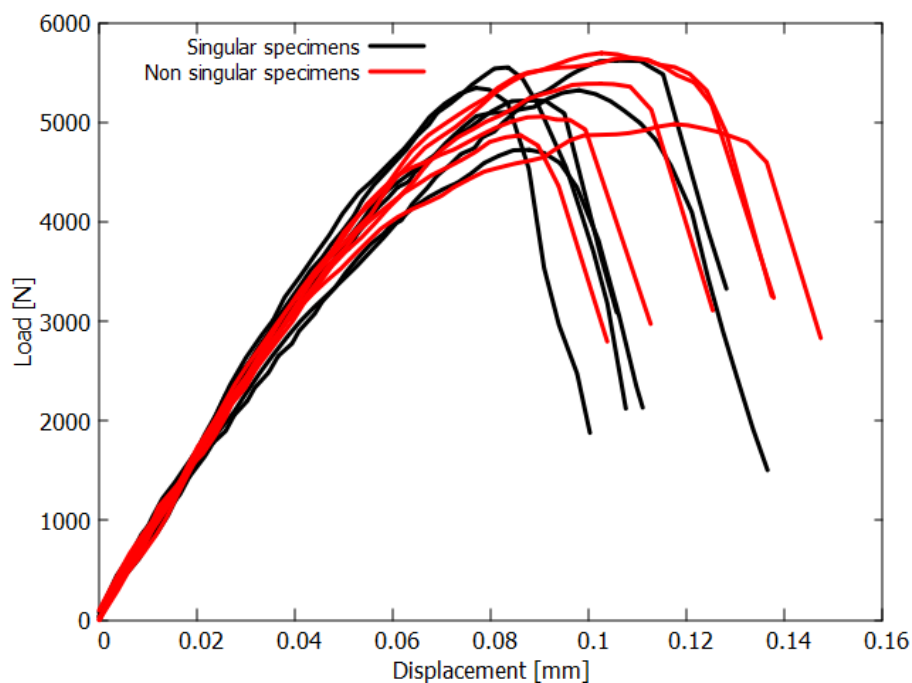


Figure 78: Singular and non-singular load-displacement curves.

3.7 VHCF tests

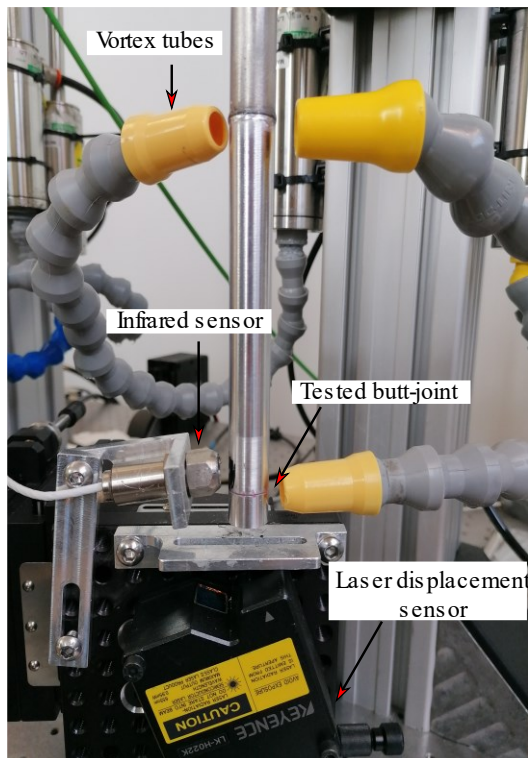
Testing specimens in the range of VHCF has been performed by using the Ultrasonic Fatigue Testing Machine (UFTM) that was designed at Politecnico di Torino (Section 2.2 , Figure 22) for this specific purpose.

The prepared adhesive joint was mechanically attached to the horn device which transmits the vibration excitation from the UFTM to the specimen under testing.

Twenty-eight coupons were tested in the stress range [10 – 19] MPa, with an $R = -1$ tension-compression loading ratio, aiming at comparing the mechanical performances among singular and non-singular joints. The selected stress range can produce only linear mechanical responses, as verified from testing the bulk adhesive material and coupons through preliminary static experiments, thus the effects of plasticity do not influence the final test outcomes.

The UFTM equipment requires specific input calibrations/verification before performing each single test such as, temperature verification interval, correct spacing between the coupon and the vortex tubes, definition of the run-out number of cycles (10^9) and, most important, the correct definition of the input displacement at the horn base to reach the desired stress level. A simple linear model was adopted to correlate the stress level to be adopted during test (known from FE modelling) and the input displacement to adopt.

In Figure 79 (a), (b) the singular and the non-singular specimen are depicted.



(a)



(b)

Figure 79: Singular (a) and non-singular (b) setups during VHCF tests.
Original from [215]

Testing coupons permitted to populate the stress – number of cycle (S-N) curve. Experimental S-N outcomes are reported in Figure 80 where adhesive-mixed-cohesive (i.e., yellow dots), cohesive failures (i.e., blue dots), and run-out (i.e., blue diamonds) have been observed for non-singular coupons. Conversely, singular joints have not experienced significant adhesive contribution to final failures but almost fully cohesive failures (i.e., red dots), and run-out (i.e., red diamonds) only.

In order to select effective failures among adhesive-mixed-cohesive ruptures for non-singular joints, a heuristic criterion based on the occupied area was adopted. It has been experimentally observed that adhesive-mixed-cohesive failures with about (or less) the 20% of adhesive detachments presented a fatigue life close to the one associated to a purely failed cohesive specimen. Moreover, at fixed applied load, the visual inspection of the S-N plot suggests that fatigue performances reduce as the adhesive area increases. Thus, the threshold of 20% was adopted as a separation criterion. Essentially, failures presenting up to the 20% of adhesive detachments were considered as valid and comparable to the

fully cohesive ruptures. Conversely, specimens with higher adhesive separations were treated as fully adhesive. To the sake of precision, the yellow dots in Figure 80 are associated to higher to 15% adhesive separations thus considered as totally adhesive.

Non-singular joints exhibited much higher fatigue performances, especially in the range [13 – 15] MPa where run-out ($N = 10^9$) have been collected, with respect to singular coupon that failed in the range of 10^7 cycles at the same stress level. Even if a sufficient run-out population was collected between [14 – 15] MPa, to approach a possible VHCF limit carefully, 13 MPa was considered the worst-case scenario.

Regarding the singular coupons, these started showing run-out in the range of 11 MPa, thus with a significantly reduced capability of sustain loads .

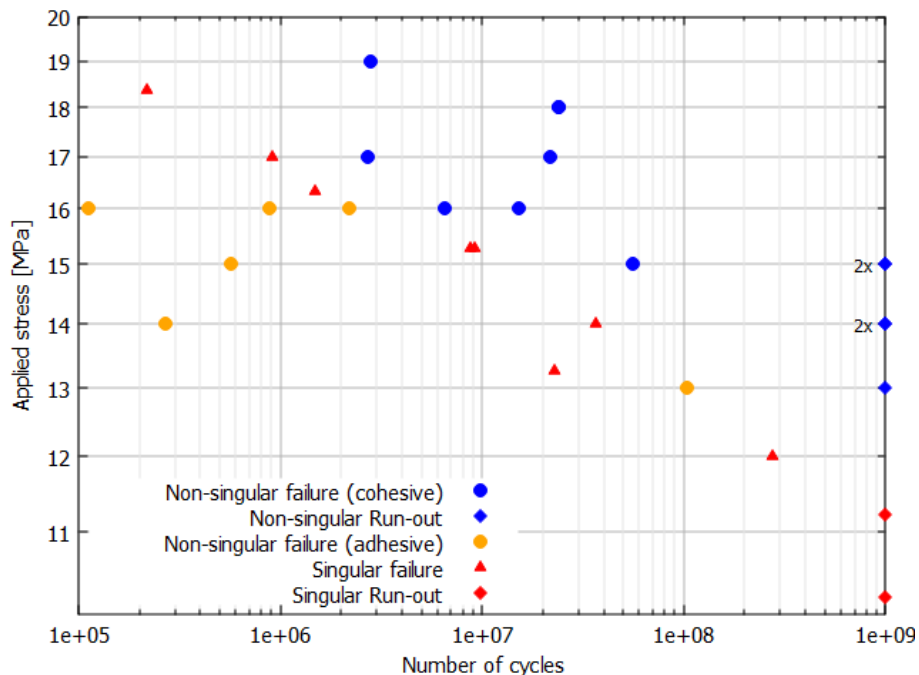


Figure 80: S-N raw data after failures or run-out. Original from [215]

The fracture surfaces of the non-singular specimens that failed cohesively are illustrated in Figure 81 where σ_a is the applied stress. Particularly, two separated regions can be identified and observed from failed coupons of Figure 81(a-c):

1. *Steady propagation*: in this area the adhesive undergoes to progressive cohesive detachments. Typically, this region can be recognized as the darker and its extension is related to the specimen cross area that

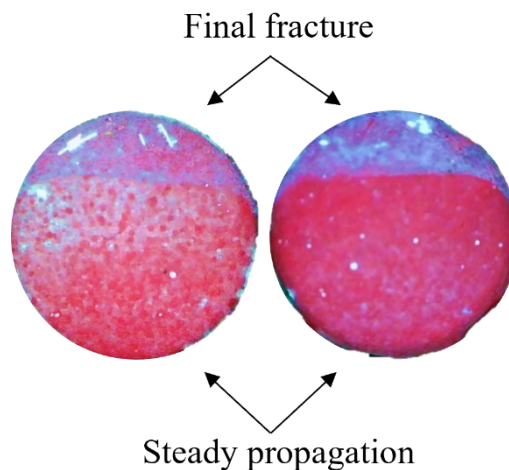
guarantees the fulfilment of the UFTM frequency requirement (i.e., the fundamental frequency is higher than 19500 Hz).

2. *Final fracture*: in this area the fracture progresses in an un-stable way and it can be recognized as it presents lighter colours.

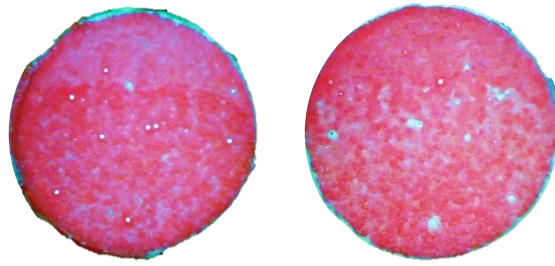
From a visual inspection, it was impossible to recognize a crack nucleation region/point (as opposite of other materials) but, surely, the external edges were not affected by nucleation mechanisms since these last were not mechanically corrupted with degradations or partial adhesive detachments that could have suggested the presence of a trigger point. Thus, wherever present, the initial damage mechanism is included in the internal parts of the steady propagation.

The absence of a clear and well-defined crack nucleation region was probably induced by the presence of glass spheres that were adopted to guarantee the uniform thickness of 0.3 mm. In fact, the steady propagation region looks like a uniformly distributed damaged area.

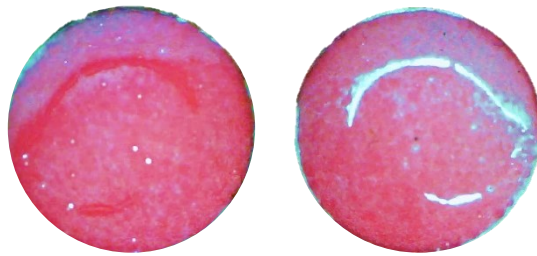
The final fracture region also presents interesting aspects. Precisely, the size remains almost constant even if the load increases. Nonetheless, it becomes less recognisable as the applied load decreases.



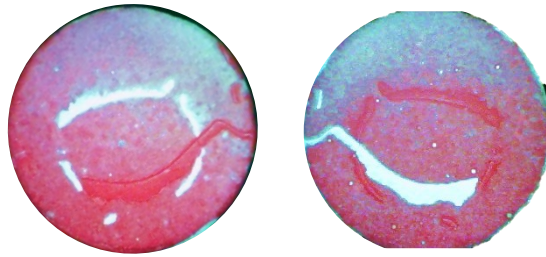
(a) $\sigma_a = 19 \text{ MPa}$



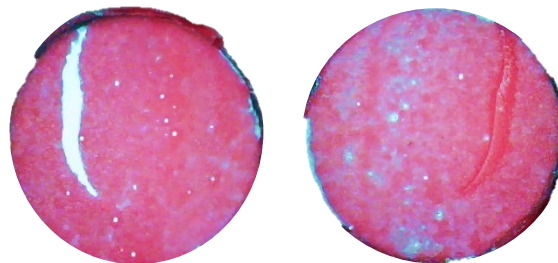
(b) $\sigma_a = 17 \text{ MPa}$



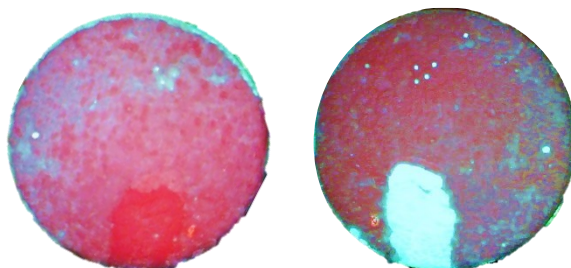
(c) $\sigma_a = 15 \text{ MPa}$



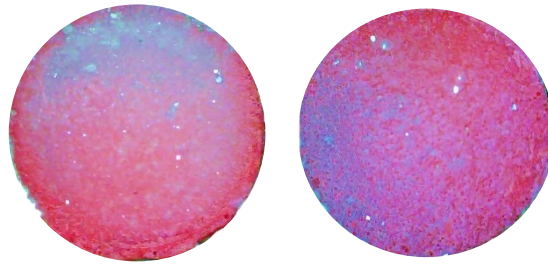
(d) $\sigma_a = 13 \text{ MPa}$ (run-out), $\sigma_a = 18 \text{ MPa}$



(e) $\sigma_a = 14 \text{ MPa}$ (run-out), $\sigma_a = 16 \text{ MPa}$



(f) $\sigma_a = 15 \text{ MPa}$ (run-out), $\sigma_a = 17 \text{ MPa}$

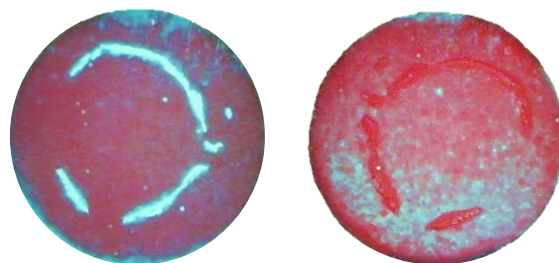


(g) $\sigma_a = 15 \text{ MPa}$ (run-out), $\sigma_a = 16 \text{ MPa}$

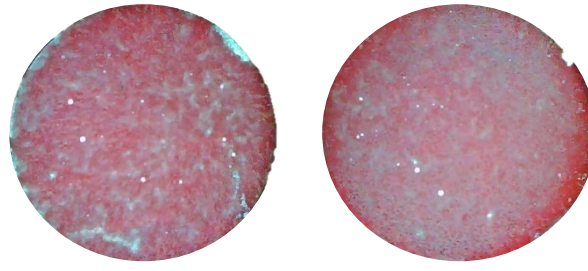
Figure 81: Fracture surfaces of non-singular specimens.

Conversely, fracture surfaces in Figure 81 (d-f) were tested under the 13 – 15 MPa stress levels, respectively, which were non-critical for the joint. Then, since the specimens have shown a run-out (theoretically, an infinite life at that stress level), it was re-tested to a higher stress level, 16 – 18 MPa respectively, without removing the adhesive layer. Highly likely, specimens without a previous test history (i.e., the new one for each applied stress level) that fail till a finite N -cycles (Figure 81(a-c)), are prone to show a clear distinction between the steady propagation and the final fracture regions compared to those that are re-tested after run-out.

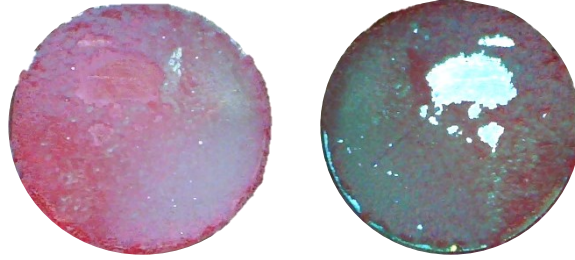
Fracture surfaces of singular specimens (the clearest that have been observed), are reported in Figure 82. These specimens, despite the presence of the singularity, do not present a distinguishable steady propagation region with respect to the final fracture area and the nucleation area/point. However, they show the highest damages/degradations in correspondence to the specimen edge, as expected as the outer region is the most critical and the weakest.



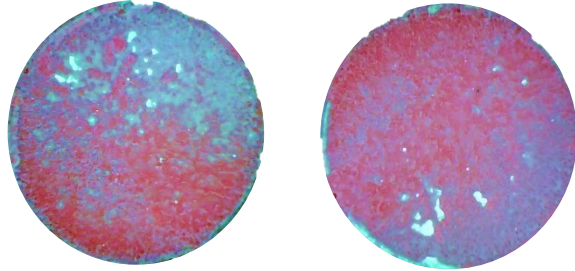
(a) $\sigma_a = 18.5 \text{ MPa}$



(b) $\sigma_a = 17 \text{ MPa}$



(c) $\sigma_a = 11 \text{ MPa}$ (run-out), $\sigma_a = 13 \text{ MPa}$



(d) $\sigma_a = 10 \text{ MPa}$ (run-out) $\sigma_a = 12 \text{ MPa}$

Figure 82: Fracture surfaces of singular specimens.

The final investigation related to the VHCF outcomes pertains the estimation of probability-stress-number of cycles (P-S-N) curves. The use of a probabilistic approach permitted to take into account the statistical distribution of the experimental data aiming at quantifying the contribution of the data scattering to the fatigue curve. To do so, the statistical approach based on the Maximum Likelihood Principle, described in Section 2.3 and recalled in short in the following, was adopted. The methodology requires the maximization of the Likelihood function reported in Eq.(3.7.1).

$$L[\boldsymbol{\theta}] = \prod_{i=1}^{n_f} f_{Y|X=x}[y_i; x_i, \boldsymbol{\theta}] \cdot \prod_{j=1}^{n_r} (1 - F_{Y|X=x}[y_j; x_j, \boldsymbol{\theta}]) \quad \text{Eq.(3.7.1)}$$

where θ is a set of parameters to be estimated, n_f the number of failures, n_r the number of run-out data, $f_{Y|X=x}$ the probability density function of the fatigue life, $F_{Y|X=x}$ the cumulative distribution function and y_i the fatigue life of the i -th specimen. The mathematical framework also assumes that the logarithm of the fatigue life follows a Gaussian distribution with a constant standard deviation and the mean dependent on the logarithmic applied stress amplitude as reported in Eq.(3.7.2)

$$\mu_Y(x) = c_Y + m_Y \cdot x \quad \text{Eq.(3.7.2)}$$

where x is the logarithm of the applied stress amplitude, $\mu_Y(x)$ the logarithm of the fatigue life, c_Y and m_Y are constant coefficients that must be determined case by case.

Numerically, the optimization Nelder–Mead simplex algorithm was adopted to maximize $L[\theta]$ thus identifying the parameters of interest.

In Figure 83 the S-N curves have been extracted for three probability levels namely $P=10\%$, $P=50\%$ (i.e., the average) and $P=90\%$. The calculation considered only the specimens that failed cohesively as well as the run-out.

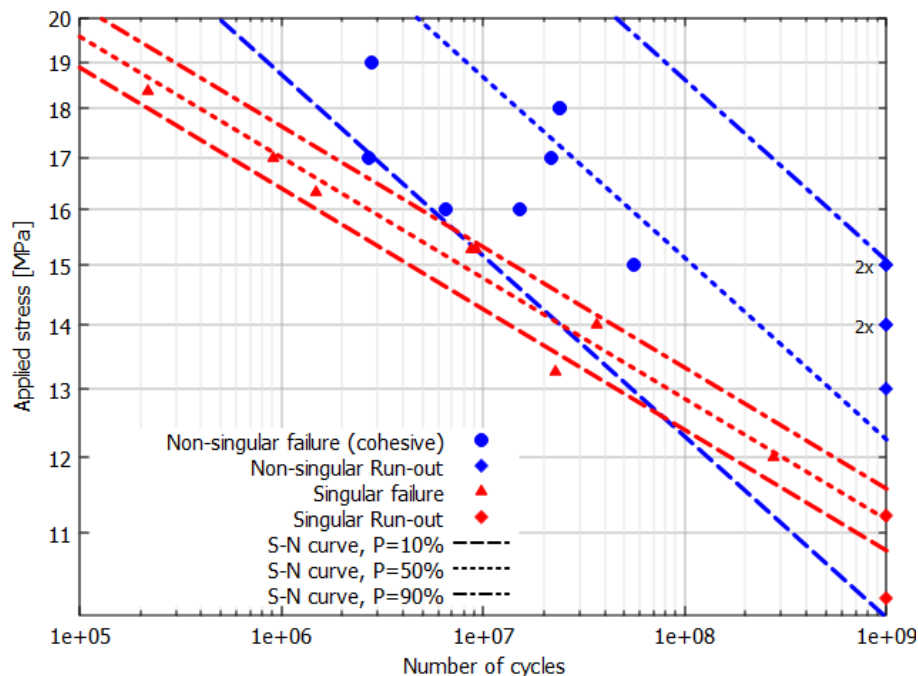


Figure 83: P-S-N curves for singular and non-singular cohesive failures. Original from [215]

Referring to the average S-N curve, non-singular specimens showed enhanced mechanical performance with respect to singular specimens, as expected. This was confirmed by an upwards shifted curve and is much more evident for the 90% probability curve. Conversely, at 10% of probability, there is an unexpected and unforeseen reduced performance that leads to the intersection between the non-singular curve and those related to the singular specimens. This phenomenon is clearly induced by the wide scatter band of non-singular failures. However, it has been quite difficult to identify the fundamental source, or a reasonably possible cause, of this distribution. Especially, when it is compared to the one of singular specimens that is very tidy with a narrow scatter. The two different distributions could have been affected by the following reason: non-singular joint is, potentially, much more sensitive compared to the singular ones. Manufacturing imperfections could jeopardize the adhesion properties at the specimen edge, thus provoking localized adhesive detachments, as visible in Figure 81(d-f). This can lead to the loss of the appropriate local adhesion properties and, in general, the joint load-bearing capability. Even though this aspect could be perceived as a weakness for non-singular joint technology, it should be seen in the framework of a manual-executed manufacturing. In fact, as an example, during the joint preparation, some passages of abrasive paper should be performed in order to increase the substrate adhesion characteristics. However, no control was possible to adopt on the applied manual force or, similarly, if some regions of the specimen would have been more subjected to the abrasion, the experimentalist was not aware of this. Indeed, the production phase was totally carried out based on the experimentalist manual skills and experience. Moreover, manufacturing effects are more pronounced on non-singular coupons due to the absence of the stress-singularity itself that is the most visible and the principal source of failures. In other words, manufacturing effects could be present in both classes of specimens, nevertheless they have a much lower importance for singular joints where the failure is totally governed by the presence of the singularity that, in terms of statistical distribution, produced narrower bands. Conversely, since non-singular joints can express the real material behaviour due to the absence of the stress-singularity, the uncontrollability of the manufacturing can introduce localized defects randomly, or surficial issues, that are expressed in wider scatter bands in terms of fatigue life and S-N curves.

From a practical perspective, the use of automatized and controlled machines, suitably developed for this scope, should be able to guarantee a common level of repeatability among specimens and bonded structures thus reducing the data variability introduced by manual operations.

3.8 Assessing loading-frequency behaviours

Assessing loading-frequency behaviours of cylindrical adhesive butt-joints was performed under the joint best conditions (i.e., non-singular specimens) as this configuration demonstrated the absence of features that can affect the correct material properties extraction. For doing this the full specimen re-design was not necessary. However, since the boundary conditions imposed by the adopted testing machine for conventional fatigue experiments (i.e., Instron® 8801 servo-hydraulic) differ from the boundary conditions applied by the UFTM for VHCF test, it was anyhow necessary to perform the FRA investigations with respect to the application of quasi-static loads to ascertain the current stress field. Indeed, the use of static analysis is justified by the fact that the frequency content of the load is negligible compared to the first natural frequency of the specimen.

Essentially, the same passages for producing the numerical model for the VHCF specimens were executed: from a representative Global model which accounts for the global structural behaviours under current boundary conditions (see Figure 86), to a refined Local description for assessing detailed stress features. For accelerating the modelling and the analysis phases, the Local non-singular model developed for the VHCF prediction, reported in Figure 59, was refurbished while changing the magnitude of applied local displacements. The numerical assessments have been performed by considering a quasi-static approach: since the natural frequencies of the specimen are in the range of thousands of Hz and traditional fatigue tests are executed in the range of tens of Hz, it seems reasonable to adopt such working hypothesis. Moreover, as illustrated in the following, fatigue tests will be performed at 5, 25, 50 Hz for assessing loading-frequency effects, thus very far from the first model resonance. As a result, in Figure 84 the extracted stress maps in the local model resulting from the application of current boundary conditions. An almost constant stress field of approximately 13 MPa was defined in most of the area of the specimen.

As the observation is closer to the adhesive-adherend external interface, there is a stress concentration. Even though the map was limited at 20 MPa for visibility, the grey region in the curved throat stands for higher stresses as in the VHCF case.

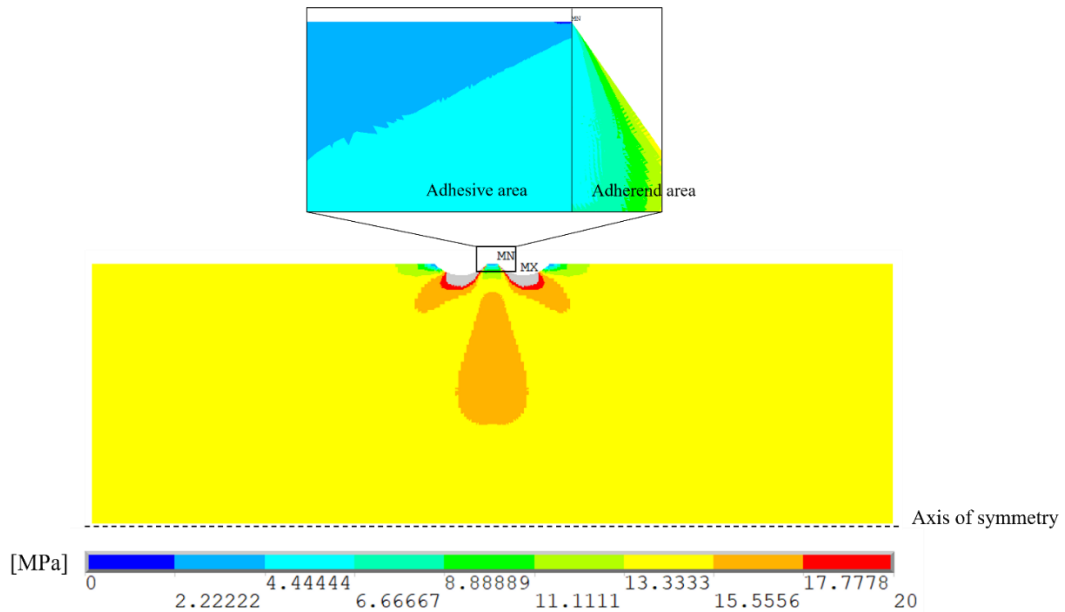


Figure 84: Longitudinal stress map resulting from a quasi-static loading condition. Original from [216]

The use of such quasi-static hypothesis requires the verification of stress distribution along the T-R directions of Figure 70. This comparison is fundamental for testing purposes in order to impose the correct loading levels during the low-frequency fatigue experiments. Thus, referring to the VHCF case as “dynamic case” and to the current investigation as “static case”, in Figure 85 (a)-(b) the longitudinal stress recovered along the T and R paths are depicted. Both case studies consider a nominal 15 MPa stress level in correspondence of the specimen axis for comparison purposes. It is evident that both loading conditions, if properly tuned in terms of external loads, can produce exactly equal internal stress components.

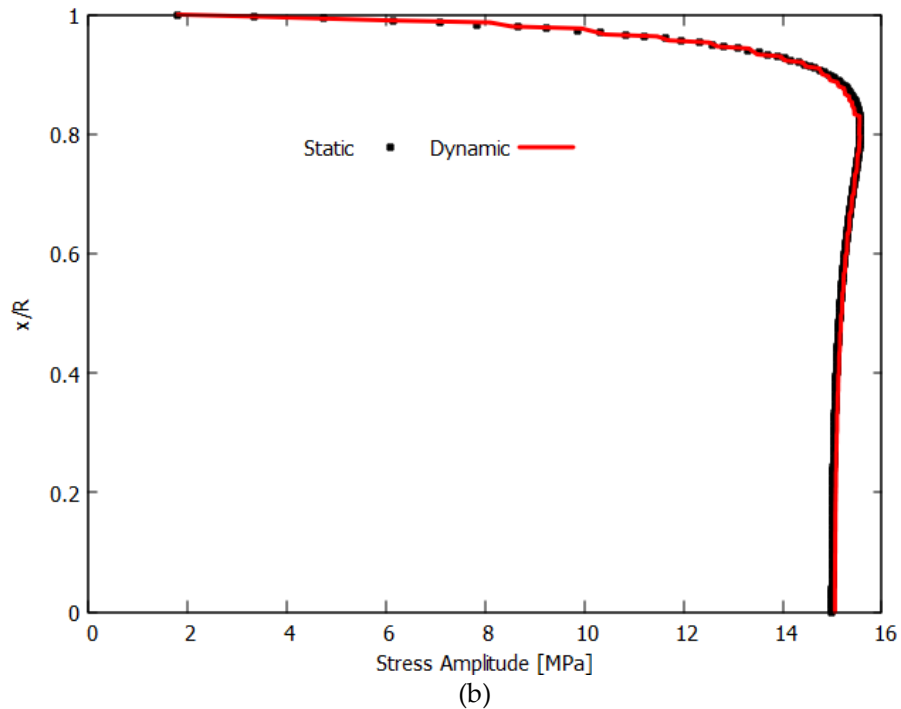
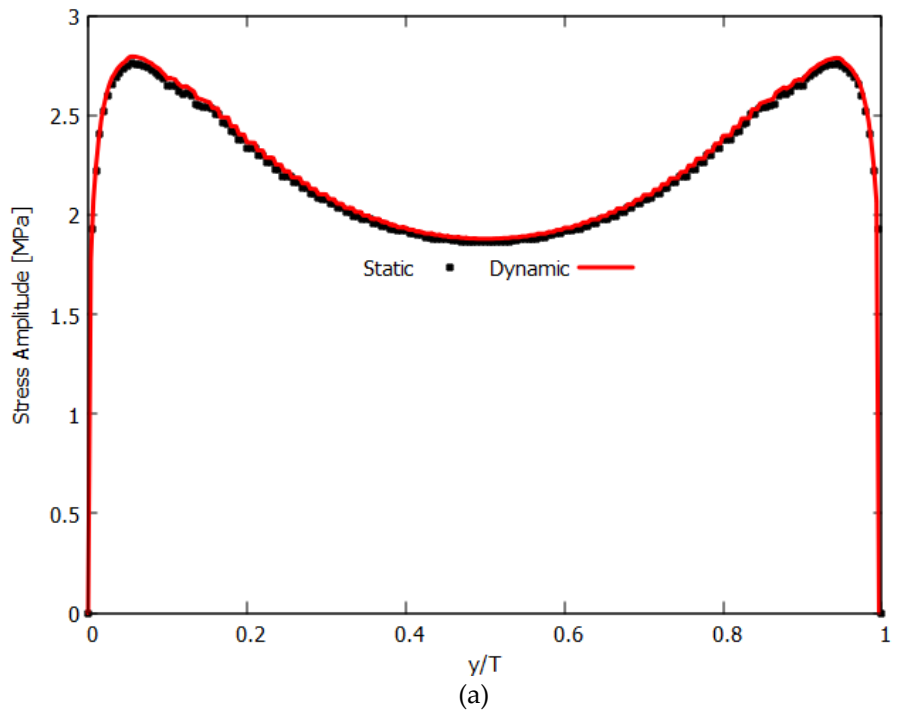


Figure 85: Recovered stress for the static and dynamic case. Original from [216]

Testing specimens required the joint manufacturing. This task was accomplished by exploiting the same manufacturing methodology developed in the case of VHCF samples but, in this case, by using the longer adherends only. Thirty-five specimens were produced and tested under 5, 25, 50 Hz produced via

the Instron® 8801 servo-hydraulic testing machine, depicted in Figure 86, with load control capabilities.

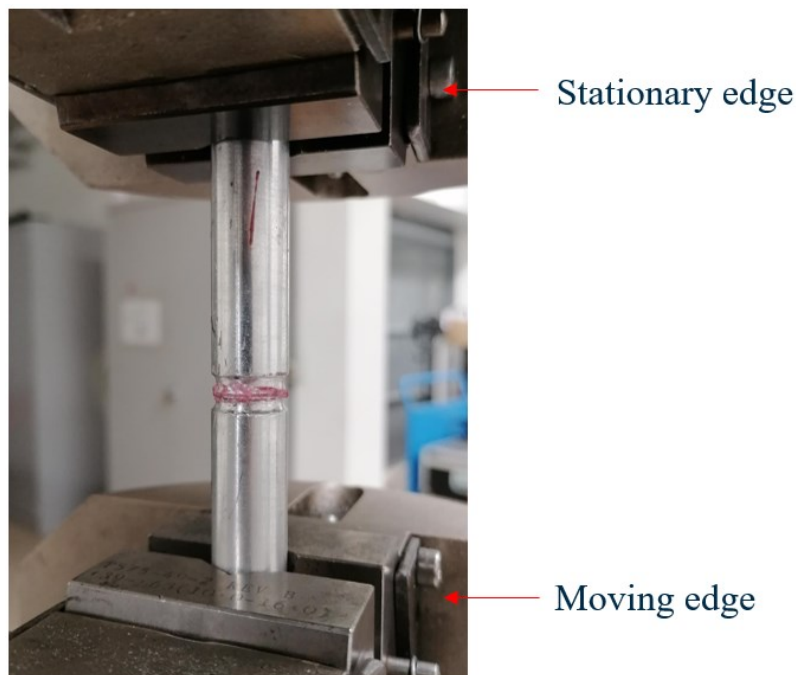


Figure 86: Boundary conditions derived from the testing configuration.

Experiments were performed between 10 – 17 MPa with a run-out threshold of $2 \cdot 10^6$ cycles as greater ranges would have been difficult to test in a reasonable time frame. In case of low-frequency fatigue tests the arrest criterion to stop the test was based on a load condition. Essentially, if the load magnitude during the sinusoidal wave dropped below the 50% of the initial external load, the coupon was considered failed and the test stopped. Such criterion was adopted to not damage the testing machine during the loading phase.

Performing such tests allowed the extracting S-N diagram as depicted in Figure 87. According to the comparative result with respect to VHCF data, the frequency-rate effect exists and is clearly highlighted. In fact, coupons under common fatigue tests failed in the High Cycle Fatigue (HCF) range, much before the VHCF data. HCF run outs were observed for the 25 and 50 Hz testing cases.

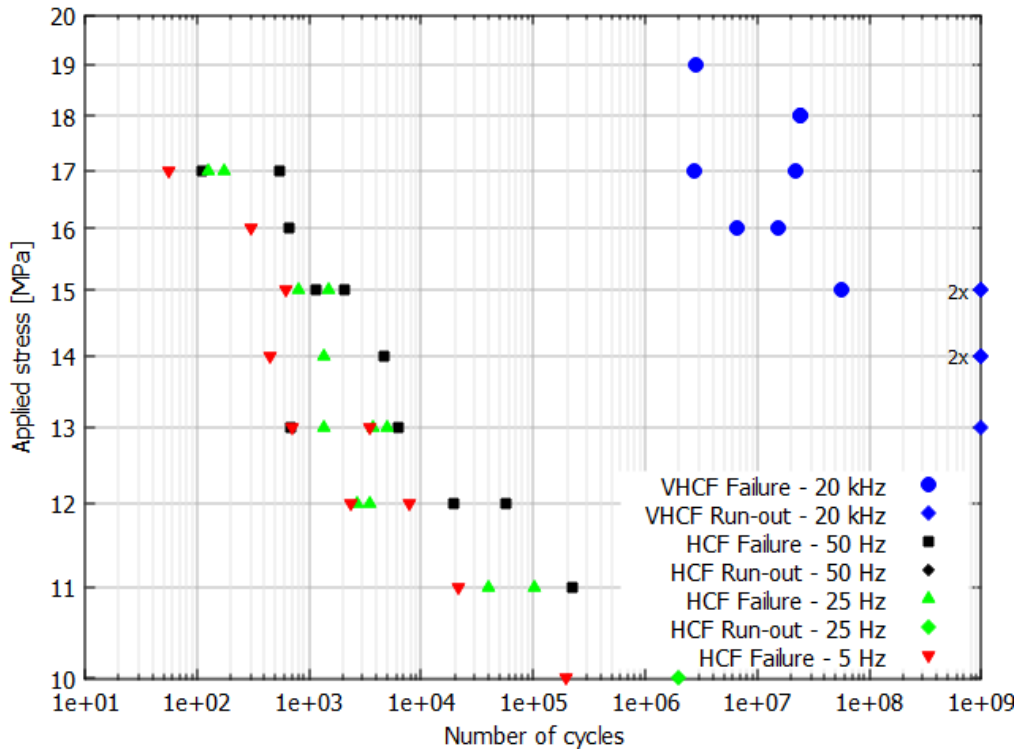


Figure 87: Loading-frequency S-N raw data after failures or run-out.

The precise evolution of the failure according to the increase of the applied testing frequency was assessed and explored through P – S – N curves already adopted in the case of VHCF test. Precisely, Eq.(3.7.1) was applied for the three applied loading frequencies and such results are illustrated in Figure 88 at P=50% in order to represent the averaged behaviours of tested specimens. P – S – N curves demonstrate the progressive enhancement of the joint endurance as the loading-frequency increases and this effect testifies the existence of a loading-rate effect for the specific case of SikaPower® 1277 adhesive.

Data scattering was associated with the analysis of the standard deviation (SD), which is reported in Table 7 for each applied frequency, both low-frequency and ultrasonic. In general, conventional fatigue tests are characterized by a lower variability as demonstrated by the maximum value of SD ≈ 0.58 at 25 Hz. This quantity increases up to ≈ 0.77 for VHCF. For completeness, even though the statistical variability is present and should be considered for real design applications, it has a very low impact on experimental results.

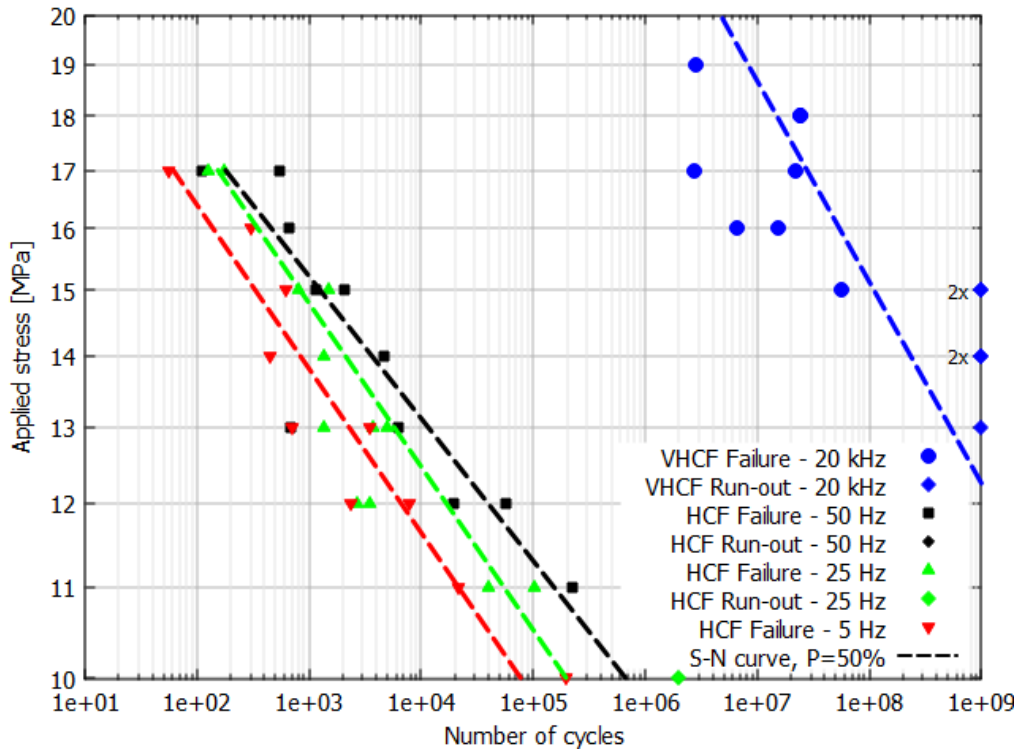


Figure 88: P-S-N curves at P=50% assessing loading-frequency effects between VHCF and conventional fatigue tests. Original from [216]

	Failures at 5 Hz	Failures at 25 Hz	Failures at 50 Hz	Failures at 20 kHz
Standard Deviation (SD)	0.3038	0.5763	0.4687	0.7691

Table 7: Standard deviation form processed data with ML and optimization.

The HCF threshold (i.e., $N=2 \cdot 10^6$) was adopted for investigating the strength distribution at the investigated frequencies for the adopted probability levels 10%, 50% and 90%. Fatigue data of both HCF and VHCF were interpolated by using a power-law model as in Eq. (3.8.1)

$$\sigma = A \cdot f^b \quad \text{Eq. (3.8.1)}$$

where σ is the experimental fatigue strength, the applied test frequency whereas A and b are the model parameters to be determined in the regression scheme. Precisely, the regression adopted the least-square method and such calculation was accomplished in a simple Excel® spreadsheet. Raw and interpolated data are presented in Figure 89. The power-law reasonably

approximates the data set with an R^2 factor higher than 0.995 for all the cases. This observation that combines both experimental data and analytical calculations would be particularly useful for extracting material parameters out of the available experimental range. In fact, the analytical model of a power-law is a good approximation of data in the selected frequency range. Moreover, it was evident that, at fixed applied external load, the sustainable number of cycles to reach the final failure increased linearly in a bi-logarithmic chart and this effect confirmed the presence of frequency-rate effects. Obviously, a more robust interpolation should consider more data, especially in the missing frequency region between ≈ 100 Hz and ≈ 10000 . However, this assessment had the potential to extrapolate the strength trend to be adopted for adhesive applications.

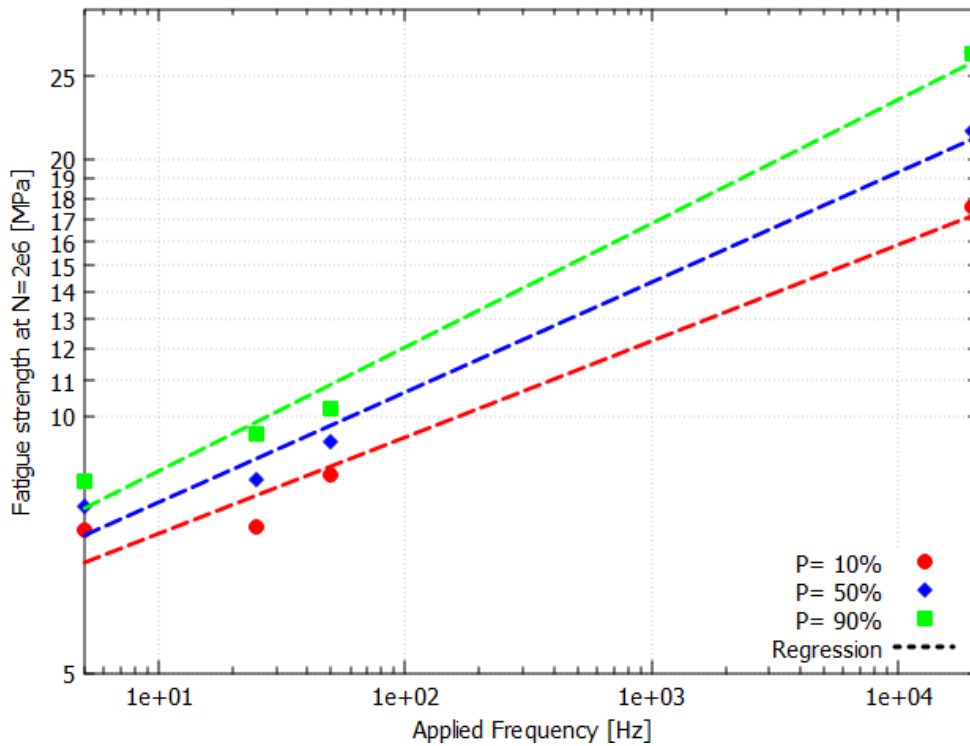


Figure 89: Strength distribution for 10%, 50%, 90% probability levels at $N=2 \cdot 10^6$ cycles. Original from [216]

4 Conclusions

The work performed in this thesis explored the adhesive joint performances under fatigue loading conditions. Two main aspects were the research object: *i*) the understanding and quantifying of the influence of the stress singularity in Very High Cycle Fatigue (VHCF) range originating between aluminium 7075 T6 substrates and thin layers of SikaPower® 1277 epoxy resin; *ii*) the quantifying of the presence of loading-frequency effects when specimens subjected to low and very high frequency excitations.

To do so, combined analytical, numerical and experimental techniques were adopted to reach the research purposes. Precisely, analytical models based on 1D vibrating structures have been successfully employed for designing the VCHF specimen whereas the inverse Bogy approach defined the geometrical conditions to remove the stress-singularity. Numerical methods based on the Finite Element (FE) Submodelling technique investigated the stress responses of designed specimens in a precise and detailed manner. Experimental fatigue testing techniques, such as the use of Ultrasonic Fatigue Testing Machine (UFTM) and conventional hydraulic testing machines (i.e., Instron®), explored the VHCF and the HCF fatigue responses.

The following general analytical conclusions can be drawn:

- The use of the inverse Bogy approach was successfully implemented in the workflow to investigate geometrical modifications (or mechanical, if necessary) that remove the stress singularity. For the specific problem of interest, two adhesive-adherend boundary configurations have been identified as possible ideal candidate namely 43.5° - 90° in plane strain and 48.2° - 90° in plane stress;
- The extended use of such approach allows the definition of real design maps and this aspect is particularly useful for real design applications;
- Attention should be given to modelling aspects when dealing with such maps. Three well separated region could be foreseen with specific safety/non-safety design consequences.

Numerical considerations:

- The use of Global-Local FE models permitted both the achievement of a suitable specimen for ultrasonic and low frequency fatigue testing and the detailed stress investigation as well;
- The application of the Global-Local technique allowed ad-hoc and precise mesh developments capable of capturing the correct behaviour of structural features of interest such as the singular and the non-singular stress trends;
- A manual FE optimization of the edge angle that interfaces with the adhesive layer guided the selection of the most suitable test configuration starting from the reference configuration arising from the inverse Bogy approach. A testing configuration of 35° - 90° was thus selected as optimal to reach the design capabilities and the experimental purposes.

Experimental considerations:

- UFTM working at 20 kHz can easily assess the VHCF range with a reasonable time frame thus permitting an extensive test campaign which can explore failure up to $N=10^9$ cycles;
- Tested joints in VHCF presented cohesive, adhesive and mixed failure for both singular and non-singular and the type of failure mostly depended on the quality of the manufacturing as this process was entirely performed manually;
- Only cohesive and mixed failures, with less than 20% of adhesive detachments, were considered as valid for estimating the S-N curves. Raw failure data showed that removing the stress singularity can produce enhanced fatigue lives compared to original singular specimens. In fact, at a fixed applied load, non-singular joints exhibited run-out data or much more life cycles;
- Statistical aspects were investigated through a specific fatigue model, whose parameters have been estimated by applying the maximum likelihood method. The application of this model permitted the proper

identification of Probability – Stress – Number of cycles (P – S – N) curves. These last revealed a wider scatter band for non-singular specimens compared to the original one. The reason behind this phenomenon relies on the major influence of manufacturing effects on non-singular joints with respect to singulars. Indeed, the tidy distribution of singular joints in the S-N plot comes from the presence of the singularity that is the first-order failure mode for such joint type;

- Loading-frequency effects were explored by using non-singular specimens without a re-design. An Instron® hydraulic testing machine was employed to assess this behaviour and joints were tested at 5, 25 and 50 Hz. Raw data clearly highlighted the presence of a loading-rate effect for the adhesive under analysis. In fact, a fixed applied alternated load, up to 5 orders of magnitude separates the fatigue life obtained at conventional frequencies and at ultrasonic frequencies;
- P – S – N curves depicted for a probability level of 50% highlighted the progressive increment of the averaged S-N curve as the frequency increases. Deviations from the data average were investigated through the Standard Deviation (SD). In general, this parameter has a low value namely SD max. ≈ 0.58 for a low-frequency testing method and SD ≈ 0.77 for an ultrasonic testing one.
- A power-law model defined for strengths at $N=2 \cdot 10^6$ was exploited to extract a stress trend across the adopted testing frequencies. This model satisfactorily approximated the stress data with an $R^2=0.995$.

Bibliography

- [1] J. Seo, I. Amatya, T. Letcher, E. Jeong, Welding versus adhesive bonding strength investigation, *Eng. Fail. Anal.* 129 (2021) 105664. <https://doi.org/10.1016/j.engfailanal.2021.105664>.
- [2] J. Antelo, A. Akhavan-Safar, R.J.. Carbas, E.A.. Marques, R. Goyal, L.F.M. da Silva, Replacing welding with adhesive bonding: An industrial case study, *Int. J. Adhes. Adhes.* 113 (2022) 103064. <https://doi.org/10.1016/j.ijadhadh.2021.103064>.
- [3] L.F.M. da Silva, R.D. Adams, Techniques to reduce the peel stresses in adhesive joints with composites, *Int. J. Adhes. Adhes.* 27 (2007) 227–235. <https://doi.org/10.1016/j.ijadhadh.2006.04.001>.
- [4] G. Scarselli, C. Corcione, F. Nicassio, A. Maffezzoli, Adhesive joints with improved mechanical properties for aerospace applications, *Int. J. Adhes. Adhes.* 75 (2017) 174–180. <https://doi.org/10.1016/j.ijadhadh.2017.03.012>.
- [5] M.K. Ben-larbi, R. Hensel, G. Atzeni, E. Arzt, E. Stoll, Orbital debris removal using micropatterned dry adhesives : Review and advances, *Prog. Aerosp. Sci.* 134 (2022) 100850. <https://doi.org/10.1016/j.paerosci.2022.100850>.
- [6] O. Volkersen, Die Nietkraftverteilung in Zugbeanspruchten Nietverbindungen mit Konstanten Laschenquerschnitten. (The rivet load distribution in lap joints with members of constant thickness subjected to tension), *Luftfahrtforschung.* 15 (1938) 41–47.
- [7] M. Goland, E. Reissner, Stresses in cemented joints, *J. Appl. Mech.* (1944) 17–27.
- [8] L.J. Hart-Smith, Adhesive-bonded double-lap joints, 3855 Lakewood Blvd,

Long Beach, California, 1973.

- [9] F. Delale, F. Erdogan, M.N. Aydinoglu, Stresses in adhesively bonded joints: a closed-form solution, *J. Compos. Mater.* 15 (1981) 249–271. <https://doi.org/10.1177/002199838101500305>.
- [10] L. Goglio, M. Rossetto, Evaluation of the Singular Stresses in Adhesive Joints, *J. Adhes. Sci. Technol.* 4243 (2009). <https://doi.org/10.1163/156856109X433018>.
- [11] D.B. Bogy, K.C. Wang, Stress singularities at interface corners in bonded dissimilar isotropic elastic materials, *Int. J. Solids Struct.* 7 (1971) 993–1005. [https://doi.org/10.1016/0020-7683\(71\)90077-1](https://doi.org/10.1016/0020-7683(71)90077-1).
- [12] P.A. Kelly, D.A. Hills, D. Nowell, The design of joints between elastically dissimilar components, *J. Strain Anal.* 27 (1992) 4525–4528.
- [13] S.E. Benzley, Representation of singularities with isoparametric Finite Elements, *Int. J. Numer. Methods Eng.* 8 (1974) 537–545.
- [14] L. Goglio, M. Rossetto, Stress intensity factor in bonded joints: Influence of the geometry, *Int. J. Adhes. Adhes.* 30 (2010) 313–321. <https://doi.org/10.1016/j.ijadhadh.2009.12.008>.
- [15] A.K. Noor, Global-local methodologies and their application to nonlinear analysis, *Finite Elem. Anal. Des.* 2 (1986) 333–346. [https://doi.org/10.1016/0168-874X\(86\)90020-X](https://doi.org/10.1016/0168-874X(86)90020-X).
- [16] Z. Wu, Design free of stress singularities for bi-material components, 65 (2004) 339–345. <https://doi.org/10.1016/j.compstruct.2003.11.009>.
- [17] Z. Wu, A method for eliminating the effect of 3-D bi-material interface corner geometries on stress singularity, 73 (2006) 953–962. <https://doi.org/10.1016/j.engfracmech.2005.10.010>.
- [18] I. Marines, X. Bin, C. Bathias, An understanding of very high cycle fatigue of metals, *Int. J. Eng. Sci.* 25 (2003) 1101–1107. [https://doi.org/10.1016/S0142-1123\(03\)00147-6](https://doi.org/10.1016/S0142-1123(03)00147-6).
- [19] M. Zimmermann, Very High Cycle Fatigue, in: *Handb. Mech. Mater.*, 2020: pp. 1–38. https://doi.org/doi.org/10.1007/978-981-10-6855-3_43-1.
- [20] A. Tridello, D.S. Paolino, G. Chiandussi, L. Goglio, An innovative testing

- technique for assessing the VHCF response of adhesively bonded joints, *Fatigue Fract. Eng. Mater. Struct.* 42 (2019) 84–96. <https://doi.org/10.1111/ffe.12874>.
- [21] A. Tridello, R. Ciardiello, D.S. Paolino, D.S. Paolino, Fatigue response up to 10E9 cycles of a structural epoxy adhesive, *Fatigue Fract. Eng. Mater. Struct.* (2020) 1–12. <https://doi.org/10.1111/ffe.13240>.
- [22] D.S. Paolino, G. Chiandussi, M. Rossetto, A unified statistical model for S-N fatigue curves: probabilistic definition, *Fatigue Fract. Eng. Mater. Struct.* 36 (2013) 187–201. <https://doi.org/10.1111/j.1460-2695.2012.01711.x>.
- [23] L. Goglio, L. Peroni, M. Peroni, M. Rossetto, High strain-rate compression and tension behaviour of an epoxy bi-component adhesive, *Int. J. Adhes. Adhes.* 28 (2008) 329–339. <https://doi.org/10.1016/j.ijadhadh.2007.08.004>.
- [24] S. Wang, W. Liang, L. Duan, G. Li, J. Cui, Effects of loading rates on mechanical property and failure behavior of single-lap adhesive joints with carbon fiber reinforced plastics and aluminum alloys, *Int. J. Adv. Manuf. Technol.* 106 (2020) 2569–2581. <https://doi.org/10.1007/s00170-019-04804-w>.
- [25] S. Wu, *Polymer Interface and Adhesion*, New York, 1982. <https://doi.org/10.1201/9780203742860>.
- [26] P.P.A. Mazza, F. Martini, B. Sala, M. Magi, M.P. Colombini, G. Giachi, F. Landucci, C. Lemorini, F. Modugno, E. Ribechini, A new Palaeolithic discovery: tar-hafted stone tools in a European Mid-Pleistocene bone-bearing bed, *J. Archaeol. Sci.* 33 (2006) 1310–1318.
- [27] G. Langejans, A. Aleo, S. Fajardo, P. Kozowyk, *Archaeological Adhesives*, Oxford Res. Encycl. Anthropol. (2022). <https://doi.org/https://doi.org/10.1093/acrefore/9780190854584.013.198>.
- [28] K.L. Mittal, A. Pizzi, *Handbook of Adhesive Technology*, New Yoirk, 2003.
- [29] P.A. Fay, A historical review of animal entrapment using adhesives, *Int. J. Adhes. Adhes.* 114 (2022) 103083. <https://doi.org/10.1016/j.ijadhadh.2021.103083>.

- [30] A. Higgins, Adhesive bonding of aircraft structures, *Int. J. Adhes. Adhes.* 20 (2000) 367–376. [https://doi.org/10.1016/S0143-7496\(00\)00006-3](https://doi.org/10.1016/S0143-7496(00)00006-3).
- [31] L.F.M. da Silva, A. Ochsener, D.R. Adams, Handbook of Adhesion Technology, Aerospace industry, in: *Handb. Adhes. Technol.*, Heidelberg, Springer-Verlag Berlin, 2011. https://doi.org/0.1007/978-3-642-01169-6_45.
- [32] S. Budhe, M.D. Banea, S. De Barros, Bonded repair of composite structures in aerospace application: a review on environmental issues, *Appl. Adhes. Sci.* 6 (2018) 1–27. <https://doi.org/10.1186/s40563-018-0104-5>.
- [33] M.D. Banea, M. Rosioara, R.J.C. Carbas, L.F.M. da Silva, Multi-material adhesive joints for automotive industry, *Compos. Part B.* 151 (2018) 71–77. <https://doi.org/10.1016/j.compositesb.2018.06.009>.
- [34] V.S. Balakrishnan, H. Seidlitz, Potential repair techniques for automotive composites: A review, *Compos. Part B.* 145 (2018) 28–38. <https://doi.org/10.1016/j.compositesb.2018.03.016>.
- [35] D.R. Speth, Y.P. Yang, G.W. Ritter, Qualification of adhesives for marine composite-to-steel applications, *Int. J. Adhes. Adhes.* 30 (2010) 55–62. <https://doi.org/10.1016/j.ijadhadh.2009.08.004>.
- [36] L. Fialho, J. Albuquerque, A.S. Pinho, A.M. Pereira, C. Monteiro, N. Olivera, S. Ferreira, M.C.L. Martins, Exploring innovative adhesive approaches to manage medical adhesive-related skin injuries (MARSI), *Int. J. Adhes. Adhes.* 130 (2024) 103636. <https://doi.org/10.1016/j.ijadhadh.2024.103636>.
- [37] M. Arandjelović, A. Petrović, D. Đorđević, S. Sedmak, A. Sedmak, S. Dikić, D. Radu, Effects of Multiple Defects on Welded Joint Behaviour under the Uniaxial Tensile Loading: Fem and Experimental Approach, *Sustainability.* 15 (2023) 761. <https://doi.org/https://doi.org/10.3390/su15010761>.
- [38] A. Chiocca, F. Frenzo, F. Aiello, L. Bertini, Influence of residual stresses on the fatigue life of welded joints. Numerical simulation and experimental tests, *Int. J. Fatigue.* 162 (2022) 106901.

<https://doi.org/doi.org/10.1016/j.ijfatigue.2022.106901>.

- [39] T.N. Nguyen, M.A. Wahab, The effect of weld geometry and residual stresses on the fatigue of welded joints under combined loading, *J. Mater. Process. Technol.* 77 (1998) 201–208. [https://doi.org/10.1016/S0924-0136\(97\)00418-4](https://doi.org/10.1016/S0924-0136(97)00418-4).
- [40] T. Shiozaki, N. Yamaguchi, Y. Tamai, J. Hiramoto, K. Ogawa, Effect of weld toe geometry on fatigue life of lap fillet welded ultra-high strength steel joints, *Int. J. Fatigue.* 116 (2018) 409–420.
- [41] A.R. Shahani, I. Shakeri, C.D. Rans, Effect of residual stress redistribution and weld reinforcement geometry on fatigue crack growth of butt welded joints, *Int. J. Fatigue.* 139 (2020) 105780.
- [42] C.D.M. Liljedahl, O. Zanellato, M.E. Fitzpatrick, J. Lin, L. Edwards, The effect of weld residual stresses and their re-distribution with crack growth during fatigue under constant amplitude loading, *Int. J. Fatigue.* 32 (2010) 735–743. <https://doi.org/10.1016/j.ijfatigue.2009.10.012>.
- [43] T. Shi, Y. Liu, Z. Liu, C. Liu, Distributions of tension and torsion in a threaded connection, *Distrib. Tens. Torsion a Threaded Connect.* 261 (2024) 108684. <https://doi.org/10.1016/j.ijmecsci.2023.108684>.
- [44] N.G. Pai, D.P. Hess, Experimental study of loosening of threaded fasteners due to dynamic shear loads, *J. Sound Vib.* 253 (2002) 585–602. <https://doi.org/10.1006/jsvi.2001.4006>.
- [45] J. Liu, X. Mi, H. Hu, L. Long, Z. Cai, J. Peng, M. Zhu, Loosening behaviour of threaded fasteners under cyclic shear displacement, *Wear.* 460–461 (2020) 203453. <https://doi.org/10.1016/j.wear.2020.203453>.
- [46] Z. Cao, M.R.W. Brake, D. Zhang, The failure mechanisms of fasteners under multi-axial loading, *Eng. Fail. Anal.* 105 (2019) 708–726. <https://doi.org/10.1016/j.engfailanal.2019.06.100>.
- [47] H. Park, Effects of stacking sequence and clamping force on the bearing strengths of mechanically fastened joints in composite laminates, *Compos. Struct.* 53 (2001) 213–221. [https://doi.org/10.1016/S0263-8223\(01\)00005-8](https://doi.org/10.1016/S0263-8223(01)00005-8).

- [48] T. Qin, L. Zhao, J. Zhang, Fastener effects on mechanical behaviors of double-lap composite joints, *Compos. Struct.* 100 (2013) 413–423. <https://doi.org/10.1016/j.compstruct.2013.01.008>.
- [49] M.C. Serena Moreno, J.J. Lòpez Cela, J.L. Martínez Vicente, J.A. Gonzales Vecino, Adhesively bonded joints as a dissipative energy mechanism under impact loading, *Appl. Math. Model.* 39 (2015) 3496–3505. <https://doi.org/10.1016/j.apm.2014.11.052>.
- [50] T. Nonnenmann, R. Beygi, R.J.C. Carbas, L.F.M. da Silva, A. Öchsner, Synergetic effect of adhesive bonding and welding on fracture load in hybrid joints, *J. Adv. Join. Process.* 6 (2022) 100122. <https://doi.org/10.1016/j.jajp.2022.100122>.
- [51] R.B. Gilmore, S.J. Shaw, The effect of temperature and humidity on the fatigue behavior of composite bonded joints, *Compos. Bond. ASTM STP 1* (1974). <https://doi.org/10.1520/STP12917S>.
- [52] Y. Zhang, A.P. Vassilopoulos, T. Keller, Environmental effects on fatigue behavior of adhesively-bonded pultruded structural joints, *Compos. Sci. Technol.* 69 (2009) 1022–1028. <https://doi.org/10.1016/j.compscitech.2009.01.024>.
- [53] D. Borrie, H.B. Liu, X.L. Zhao, R.K. Singh Raman, Y. Bai, Bond durability of fatigued CFRP-steel double-lap joints pre-exposed to marine environment, *Compos. Struct.* 131 (2015) 799–809. <https://doi.org/10.1016/j.compstruct.2015.06.021>.
- [54] F. Castro Sousa, A. Akhavan-Safar, R.J.C. Carbas, E.A.S. Marques, A.Q. Barbosa, L.F.M. da Silva, Experimental study on the influence of environmental conditions on the fatigue behaviour of adhesive joints, 175 (2023). <https://doi.org/10.1016/j.ijfatigue.2023.107752>.
- [55] J. Pang, Y. Du, K. Wu, P. Hu, W. Li, Fatigue Analysis of Adhesive Joints Under Vibration Loading Vibration Loading, *J. Adhes.* 89 (2013) 899–920. <https://doi.org/10.1080/00218464.2013.764829>.
- [56] P.N.B. Reis, J.F.R. Monteiro, A.M. Pereira, J.A.M. Ferreira, J.D.M. Costa, Fatigue behaviour of epoxy-steel single lap joints under variable frequency, *Int. J. Adhes. Adhes.* 63 (2015) 66–73.

<https://doi.org/10.1016/j.ijadhadh.2015.08.008>.

- [57] J.J.M. Machado, E.A.S. Marques, L.F.M. da Silva, Adhesives and adhesive joints under impact loadings : An overview, *J. Adhes.* 94 (2018) 421–452. <https://doi.org/10.1080/00218464.2017.1282349>.
- [58] N. Taniguchi, T. Nishiwaki, H. Kawada, Tensile strength of unidirectional CFRP laminate under high strain rate Tensile strength, *Adv. Compos. Mater.* 16 (2007) 167–180. <https://doi.org/10.1163/156855107780918937>.
- [59] Y. Goda, T. Sawa, Study on the Effect of Strain Rate of Adhesive Material on the Stress State in Adhesive Joints, *J. Adhes.* 87 (2011) 766–779. <https://doi.org/10.1080/00218464.2011.597308>.
- [60] B.R.K. Blackman, A.J. Kinloch, F.S. Rodriguez Sanchez, W.S. Teo, J.G. Williams, The fracture behaviour of structural adhesives under high rates of testing, *Eng. Fract. Mech.* 76 (2009) 2868–2889. <https://doi.org/10.1016/j.engfracmech.2009.07.013>.
- [61] C. Sun, M.D. Thouless, A.M. Waas, J.A. Schroeder, P.D. Zavattieri, Rate effects in mode-II fracture of plastically deforming , adhesively bonded structures, *Int. J. Fract.* 156 (2009) 111–128. <https://doi.org/10.1007/s10704-009-9339-2>.
- [62] K.B.N.V.S. Ganesh Gupta, M.M. Hiremath, B. Sen, R.K. Prusty, B.C. Ray, Influence of loading rate on adhesively bonded Tin-glass/epoxy single lap joint, *Mater. Today Proc.* 26 (2020) 1850–1854. <https://doi.org/10.1016/j.matpr.2020.02.406>.
- [63] M.D. Banea, F.S.M. de Sousa, L.F.M. da Silva, R.D.S.G. Campilho, A.M. Bastos de Pereira, Effects of Temperature and Loading Rate on the Mechanical Properties of a High Temperature Epoxy Adhesive, *J. Adhes. Sci.* 25 (2011) 2461–2474. <https://doi.org/10.1163/016942411X580144>.
- [64] Z. Jia, G. Yuan, H. Ma, D. Hui, K. Lau, Tensile properties of a polymer-based adhesive at low temperature with different strain rates, *Compos. Part B.* 87 (2016) 227–232. <https://doi.org/10.1016/j.compositesb.2015.10.013>.
- [65] Z. Jia, D. Hui, G. Yuan, J. Lair, K. Lau, F. Xu, Mechanical properties of an epoxy-based adhesive under high strain rate loadings at low temperature environment, *Compos. Part B.* 105 (2016) 132–137.

<https://doi.org/10.1016/j.compositesb.2016.08.034>.

- [66] G. Viana, J. Machado, R. Carbas, M. Costa, L.F.M. da Silva, M. Vaz, M.D. Banea, Strain rate dependence of adhesive joints for the automotive industry at low and high temperatures, *J. Adhes. Sci. Technol.* 4243 (2018) 1–18. <https://doi.org/10.1080/01694243.2018.1464635>.
- [67] F. Zhang, X. Yang, Y. Xia, Q. Zhou, H. Wang, T. Yu, Experimental study of strain rate effects on the strength of adhesively bonded joints after hygrothermal exposure, *Int. J. Adhes. Adhes.* 56 (2015) 3–12. <https://doi.org/10.1016/j.ijadhadh.2014.07.008>.
- [68] ECSS-E-HB-32-21A, Adhesive bonding handbook, Noordwijk, The Netherlands, 2011.
- [69] R.R. Talreja, C. V Singh, *Damage and Failure of Composite Materials*, Cambridge University Press, 2012.
- [70] G.E.P. Box, Science and statistic, *J. Am. Stat. Assoc.* 71 (1976) 791–799. <https://doi.org/10.1080/01621459.1976.10480949>.
- [71] W.C. Carpenter, A Comparison of Numerous Lap Joint Theories for Adhesively Bonded Joints, *J. Adhes.* 35 (1991) 55–73. <https://doi.org/10.1080/00218469108030435>.
- [72] F.M. da S. Lucas, J.C. das N. Paulo, R.D. Adams, A. Wang, J.K. Spelt, Analytical models of adhesively bonded joints — Part II: Comparative study, *Int. J. Adhes. Adhes.* 29 (2009) 331–341. <https://doi.org/10.1016/j.ijadhadh.2008.06.007>.
- [73] L.F.M. da Silva, P.J.C. das Neves, R.D. Adams, J.K. Spelt, Analytical models of adhesively bonded joints — Part I: Literature survey, *Int. J. Adhes. Adhes.* 29 (2009) 319–330. <https://doi.org/10.1016/j.ijadhadh.2008.06.005>.
- [74] L.D.C. Ramalho, R.D.S.G. Campilho, J. Belinha, L.F.M. da Silva, Static strength prediction of adhesive joints: A review, *Int. J. Adhes. Adhes.* 96 (2020) 102451. <https://doi.org/10.1016/j.ijadhadh.2019.102451>.
- [75] K. Tserpes, A. Barroso-Caro, P.A. Carraro, V.C. Beber, I. Floros, W. Gamon, M. Kozłowski, F. Santandrea, M. Shahverdi, D. Skejić, C. Bedon,

- V. Rajčić, A review on failure theories and simulation models for adhesive joints, *J. Adhes.* (2021) 1–62. <https://doi.org/10.1080/00218464.2021.1941903>.
- [76] R.Q. Rodriguez, W.P. de Paiva, P. Sollero, M.R.B. Rodrigues, E.L. da Albuquerque, Failure criteria for adhesively bonded joints, *Int. J. Adhes. Adhes.* 37 (2012) 26–36. <https://doi.org/10.1016/j.ijadhadh.2012.01.009>.
- [77] E. Dragoni, L. Goglio, Adhesive stresses in axially-loaded tubular bonded joints – Part I: Critical review and finite element assessment of published models, *Int. J. Adhes. Adhes.* 47 (2013) 35–45. <https://doi.org/10.1016/j.ijadhadh.2013.09.009>.
- [78] X. He, A review of finite element analysis of adhesively bonded joints, *Int. J. Adhes. Adhes.* 31 (2011) 248–264. <https://doi.org/10.1016/j.ijadhadh.2011.01.006>.
- [79] L.D.C. Ramalho, I.J. Sánchez-Arce, D.C. Gonçalves, J. Belinha, R.D.S.G. Campilho, Numerical analysis of the dynamic behaviour of adhesive joints: A review, *Int. J. Adhes. Adhes.* 118 (2022) 103219. <https://doi.org/10.1016/j.ijadhadh.2022.103219>.
- [80] D.J. Allman, A theory for elastic stresses in adhesive bonded lap joints, *J. Mech. Appl. Math.* (1977) 415–436.
- [81] J.R. Renton, W J; Vinson, Analysis of Adhesively Bonded Joints Between Panels of Composite Materials, *J. Appl. Mech.* 2 (1977) 101–106.
- [82] J.R. Renton, W J; Vinson, The Efficient Design of Adhesive Bonded Joints, *J. Adhes.* 7 (1977) 175–193. <https://doi.org/10.1080/00218467508075049>.
- [83] Z.J. Wu, A. Romeijnb, J. Wardenier, Stress expressions of single-lap adhesive joints of dissimilar adherends, *Compos. Struct.* 38 (1997) 273–280.
- [84] M.Y. Tsai, D.W. Oplinger, J. Morton, Improved theoretical solution for adhesive lap joints, *Int. J. Solids Struct.* 35 (1998) 1163–1185. [https://doi.org/10.1016/S0020-7683\(97\)00097-8](https://doi.org/10.1016/S0020-7683(97)00097-8).
- [85] I.U. Ojalvo, H.L. Eidinoff, Bond Thickness Effects upon Stresses in Single-Lap Adhesive Joints, *AIAA J.* 16 (1978) 204–211.

- [86] D.W. Oplinger, Effects of adherend deflections in single lap joints, 31 (1994) 2565–2587.
- [87] X. Zhao, R.D. Adams, L.F.M. da Silva, A new method for the determination of bending moments in single lap joints, *Int. J. Adhes. Adhes.* 30 (2010) 63–71. <https://doi.org/10.1016/j.ijadhadh.2009.09.001>.
- [88] Z. Jiang, S. Wan, A. Song, An alternative solution for the edge moment factors of the unbalanced adhesive single-lap joint in tension, *Int. J. Adhes. Adhes.* 75 (2017) 1–16. <https://doi.org/10.1016/j.ijadhadh.2017.01.011>.
- [89] L.J. Hart-Smith, *Adhesive-bonded single-lap joints*, 3855 Lakewood Blvd, Long Beach, California, 1973.
- [90] L. Tong, N.S. Wales, Bond strength for adhesive-bonded single-lap joints, *Acta Mech.* 117 (1996) 101–113.
- [91] Q. Luo, L. Tong, Fully-coupled nonlinear analysis of single lap adhesive joints, *Int. J. Solids Struct.* 44 (2007) 2349–2370. <https://doi.org/10.1016/j.ijsolstr.2006.07.009>.
- [92] D.A. Bigwood, A.D. Crocombe, Elastic analysis and engineering design formulae for bonded joints, *Int. J. Adhes. Adhes.* 9 (1989) 229–242.
- [93] L. Goglio, M. Rossetto, Precision of the one-dimensional solutions for bonded double lap joints, *Int. J. Adhes. Adhes.* 31 (2011) 301–314. <https://doi.org/10.1016/j.ijadhadh.2010.10.004>.
- [94] Q. Luo, L. Tong, Linear and higher order displacement theories for adhesively bonded lap joints, *Int. J. Solids Struct.* 41 (2004) 6351–6381. <https://doi.org/10.1016/j.ijsolstr.2004.05.024>.
- [95] J.J. Radice, J.R. Vinson, On the analysis of adhesively bonded structures : A high order semi-elastic adhesive layer model, *Compos. Sci. Technol.* 68 (2008) 376–386. <https://doi.org/10.1016/j.compscitech.2007.06.024>.
- [96] T. Sawa, J. Liu, K. Nakano, J. Tanaka, A two-dimensional stress analysis of single-lap adhesive joints of dissimilar adherends subjected to tensile loads, *J. Adhes. Sci. Technol.* 14 (2000) 43–66. <https://doi.org/10.1163/156856100742104>.
- [97] J.L. Lubkin, E. Reissner, *Stress Distribution and Design Data for Adhesive*

- Lap Joints Between Circular Tubes, *Trans. ASME*. 78 (1956) 1213–1221.
<https://doi.org/https://doi.org/10.1115/1.4013993>.
- [98] Y.P. Shi, S. Cheng, Analysis of Adhesive-Bonded Cylindrical Lap Joints Subjected to Axial Load, *J. Eng. Mech.* 119 (1993) 584–602.
[https://doi.org/https://doi.org/10.1061/\(ASCE\)0733-9399\(1993\)119:3\(584\)](https://doi.org/https://doi.org/10.1061/(ASCE)0733-9399(1993)119:3(584)).
- [99] H. Nayeb-Hashemi, J.N. Rossettos, A.P. Melo, Multiaxial fatigue life evaluation of tubular adhesively bonded joints, *Int. J. Adhes. Adhes.* 17 (1997) 55–63. [https://doi.org/https://doi.org/10.1016/S0143-7496\(96\)00023-1](https://doi.org/https://doi.org/10.1016/S0143-7496(96)00023-1).
- [100] N. Pugno, A. Carpintieri, Tubular adhesive joints under axial load, *Trans. ASME*. 70 (2003) 832–839. <https://doi.org/10.1115/1.1604835>.
- [101] O. Nemes, F. Lachaud, Contribution to the study of cylindrical adhesive joining, *Int. J. Adhes. Adhes.* 26 (2006) 474–480.
<https://doi.org/10.1016/j.ijadhadh.2005.07.009>.
- [102] O. Nemes, F. Lachaud, Journal of Adhesion Science and Modeling of Cylindrical Adhesively Bonded Joints, *Int. J. Adhes. Bond. Joints*. 23 (2009) 1383–1393. <https://doi.org/10.1163/156856109X432983>.
- [103] H. Saito, H. Tani, Vibration of bonded beams with a single lap adhesive joint, *J. Sound Vib.* 92 (1984) 299–309.
[https://doi.org/https://doi.org/10.1016/0022-460X\(84\)90563-7](https://doi.org/https://doi.org/10.1016/0022-460X(84)90563-7).
- [104] S. He, M.D. Rao, Vibration analysis of adhesively bonded lap joint, part I: theory, *J. Sound Vib.* 152 (1992) 405–416.
[https://doi.org/https://doi.org/10.1016/0022-460X\(92\)90478-G](https://doi.org/https://doi.org/10.1016/0022-460X(92)90478-G).
- [105] M.D. Rao, S. He, Vibration analysis of adhesively bonded lap joint, part II: numerical solution, *J. Sound Vib.* 152 (1992) 417–425.
[https://doi.org/https://doi.org/10.1016/0022-460X\(92\)90479-H](https://doi.org/https://doi.org/10.1016/0022-460X(92)90479-H).
- [106] J. Pirvics, Two Dimensional Distributions in Adhesive Bonded Composite Structures, *J. Adhes.* 6 (1974) 207–228.
<https://doi.org/10.1080/00218467408075027>.
- [107] R.D. Adams, N.A. Peppiatt, Stress Analysis of Adhesive Bonded Tubular Lap Joints Stress Analysis of Adhesive Bonded Tubular Lap Joints, *J.*

- Adhes. 9 (1977) 1–18. <https://doi.org/10.1080/00218467708075095>.
- [108] R.D. Adams, J.A. Harris, The influence of local geometry on the strength of adhesive joints, *Int. J. Adhes. Adhes.* 7 (1987) 69–80.
- [109] R.D. Adams, V. Mallick, A Method for the Stress Analysis of Lap Joints A Method for the Stress Analysis of Lap Joints, *J. Adhes.* 38 (1992) 199–217. <https://doi.org/10.1080/00218469208030455>.
- [110] R.D. Adams, N.A. Peppiatt, Stress analysis of adhesive-bonded lap joints, *J. Strain Anal. Eng. Des.* 9 (1974) 185–196. <https://doi.org/10.1243/03093247V093185>.
- [111] R.D. Adams, Stress analysis of axisymmetric butt joints loaded in torsion and tension, *J. Strain Anal. Eng. Des.* 13 (1978) 1–10. <https://doi.org/10.1243/03093247V131001>.
- [112] A.D. Crocombe, R.D. Adams, Influence of the Spew Fillet and other Parameters on the Stress Distribution in the Single Lap Joint, *J. Adhes.* 13 (1981) 141–155. <https://doi.org/10.1080/00218468108073182>.
- [113] J.A. Harris, R.D. Adams, Strength prediction of bonded single lap joints by non-linear finite element methods, *Int. J. Adhes. Adhes.* 4 (1984) 65–78.
- [114] M. You, Z. Yan, X. Zheng, H. Yu, Z. Li, A numerical and experimental study of adhesively bonded aluminium single lap joints with an inner chamfer on the adherends, *Int. J. Adhes. Adhes.* 28 (2007) 71–76. <https://doi.org/10.1016/j.ijadhadh.2007.06.001>.
- [115] M. You, Z. Li, X. Zheng, S. Yu, G. Li, D. Sun, A numerical and experimental study of preformed angle in the lap zone on adhesively bonded steel single lap joint, *Int. J. Adhes. Adhes.* 29 (2009) 280–285. <https://doi.org/10.1016/j.ijadhadh.2008.07.001>.
- [116] S. Kumar, P.C. Pandey, Behaviour of Bi-adhesive Joints, *J. Adhes. Sci. Technol.* 24 (2010) 1251–1281. <https://doi.org/10.1163/016942409X12561252291982>.
- [117] A.D. Crocombe, Y.X. Hua, W.K. Loh, M.A. Wahab, I.A. Ashcroft, Predicting the residual strength for environmentally degraded adhesive lap joints, *Int. J. Adhes. Adhes.* 26 (2006) 325–336.

<https://doi.org/10.1016/j.ijadhadh.2005.04.003>.

- [118] A. Mubashar, I.A. Ashcroft, G.W. Critchlow, A.D. Crocombe, Modelling Cyclic Moisture Uptake in an Epoxy Adhesive, *J. Adhes.* 85 (2009) 711–735. <https://doi.org/https://doi.org/10.1080/00218460902997224>.
- [119] L.F.M. da Silva, R.D. Adams, Stress-free temperature in a mixed- adhesive joint, *J. Adhes. Sci. Technol.* 20 (2006) 1705–1726. <https://doi.org/10.1163/156856106779024436>.
- [120] L.F.M. da Silva, R.D. Adams, Adhesive joints at high and low temperatures using similar and dissimilar adherends and dual adhesives, *Int. J. Adhes. Adhes.* 27 (2007) 216–226. <https://doi.org/10.1016/j.ijadhadh.2006.04.002>.
- [121] L.F.M. da Silva, R.D. Adams, Joint strength predictions for adhesive joints to be used over a wide temperature range, *Int. J. Adhes. Adhes.* 27 (2007) 362–379. <https://doi.org/10.1016/j.ijadhadh.2006.09.007>.
- [122] L.D.R. Grant, R.D. Adams, F.M. Lucas, Experimental and numerical analysis of single-lap joints for the automotive industry, *Int. J. Adhes. Adhes.* 29 (2009) 405–413. <https://doi.org/10.1016/j.ijadhadh.2008.09.001>.
- [123] A. Kaya, M.S. Tekeliog, F. Findik, Effects of various parameters on dynamic characteristics in adhesively bonded joints, *Mater. Lett.* 58 (2004) 3451–3456. <https://doi.org/10.1016/j.matlet.2004.07.001>.
- [124] X. He, Numerical and experimental investigations of the dynamic response of bonded beams with a single-lap joint, *Int. J. Adhes. Adhes.* 37 (2012) 79–85. <https://doi.org/10.1016/j.ijadhadh.2012.01.008>.
- [125] X. He, Finite element analysis of torsional free vibration of adhesively bonded single-lap joints, *Int. J. Adhes. Adhes.* 48 (2014) 59–66. <https://doi.org/10.1016/j.ijadhadh.2013.09.017>.
- [126] D.S. Dugdale, Yielding of steel sheets containing slits, *J. Mech. Phys. Solids.* 8 (1960) 100–104. [https://doi.org/10.1016/0022-5096\(60\)90013-2](https://doi.org/10.1016/0022-5096(60)90013-2).
- [127] G.I. Barenblatt, The Mathematical Theory of Equilibrium Cracks in Brittle Fracture, *Adv. Appl. Mech.* 7 (1962) 5–129. [https://doi.org/10.1016/S0065-2156\(08\)70121-2](https://doi.org/10.1016/S0065-2156(08)70121-2).
- [128] A. Hillerborg, M. Modéer, P.E. Petersson, Analysis of crack formation and

- crack growth in concrete by means of fracture mechanics and finite elements, *Cem. Concr. Res.* 6 (1976) 773–781. [https://doi.org/10.1016/0008-8846\(76\)90007-7](https://doi.org/10.1016/0008-8846(76)90007-7).
- [129] H. Khoramishad, A.D. Crocombe, K.B. Katnam, I.A. Ashcroft, Predicting fatigue damage in adhesively bonded joints using a cohesive zone model, *Int. J. Fatigue.* 32 (2010) 1146–1158. <https://doi.org/10.1016/j.ijfatigue.2009.12.013>.
- [130] R.D.S.G. Campilho, *Strength prediction of adhesively-bonded joints*, Taylor & Francis, 2017.
- [131] G. Alfano, On the influence of the shape of the interface law on the application of cohesive-zone models, *Compos. Sci. Technol.* 66 (2006) 723–730. <https://doi.org/10.1016/j.compscitech.2004.12.024>.
- [132] R.D.S.G. Campilho, M.D. Banea, J.A.B.P. Neto, L.F.M. Silva, Modelling adhesive joints with cohesive zone models: effect of the cohesive law shape of the adhesive layer, *Int. J. Adhes. Adhes.* 44 (2013) 48–56. <https://doi.org/10.1016/j.ijadhadh.2013.02.006>.
- [133] P.A. Gustafson, A.M. Waas, The influence of adhesive constitutive parameters in cohesive zone finite element models of adhesively bonded joints, *Int. J. Solids Struct.* 46 (2009) 2201–2215. <https://doi.org/10.1016/j.ijsolstr.2008.11.016>.
- [134] R.D.S.G. Campilho, M.D. Banea, J.A.B.P. Neto, L.F.M. da Silva, Modelling of Single-Lap Joints Using Cohesive Zone Models: Effect of the Cohesive Parameters on the Output of the Simulations Modelling of Single-Lap Joints Using Cohesive Zone Models: Effect of the Cohesive Parameters on the Output of the Simulations, *J. Adhes.* 88 (2012) 513–533. <https://doi.org/10.1080/00218464.2012.660834>.
- [135] C. Bathias, There is no infinite fatigue life in metallic materials, *Fatigue Fract. Eng. Mater. Struct.* 22 (1999) 559–565. <https://doi.org/10.1046/j.1460-2695.1999.00183.x>.
- [136] C. Bathias, L. Drouillac, P. Le François, How and why the fatigue S-N curve does not approach a horizontal asymptote, *Int. J. Fatigue.* 23 (2001) 143–151. [https://doi.org/10.1016/s0142-1123\(01\)00123-2](https://doi.org/10.1016/s0142-1123(01)00123-2).

- [137] I. Marines-garcia, P.C. Paris, H. Tada, C. Bathias, Fatigue crack growth from small to long cracks in VHCF with surface initiations, *Int. J. Fatigue*. 29 (2007) 2072–2078. <https://doi.org/10.1016/j.ijfatigue.2007.03.015>.
- [138] Y. Murakami, S. Beretta, Small Defects and Inhomogeneities in Fatigue Strength: Experiments, Models and Statistical Implications, *Extremes*. 2 (1999) 123–147. <https://doi.org/10.1023/A:1009976418553>.
- [139] Y. Murakami, Material defects as the basis of fatigue design, *Int. J. Fatigue*. 41 (2012) 2–10. <https://doi.org/10.1016/j.ijfatigue.2011.12.001>.
- [140] B. Pyttel, D. Schwerdt, C. Berger, Very high cycle fatigue - Is there a fatigue limit?, *Int. J. Fatigue*. 33 (2011) 49–58. <https://doi.org/10.1016/j.ijfatigue.2010.05.009>.
- [141] A. Tridello, C.B. Niutta, M. Rossetto, F. Berto, D.S. Paolino, Statistical models for estimating the fatigue life , the stress – life relation , and the P-S-N curves of metallic materials in Very High Cycle Fatigue : A review, *Fatigue Fract. Eng. Mater. Struct.* (2022) 332–370. <https://doi.org/10.1111/ffe.13610>.
- [142] W.P. Mason, Piezoelectric crystals and their application to ultrasonic, New York, 1949.
- [143] L.E. Willert, Ultrasonic fatigue, *Int. Met. Rev.* 25 (1980) 65–77. <https://doi.org/10.1179/imtr.1980.25.1.65>.
- [144] A. Rotem, Accelerated fatigue testing method, *Int. J. Fatigue*. 3 (1981) 211–215. [https://doi.org/10.1016/0142-1123\(81\)90023-2](https://doi.org/10.1016/0142-1123(81)90023-2).
- [145] L.E. Willert, Ultrasonic fatigue Ultrasonic fatigue, *Int. Met. Rev.* 25 (1980) 65–78. <https://doi.org/10.1179/imtr.1980.25.1.65>.
- [146] I.C. Rosca, M.I. Pop, N. Cretu, Experimental and numerical study on an ultrasonic horn with shape designed with an optimization algorithm, *Appl. Acoust.* 95 (2015) 60–69. <https://doi.org/10.1016/j.apacoust.2015.02.009>.
- [147] P. Costa, M. Vieira, L. Reis, A. Ribeiro, M. de Freitas, New specimen and horn design for combined tension and torsion ultrasonic fatigue testing in the very high cycle fatigue regime, *Int. J. Fatigue*. 103 (2017) 248–257. <https://doi.org/10.1016/j.ijfatigue.2017.05.022>.

- [148] S. Lin, H. Guo, J. Xu, Actively adjustable step-type ultrasonic horns in longitudinal vibration, *J. Sound Vib.* 419 (2018) 367–379. <https://doi.org/10.1016/j.jsv.2018.01.033>.
- [149] Testing equipment at Politecnico di Torino, (n.d.). https://www.dimeas.polito.it/la_ricerca/gruppi/meccanica_dei_materiali_e_delle_giunzioni_modelli_fatica_impatto_e_prove/attrezzature_disponibili.
- [150] A. Tridello, D.S. Paolino, G. Chiandussi, M. Rossetto, VHCF response of AISI H13 steel: assessment of size effects through Gaussian specimens, *Procedia Eng.* 109 (2015) 121–127. <https://doi.org/10.1016/j.proeng.2015.06.218>.
- [151] A. Tridello, VHCF response of Gaussian specimens made of high-strength steels: comparison between unrefined and refined AISI H13, *Fatigue Fract. Eng. Mater. Struct.* 40 (2017) 1676–1689. <https://doi.org/10.1111/ffe.12610>.
- [152] J.M. Zhang, S.X. Li, Z.G. Yang, G.Y. Li, W.J. Hui, Y. Weng, Influence of inclusion size on fatigue behavior of high strength steels in the gigacycle fatigue regime, *Int. J. Fatigue.* 29 (2007) 765–771.
- [153] K.S. Ravi Chandran, Duality of fatigue failures of materials caused by Poisson defect statistics of competing failure modes, *Nat. Mater.* 4 (2005) 303–308.
- [154] G.T. Cashman, A review of competing modes fatigue behavior, *Int. J. Fatigue.* 32 (2010) 492–496.
- [155] ASTM E739–91 Reapproved 2004. Standard Practice for Statistical Analysis of Linear or Linearized Stress-Life (S-N) and Strain-Life (ϵ -N) Fatigue Data, ASTM, Philadelphia, USA., 2004.
- [156] ISO standard 12107:2003. Metallic Materials– Fatigue Testing– Statistical Planning and Analysis of Data., ISO, Geneve, Switzerland., 2003.
- [157] S. Ross, A first course in probability, 8th editio, Pearson, 2010.
- [158] W. Nelson, Accelerated Testing: Statistical Models, Test Plans, and Data Analyses, JohnWiley & Sons, New York, USA, 1990.
- [159] D.S. Paolino, A. Tridello, G. Chiandussi, M. Rossetto, Statistical

- distributions of Transition Fatigue Strength and Transition Fatigue Life in duplex S–N fatigue curves, *Theor. Appl. Fract. Mech.* (2015) 31–39. <https://doi.org/dx.doi.org/10.1016/j.tafmec.2015.07.006>.
- [160] D.S. Paolino, A. Tridello, G. Chiandussi, M. Rossetto, Statistical estimation of duplex S–N curves, *Key Eng. Mater.* 664 (2015) 285–294. <https://doi.org/10.4028/www.scientific.net/KEM.664.285>.
- [161] J.N. Timoshenko, S.P.; Goodier, *Theory of Elasticity*, McGraw Hil, 1951.
- [162] M.L. Williams, Stress Singularities Resulting From Various Boundary Conditions in Angular Corners of Plates in Extension, *J. Appl. Mech.* (1952) 526–528. <https://doi.org/10.1115/1.4010553>.
- [163] M.L. Williams, On the stress distribution at the base of a stationary crack, *J. Appl. Mech.* (1956) 109–114. <https://doi.org/10.1115/1.3640470>.
- [164] M.L. Williams, the Stresses Around a Fault or Crack in Dissimilar Media, *Bull. Seismol. Soc. Am.* 49 (1959) 199–204.
- [165] A.H. England, On stress singularities in linear elasticity, *Int. J. Eng. Sci.* 9 (1971) 571–585.
- [166] M.L. Dunn, W.A.N. Suwlto, S. Cunningham, Stress intensities at notch singularities, *Eng. Fract. Mech.* 57 (1997) 417–430.
- [167] G.B. Sinclair, Stress singularities in classical elasticity – I: Removal , interpretation , and analysis, *Appl. Mech. Rev.* 57 (2004). <https://doi.org/10.1115/1.1762503>.
- [168] G.B. Sinclair, Stress singularities in classical elasticity — II : Asymptotic identification, *Appl. Mech. Rev.* (2004). <https://doi.org/10.1115/1.1767846>.
- [169] P. Lazzarin, R. Zambardi, P. Livieri, Plastic notch stress intensity factors for large V-shaped notches under mixed load conditions, *Int. J. Fract.* (2001) 361–377.
- [170] M. Ciavarella, G. Meneghetti, On fatigue limit in the presence of notches : classical vs . recent unified formulations, *Int. J. Fatigue.* 26 (2004) 289–298. [https://doi.org/10.1016/S0142-1123\(03\)00106-3](https://doi.org/10.1016/S0142-1123(03)00106-3).
- [171] A.B. De Morais, Calculation of stress intensity factors by the force method, *Eng. Fail. Anal.* 74 (2007) 739–750.

<https://doi.org/10.1016/j.engfracmech.2006.06.017>.

- [172] F. Berto, P. Lazzarin, A. Kotousov, S. Harding, Out-of-plane singular stress fields in V-notched plates and welded lap joints induced by in-plane shear load conditions, *Fatigue Fract. Eng. Mater. Struct.* (2010) 291–304. <https://doi.org/10.1111/j.1460-2695.2010.01518.x>.
- [173] F. Zhu, X. Ji, P. He, B. Zheng, K. Zhang, On stress singularity at crack tip in elasticity, *Results Phys.* 13 (2019) 102210. <https://doi.org/10.1016/j.rinp.2019.102210>.
- [174] W. Shen, Y. Qiu, Y. Hu, E. Liu, J. Pan, A simplified method for evaluating singular stress field of V-shaped and U-shaped notches with different opening angle, *Ocean Eng.* 210 (2020). <https://doi.org/10.1016/j.oceaneng.2020.107352>.
- [175] D. Radaj, State-of-the-art review on extended stress intensity factor concepts, *Fatigue Fract. Eng. Mater. Struct.* (2013) 1–28. <https://doi.org/10.1111/ffe.12120>.
- [176] D.B. Bogy, Edge-bonded dissimilar Orthogonal Elastic wedges under normal and shear loading, *J. Appl. Mech.* (1968) 460–466.
- [177] J. Dundurs, Discussion on Edge-bonded dissimilar orthogonal Elastic wedges under normal and shear loading, *J. Appl. Mech.* (1969) 650–652.
- [178] D.B. Bogy, Two edge-bonded elastic wedges of different materials and wedge angles under surface tractions, *J. Appl. Mech.* 38 (1971) 377–386. <https://doi.org/10.1115/1.3408786>.
- [179] V.. Hein, F. Erdogan, Stress Singularities in a Two-Material Wedge, *Int. J. Fract. Mech.* 7 (1971) 317–330.
- [180] Y.-H. Liu, J.-Q. Xu, H.-J. Ding, Order of singularity and singular stress field about an axisymmetric interface corner in three-dimensional isotropic elasticity, *Int. J. Solids Struct.* 36 (1999) 4425–4445.
- [181] H.L. Groth, Stress singularities and fracture at interface corners in bonded joints, *Int. J. Adhes. Adhes.* 8 (1988).
- [182] E.. Reddy Jr., Intensity interface of the stress singularity at the corner between a bonded elastic and rigid layer, *Eng. Fract. Mech.* 36 (1990) 575–

583.

- [183] E.D. Reedy Jr., Intensity of the stress singularity at the interface corner of a bonded elastic layer subjected to shear, *Eng. Fract. Mech.* 38 (1991) 273–281.
- [184] C.H. Wang, L.R.F. Rose, Compact solutions for the corner singularity in bonded lap joints, *Int. J. Adhes. Adhes.* 20 (2000) 145–154.
- [185] N.A. Akisanya, A.R.; Fleck, Interfacial cracking from the free-edge of a long bi-material strip, *Int. J. Solids Struct.* 34 (1997) 1645–1665.
- [186] A.R. Akisanya, C.S. Meng, Initiation of fracture at the interface corner of bi-material joints, *J. Mech. Phys. Solids.* 51 (2003) 27–46.
- [187] D.R. Lefebvre, D.A. Dillard, A Stress Singularity Approach for the Prediction of Fatigue Crack Initiation in Adhesive Bonds . Part 1 : Theory, *J. Adhes.* 70 (1999) 119–138. <https://doi.org/10.1080/00218469908010490>.
- [188] P. Lazzarin, M. Quaresimin, P. Ferro, A two-term stress function approach to evaluate stress distributions in bonded joints of different geometries, *J. Strain Anal. Eng. Des.* 37 (2002) 385–398. <https://doi.org/10.1243/030932402760203856>.
- [189] M. Quaresimin, M. Ricotta, Stress intensity factors and strain energy release rates in single lap bonded joints in composite materials, *Compos. Sci. Technol.* 66 (2006) 647–656. <https://doi.org/10.1016/j.compscitech.2005.07.036>.
- [190] N.H. Chen D.H., Intensity of singular stress field near the interface edge point of a bonded strip, *Trans JSME.* 59 (1993).
- [191] R. Li, N. Noda, R. Takaki, Y. Sano, Y. Takase, T. Miyazaki, Most suitable evaluation method for adhesive strength to minimize bend effect in lap joints in terms of the intensity of singular stress field, *Int. J. Adhes. Adhes.* 86 (2018) 45–58. <https://doi.org/10.1016/j.ijadhadh.2018.08.006>.
- [192] N. Noda, F. Ren, R. Takaki, Z. Wang, K. Oda, T. Miyazaki, Intensity of singular stress field over the entire bond line thickness range useful for evaluating the adhesive strength for plate and cylinder butt joints, *Int. J. Adhes. Adhes.* 85 (2018) 234–250.

<https://doi.org/10.1016/j.ijadhadh.2018.05.013>.

- [193] T.P. Lang, P.K. Mallick, Effect of spew geometry on stresses in single lap adhesive joints, *Int. J. Adhes. Adhes.* 18 (1998) 167–177.
- [194] R. Breto, A. Chiminelli, M. Lizaranzu, R. Rodríguez, Study of the singular term in mixed adhesive joints, *Int. J. Adhes. Adhes.* 76 (2017) 11–16. <https://doi.org/10.1016/j.ijadhadh.2017.02.002>.
- [195] P. Galvez, N. Noda, R. Takaki, Y. Sano, T. Miyazaki, J. Abenojar, M. Angel, Intensity of singular stress field (ISSF) variation as a function of the Young's modulus in single lap adhesive joints, *Int. J. Adhes. Adhes.* 95 (2019). <https://doi.org/10.1016/j.ijadhadh.2019.102418>.
- [196] A. Barroso, J.C. Marín, V. Manti, F. París, *International Journal of Adhesion and Adhesives* Premature failures in standard test specimens with composite materials induced by stress singularities in adhesive joints, 97 (2020). <https://doi.org/10.1016/j.ijadhadh.2019.102478>.
- [197] K.J. Bathe, *Finite Element Procedures in Engineering Analysis*, (1996).
- [198] G.B. Sinclair, Effective Convergence Checks for Verifying Finite Element Stresses at Two-Dimensional Stress Concentrations, 1 (2017) 1–8. <https://doi.org/10.1115/1.4034977>.
- [199] G.B. Sinclair, J.R. Beisheim, A.A. Kardak, On the detection of stress singularities in finite element analysis, *J. Appl. Mech. Trans. ASME.* 86 (2019) 1–18. <https://doi.org/10.1115/1.4041766>.
- [200] G.B. Sinclair, On ensuring structural integrity for configurations with stress singularities : a review, (2016) 523–535. <https://doi.org/10.1111/ffe.12425>.
- [201] S.S. Pageau, S.B. Biggers, Enrichment of Finite Elements with numerical solutions for singular stress field, *Int. J. Numer. Methods Eng.* 40 (1997) 2693–2713.
- [202] Z. Xia, M. Al, A. Khan, K. Chowdhuri, F. Ju, A New Test Method for the Measurement of Normal- Shear Bonding Strength at Bi-Material Interface A New Test Method for the Measurement of Normal-Shear Bonding Strength at Bi-Material Interface, *Mech. Adv. Mater. Struct.* 20 (2013) 571–579. <https://doi.org/10.1080/15376494.2011.643278>.

- [203] A. Barroso, B. Lauke, V. Manti, F. París, Tensile and shear strength of bimaterial interfaces within composite materials, *Compos. Sci. Technol.* 124 (2016) 81–88. <https://doi.org/10.1016/j.compscitech.2016.01.003>.
- [204] A.Y. Fedorov, V.P. Matveenko, Designing of interlayers between materials with minimum stress level at the interface, *Int. J. Adhes. Adhes.* 111 (2021) 102963. <https://doi.org/10.1016/j.ijadhadh.2021.102963>.
- [205] O.C. Zienkiewicz, *The Finite Element Method for Solid and Structural Mechanics*, Butterworth-Heinemann, 2000.
- [206] O.C. Zienkiewicz, *The Finite Element Method - its Basis and Fundamentals*, Butterworth-Heinemann, 2000.
- [207] J.B. Ransom, N.F. Knight, Global/local stress analysis of composite panels, *Comput. Struct.* 37 (1990) 375–395. [https://doi.org/10.1016/0045-7949\(90\)90027-Y](https://doi.org/10.1016/0045-7949(90)90027-Y).
- [208] J.N. Reddy, On computational schemes for global-local stress analysis, Conference (1989).
- [209] G.M.L. Gladwell, *Practical approximation theory*, Univ. Waterloo Press. Ontario. (1974).
- [210] R.R. Craig, A.J. Kurdila, *Fundamentals of structural dynamics*, John Wiley & Sons, Hoboken, New Jersey, 2006.
- [211] Technical description of SikaPower 1277, (n.d.). <https://ita.sika.com/it/industria/trasporti/adesivi-per-metalli/sikapower-1277.html>.
- [212] A. International, Standard Test Methods for Tension Testing of Metallic Materials, E8/E8M – 21, (2021). https://doi.org/10.1520/E0008_E0008M-21.
- [213] BS EN ISO 527-3:2018. *Plastics – Determination of tensile properties*, (2018).
- [214] H. Mevada, D. Patel, Experimental determination of structural damping of different materials, *Procedia Eng.* 144 (2016) 110–115. <https://doi.org/10.1016/j.proeng.2016.05.013>.
- [215] D. Pederbelli, L. Goglio, A. Tridello, D.S. Paolino, Effects of singular and

non-singular stress fields on very high cycle fatigue life of adhesive joints,
Fatigue Fract. Eng. Mater. Struct. (2023) 1–16.
<https://doi.org/10.1111/ffe.14171>.

- [216] D. Pederbelli, L. Goglio, D.S. Paolino, M. Rossetto, A. Tridello, Effect of Loading Frequency on the Fatigue Response of Adhesive Joints up to the VHCF Range, Appl. Sci. 13 (2023) 12967.
<https://doi.org/10.3390/app132312967>.